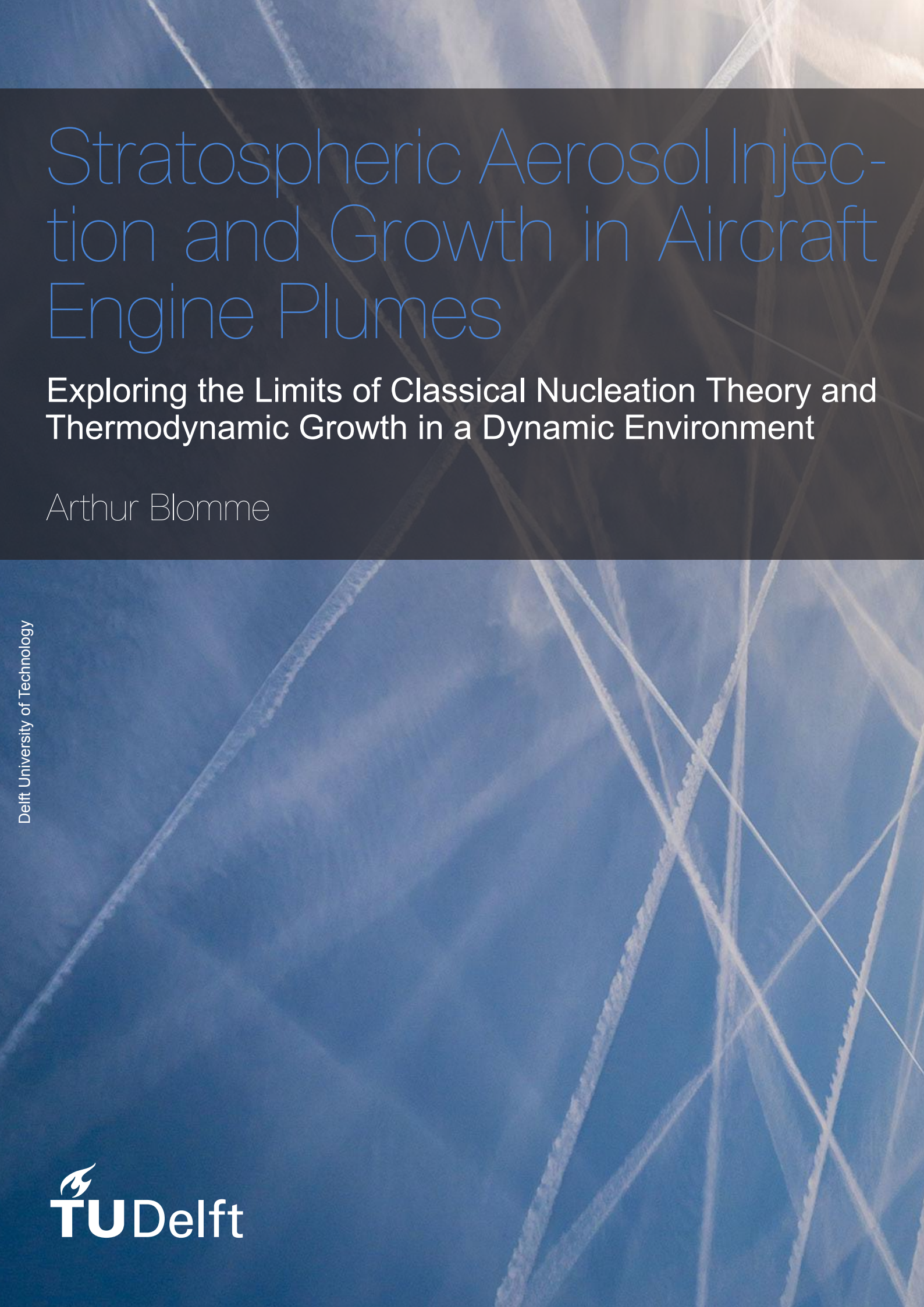

Stratospheric Aerosol Injection and Growth in Aircraft Engine Plumes

Exploring the Limits of Classical Nucleation Theory and Thermodynamic Growth in a Dynamic Environment

Arthur Blomme

Delft University of Technology

TU Delft

Stratospheric Aerosol Injection and Growth in Aircraft Engine Plumes

Exploring the Limits of Classical Nucleation Theory and Thermodynamic Growth in a Dynamic Environment

by

Arthur Blomme

in partial fulfillment of the requirements for the degree of
Master of Science in Aerospace Engineering at the Delft University of Technology.

Student number:	4551176
Supervisors:	Dr. Steven J. Hulshoff MSc. Iris de Vries MSc. Martin Janssens
Thesis Committee:	Dr. Marc I. Gerritsma Dr. Steven J. Hulshoff Dr. Feijia Yin
Institution:	Delft University of Technology
Place:	Faculty of Aerospace Engineering, Delft
Project Duration:	March, 2022 - April, 2023

Cover Image: Contrails over Benelux, North Sea & Baltic Sea (EUMETSAT, 2004)

TU Delft

Acknowledgments

I would like to express my gratitude to my academic supervisor, Prof. Steven Hulshoff, who has been a source of continued support over the past couple of months. I cannot thank my academic advisors, Iris de Vries and Martin Janssens, enough. Their devotion and passion for Atmospheric Sciences is something I will continue to cherish. Our weekly meetings were always a delight to attend, often resulting in new insights, and new research paths to explore. Thanks for making my master thesis a work of boundless curiosity and drive, instead of the strenuous exercise it often turns out to be.

My gratitude goes out overseas to Dr. Colleen Golja living in Cambridge, Massachusetts, who gratefully shared her scientific knowledge on modeling aerosol microphysics, with the occasional piece of advice on life. Her openness to scientific collaboration is worthy of recognition. Furthermore, I want to thank Alex for providing the necessary support material to complete my research.

A heartfelt thanks to my roommates Simon, Bart H., Bart D., Florian, Simone, Marcello, Thomas, Mathieu, Sebastien, Panagiotis, and Shishi, for being my family, therapist, nightlife caretaker, deadline companion, and boulder buddy.

To my greatest supporter, Inez, whom I have loved since our first dance. My source of motivation, cheerfulness, and patience. You bring out the best in me. To Jessica and Sven, my long-distance unapologetic friends.

Last but not least, I am forever thankful to my parents, Jan and Veronique. For sharing your values, love, strength, and wisdom. None of this would have been possible without you. To my brothers and sisters, thanks for all the laughs.

Arthur Blomme
Delft, April 2023

Abstract

Stratospheric Aerosol Injection (SAI) is a geoengineering method to mitigate the effects of increased greenhouse gas concentrations in the Earth's atmosphere, and to prevent further global warming. SAI does not reverse climate change, it merely counteracts its symptoms by offsetting the radiative forcing of greenhouse gases, and it should be accompanied by aggressive programmes of Carbon Dioxide Removal to cool down the climate. Operational studies suggest that the injection of condensable vapor from specialized high-altitude aircraft would be a reasonable option to form the desired aerosol particles. Yet, remarkably little is known about the growth evolution of aerosol inside a jet engine wake, especially in light of SAI where high initial concentrations of condensable vapor are injected into the exhaust stream. The lack of resolution in the flow field obscures a lot of the intricacies of the aerosol formation process, and raises serious doubts on the steerability of SAI, which is the capacity to spatially and temporally control its effects both in nature and scale. Without reassurance that the steerability requirement can be satisfied, the potential risks to the global ecosystem would be too high. In this respect, the study investigates the mechanisms within the near-field of a jet engine wake that lead to the creation of aerosols and subsequent growth, when accounting for local variations in temperature and relative humidity. This is done through a decoupled plume dispersion model that includes a flow solver which resolves the average velocity and turbulent intensity of the flow, a sectional chemistry module which includes all the relevant microphysical processes that affect aerosol growth, and a diffusion-advection model which calculates the displacement of aerosol, vapor, and chemiions in the flow field. In addition, several modeling errors are identified in classical thermodynamic approaches to high-density aerosol formation. Results demonstrate that the onset of particle formation in the plume is complex, and is heavily dependent on the injection concentration of sulfuric acid vapor and the mixing rate of the plume. Different aerosol particle sizes are formed depending on the location in the plume, leading to a non-uniform distribution of the volume-mean radius across the plume's cross-sectional area. There is also a strong indication that core particles experience preferential growth, which implies that the final particle distribution at the end of the plume's lifetime might not be as uni-modal as self-limited theory predicts. The study concludes with a list of recommendations to solve the challenges that remain in order to truly understand the early growth evolution of sulfate aerosol in a jet engine wake.

Contents

Nomenclature

Abbreviations

Abbreviation	Definition
AEAP	Atmospheric Effects of Aviation Program
APCEMM	Aircraft Plume Chemistry, Emissions, and Microphysics Model
BHN	Binary Homogeneous Nucleation
CERN	European Organization for Nuclear Research
CIAP	Climatic Impact Assessment Program
CLOUD	Cosmics Leaving OUtdoor Droplets experiments
CN	Condensation Nuclei
CNT	Classical Nucleation Theory
CTM	Chemistry-Transport Model
GCM	General Circulation Model
GPM	Gaussian Plume Model
GSP	Gas turbine Simulation Program
IIC	Ion-Induced Coagulation
IIN	Ion-Induced Nucleation
IMN	Ion-Mediated Nucleation
IPCC	Intergovernmental Panel on Climate Change
LES	Large-Eddy Simulation
LTO	Landing and Takeoff
PDM	Plume Dispersion Model
PDM	Permanent Dipole Moment
nvPM	Non-volatile Particulate Matter
vPM	Volatile Particulate Matter
PSD	Particle Size Distribution
QC	Quantum-Chemical
RANS	Reynolds-Averaged Navier-Stokes equations
SAI	Stratospheric Aerosol Injection
SRM	Solar Radiation Management
THN	Ternary Homogeneous Nucleation
VMR	Volume-Mean Radius

Symbols

Symbol	Definition	Unit
a	Speed of sound	[m s^{-1}]
A_c	Cross-sectional area	[m^2]
$A_{p,t}$	Total particle surface area per unit volume	[µm^2 cm^{-3}]
A_s	Surface area	[µm^2]
b_a	Accommodation coefficient	[-]
b_s	Sticking coefficient	[-]
B	Particle mobility	[s kg^{-1}]
c_v	Specific heat capacity at constant volume	[J kg^{-1} K^{-1}]
$\bar{c}$	Mean of the magnitude of the velocity of a particle	[m s^{-1}]
C	Pre-exponential term of the nucleation rate	[-]
C_D	Calibration constant of the k-ϵ_k turbulence model	[-]
CFL	Courant-Friedrichs-Lewy number	[-]
d	diameter	[µm]
$\hat{d}_{pg}$	Median particle diameter	[µm]
D_B	Brownian diffusion coefficient	[cm^2 s^{-1}]
D_M	Molecular diffusion coefficient	[cm^2 s^{-1}]
D_T	Turbulent diffusion coefficient	[cm^2 s^{-1}]
e	Euler's number (= 2.71828182...)	[-]
E_{coag}	Coagulation or collection efficiency	[-]
EI	Emission index	[g kg^{-1}]
f	Net body forces per unit mass acting on a fluid	[N kg^{-1}]
f_{co}	Correction factor for heteromolecular condensation	[-]
f_{cu}	Cunningham correction factor	[-]
f_{ee}	Electrostatic enhancement factor	[-]
f_{h}	Correction factor for heterogeneous nucleation	[-]
f_{m}	Scaled mixing parameter	[-]
f_{t}	Scaled time parameter	[-]
f_{FSM}	Fuel sulfur mass content fraction	[g kg^{-1}]
f_{HS}	Fraction of SO_x oxidized to S(VI)	[-]
F	Force	[N]
FF	Fuel flow rate	[kg s^{-1}]
g	Gravitational acceleration	[m s^{-2}]
G	Gibbs free energy	[J]
ΔG	Gibbs free energy of nucleus formation	[J]
I	Sources or sinks of aerosol	[cm^{-3} s^{-1}]
J	Nucleation rate	[cm^{-3} s^{-1}]
k	Boltzmann constant (= 1.380649 $\times$ 10^{-23})	[J K^{-1}]

Symbol	Definition	Unit
k_t	Turbulent kinetic energy	[cm^2 s^{-2}]
K	Coagulation kernel	[cm^3/(particle s)]
Kn	Knudsen number	[-]
L_0	Permanent electric dipole moment	[C m]
Le	Lewis number	[-]
m	Mass	[g]
M	Molar mass	[g mol^{-1}]
Ma	Mach number	[-]
n	Number of molecules	[mol]
$n_N(\,)$	Number distribution function	[-]
N_A	Avogadro constant (= 6.02214076 $\times$ 10^{23})	[mol^{-1}]
N	Number concentration	[cm^{-3}]
$N_{p,t}$	Total number concentration of particles per unit volume	[cm^{-3}]
p	Partial vapor pressure	[Pa]
p^s	Saturation vapor pressure	[Pa]
$p^\dagger$	Partial vapor pressure incl. the effect of curvature	[Pa]
p°	Vapor pressure of a pure species over a flat surface	[Pa]
P	Pressure	[Pa]
P()	Probability function	[-]
Pr$_t$	Turbulent Prandtl number	[-]
q	Electrical charge	[C]
q_0	Elementary charge (= 1.60217663 $\times$ 10^{-19})	[C]
q_T	Thermal conductivity	[N s^{-1} K^{-1}]
$\dot{q}$	Rate of volumetric heat addition per unit of mass	[J kg^{-1} s^{-1}]
$\dot{Q}'_\mathrm{visc}$	Energy flux of heat due to viscous forces	[N m^{-2} s^{-1}]
Re	Reynolds number	[-]
r	Radius	[µm]
r^*	Radius of critical embryo	[nm]
R_u	Universal gas constant (= 8.31446261)	[J K^{-1} mol^{-1}]
$R_\mathrm{g,av}$	Average growth rate due to condensation	[cm^{-2} s^{-1}]
RH	Relative Humidity	[%]
S	Entropy	[J K^{-1}]
S_{ij}	Mean shear rate tensor	[s^{-1}]
Sc$_t$	Turbulent Schmidt number	[-]
SR	Saturation ratio	[-]
t	Time	[s]
T	Temperature	[K]
$\mathbf{u}$	3D velocity vector	[m s^{-1}]
$\overline{\mathbf{u}}$	Expectation of the 3D velocity vector	[m s^{-1}]

Symbol	Definition	Unit
$\tilde{\mathbf{u}}$	3D Favre-averaged velocity vector	[m s^{-1}]
$\mathbf{u}'$	3D vector with the velocity fluctuations	[m s^{-1}]
u	Fluid speed	[m s^{-1}]
u_{ac}	Aircraft's true airspeed	[m s^{-1}]
u_t	Terminal settling velocity of a particle	[m s^{-1}]
U	Internal energy	[J]
$\bar{v}$	Average volume per molecule	[nm^3]
V	Volume	[m^3]
$V_{p,t}$	Total particle volume inside a volume parcel	[µm^3 cm^{-3}]
w	Thermal diffusivity	[cm^2 s^{-1}]
$\dot{W}'_{\text{visc}}$	Energy flux of work due to viscous forces	[N m^{-2} s^{-1}]
(x, y, z)	Cartesian coordinates denoting position	[m]
x	Mole fraction	[-]
Z	Zeldovich non-equilibrium factor	[-]
α	Ion-ion recombination coefficient	[cm^3 s^{-1}]
β	Impingement rate	[cm^{-2} s^{-1}]
γ	Activity coefficient	[-]
Γ	Activity	[-]
δ	Mean distance from the center of a sphere	[µm]
δ_{ij}	Kronecker delta	[-]
ϵ_t	Dissipation rate of turbulent kinetic energy	[cm^2 s^{-3}]
ε	Permittivity	[F m^{-1}]
ζ	Angle related to ΔG and β	[rad]
η_B	Batchelor length scale	[m]
η_K	Kolmogorov length scale	[m]
θ	Contact angle	[rad]
λ	Mean free path	[µm]
μ	Dynamic viscosity	[N s m^{-2}]
μ_b	Bulk (or second) viscosity	[N s m^{-2}]
ν	Kinematic viscosity	[m^2 s^{-1}]
ν_t	Eddy viscosity	[m^2 s^{-1}]
ξ	Fuel-to-air equivalence ratio	[-]
π	The constant pi (= 3.14159265...)	[-]
ρ	Density	[kg m^{-3}]
σ	Surface tension	[N m^{-1}]
σ_g	Geometric standard deviation	[-]
ς	Molar volume	[m^3 mol^{-1}]
$\boldsymbol{\tau}_{\text{visc}}$	Viscous stress tensor	[N m^{-2}]

Symbol	Definition	Unit
τ	Characteristic time scale	[s]
ϕ	Chemical potential	[J mol^{-1}]
χ	Volume mixing ratio	[-]
ψ	Thermodynamic affinity	[J mol^{-1}]
Ψ	Electrostatic potential	[V]
ω	Specific dissipation rate of turbulent kinetic energy	[s^{-1}]

Chemical Compounds

Molecule	Name
C	Carbon
CO	Carbon monoxide
CO_2	Carbon dioxide
C_nH_m	Kerosene
CH_4	Methane
HC	Hydrocarbons
HCO^+	Formyl cation
HNO_3	Nitric acid
H_2CO	Formaldehyde
H_2O	Water
H_2SO_4	Sulfuric acid
HSO_4^-	Hydrogen sulfate anion
H_3O^+	Hydronium cation
NH_3	Ammonia
N_2	Nitrogen
NO_x	Nitrogen oxides
NO^+	Nitrosonium cation
NO_2^-	Nitrite anion
NO_3^-	Nitrate anion
O_2	Oxygen
S	Sulfur
SO_x	Sulfur oxides
SO_3^-	Sulfite anion

List of Figures

List of Tables

1

Introduction

"Nothing in life is to be feared, it is only to be understood.
Now is the time to understand more, so that we may fear less."
- Marie Curie, Nobel prize in Physics and Chemistry

Stratospheric Aerosol Injection or SAI is a mitigation strategy to battle global warming and part of a larger group of measures that tries to balance Earth's energy budget, i.e. the equilibrium between incoming solar energy and outgoing energy from Earth in the form of radiation. SAI belongs to a group of Solar Radiation Management (SRM) techniques, which focuses on increasing Earth's reflective ability (albedo) by means of cloud creation and modification or the introduction of artificial reflective surfaces. SRM, in turn, is one out of two major fields in Geoengineering or 'Climate' Engineering next to Carbon Dioxide Removal (CDR) (Shepherd et al., 2009). It is important to stress that SRM does not revert climate change, it merely counteracts its related symptoms by offsetting the radiative forcing by greenhouse gases in an effort to limit the global temperature increase. CDR, on the other hand, centers on the direct removal of carbon dioxide (CO_2) from the atmosphere because it is the largest contributor to global warming (in terms of its atmospheric lifetime) among other greenhouse gases such as methane (CH_4) and nitrous oxide (N_2O). Hence, it tries to remove the root cause of climate change (Shepherd et al., 2009).

The concept of SAI, first proposed by Budyko (1977), mimics that of natural sulfate aerosol injection into the atmosphere during volcanic eruptions. Through oxidization and in the presence of water, aerosols are formed which scatter sunlight and lower the incoming amount of short-wave solar radiation. It has been shown that increased concentrations of sulfate-based aerosols in the atmosphere lead to cooler weather temperatures. Natural sinks in the troposphere eventually 'clean up' the excess of aerosol after a 1 or 2 years via 'atmospheric removal'. Because the sulfur cycle is a natural and well-understood process, sulfur-based aerosols are the prime candidate for SAI. Although better performing engineered (solid) aerosols exist such as alumina-, diamond- and calcite-based particles, their long-term effects (and associated risks) are still uncertain due to the lack of natural analogues (Pierce et al., 2010, Weisenstein et al., 2015). Ever since its introduction, SAI has been subject to scrutiny because of the inherent risks that it entails. When Nobel Prize winner in Chemistry, Paul J. Crutzen, expressed his support for SAI as an 'emergency' measure in his essay on albedo enhancement, see Crutzen (2006), he rekindled a heavy debate on the ethical implications of this research. Potential adverse effects are ozone depletion, ocean acidification, precipitation reduction and lower stratospheric

warming (Pierce et al., 2010, Rasch et al., 2008), all of which can lead to starvation and extinction of flora and fauna. Apart from scientific and ethical considerations, there are numerous operational, financial, legal and societal obstacles that need to be overcome to see this method correctly implemented. Yet, natural disasters are on the rise and the average global temperature increase since pre-industrial times has already surpassed 1 °C while the rate of temperature increase has doubled over the last decades (Lindsey & Dahlman, 2022). Scientists are increasingly worried that the limit of a 2 °C temperature increase, imposed by the United Nations, will not be met (UNFCCC United Nations / Framework Convention on Climate Change, 2015). In order to prevent surpassing the 'point of no return', it is becoming more and more plausible that some form of SAI will be implemented in the future where the expected benefits might outweigh the risks. Because of the high potential liability towards society, it is important that any work on SAI and its effects happens in a transparent way and it should not waver our responsibility to increase our efforts to reduce greenhouse gas emissions.

1.1. Problem Statement

In the past, research on SAI has been confined to simulations and predominantly focused on the global domain using model grid boxes that span at least 100 km and where it is assumed that the injected aerosol is mixed instantaneously (instantaneous dispersion) (Golja et al., 2021). Examples are Weisenstein et al. (1997), Vattioni et al. (2019) and P. Irvine et al. (2019). They concluded that it would be possible to stabilize Earth's temperature by producing large amounts of Accumulation-Mode (0.1 - 1.0 µm) sulfate particles (AM H_2SO_4-H_2O) which requires anywhere between 10 to 20 Mt of sulfur per year depending on the required optical depth (Pierce et al., 2010; Rasch et al., 2008). Operational studies then quickly concluded that specialized high-altitude aircraft, none of the like which are available today, would the best solution to transfer such quantities to the lower stratosphere, as high as 20 km, and distribute them by injecting H_2SO_4 vapor into the jet engine plume. The need for such high altitudes stems from the required minimum atmospheric lifetime of the aerosol (P. J. Irvine et al., 2016). The requirements for a new type of aircraft and the cost of this operation were investigated by Janssens et al. (2020) and de Vries et al. (2020).

As pointed out by Vattioni et al. (2019) and Floerchinger et al. (2020), remarkably little is known about the growth evolution of aerosol inside a jet engine plume nor the mechanical methods to manually inject condensable vapor into the wake. Partly due to a lack of experimental investigation in light of cost and safety considerations, but more importantly because the spatial and temporal scales hamper accurate simulations. The problem is often subdivided into a near-field plume dispersion model (PDM) and a global general circulation model (GCM) or chemistry-transport model (CTM) (Vattioni et al., 2019). The focus of this research relates to the former as there are still large uncertainties on the microphysical processes that govern aerosol growth inside an expanding jet engine plume and they are crucial to control the desired size and optical properties of the steady-state aerosol in the far-field. There is a need for high-fidelity simulations of realistic SAI missions before attempting any large scale experimental investigation. The injection of condensable vapor in a jet engine wake to produce aerosol can be simulated with PDMs which are a subfield of atmospheric dispersion modeling (ADM). Simple and validated PDMs exist such as the works from Petry et al. (1998) and Kraabøl et al. (2000), which are both steady-state Gaussian plume models (GPMs), however they are limited to non-reactive, homogeneous flows with low-intensity turbulence and uniform diffusivity (Zannetti, 2013). The wake behind a jet engine is a highly turbulent free shear flow characterized by strong velocity gradients where the magnitude of diffusivity is strongly dependent on the radial distance from the jet core. In addition, the emission of ions and non-volatile particulate matter (mostly soot) by a jet engine in combination with elevated exhaust gas concentrations can result in complex non-linear chemical reaction rates that affect the growth evolution of the aerosol (Starik, 2007). Therefore, to simulate aerosol growth and dispersion in a jet wake after injection of gaseous vapor, hybrid PDMs need to be developed which should contain

the following three modules as a minimum: (1) a detailed flow solver that potentially includes the effects of aircraft wake interactions (plume morphology) to capture the velocity field and turbulent diffusivity inside the flow; (2) a microphysical model that simulates the different aerosol growth processes after injection of condensable vapor in the wake and resolves the steady-state particle size distribution (PSD); and (3) a diffusion-advection scheme which models the motion of the aerosol and vapor throughout the plume and connects the other two modules. Yet, to the author's knowledge, only two PDM-based SAI studies (Pierce et al., 2010, Benduhn et al., 2016) exist that try to simulate stratospheric aerosol injection through means of an aircraft. Both studies concluded that it is possible to achieve particle sizes of approximately 0.1 µm, but lack detail in the flow field and plume morphology and omit some key chemical processes that account for heterogeneous and ion-induced growth. This gap poses a significant risk for the steerability of SAI, which is the capacity to spatially and temporally control its effects both in nature and scale (Benduhn et al., 2016), and this provides the main motivation for this research.

1.2. Research Objective

If a standard Gaussian plume model is used, the lack of spatial and temporal resolution in the flow field impedes the ability to accurately capture the fluctuations in velocity, temperature and relative humidity throughout the plume. This obscures a lot of the intricacies of the aerosol formation process in the early stages of the wake. This research aims to investigate the processes related to aerosol growth in a realistically simulated jet engine plume by solving the Reynolds-averaged Navier Stokes (RANS) equations for the first milliseconds and as far as the end of the momentum-driven jet regime. This is achieved with a decoupled PDM that includes a flow solver which resolves the average velocity and turbulent intensity of the flow, a sectional chemistry module which includes all the relevant microphysical processes that affect aerosol growth, and a diffusion-advection model which calculates the displacement of aerosol, vapor, and chemiions in the flow field. The goal is to ensure steerability of SAI in a way that accurate predictions can be made on the aerosol size distribution after injection of H_2SO_4 gas in the jet engine wake. Prior to this numerical investigation, a literature review was conducted on the modeling approaches concerning the microphysical processes to identify any missing links that should be included, and to establish a correct methodology in simulating an SAI scenario where high concentrations of condensable H_2SO_4 vapor are injected into the highly turbulent wake of an aircraft jet engine.

1.3. Report Outline

The report consists of seven chapters, proceeding with Chapter 2 that discusses the fundamental principles behind aerosol mechanics within a jet engine's wake, providing a basis for the study's methodology in subsequent chapters. Chapter 3 details the scope of this research, followed by the research questions, and verification and validation methods e. Moving on to Chapter 4, the developed plume dispersion model is presented, explaining its assumptions and parameters. Chapter 5 presents and discusses the results obtained from applying the plume dispersion model to different case scenarios. The interpretation of results is then presented in Chapter 6, where the results are compared with the literature and the limitations of the study are discussed. Finally, Chapter 7 summarizes the main findings of the study and presents recommendations for further research to improve the accuracy of the model and its application in SAI research.

2

Aerosol Mechanics in a Jet Engine Wake

This chapter presents the literature review on aerosol mechanics in a jet engine wake, as part of a larger investigation on SAI where condensable H_2SO_4 is distributed in the lower stratosphere by injecting it into the wake of an aircraft. Section 2.1 starts out by introducing the 'discrete' particle size distribution to track an aerosol population over time and talks about the thermodynamic properties of an aqueous H_2SO_4 solution. This is followed by a discussion on particle-fluid interactions and the relevance of the free molecular flow regime in Section 2.2. It introduces the concept of Brownian motion and the different types of diffusion a particle might experience. Next, Section 2.3 talks about the various components that can be found in the wake of jet engine and what effect they have on aerosol formation. This is useful to understand the relevance of various microphysical processes, starting with the nucleation phase or particle formation in Section 2.4. This section summarizes the known processes that lead to particle creation and focuses on classical nucleation theory which is the standard modeling approach in a lot of simulations. A second microphysical growth process, condensation (or evaporation when shrinking), is discussed in Section 2.5. Thereafter, the third and last growth process called coagulation, is discussed under Section 2.6. The review is concluded with Section 2.7 which talks about the relative impact of the different aerosol growth processes as part of an aircraft plume environment which is highly dynamical.

2.1. Aerosol Particle Properties

To understand the analysis in the next chapters, it is important to adopt a consistent terminology to describe aerosols and their distribution. In chemistry, an aerosol is defined as a colloidal suspension of particles dispersed in a gas[1]. The particles can attain a solid state or appear in liquid form, in case of the latter they are often referred to as droplets. Because a mixed state of both solid and liquid compounds exists as well, this study chooses to describe them more generally as particulate matter or particles. Besides the nature of the particles, aerosols are also categorized according to their size. The term 'colloidal' in the definition above somewhat constrains the dimension of aerosols to particles with a diameter of 1 nm to approximately 10 µm. So they are slightly bigger than ordinary molecules, yet smaller than an average blood cell or most living microbes in our body. This is an incredible size range (i.e. four orders of magnitude) as a particle with a diameter of 10 µm contains 10^{12} times more volume than one with a diameter of 1 nm; that is proportional to about a trillion more molecules per

[1] https://www.oed.com/oed2/00003595 (Accessed on 17-06-2022)

particle. It is the size of the particle that determines its ability to scatter light, retain heat, but also its atmospheric lifetime. Therefore, the particle size distribution is key to tracking the growth evolution of a polydisperse population (i.e. particles of varied sizes) in order to obtain the desired dimensions. The classification of aerosols in terms of size is not trivial and Section 2.1.1 addresses some common pitfalls regarding particle size distributions which often lead to confusion or incorrect interpretation of statistical data. This holistic interpretation is followed by Section 2.1.2 that zooms in on the chemical composition of a single aerosol particle and how the individual mole fractions of H_2SO_4 and H_2O vary with relative humidity (RH) and temperature (T).

2.1.1. Size Distributions

This section's introduction touched briefly upon the large range in volume (and mass) when dealing with aerosol particles leading to difficulties in representing their size distributions truthfully. It is common to subdivide the particle size range into discrete intervals or 'bins' as they are often called. Typically, the resolution of the bin distribution is geometrically progressive which means the volume ratio between adjacent bins is constant (Yu & Turco, 1998). For example, Golja et al. (2021) divide the size range of sulfate aerosol into 40 logarithmically spaced bins with a volume ratio of 2, effectively doubling the particle volume between adjacent bins. The particle diameters range from 0.39 nm to 3.2 µm. Similarly, Pierce et al. (2010) use 43 logarithmically spaced bins and a volume ratio of 2. Their size range covers diameters of 0.6 nm up to 10 µm. Usually, the smallest bin corresponds to particle sizes that originate from homogeneous nucleation as discussed in Section 2.4. One should be careful drawing any conclusions from a particle size distribution where the discrete resolution of particle bins is too crude. If the volume ratio between adjacent bins is too large, artificial abundances of small and large particles are created that broaden the size distribution and lower peak concentrations. When a particle reaches the next highest or lowest bin, its mass is instantly distributed uniformly across that bin, and the next time step no distinction is made between particles that just entered a certain size bin or particles that resided there before. As a result, mass distributions can shift rapidly which is unrealistic (Jacobson & Turco, 1995). This is a case of numerical diffusion and it yields unrealistic mass distribution in situations where strong condensation rates occur. It happens to a lesser extent during the coagulation stage as well. Turco and Yu (1998) further investigated this issue to conclude that volume ratios of 2 or less are acceptable, while a ratio of 1.5 or less is preferable. It is possible to make use of a variable bin size structure to accommodate for the rapidly shifting aerosol sizes and to reduce numerical diffusion. Jacobson and Turco (1995) proposed a model where the volume of the bin changes in conjunction with its particles, all the particles grow/shrink simultaneously within their respective bin. This gives better flexibility but at a higher computational cost.

While the bin discretization simplifies the categorization process, it inherently has a number of drawbacks. The first one being a loss of detail or structure inside a bin. Instead of a continuous function, one obtains a histogram such as the distributions shown in Fig. 2.1. The comparison in this figure also highlights the importance of normalizing number concentrations by the size interval they belong to. As you can see, this normalization step alters the statistical interpretation of the distribution significantly. While Fig. 2.1a seems to indicate that almost all particles are bigger than 0.1 µm, Fig. 2.1b would suggest that roughly 50% of the particles is smaller than 0.1 µm (Seinfeld & Pandis, 2016). The attentive reader might notice that a lot of the detail in Fig. 2.1b is lost due to the normalization step because most of the particles are concentrated in the lower size range, resulting in a sharp peak. This is solved by imposing a mathematical transformation which expresses the particle diameter d_p on a logarithmic scale; commonly as either $\ln(d_p/1)$ or $\log(d_p/1)$. The value in the denominator is a reference value (here taken to be 1 µm), because formally you cannot take the logarithm of a dimensional quantity (Seinfeld & Pandis, 2016). This allows for a much wider range of values to be depicted in a single graph without loss of statistical comprehension. However, caution is advised when comparing logarithmic distributions, as

seemingly small differences to the eye can actually correspond to large numerical deviations.

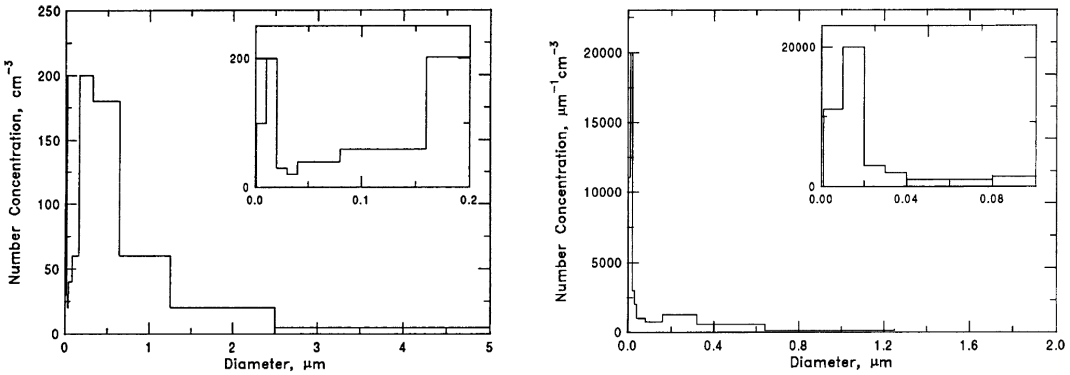

(a) No normalization (unit: cm^{-3})

(b) Normalized by particle size bin width (unit: μm^{-1} cm^{-3})

Figure 2.1: Histogram of aerosol particle number concentrations vs. the size range for the distribution (Seinfeld & Pandis, 2016)

Let us introduce a mathematical framework to express particle properties in. Suppose the discretization of particle size is sufficiently smooth such that we can describe the number distribution of particles as a continuous function $n_N(\ln d_p)$ where:

$$n_N\left(\ln d_p\right) \mathrm{d}\left(\ln d_p\right) = \text{number of particles per cm}^3 \text{ of air in the size range } \ln d_p \text{ to } \ln d_p \, \mathrm{d}\left(\ln d_p\right)$$

Integrate this expression from -∞ to ∞ to obtain the total number concentration of particles $N_{p,t}$, as defined by (Seinfeld & Pandis, 2016) through Eq. (2.1). This value is equal to the area below the distribution in the top half of Fig. 2.2. Other properties such as total particle surface area $A_{p,t}$ and total particle volume $V_{p,t}$ (for a spherical droplet) then simply follow from Eq. (2.2) and (2.3).

$$N_{p,t} = \int_{-\infty}^{\infty} n_N\left(\ln d_p\right) \mathrm{d} \ln d_p \quad \left(\mathrm{cm}^{-3}\right) \tag{2.1}$$

$$A_{p,t} = \pi \int_{-\infty}^{\infty} d_p^2 \, n_N\left(\ln d_p\right) \mathrm{d} \ln d_p \quad \left(\mu\mathrm{m}^2 \ \mathrm{cm}^{-3}\right) \tag{2.2}$$

$$V_{p,t} = \frac{\pi}{6} \int_{-\infty}^{\infty} d_p^3 \, n_N\left(\ln d_p\right) \mathrm{d} \ln d_p \quad \left(\mu\mathrm{m}^3 \ \mathrm{cm}^{-3}\right) \tag{2.3}$$

Often it is not useful to represent an entire dataset through a distribution function $n_N(\ln d_p)$ so statistical approximations are used instead. It turns out that atmospheric aerosols tend to spread lognormally in terms of size, which means the logarithm of the particle diameter follows a normal or Gaussian distribution. This is very common in nature for complex processes which are affected by a lot of factors. This is why the bell curve shapes appear in Fig. 2.2, although they might be shifted and/or have larger spread around the mean size. The normal distribution of d_p is given by Eq. (2.4).

$$n_N\left(d_p\right) = \frac{\mathrm{d}N}{\mathrm{d}d_p} = \frac{N_t}{(2\pi)^{1/2} d_p \ln \sigma_g} \exp\left(-\frac{\left(\ln d_p - \ln \hat{d}_{pg}\right)^2}{2 \ln^2 \sigma_g}\right) \tag{2.4}$$

where $\hat{d}_{pg}$, defined as Eq. (2.5), is the median particle diameter and σ_g is the geometric standard deviation which is an indication of the spread of the data around the median diameter.

$$\hat{d}_{pg} = \frac{1}{N_t} \int_0^{\infty} d_p n_N\left(d_p\right) \mathrm{d}d_p \quad \left(\mu\mathrm{m}^3\right) \tag{2.5}$$

The mathematical expressions above increase our understanding of aerosol behavior in more than one way and it is insightful to look at Fig. 2.2 which depicts a common size distribution of atmospheric

particles. Notice that the horizontal scale is logarithmically distributed. This illustration reveals some important features of atmospheric aerosols, such as their different modes and typical bell-shaped curves. Figure 2.2 reveals that the particle size distribution (PSD) (and surface/volume distribution) tends to exhibit different modes which are a result of aerosol growth mechanics[2].

In the atmosphere, ultrafine particles, or particles with a diameter below 0.1 µm, appear in much greater numbers while particle concentrations closer to 1 µm are practically negligible. However, the particle volume distribution in the lower panel indicates that particles above 0.1 µm contain almost all aerosol volume (Seinfeld & Pandis, 2016). The reason larger particles have smaller numbers is because they are formed out of the clustering of ultrafine particles and naturally the number has to go down as particles combine to achieve growth. In addition, an atmospheric removal process called sedimentation is much more dominant at this scale leading to a decline in the particle population (Weisenstein et al., 1997). The fact that larger particles have shorter atmospheric lifetimes has important implications on the effectiveness of SAI, as mentioned previously in Section 1.2.

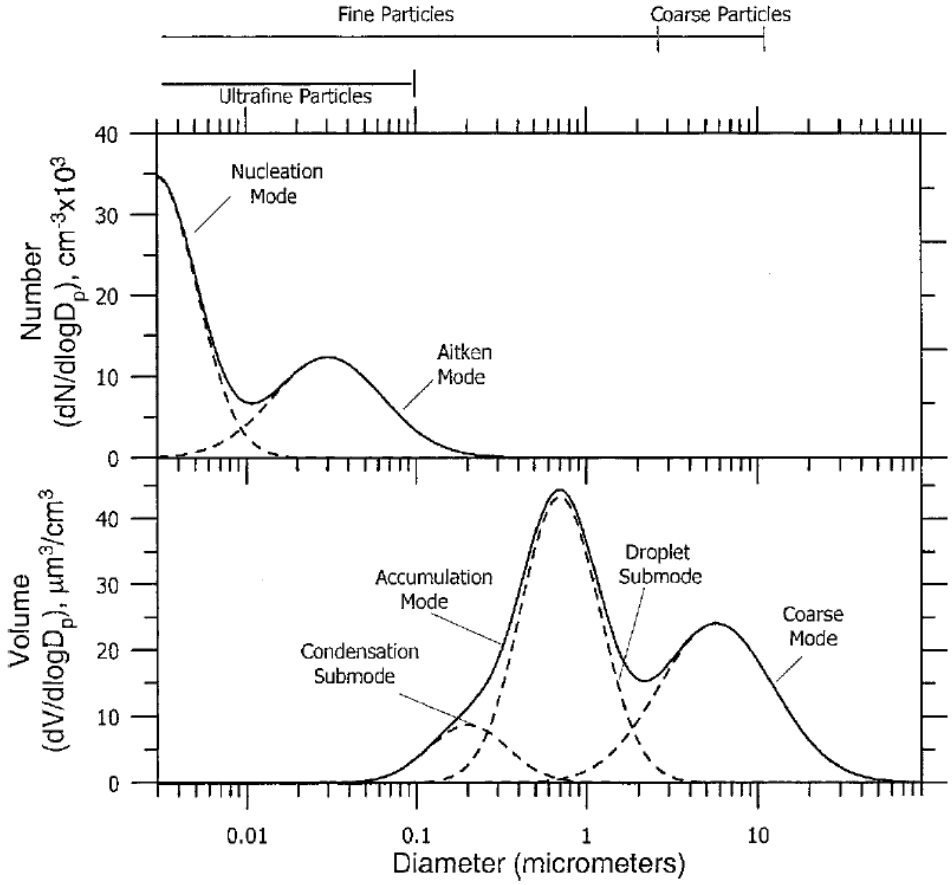

Figure 2.2: Typical number and volume distributions of atmospheric particles with the different modes (Seinfeld & Pandis, 2016)

Now, remember that the objective is to create sulfate aerosol particles of a certain size to maximize their scattering ability and lifetime. This is achieved by injecting condensable vapor into the wake behind the jet engine of an aircraft, and as a result the initial source of new particles that result from gas-to-particle conversion all belong to the Nucleation mode (see also Section 2.4 on particle formation). Particles in this category are typically between 1 and 10 nm. They grow rapidly into Aitken mode particles through condensation of gas and water vapor onto the pre-existing condensation nuclei (CN). Their size range is roughly 10 - 100 nm. At about 50 nm, coagulation starts to become dominant. Coagulation is a kinetic process of collision and fusion between particles. This is the main contributor to growth and together

[2] https://www.dwd.de/EN/research/observing_atmosphere/composition_atmosphere/aerosol/cont_nav/particle_size_distribution_node.html (Accessed on 17-06-2022)

with condensation results in particles with a size of 0.1 to about 1 µm, called the Accumulation mode. Lastly, there are solid particles with sizes >1 µm that result from mechanical processes, fittingly called Coarse mode particles. This includes dust, salt, soot and many other categories (Seinfeld & Pandis, 2016). While small in number, they can act as CN and are highly competitive at scavenging Nucleation mode particles early on in the growth process (Yu & Turco, 1998).

Thus, most Accumulation mode particles are obtained through growth of Nucleation and Aitken mode particles. In the case of an isolated aircraft engine that emits particles in its wake, the PSD inside a volume parcel would steadily shift from Nucleation mode particles to Accumulation mode sizes over time. Yet, the atmosphere contains background aerosol as well and they will interact with the wake. They scavenge freshly nucleated particles early on in the plume and use the same vapor source to continue growing through condensation. Ideally, this is taken into account during the growth process as part of the turbulent entrainment of ambient air in the engine plume.

2.1.2. Chemical Composition & Thermodynamics

Pure sulfate aerosol consists of H_2SO_4 and H_2O, and its weight composition has a significant impact on its thermodynamic properties. Therefore it is essential to have a good estimate of the mole fraction of its individual components. Aerosol thermodynamics is a complicated subject and a detailed analysis of its mechanics is outside the scope of this research. This section focuses on the fundamental relations that explain how certain parameters influence sulfate aerosol composition, and at times, chooses to omit rigorous derivations to simplify the discussion.

To start, the equilibrium condition that governs the phase distribution of vapor and particulate matter is closely related to the laws of thermodynamics. For a closed system, this is typically given as Eq. (2.6), which combines the first and second law of thermodynamics. However, if the system is open to its environment and the number of molecules inside the system is allowed to vary, a third term is added to account for the change in internal energy due to a change in composition and Eq. (2.6) becomes Eq. (2.7). This third term is called the chemical potential ϕ and it can be the cause of a chemical reaction or mass transfer between two phases (Seinfeld & Pandis, 2016).

$$\mathrm{d}U = T\mathrm{d}S - P\mathrm{d}V \tag{2.6}$$

where U (J) is the internal energy of the system, T (K) is the temperature, S (J K^{-1}) is the entropy inside the system, P (Pa) is the pressure and V (m^3) is the volume.

$$\mathrm{d}U = T\mathrm{d}S - P\mathrm{d}V + \sum_{i=1}^{k} \phi_i \mathrm{d}n_i \tag{2.7}$$

with ϕ (J mol^{-1}) being the chemical potential, n_c (mol) is the number of molecules of a species c and k is the number of species inside a system.

Now, chemists often prefer a different formulation of this law through means of a thermodynamic potential, the Gibbs free energy G. This variable is crucial in the formulation of classical nucleation theory (CNT). A system that attempts to obtain chemical equilibrium under constant pressure and temperature, will always try to minimize this potential. Its differential form is the Legendre transformation of Eq. (2.7) and shown here as Eq. (2.8). Notice that the independent variables have now changed to pressure and temperature, which are much more convenient to measure during an experiment.

$$\mathrm{d}G = -S\mathrm{d}T + V\mathrm{d}P + \sum_{i=1}^{k} \phi_i \mathrm{d}n_i \tag{2.8}$$

Note that the chemical potential ϕ is the partial molar Gibbs free energy and G can be written as Eq. (2.9).

$$G = \sum_{i=1}^{k} \phi_i n_i \tag{2.9}$$

If you insert the derivative from Eq. (2.9) into Eq. (2.8) and rewrite, the final form is what is known as the Gibbs-Duhem equation, or Eq. (2.10). This relation indicates that the chemical potentials of different species inside a system change when the pressure or temperature of that system changes (Seinfeld & Pandis, 2016).

$$-S\mathrm{d}T + V\mathrm{d}P = \sum_{i=1}^{k} n_i \mathrm{d}\phi_i \tag{2.10}$$

Under the assumption that pressure and temperature are constant (steady-state), it is possible to transform Eq. (2.10) into an expression that is used to retrieve the weight composition of a binary mixture (e.g. H_2SO_4-H_2O). This relation is defined here as Eq. (2.11) according to Poling et al. (2001).

$$x_1 \left(\frac{\partial \ln \gamma_1}{\partial x_1} \right)_{T,P} = x_2 \left(\frac{\partial \ln \gamma_2}{\partial x_2} \right)_{T,P} \tag{2.11}$$

where x_i is the mole fraction of a species i and γ_i is the associated activity coefficient, which is a measure for the deviation from the chemical potential of an ideal solution.

The parentheses denote an isobaric and isothermal process. In reality it is not possible to vary the mole fraction x while keeping both P and T constant. but usually the activity coefficient γ has a weak dependence on P and it is generally accepted to apply Eq. (2.11) to isothermal data. This equation proves that the activity coefficients of the individual compounds inside a solution are dependent on each other through a partial differential equation. Moreover, it is one of the few thermodynamically consistent methods that allows scientists to extrapolate the partial vapor pressures of a fluid mixture from limited experimental data. In the past, weight composition parameterizations for the case of H_2SO_4-H_2O aerosols were often limited due to a lack of experimental data. A regularly used parameterization for the composition of sulfate aerosols in the stratosphere was the one from Steele and Hamill (1981) based on a model from Gmitro and Vermeulen (1964). This was improved upon by Tabazadeh et al. (1997), based on a model from Clegg and Brimblecombe (1995) that uses liquid-phase thermodynamic data to determine the liquid water activity, and under the assumption that the aerosol is in equilibrium with the water vapor. They are relatively accurate for the purpose of determining the weight composition of microscopic particles, but not those of nanoscale (molecular) clusters that are formed during nucleation; they require more advanced methods. Those models calculate the liquid activity coefficients of both water and sulfuric acid based on the presence of hydrates and solve Eq. (2.11) iteratively to obtain the mole fraction of H_2SO_4 simultaneously with the cluster size (Vehkamäki et al., 2002, Määttänen et al., 2017). This is discussed further in Section 2.4 on particle formation.

The reason for the activity coefficient stems from the fact that atmospheric aerosols are usually non-ideal aqueous solutions. They do not obey Raoult's law, which states that the partial pressure of each component is equal to the vapor pressure of the pure species multiplied by its mole fraction in the mixture[3]. Thus, the law needs to be scaled with an activity coefficient γ as shown in Eq. (2.12).

$$p_i = p_i^{\circ} \gamma_i x_i \tag{2.12}$$

where p (Pa) is the partial pressure of the compound inside the solution and p° (Pa) is the equilibrium vapor pressure of the pure species over a flat surface.

If the partial vapor pressure of a component in an aerosol exceeds its saturation vapor pressure, it evaporates and the aerosol will continue to shrink until a new equilibrium is obtained. Typically, the

[3] https://www.sciencedirect.com/topics/chemistry/raoults-law (Accessed on 02-07-2022)

partial pressures for H_2SO_4-H_2O are much lower than predicted by Raoult's law ($\gamma < 1$) as illustrated by Hamill et al. (1982) in Fig. 2.3. This occurs when the adhesive forces between H_2SO_4 and H_2O are greater than the cohesive forces between H_2SO_4 and H_2SO_4 or H_2O and H_2O. This is the consequence of the two strong hydrogen bonds that are created between H_2SO_4 and H_2O, which is not possible in case of two water molecules due to geometric constrictions. As a result, both species won't escape from the solution as readily as Raoult's law would predict. This is the reason why H_2SO_4-H_2O is hygroscopic which means it is able to absorb large amounts of water vapor, also in the case of low relative humidity (RH). To summarize what is said above, activity coefficients are crucial to determine the partial vapor pressures in a water-sulfuric acid solution, while the vapor pressure determines whether or not a particle grows or evaporates. They are dependent on temperature, pressure and the mole fraction of all substances in the system (Merikanto et al., 2016, Seinfeld and Pandis, 2016, Vehkamäki et al., 2002).

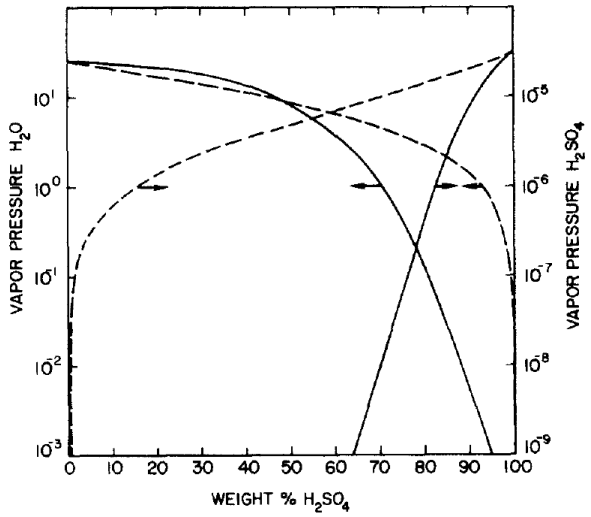

Figure 2.3: Schematic representation of the variation in the vapor pressures (in mm Hg) of water and sulfuric acid in an H_2SO_4-H_2O solution (solid lines). The dashed lines represent the idealized vapor pressures of a binary system obeying Raoult's law (Hamill et al., 1982)

Apart from the activity coefficients, there are other factors that influence the vapor pressure. In the presence of a curved interface, as is the case for the surface of a droplet, one can show that the the vapor pressure needs to be scaled with the radius of the particle through Eq. (2.13). This relation has many names but the way it is formulated here, it is often denoted as the Ostwald-Freundlich equation which is a derivation of the Kelvin equation (von Helmholtz, 1886).

$$p^{\dagger} = p^{\circ} \exp\left(\frac{2\sigma M}{R_u T \rho_l r_p}\right) \quad \text{(Pa)} \tag{2.13}$$

where $p^{\dagger}$ (Pa) is the actual equilibrium partial pressure incl. the effect of curvature, σ (N m^{-1}) is the surface tension, M (kg mol^{-1}) is the molar mass, $R_u = 8.31446261$ (J K^{-1} mol^{-1}) is the universal gas constant, ρ_l (kg m^{-3}) is the liquid-phase density and r_p (µm) is the particle's radius

Notice that the vapor pressure over a curved surface always exceeds that of the one over a flat surface (because all the terms under the exponential function are positive) which is commonly denoted as the curvature effect, or otherwise called the Kelvin effect (Seinfeld & Pandis, 2016). This has some big implications for the growth mechanics of aerosols because smaller particles will evaporate more easily than larger ones and larger ones are more likely to grow during condensation. In case of aqueous H_2SO_4, the effect of curvature starts to play a role for particles with diameters below 0.1 µm, as illustrated in Fig. 2.4. In case of increasing curvature, a higher mole fraction of H_2SO_4 is required to increase the particle's hygroscopicity and maintain its equilibrium. The graph also shows that the equi-

librium composition varies with RH because the water activity coefficient γ_{H_2O} in an aqueous solution is approximately equal to RH. If RH decreases, less water vapor is present in the vicinity of the aerosol and the mole fraction of H_2SO_4 needs to go up to increase the hygroscopic effect and maintain equilibrium.

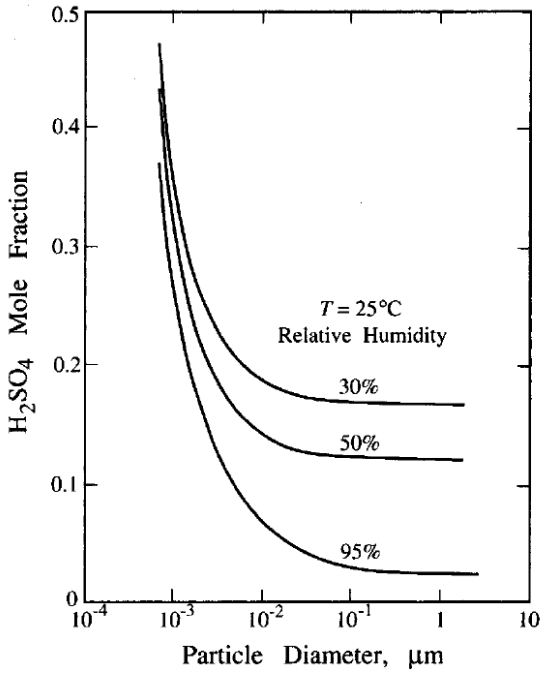

Figure 2.4: Equilibrium concentration of H_2SO_4 in an H_2SO_4-H_2O solution as a function of RH and d_p (Seinfeld & Pandis, 2016)

2.2. Particle Behavior in a Fluid

To understand the different modeling approaches to particle growth, that are presented later in this chapter, it is useful to introduce some fundamental relations that describe the behavior of particles suspended in a fluid. The particle-fluid interactions in a flow depend on the size of the particle and the fluid it moves through. The movement of ultrafine particles, for example, depends strongly on individual interactions with the fluid's molecules. The study of different particle flow regimes is the focus of Section 2.2.1. Section 2.2.2 extends on that by introducing Brownian motion, a chaotic transport mechanic related to the thermal motion of a fluid's molecules. Finally, it is helpful to consider the concept of diffusion and its variety of sources, because it has a big influence on aerosol growth and the PSD. This is the topic of Section 2.2.3.

2.2.1. Particle Flow Regimes

The mathematical frameworks in Section 4.1 that describe fluid mechanics are derived for continuum flow; the microscopic nature of the flow or interaction between individual particles is ignored. In most aerodynamic cases, this assumption is generally valid and it is applied here to study the velocity field and diffusivity of the wake behind an aircraft engine. However, the microphysical processes that govern aerosol growth act on an entirely different scale. They deal with particles the size of a few molecules and the kinetic interaction between an aerosol particle and the fluid has to be accounted for. The similarity parameter that describes the nature of the fluid with respect to the suspended particle is the Knudsen number Kn, which is the ratio of the molecular mean free path length over the particle radius (Seinfeld & Pandis, 2016). Equation 2.14 reveals that the Knudsen number is actually the ratio of two other similarity parameters, the Mach number Ma of the fluid and the particle Reynolds number Re_p.

$$\mathrm{Kn} = \frac{\mathrm{Ma}}{\mathrm{Re}_p} = \frac{u}{a}\frac{a\lambda}{ur_p} = \frac{\lambda}{r_p} \tag{2.14}$$

in which u (m s^{-1}) is the fluid velocity relative to the particle, a (m s^{-1}) is the speed of sound and λ (µm) is the mean free path of the fluid, which is the average distance until a particle changes its direction or energy as a result of a collision.

The Mach number is the ratio of the fluid velocity over the speed of sound and thus depends on the temperature of the surrounding fluid. It is a measure for the compressibility of the flow and given by Eq. (2.15). The particle Reynolds number represents the ratio of steady inertia forces over the viscous forces and is defined according to Eq. (2.16).

$$\mathrm{Ma} = \frac{u}{a} \tag{2.15}$$

$$\mathrm{Re}_p = \frac{ur_p}{\nu} = \frac{ur_p}{a\lambda} \tag{2.16}$$

where $\nu \approx a\lambda$ (m^2 s^{-1}), is the kinematic viscosity of the fluid (van Pelt et al., 2020). Refer to Eq. (2.24).

The Knudsen number is an important indication for the fluid regime that a particle experiences. Depending on the value of Kn, three regimes can be identified. They are illustrated in Fig. 2.5.

(a) Kn $\ll 1$: Continuum regime

(b) Kn ~ 1 : Transition regime

(c) Kn $\gg 1$: Free-molecular or kinetic regime

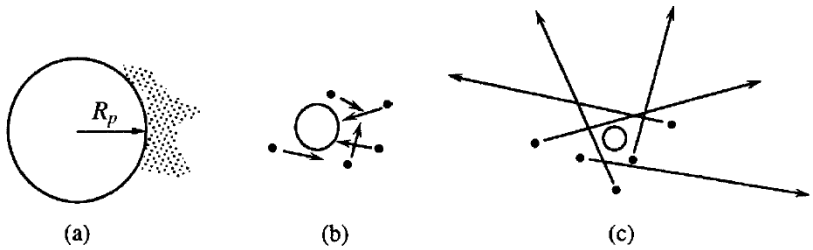

Figure 2.5: Schematic of the three regimes of suspending fluid–particle interactions; (a) continuum regime; (b) transition regime; (c) free molecular (kinetic) regime. Adapted from Seinfeld and Pandis (2016).

Suppose an aerosol particle is several orders bigger than its mean free path in the surrounding gas (Kn $\ll$ 1), as is the case for (a) in Fig. 2.5. Then the aerosol's interaction with its surroundings is approximately constant. The aerosol perceives the surrounding gas as a continuum and it is possible to use macroscopic state properties of the flow to estimate particle transport effects. If the aerosol is substantially smaller than λ, on the other hand (Kn $\gg$ 1), the aerosol is virtually indistinguishable from a gas molecule and it becomes subject to the kinetic interactions between gas particles as shown in (c). Macroscopic relations do not apply here because single particle interactions result in a large behavioral change of the aerosol and this is one of the key shortcomings of classical nucleation theory as discussed in Section 2.4.1. The transition regime is a grey zone where both macroscopic and molecular particle transport properties are of importance and need to be accounted for.

The atmospheric mean free path increases with altitude due to variations in temperature and pressure; the stratospheric mean free path is about 1 µm, which is ten times larger than at sea level (Hamill, Toon, et al., 1977). Higher density or larger molecule sizes of the ambient air lead to a decrease in λ

and thus Kn. Calculating the ambient mean free path inside an engine plume is not trivial due to the large number of constituents and uncertainty on the average molecule and particle size. Because air is by far the largest fraction inside a plume parcel, λ can be approximated using Eq. (2.17) from Seinfeld and Pandis (2016) for a 'pure' gas or air in this case.

$$\lambda_{\text{air}} = \frac{2\mu_{\text{air}}}{P\left(8M_{\text{air}}/\pi R_u T\right)^{1/2}} \quad (\mu\text{m}) \tag{2.17}$$

where μ (N s m^{-2}) is the dynamic viscosity.

For an engine outlet temperature of 600 K and a pressure of 5 kPa, this results in a mean free path of 3 µm. Thus, λ varies approximately between 1 - 3 µm from the engine exit until the plume has reached background stratospheric conditions. This implies that particles with a diameter of $d_p = 0.2 - 0.6$ µm or less will experience free molecular flow. Remember from Section 2.1 that particles, which originate from nucleation, are within 1 - 10 nm. Modeling nucleation according to assumptions that relate to continuum flow is therefore a fundamental error and leads to uncertainty in the nucleation rate. Please consult Section 2.4.1 for more details.

Non-continuum effects also play a role in the motion of aerosols, and more specifically in the settling velocity which determines their lifetime in the lower stratosphere. Although photolysis in the upper stratosphere results in a reduction of particulate matter, aerosols in the lower part are predominantly removed by sedimentation or gravitational settling (Weisenstein et al., 1997). The terminal settling velocity u_t of an aerosol particle can be derived using Stokes' law describing particle drag and is given by Eq. (2.18), where the effect of buoyancy is neglected as only the particle density is considered ($\rho_p \gg \rho_{\text{fluid}}$). However, because Stokes' law is derived for continuum flow, a correction needs to be applied to account for particles in the free molecular regime. In this case, the no-slip boundary condition does not hold and Ebenezer Cunningham derived a slip correction factor f_{cu} to reduce the amount of drag that is predicted by Stokes' law (Seinfeld & Pandis, 2016). The Cunningham correction factor is formulated as Eq. (2.19).

$$u_t = \frac{1}{18}\frac{d_p^3 \rho_p g f_{\text{cu}}}{\mu} \tag{2.18}$$

with ρ_p (kg m^{-3}) being the particle density, g (m s^{-2}) is the gravitational acceleration and f_{cu} is the Cunningham correction factor.

$$f_{\text{cu}} = 1 + \frac{2\lambda}{d_p}\left[1.257 + 0.4\exp\left(-\frac{1.1 d_p}{2\lambda}\right)\right] \tag{2.19}$$

Note that the derivation above is only valid for $\text{Re}_p < 0.1$ where the particle travels at its terminal velocity. For larger Reynolds numbers the drag force needs to be reformulated through means of a drag coefficient (Seinfeld & Pandis, 2016).

The involvement of non-continuum physics is an important driver of the particle size requirement in a potential SAI mission. For example, a particle with a diameter of 1 µm in the lower stratosphere has a terminal velocity of $\sim$ 70 cm h^{-1}, while a smaller particle with $d_p = 0.01$ µm only settles with a speed of $\sim$ 0.6 cm h^{-1}. Hence, the stratospheric lifetime of the smaller particle is a hundred times longer. This has big implications for the injection rate of H_2SO_4 and the required global sulfur burden. Although smaller particles generally settle very slowly under gravitation, they are subjective to Brownian diffusion which is the subject of the next section.

2.2.2. Brownian Motion

The previous section stressed the importance of the molecular mean free path and its role in how aerosol particles behave when suspended inside a fluid. There it was shown that aerosols smaller

than 1 µm start to experience free-molecular flow and cannot be modeled solely through continuum mechanics. The study of submicroscopic particle interactions and their influence on the thermodynamic state of gases is called the kinetic theory of gases. Thanks to some major breakthroughs in the early 20th century, scientists were able to prove e.g. the existence of atoms and even make them quantifiable using this newly founded mathematical framework. It eventually resulted in the first statistical analysis of Brownian motion and its relation to transport properties such as viscosity and mass diffusivity.

Brownian motion is the pseudorandom behavior of submicroscopic particles suspended in a fluid due to individual collisions with the fluid's molecules. It is named after botanist Robert Brown who witnessed the erratic movement of dust particles in water under a microscope. Macroscopic particles do not show this behavior because they are too large to drastically change the direction or intensity of their movement based on a single collision. Because Brownian motion is random, by definition, the mean displacement of a large number of identical submicroscopic particles is equal to zero. However, it is possible to quantify the intensity by which the movement occurs by computing the mean square displacement. First derived by Sutherland (1905), and later by Einstein (1905) in an alternate way, the mean square displacement due to Brownian motion in a given direction is given by Eq. (2.20). Note that Brownian motion is assumed to be isotropic.

$$\langle x^2 \rangle = \langle y^2 \rangle = \langle z^2 \rangle = \frac{2kTf_{\text{cu}}}{3\pi\mu d_p} t \quad (\text{m}^2) \tag{2.20}$$

where k (J K^{-1}) is the Boltzmann constant and t (s) is time. Remarkably, a very similar expression is obtained when Brownian motion is related to macroscopic diffusion through Fick's second law, which is a partial differential equation formulated as Eq. (2.21) in one dimension (remark its similarity with the heat equation which models heat conduction in case of a temperature gradient) (Fick, 1855). The full derivation is given in Seinfeld and Pandis (2016) but the final expression is Eq. (2.22). The diffusion coefficient D_B is then given by Eq. (2.23), otherwise known as Brownian diffusivity. This relation is famously known as the Stokes-Einstein(-Sutherland) equation, with the inclusion of the Cunningham correction factor f_{cu}.

$$\frac{\partial N}{\partial t} = D\frac{\partial^2 N}{\partial x^2} \tag{2.21}$$

where N (cm^{-3}) is the particle number concentration.

$$\langle x^2 \rangle = 2D_B t \quad (\text{µm}^2) \tag{2.22}$$

$$\begin{aligned} D_B &= \frac{kTf_{\text{cu}}}{3\pi\mu d_p} \quad (\text{µm}^2\,\text{s}^{-1}) \\ &= kTB \end{aligned} \tag{2.23}$$

where B (s kg^{-1}) is called the particle mobility.

2.2.3. Diffusion

At this point, it is informative to discuss the concept of mass, or momentum, diffusion and its various types. Mass diffusion is a transport process that results in the equalization of substance concentrations in a system[4]. Generally, three types of diffusion are identified: molecular diffusion, Brownian diffusion and turbulent diffusion. Other diffusion processes related to temperature, pressure and electrical charge are alternate forms of the mechanics that govern molecular diffusion and will not be treated here. Different diffusion processes are commonly attributed for by their specific diffusion coefficient or the process's contribution to the rate of diffusion. Brownian motion and its diffusion coefficient D_B

[4] https://www.thermopedia.com/content/695/ (Accessed on 25-09-2022)

have been discussed elaborately in Section 2.2.2. It is the random motion of ultrafine particles in a fluid resulting from individual collisions with the fluid's molecules. It leads to unidirectional dispersion of ultrafine particles under all conditions.

Molecular diffusion, on the other hand, has a direction. It describes the movement of a substance from a region of high concentration towards one with a lower concentration. It is driven by the gradient in chemical potential ϕ or Gibbs free energy, where the direction has the opposite the sign of the gradient. Molecular diffusion is closely related to viscosity, which is a measure of the fluid's intermolecular resistance against motion. In fact, the molecular diffusion coefficient D_M, which is the rate of momentum diffusivity, is approximately equal to the kinematic viscosity. In one dimension, viscosity is directly proportional to the molecular mean free path of a fluid through Eq. (2.24), which can be derived using kinetic theory of gases (Trachenko and Brazhkin, 2020, Smits, 1999) Although the equality involving the speed of sound is not entirely correct, it is a regularly used assumption in gas dynamics.

$$\frac{\mu}{\rho} = \nu = D_M \approx \frac{1}{3}\lambda\bar{c} \approx \lambda a \quad (\mu\text{m}^2\,\text{s}^{-1}) \tag{2.24}$$

where $\bar{c}$ (m s^{-1}) is the mean magnitude of the velocity of a particle and in this case the average molecular speed given by Eq. (2.25). This expression is used in Section 2.5 to estimate the diffusion coefficient D_M in the gas-like regime of molecular dynamics, given by Eq. (2.60).

$$\bar{c} = \sqrt{\frac{8}{\pi} \cdot \frac{kT}{m}} \quad (\text{m}\,\text{s}^{-1}) \tag{2.25}$$

with m (kg) being the the mass of one molecule of gas.

Finally, a third form of diffusion, and arguably the most efficient, happens through turbulence. Turbulence is the overarching term for pressure and velocity fluctuations in a flow, and it has four characteristic traits: it is irregular (unpredictable), diffusive (transport of mass, momentum, heat), rotational (contains fluctuating vorticity) and dissipative (removal of kinetic energy) (Roberts & Webster, 2002). The field of turbulence is complex, and remains one of the least understood phenomena in modern physics. This section focuses purely on its ability to transport particles through diffusion and deliberately ignores large parts of theory to maintain the overview. Now, the velocity fluctuations in a turbulent flow are the result of vortical motion or 'eddies', which are spatial structures in the flow. Researchers have tried to model the transport or diffusion of mass due to turbulent velocity fluctuations using Reynolds analogy, which is the observation that the transport of heat or mass in a turbulent flow depends on the same eddies. To this end, scientists have come up with a set of empirically-determined dimensionless parameters that quantify the relative magnitudes of mass, momentum and heat transfer. The main parameter of interest is the turbulent Schmidt number Sc_t given by Eq. (2.26), which is the ratio of momentum diffusivity and mass diffusivity. It is the product of two other dimensionless numbers: the turbulent Prandtl number Pr_t (the ratio of momentum diffusivity and thermal diffusivity) and the Lewis number Le_t (the ratio of thermal diffusivity to mass diffusivity). It can also be shown that the turbulent Schmidt number equals the squared fraction of the Kolmogorov and Batchelor length scales η_K and η_B. The former is related to turbulent energy dissipation among the smallest eddies, while the latter is an estimate for the scale at which molecular diffusion acts (Forstall Jr. and Shapiro, 1950, Roberts and Webster, 2002).

$$\text{Sc}_t = \text{Pr}_t \cdot \text{Le}_t = \frac{\nu_t}{w}\frac{w}{D_T} = \frac{\nu_t}{D_T} \sim \left(\frac{\eta_K}{\eta_B}\right)^2 \tag{2.26}$$

where ν_t (cm^2 s^{-1}) is the 'eddy viscosity', w (cm^2 s^{-1}) the thermal diffusivity, and D_T (cm^2 s^{-1}) the turbulent mass diffusion coefficient. Note that the turbulent diffusion coefficient is dependent on the time scale of the motion because the Schmidt number is determined by the nature of the turbulence

and thus depends on the flow dynamics (Forstall Jr. & Shapiro, 1950).

The turbulent diffusion of momentum is modeled through a quantity called the eddy viscosity, in analogy to kinematic viscosity (or intermolecular shear). However, it has no physical relevance, and only approximates reality well in certain cases. The eddy viscosity ν_t is an important field property which can be computed through calibrated turbulence model parameters based on the assumption of isotropic turbulence (Franke et al., 2004), and is given by Eq. (2.27).

$$\nu_t = C_D \frac{k_t^2}{\epsilon_t} \quad (\mathrm{cm^2\,s^{-1}}) \tag{2.27}$$

with C_D, a calibration constant, k_t ($\mathrm{m^2\,s^{-2}}$), the turbulent kinetic energy, and ϵ_t ($\mathrm{m^2\,s^{-3}}$), the dissipation rate of the turbulent kinetic energy.

With the use of Eq. (2.26) and Eq. (2.27), an approach is obtained to model mass diffusion through turbulence, but it remains doubtful whether this approach is accurate because it has no grounded physical basis and the correct value of S_{c_t} remains heavily bound to the local flow conditions (Tominaga & Stathopoulos, 2007). Forstall Jr. and Shapiro (1950) investigated the transfer of momentum and mass in in coaxial gas jets experimentally and concluded that Lewis numbers are close to unity, while the Prandtl number is approximately equal to 0.7 resulting in a Schmidt number of 0.7 (Kärcher, 1995). The influence of a variation in S_{c_t} will be further investigated as part of this research.

2.3. Engine Wake Composition

In order to understand the relative importance of specific microphysical processes inside an aircraft engine plume, it is important to have a good overview of the wake's constituents and the chemical interactions that occur shortly after combustion. The need for specialized aircraft and propulsion design was discussed by Janssens et al. (2020), but this section will describe engine emissions in general due to the high uncertainty on engine type. What might be surprising is that only 8.5% of the total mass flow exiting a modern turbofan engine with high bypass ratio can be attributed to combustion products, while the remaining 91.5% is ambient air passing through the engine (Daley, 2016). The composition of that small fraction of combustion products is the focus of Section 2.3.1, followed by an in-depth look at chemiions and their effects in Section 2.3.2 as they might play a big role in the development of H_2SO_4-H_2O aerosols.

2.3.1. Combustion Products

Combustion is a complex chemical reaction that involves oxygen and produces heat as well as light. The intricacies of this process lie outside the scope of this project, this study chooses to focus merely on the products resulting from this reaction next to its reactants. Figure 2.6 depicts the chemical compounds that partake in combustion. The fuel, kerosene, is a hydrocarbon mixture that is supplemented with several additives. In an ideal situation, besides the unaltered components of ambient air (nitrogen (N_2) and oxygen (O_2)), the combustion products mainly consist of carbon dioxide (CO_2) and water vapor (H_2O) and their proportions depends on the specific carbon-to-hydrogen ratio of the kerosene (C_nH_m). It is safe to assume that there is about 2.5 times more CO_2 than H_2O in the engine wake. Because the fuel is supplemented with sulfur (S) to increase its lubricity, small fractions of sulfate dioxide (SO_2) are created as well. However, incomplete combustion results in several residual products such as nitrogen oxides (NO_x), hydrocarbons (HC), carbon monoxide (CO), sulfur oxides (SO_x), and soot (Daley, 2016). Especially those last two components are of interest to SAI as they both participate in the formation of sulfate aerosols in the engine wake and might influence the injection strategy. Particulate matter in the wake is either volatile (vPM) or non-volatile (nvPM) and the difference lies in the composition of its core. "Upon evaporation at modest temperatures, volatile particles do not leave a residual core of

sufficient size to be detected as a condensation nucleus. Non-volatile particles on the other hand leave a detectable refractory core" (Yu & Turco, 1998). While soot belongs to the latter, sulfur oxides in the wake combine with water vapor to form aqueous H_2SO_4 solutions which are a type of vPM.

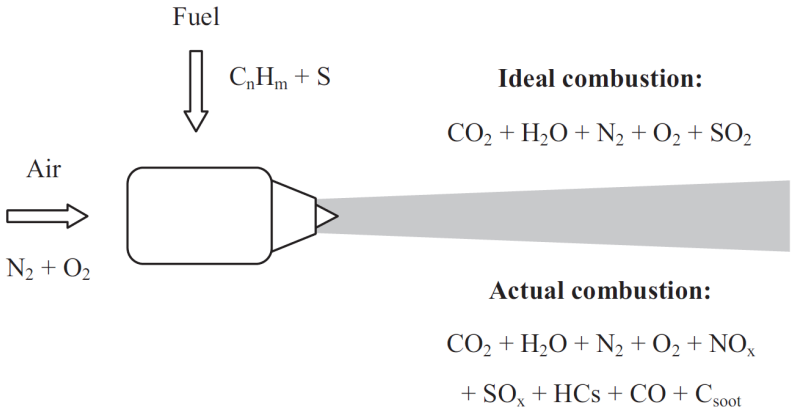

Figure 2.6: Aircraft engine emissions under ideal and realistic conditions (Daley, 2016)

It is common practice to categorize emissions in terms of an emission index (EI) which is the amount of mass (grams) emitted per mass (kilogram) of fuel burned[5]. Table 2.1 lists emission data for non-LTO (landing and takeoff) stages (assumed to be cruise), retrieved from a combination of sources. The data are global averages of various aircraft and engine types flying at altitudes between 10 to 15 km. The data from Daley (2016) is largely obtained in light of NASA's 'Atmospheric Effects of Aviation Program' (AEAP) at the end of the 20th century (Friedl et al., 1997) and summarized by the Intergovernmental Panel on Climate Change (IPCC) in their report on 'Aviation and the Global Atmosphere'. Although most species besides CO_2 and H_2O only appear in small quantities, they still have a disproportional effect on the atmosphere over longer time spans (Fritz et al., 2020). Note that EIs are strongly sensitive to engine type, thrust settings and flight altitude. As as result, this data is expected to vary for altitude corresponding to the lower stratosphere (> 20 km). Because this study is mainly interested in the concentration of H_2O, which remains constant with altitude, and the total content of nvPM for hetereogeneous nucleation, which is almost negligible with the advances in turbofan machinery, the error related to the altitude difference is considered acceptable knowing that the uncertainty on engine characteristics outweighs the variation in emissions with altitude.

Table 2.1: Typical aircraft emission indices under cruise conditions. Data retrieved from [a](Quadros et al., 2022), [b](Daley, 2016)

Species	**Emission Index EI (g/kg-fuel)**	
	Quadros[a]	IPCC[b]
CO_2	3155	3160
H_2O	1237	1230
NO_x	15.0 - 15.5	11.1 - 15.4
CO	2.2 - 2.6	1 - 3.5
HC	0.1 - 0.2	0.2 - 1.3
SO_x	0.5 - 1.0	1.0
nvPM	0.03 - 0.04	< 0.1

As mentioned earlier, almost all of the sulfur in the fuel oxidates to form SO_2, but a minor fraction f_{HS} is more highly oxidized to the $S(VI)$ radical, which are SO_3 and H_2SO_4 molecules. While the fraction

[5]https://www.easa.europa.eu/downloads/45576/en (Accessed on 21-06-2022)

of H_2SO_4 has been a point of uncertainty in the past, it is now commonly accepted that f_{HS} lies below $1-2\%$ and it decreases as the fuel sulfur content increases (Penner et al., 1999; Rasch et al., 2008). The SO_2 molecule eventually also undergoes oxidization to form sulfur trioxide (SO_3), and subsequently sulfuric acid (H_2SO_4) following the reaction sequence under (2.28) (Weisenstein et al., 1997).

$$\begin{aligned} SO_2 + OH + M &\rightarrow HSO_3 + M \\ HSO_3 + O_2 &\rightarrow SO_3 + HO_2 \\ SO_3 + H_2O + H_2O &\rightarrow H_2SO_4 + H_2O \end{aligned} \tag{2.28}$$

where M is a non-reacting molecule that absorbs a portion of the reaction energy. Note that the conversion from SO_2 to SO_3 is time-limited and takes up to a few weeks, while the transformation of SO_3 into H_2SO_4, in the presence of water vapor, is almost quadratic and happens instantly. Thus, it is assumed that all SO_3 in the wake at the time of emission is equivalent to H_2SO_4 (Sander et al., 2006; Weisenstein et al., 1997).

In favor of the discussion on microphysical processes in subsequent chapters, it is helpful to express the EIs from Table 2.1 in terms of volume mixing ratios or concentrations. Both are used in atmospheric sciences. The volume mixing ratio χ is the number of moles of the gas divided by the number of moles of air, while the concentration is the number of molecules per volume of air[6]. The volume mixing ratios at the engine exit plane based on mass conservation laws according to Schumann et al. (1996) are shown in Eq. (2.29) - (2.31).

$$\chi_{H_2O,\text{exit}} = \frac{EI_{H_2O} \cdot FF \cdot M_{\text{air}}}{M_{H_2O} \cdot \rho_{\text{air}} \cdot A_{c,\text{exit}} \cdot u_{\text{ac}}} \tag{2.29}$$

$$\chi_{SO_2,\text{exit}} = \frac{f_{\text{FSM}} \cdot (1 - f_{\text{HS}}) \cdot FF \cdot M_{\text{air}}}{M_S \cdot \rho_{\text{air}} \cdot A_{c,\text{exit}} \cdot u_{\text{ac}}} \tag{2.30}$$

$$\chi_{H_2SO_4,\text{exit}} = \frac{f_{\text{FSM}} \cdot f_{\text{HS}} \cdot FF \cdot M_{\text{air}}}{M_S \cdot \rho_{\text{air}} \cdot A_{c,\text{exit}} \cdot u_{\text{ac}}} \tag{2.31}$$

where FF ($kg\,s^{-1}$) is the fuel flow rate, EI_i ($g\,kg^{-1}$) is the emission index for for a species i, M_i ($g\,mol^{-1}$) the molar mass of species i, ρ_{air} ($g\,m^{-3}$) is the air density in the plume, f_{FSM} ($g\,kg^{-1}$) is the fuel sulfur mass content, $A_{c,\text{exit}}$ (m^2) is the initial cross-sectional area of the plume, and u_{ac} ($m\,s^{-1}$) is the true air speed of the aircraft. To get the species' number concentration N_i, apply a conversion using the ideal gas law and ratio of molecular weights as shown in Eq. (2.32).

$$N_i = \frac{N_A P_{\text{air}}}{R_u T_{\text{air}}} \chi_i \quad (\text{molecules}/\mu m^3) \tag{2.32}$$

with N_A (mol^{-1}), being the Avogadro constant; R_u ($J\,K^{-1}\,mol^{-1}$), the universal gas constant; P_{air} (Pa) and T_{air} (K) are the pressure and temperature of air inside the plume; χ_i is the volume mixing ratio of a species i.

It is now possible to create an estimate of the amount of particles present at the engine exit using operational data from the preliminary case study of Janssens et al. (2020). Assume that the propulsion requirements result in fuel flow rate FF of 0.4056 $kg\,s^{-1}$ if the aircraft is to fly 210 $m\,s^{-1}$, but the value used for u_{ac} is the engine exit speed of 450 $m\,s^{-1}$. The fuel sulfur content f_{FSM} is about 0.06% by weight, or 0.6 $g\,kg^{-1}$ in accordance with Quadros et al. (2022). Next, the engine exit area A_{exit} is equal to 3.0 m^2. As a crude approximation, the pressure inside the plume is equal to the ambient conditions in the lower stratosphere at 21 km, so about 5.0 kPa. The temperature of the core exit flow is about 600 K, and correspondingly the air density is equal to 0.029 $kg\,m^{-3}$. Then, with the use of Eq. (2.29) -

[6] https://www.e-education.psu.edu/meteo300/node/534 (Accessed on 22-06-2022)

(2.31) and Eq. (2.32), the concentration levels listed in Table 2.2 are obtained.

Table 2.2: Estimated emission concentrations at engine exit for stratospheric conditions

Species	Concentration (molecules/cm^3)
H_2O	1.2×10^{16}
SO_2	3.4×10^{12}
H_2SO_4	3.4×10^{10}
nvPM	$\sim 10^7$ soot particles*

*Estimation based on 10^{15} particles of soot/kg fuel (Quadros et al., 2022; Starik, 2007).

The results from Table 2.2 match with the predictions from Zhao and Turco (1995), who estimate a water vapor concentration of 3.5×10^{16} molecules/cm^3. They predict that the relative ratio of H_2O to H_2SO_4 is about 10^6 to 10^7 which is similar to what is shown here. The small differences that arise might be attributed to a different choice of engine parameters. However, in case of SAI missions, the amount of H_2SO_4 might increase to the order of 10^{15} - 10^{18} molecules/cm^3, as estimated by Benduhn et al. (2016). This would bring the amount of water to sulfuric acid in balance and this might have significant consequences on the underlying modeling assumptions in binary nucleation theory, which is discussed in Section 2.4.1. Note that the background water vapor concentration can be as large as 10^{13} molecules/cm^3 according to Zhao and Turco (1995).

As indicated before, the concentration of nvPM is a point of concern as well due to their ability to interact with and scavenge the volatile plume particles, as well as act as CN (Turco & Yu, 1999). Among nvPM are metals and organics (unburned hydrocarbons), but it is assumed that the bulk of the nvPM emitted by an aircraft engine can be classified as soot and contemporary estimates of the initial concentration are about 10^7 particles/cm^3 (Starik, 2007). This is based on the initial concentration in the combustion chamber, but the exact amount that exits the engine is highly uncertain and might be considerably lower depending on the engine, the power setting and flight level. This is why the role of soot in the aerosol growth process remains difficult to assess. Turco and Yu (1999) argue that soot is not able to compete effectively with volatile plume particles because their number concentration is not big enough. Rasch et al. (2008) claim that the amount of soot is less than 1% of the total number of emitted particles, which means that 99% is volatile. This might sound unreasonable, if not for the observation from Hofmann and Rosen (1978), where they measured a volatile fraction of 80%, but the real fraction is probably significantly higher because the instrumentation at the time was unable to measure ultra-fine, highly concentrated volatile aerosols, as pointed out by Turco and Yu (1997). Besides their number, the average soot particle size also plays a role. Based on field collections, the size distribution of soot at the engine exit can be represented as log-normal function with a mean particle diameter $\overline{d}_{pg} = 20$ nm and a standard deviation $\sigma_g = 1.4$, with an upper limit of 80 nm (Yu & Turco, 1998). Thus, freshly emitted soot particles are usually small and highly hydrophobic. The smaller they are, the less likely they are to act as CN (Zhao & Turco, 1995). A soot particle is initially 'activated', meaning accessible for aerosol accumulation, either through heterogeneous nucleation or coagulation with an acid droplet. Once the solid is coated by a layer of aqueous H_2SO_4, it is able to grow through condensation of additional vapor and obtain radii that are up to 12 times the size of its solid core. According to Starik (2007), about 10% of the soot particles are already activated upon creation in the combustion chamber because of solvable impurities that attach to the carbon cluster. From the remaining 90%, depending on the fuel sulfur content only 5-15$\%$ is activated through coagulation (for $d_p < 15$ nm) and heterogeneous nucleation (for $d_p > 15$ nm). The fraction that effectively partakes in the microphysical processes related to H_2SO_4 might thus be closer to the order of 10^6 particles/cm^3. Unfortunately, the picture becomes even more complex once you start looking into the effects of ion presence in the wake.

2.3.2. Chemiions

The term chemi-ionization, as introduced by pioneer Hartwell Calcote, describes a process that involves the formation of an ion during a chemical reaction between a gas molecule and a particle in an excited state that also involves the creation of new bonds (Calcote, 1948). An ion is an atom or molecule with a net electrical charge q (C), further subdivided into cations (positive charge) and anions (negative charge) depending on the balance between electrons and protons. Chemi-ionization naturally occurs during the combustion of e.g. hydrocarbons or kerosene, and it generates a copious amount of anions and cations inside the combustor of a turbofan engine (Starik, 2007). Most studies on ion formation are based on experiments with flames, using mass spectrometry to measure the ion concentration N_{ion}. This revealed that ion composition strongly depends on the fuel-to-air equivalence ratio ξ and on the type of fuel (Fialkov, 1997). Yet, this complicates matters because modern combustion chambers operate in diffusion mode which results in a wide range of fuel-air mixing ratios and consequently in a large group of different ion types. Starik (2007) has created an elaborate overview of the various chemiions that might appear in a turbofan engine and their relationships as shown in Fig. 2.7.

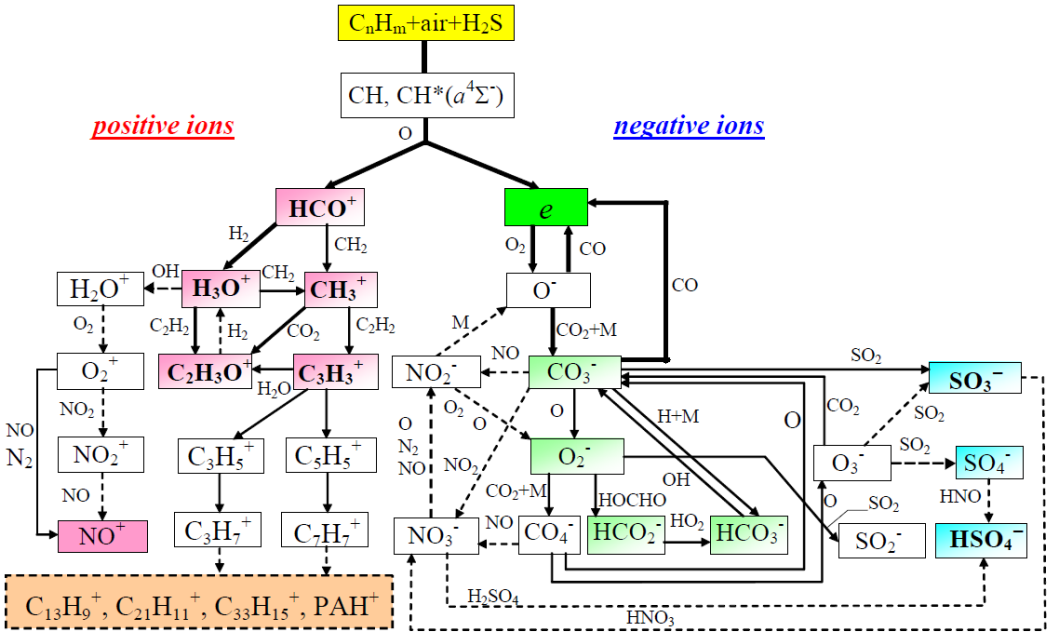

Figure 2.7: Schematic of ion formation in hydrocarbon+air flame (Starik, 2007)

Although the complexity of this picture might be unsettling at first glance, the initial formations steps are explained rather elegantly by Yu and Turco (1997) and the chemical reactions from (2.33).

$$\begin{aligned} \mathrm{CH} + \mathrm{O} &\rightarrow \mathrm{HCO}^+ + e \\ \mathrm{CH}\left(^2\Sigma^+\right) + \mathrm{O} &\rightarrow \mathrm{HCO}^+ + e \\ \mathrm{HCO}^+ + \mathrm{H_2O} &\rightarrow \mathrm{H_3O}^+ + \mathrm{CO} \end{aligned} \tag{2.33}$$

Chemiions are created during the oxidization of a (radical) hydridocarbon molecule (CH) as this results in the loss of an electron e and the creation of the formyl cation (HCO^+). The cations exchange protons with H_2O and eventually transform into hydronium cations (H_3O^+) at a rate exceeding 10^{-9} cm^3 s^{-1} (Yu & Turco, 1997). H_3O^+, acting as core ion, will subsequently start to form clusters with H_2O and other polar molecules at similar rates. The free electrons, on the other hand, are rapidly scavenged by O_2 molecules which are omnipresent. They form O_2^-, which eventually reacts with nitrogen and sulfur species to form the stable anions of nitrate (NO_3^-) and hydrogen sulfate (HSO_4^-). These anions

are likely to cluster with sulfuric acid and form agglomerations such as $HSO_4^- \cdot (H_2SO_4)_n$ at an ion-molecule reaction rate which is greater than 10^{-9} cm^3 s^{-1} (Viggiano et al., 1980).

When Frenzel and Arnold (1994) first confirmed the expected presence of sulfuric acid-based cluster ions in jet engine plumes, it sparked the theory of ion-induced nucleation (IIN) and coagulation (IIG). Chemiions induce particle nucleation by lowering the Gibbs free energy of formation, they stabilize clusters by introducing an electric field that increases the binding energy of sulfuric acid and water clusters, and they help keep the molecules together (Merikanto et al., 2016); they enhance neutral coagulation through electrostatic attraction and repulsion (Yu & Turco, 1998); and they are responsible for the partial activation of soot particles into CN (Savel'ev & Starik, 2006). It turns out that ions inside the combustor tend to attach to soot clusters, attracting water soluble compounds (impurities) such as organic sulfates, sulfur-containing ions, and organic molecules on the surface of soot particles which make them highly hydrophilic (see the end of Section 2.3.1). This is only a minor part though, the main fraction forms neutral clusters or particles with a small charge ($q \leq 2e$). These particles can not accumulate polar molecules within a combustor and are hydrophobic until they are either activated through through coagulation or heterogeneous nucleation (Starik et al., 2006).

The realization that chemiions could acts as precursors for volatile aerosol particles, led researchers to believe that they were responsible for the discrepancy between observations and the theoretical nucleation rates of aerosol (Yu & Turco, 1998). Multiple experimental investigations, supplemented by numerical analyses inside the combustor, have since then increased our understanding of mechanisms and principal pathways of ion formation (Starik, 2007). While the population of chemiions initially consists of elementary ions such as the cations N_2^+, O_2^+, N^+, and the anion O_2^-, they are usually short-lived and rapidly cluster together. Interestingly enough, it appears that the charge sign of cluster ions influences their composition and size (Arnold, 2006). Positively charged clusters will attract molecules that have a higher proton affinity and therefore often contain less H_2SO_4. Although H_2O has a similar proton affinity as H_2SO_4, the water content for positively and negatively charged clusters does not seem to vary as the result of a dynamical advantage when the water content is significantly higher than other species, such as is the case for jet engines (see Table 2.2) (Benduhn, 2008). Note that soot clusters tend to be more positively charged because they attract cations (NO^+, H_3O^+) more easily due to to their smaller mass, as compared to anions (HSO_4^-, NO_3^-) (Starik, 2007).

Observations and numerical studies have shown that NO^+, H_3O^+, SO_3^-, HSO_4^-, and NO_3^- are the only chemiions that are still abundant at the combustor exit. Kiendler et al. (2000) found some traces of larger organic ions such as $C_xH_yO^+$ and $C_xH_yO^-$ in their laboratory experiments which are remnants of the early combustion process where large biomolecules are formed and hydrocarbons such as $C_2H_3O^+$ have the largest maximum concentration reaching up to 10^{11} to 10^{12} ions$/$cm^3 (Starik, 2007). This charge concentration is drastically reduced, however, in the milliseconds that follow combustion. The process of ion-ion recombination leads to the neutralization of charge and results in maximum concentrations around 10^8 to 10^9 ions$/$cm^3 for the small molecular ions of interest roughly 0.01 seconds after ejection from the combustion zone. The associated ion-ion recombination coefficient α is equal to 10^{-7} to 10^{-6} cm^3 s^{-1} (Yu & Turco, 1998). Yet, Starik (2007) argues that a maximum concentration of both anions and cations equal to about 2×10^7 to 10^8 ions$/$cm^3 is more realistic based on the measurements from Haverkamp et al. (2004). The amount of molecular ions at the engine exit increases with f_{FSM}: if the fuel sulfur content drops, the concentration of NO_3^- and NO_2^- ions becomes more apparent.

It is mentioned several times already that large ionic clusters are formed inside the wake. The mixing process and the entrainment of ambient air into the plume leads to a variety of agglomerations. They usually consist of large clusters involving a core anion and sulfuric or nitric acid: e.g. $HSO_4^- (H_2SO_4)_n (H_2O)_m$, $NO_3^- (HNO_3)_n (H_2O)_m$, $HSO_4^- (HNO_3)_n$, and $HSO_4^- (SO_3)$ with n = 1 - 3, m = 1 - 9. Clusters with a core cation occur as well such as $H_3O^+ (H_2CO) (H_2O)_m$ and $H_3O^+ (H_2O)_m$ (Arnold et al., 1999, Schumann et al., 2002, Starik, 2007). It is still unclear as to what percentage of

molecular ions participates in cluster formation. Measurements from Arnold et al. (1998) indicate that the ion cluster concentration drops to $10^4 - 10^5$ ion clusters$/cm^3$ 50 m behind the engine. Moreover, Arnold (2006) argues that the amount of cluster ions increases with the amount of precursor gas that is available. This is the result of the higher process efficiency that is a function of the number concentration of the source species (Benduhn, 2008). Figure 2.8 designates the evolution from molecular ion sizes to large-scale cluster formation for increasing H_2SO_4 concentrations. Remark that the lowest $N_{H_2SO_4}$ only involves the creation of nitric acid clusters, which is analogous to the case where $f_{FSM} = 0$ in a combustion process. Notice that the PSD (here represented through a spectral mass distribution) has a bimodal shape, which is a characteristic of a dynamical growth process that involves two stable composition ranges (Benduhn, 2008). This duality appears in processes that involve ion-induced particle growth, which is explained in Section 2.6.2.

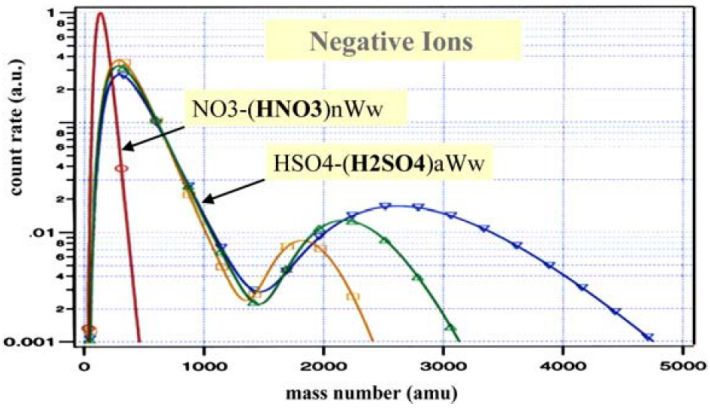

Figure 2.8: Mass distributions of negative cluster ions measured in a laboratory flow reactor experiment. The four mass distributions correspond to different gaseous H_2SO_4 concentrations, as part of SO_2 (red - lowest / blue - highest). For the lowest $N_{H_2SO_4}$ the ions are $NO_3^- (HNO_3)_a (H_2O)_w$ cluster ions and for the 3 cases with elevated H_2SO_4 the ions are $HSO_4^- (H_2SO_4)_a (H_2O)_w$ cluster ions. From Arnold (2006) who adapted it from Wilhelm et al. (2004).

To conclude this section, it is insightful to return to the injection strategy as part of a SAI mission. It is clear that molecular- and cluster-sized chemiions are present in the wake and large organic ions take part in the combustion process. In case the desired PSD of H_2SO_4 aerosol is constrained, it might be best to avoid the injection of H_2SO_4 in or even close to the core flow exit because of the uncertainty on growth implications as the result of cluster presence. Instead, the introduction of gaseous sulfuric acid in the bypass flow would avoid the major part of charge concentration inside the plume until dilution and ion recombination have neutralized most of the charge in the wake. The role of ion recombination and dilution is taken into account in Section 2.4.2 on IIN because it affects the lifetime of an ion and limits the amount of sulfuric acid molecules a critical cluster can absorb. As opposed to Yu and Turco (1998), it should be stressed that there is still no decisive answer to what really is the cause behind the large amount of grown volatile particles to be found in jet engine wakes because the ion concentration that (Starik, 2007) suggests is too low to explain observational data. Instead, it is likely the cumulative effect of various processes at work and an increased understanding of cluster forming and enhanced heterogeneous nucleation might be the missing link. The next chapters explain the various process that are known to take part in more detail.

2.4. Particle Formation

Volatile particles appear in an engine wake as the result of two distinct processes: either they are emitted directly as chemical byproducts of the combustion process, or they are nucleated from condensable vapor in the subsequent stages of the aircraft plume. Particles that are created through the former operation are denoted as ‘primary aerosols’ while the latter are called ‘secondary aerosols’ (Turco & Yu,

1997). The previous chapters showed that the number of volatile aerosol particles depends on engine and combustor design, the fuel sulfur content and flight altitude (Starik, 2007). Because of the high uncertainty on the IINer mechanics that are at play during combustion, and possibly the existence of large organic ion clusters, Section 2.3.2 concluded that it would be best to inject the gas-phase sulfuric acid somewhere towards the end of the engine train or even in the by-pass flow stream. Therefore, the major part of particle formation would happen through secondary aerosol growth and it safe to neglect the influence of primary aerosol.

Secondary aerosol production can happen trough a number of ways and it involves almost always some type of nucleation barrier, which is a probability function that governs the formation of clusters against the trend of cluster decay. Nucleation has two roles in an engine wake, it creates new particles from the vapor phase through homogeneous nucleation and it activates pre-existing particles, like soot, such that they become CN (Yu & Turco, 1998). This activation process, called heterogeneous nucleation, has been touched upon earlier in Section 2.3.1 and it describes the buildup of particulate matter onto a foreign substance or surface. If the gas-to-particle conversion involves multiple species, it is called heteromolecular nucleation as opposed to homomolecular nucleation in the case of a single species. The transformation of gaseous to aqueous H_2SO_4 involves H_2O and because it is a two-component system, it is more often referred to as 'binary nucleation'.

While there have been studies on the possibility of ternary homogeneous nucleation (THN) involving nitric acid (H_2SO_4-HNO_3-H_2O) and ammonia (H_2SO_4-H_2O-NH_3), they are not considered in this study. Pueschel et al. (1989) have shown the existence of HNO_3 in stratospheric particles and Kiang et al. (1975) suggest their formation process might be more favorable than binary homogeneous nucleation (BHN). Yet, based on Miller et al. (2003), the EI of HNO_3 in an engine wake is estimated to below 0.1 g/kg and its influence on the nucleation process in the case of high H_2SO_4 concentrations will be rather small (see also Section 2.3.1). Ammonia on the other hand is typically not present in the emissions of an aircraft, but it might be in the future as part of alternative jet fuels to achieve zero-emission aviation goals[7]. It is known to increase the nucleation rates of sulfuric acid particles by several orders of magnitude by stabilizing the critical clusters and possible aiding in the process of ion-mediated nucleation (Yu, 2006a, Kirkby et al., 2011). Therefore, the effect of NH_3 should be taken into account whenever these new type of fuels come into effect, but until then they are omitted from this theoretical discussion. In general, it is probably safe to neglect any THN when the binary system is kinetically limited, such as is the case for the high H_2SO_4 injection rates for SAI missions. The kinetic regime is the collisional limit of any nucleation process where the free energy barrier that inhibits the formation process vanishes. As a result, the particle formation rate cannot be enhanced by the presence of any third chemical species (Merikanto et al., 2016). Barrierless kinetic particle formation (BKPF) is discussed as an extension of classical nucleation theory (CNT) in Section 2.4.2.

Another possible particle formation mechanic is ion-induced nucleation (IIN), which requires the presence of chemiions. Because it involves a third body, it is sometimes seen as part of THN, although it is often treated as a separate pathway to particle creation due to various distinct effects, inherent to ions. For example, Yu and Turco (2001) argue that ions are not involved continuously throughout the formation process because they undergo neutral stages during the particle growth process. Charged critical clusters lose their advantages of enhanced stability and growth once they combine with ions from the opposite sign (please read Section 2.3.2 on chemiions and their effects). Therefore, they employ a kinetic model to simulate the dynamic interaction between neutral and charged clusters and prefer to speak of ion-mediated nucleation (IMN) as opposed to IIN, because they include the unstable size range (Yu, 2003, Benduhn, 2008). This kinetic approach to modeling nucleation is part of a larger effort to work around the deficiencies of CNT, which are discussed in Section 2.4.1. Examples of the kinetic treatment of the nucleation process are Yu (2006b) and Lovejoy et al. (2004), who consider particle

[7] https://www.ammoniaenergy.org/articles/nasa-boeing-ucf-to-study-zero-carbon-ammonia-jet-fuel/ (Accessed on 10-07-2022)

dynamics such as attachment and disintegration. While this new approach is fundamentally more correct, Benduhn (2008) finds that the uncertainties related to this mechanical method are arguably just as as large as the thermodynamical approach by e.g. Laakso et al. (2002) due to a lack of experimental validation. Besides, the computational load of the thermodynamic model is a few orders smaller.

The need for computationally efficient models is driven by the spatial and temporal scale of the problem (see Section 1.1). To save time, thermodynamic models and the calculation of nucleation rates are parameterized, which can decrease computation time considerably. Despite its shortcomings, recent papers still use CNT to model particle formation in global atmospheric models because of its simplicity, although with the inclusion of hydrate theory (Vehkamäki et al., 2002). While other theoretical approaches exist such as the aforementioned kinetic models or methods that involve the use of potentials, this study will explain and apply particle formation through CNT and hydrate theory. The possible impact of hydration of gaseous H_2SO_4 on nucleation, first proposed by Heist and Reiss (1974) and reexamined by Jaecker-Voirol et al. (1987), can be significant in locations with large concentrations of water vapor. Hydrates are small bound molecular clusters that contain at least one H_2SO_4 molecule and multiple H_2O molecules. They stabilize the vapor and hinder nucleation as it is energetically more difficult to create aerosol from hydrates instead of free sulfuric acid molecules (Vehkamäki et al., 2002, Määttänen et al., 2017).

Zhao and Turco (1995) argued in the past that hydrate theory was premature because it suffered from the same deficiencies as CNT and Yue and Deepak (1982) found that it had no significant effect in stratospheric conditions, but the high vapor concentrations behind the engine do not allow for the omission of hydrate effects. Now, following a series of quantum chemical experiments, Merikanto et al. (2016) claim that the inclusion of hydrates has improved the predictive power of CNT in line with experiments, but the accuracy of CNT as a whole remains questionable. One of the first and widely used models that included the effects of hydrates was the parameterization by Vehkamäki et al. (2002), but this model suffers from the limitation that it only applies to a small RH range while the critical clusters should contain at least four molecules. This was the result of experimental issues related to contamination by trace gases and the minimum measurable particle size. Recently, the Cosmics Leaving OUtdoor Droplets (CLOUD) experiments at European Organization for Nuclear Research (CERN) resulted in unprecedented qualitative data on sulfuric acid-water particle formation rates, with the inclusion of ions (Duplissy et al., 2016). The parameterization of Määttänen et al. (2017) makes use of this newly obtained dataset to improve upon Vehkamäki et al. (2002) by including ion-induced nucleation, for critical clusters that approach the one component limit, and for extreme dry conditions. Yet, their temperature range is not sufficient to study the 600+ K conditions at an engine exit. The intent for this study is to use BKPF theory and try to bridge the gap between the high temperature region and the start of the validity range of the parameterization. For this to work, the H_2SO_4 vapor concentration needs to remain sufficiently high such that the application BKPF remains valid. This only needs to last for the first milliseconds past emission until diffusion has lowered the temperature level sufficiently.

In search for processes that might explain the discrepancy between observed particle sizes and predicted nucleation rates in the atmosphere, scientists have come up with various explanations. The most likely mechanisms have been introduced in the previous paragraphs, but for sake of completeness, there are two remaining phenomena that this study would like to point out. Firstly, the effect of cluster-cluster interaction during nucleation. The concentration of H_2SO_4 monomers is actually smaller than the concentration of clusters inside a steady-state vapor. Since CNT considers the growth rate of a critical embryo past the saddle point of the Gibbs free energy and it probably does not grow one monomer at the time, it is worth investigating. Suzuki and Mohnen (1981) found that cluster-cluster interaction actually lowers the nucleation rate, but the influence on BHN is negligible. Secondly, Friend et al. (1980) proposed the creation of CN through coagulation of HSO_x radicals, but the uncertainty on their reaction sequence, oxidization rate and vapor pressure makes it difficult to incorporate them in

this study. Therefore, both processes will not be considered in this work. This study will explain the particle formation process through classical nucleation theory Section 2.4.1, including its limitations, and focusing on binary homogeneous nucleation. Followed by Section 2.4.2 which extends on BHN to account for heterogeneous nucleation, ion-induced nucleation and kinetic particle formation. The reader might wonder why homomolecular (or pure) nucleation of water and sulfuric acid particles is not considered. Previous investigations from Hamill, Kiang, et al. (1977) and Zhao and Turco (1995) showed that the saturation ratios are too low to allow for pure nucleation of water droplets or sulfuric acid droplets. Yet, homomolecular nucleation of H_2SO_4 is actually partially accounted for in BKPF theory. Under extreme saturation ratios (especially in the case of SAI), the one-component limit is reached and the formation of a pure sulfuric acid particle is feasible; but in subsequent growth stages pure particles will almost always take up water by condensation, if not trough coagulation with a binary H_2SO_4-H_2O particle.

2.4.1. Classical Nucleation Theory: Binary Homogeneous Nucleation

Nucleation is a stochastic process that can be described by $P \sim \exp(\Delta G/kT)$, which is a Boltzmann probability distribution where ΔG is the Gibbs free energy of nucleus formation. This nucleus is also referred to as a cluster of monomers, and still early in the forming process, might be called an embryo which pertains to its unstable state. As already mentioned in the introduction to this section, nucleation either creates particles from the vapor phase or activates particle surface areas for condensation (Yu & Turco, 1998). The first quantitative description of nucleation was formulated almost a century ago with the pioneering work of Volmer and Weber (1926) and further refined/completed by Becker and Döring (1935) and Zeldovich (1943). These three works together form the basis of what is known as classical nucleation theory (CNT), a phenomenological approach that makes use of macroscopic quantities and continuum dynamics to describe the onset of phase separation in a supersaturated system[8,9]. Following the nominal work of Flood (1934) on heteromolecular nucleation, Reiss (1950) adopted CNT to create a full treatment of binary nucleation. In BHN, particle formation can still occur when two vapor species are not supersaturated as long as both participating vapor species are supersaturated with respect to the liquid solution (the aerosol) (Seinfeld & Pandis, 2016). However, the influential work from Stauffer (1976) pointed out several thermodynamic inconsistencies in Reiss's work and proposed a revised version of CNT. More modern approaches now include the most thermodynamically consistent versions of CNT, including hydrate effects (e.g. Laakso et al. (2002)), and experimentally-determined quantum-chemical (QC) activity coefficients (Noppel et al., 2002, Merikanto et al., 2016), otherwise called QC normalized CNT.

Limitations

Standard CNT has been criticized in the past because it is an approximative theory. The dissertation from Benduhn (2008) does an excellent job at explaining the various shortcomings of CNT, but this work will only mention them briefly to inform the reader about their existence. To start, CNT does not incorporate unstable particle dynamics. It assumes instantaneous thermodynamic equilibrium which is not reality. This issue also arises in the construction of parameterizations based on steady-state laboratory experiments. These conditions are not representative of the highly dynamical environment that is encountered in the wake of an aircraft. This relates back to the kinetic treatment of particle formation by Yu (2006b) because he believes that the unstable stages during the formation of the critical cluster have a large impact on effective nucleation rates. To this end, evaporation of clusters is one the biggest uncertainties during particle formation (F. Yu, personal communication, November 10, 2022). On the other hand, a study by Modgil et al. (2005) seems to indicate that particle dynamics

[8] https://www.mpikg.mpg.de/864538/Nucleationlecture.pdf (Accessed on 20-07-2022)
[9] http://spider.science.strath.ac.uk/cmac/files/media/PNCPathway.pdf (Accessed on 20-07-2022)

react sufficiently fast to fluctuations in ambient conditions to justify this assumption. Secondly, the law of mass action is not satisfied, which implies that for a chemical reaction in equilibrium, the ratio between the concentration of reactants and products is constant. Researchers circumvent this by assuming that, close to an equilibrium state, stable and unstable system assumptions apply simultaneously. This allows for the formation of new particles while assuming thermodynamic equilibrium. This problem, however, is solved in QC-normalized CNT Merikanto et al. (2016). A third assumption and arguably the most intrusive one, is the application of the capillarity approximation, i.e., the assumption that the critical nucleus surface tension equals the surface tension of a flat interface (Laaksonen & Napari, 2001). This entails the application of the liquid drop model to scale macroscopic (bulk) properties to molecular-sized clusters. The liquid drop model is part of continuum dynamics which does not apply to microscopic particles submerged in a fluid, as was shown in Section 2.2.1. The incorrect description of properties such as surface tension and subsequently partial vapor pressures on the smallest scale are the major cause of large errors in predicted nucleation rates, especially because smaller clusters result in the highest formation rates (Merikanto et al., 2016). During an SAI mission, H_2SO_4 saturation levels behind the jet engine are very high so the cluster sizes will only consist of a few molecules (< 5 molec.) and CNT is expected to fail (Yu & Turco, 1998). Yet, based on a series of Monte Carlo simulations of clusters in an imperfect vapor, Merikanto et al. (2007) showed that CNT and the inclusion of the liquid droplet model are suited to describe the work required to form small clusters, given a experimentally-determined correction factor for clusters with less than 10 molecules which is constant for all sizes. Now, the final two assumptions are related to particle formation in the presence of ions. The fourth premise is the use of the the Kelvin-Thomson equation to calculate the nucleation barrier in the presence of charged particles (see extension 2.4.2). It has been shown that this relation performs poorly on cluster level, when dipole interactions start to become important (Yu, 2005). This partly stems from the third assumption on the liquid drop model. Lastly, Yu (2002) warns that classical IIN incorrectly assumes that the formation rate is a linear function of ion concentrations. Beyond a threshold concentration, the ion's lifetime decreases due to increased neutralization and this impedes nucleation as particle disintegration is enhanced. It is clear that CNT has some fundamental limitations and for some extreme conditions this leads to deviations of up to ten orders of magnitude between experimental and simulated nucleation rates. Yet, other methods still have comparable levels of uncertainty at a much higher computational cost (Benduhn, 2008).

Thermodynamic model

Merikanto et al. (2016) apply advanced algebraic methods to create their nucleation model which can be difficult to follow. For the purpose of this discussion, the explanation of BHN will be simplified in accordance with the explanation from Seinfeld and Pandis (2016) to keep a clear overview. The overarching equation to predict the neutral homogeneous nucleation rate J according to CNT is given by Eq. (2.34), which includes the Boltzmann probability distribution.

$$J_{\text{neutral,hom}} = C \exp\left(\frac{-\Delta G^*}{kT}\right) \quad (\text{embryos formed}/(\text{cm}^3\text{s})) \tag{2.34}$$

where C is a pre-exponential term or kinetic pre-factor (see Section 2.4.2) and ΔG^* (J) is the energy that is required to form a critical embryo (where the asterisk denotes properties related to the critical cluster). It is the saddle point or local minimum of the Gibbs free energy change due to particle formation ΔG which is a function of temperature and aerosol composition.

Locating this saddle point in a thermodynamic consistent way has been the reason for the revision of CNT by e.g. Stauffer (1976), Mirabel and Reiss (1987). Note that Merikanto et al. (2016) prefer to use the terminology 'work of formation' instead of Gibbs free energy. The general expression for ΔG is Eq. (2.35). In the case of two nucleating species (BHN) and under the assumption of a spherical

droplet forming, this becomes Eq. (2.36). The presence of ions or hydrate formation are omitted for now.

$$\Delta G = \Delta G_{\text{volume}} + \Delta G_{\text{surface}} = -n\psi + A_s\sigma \quad \text{(J)} \tag{2.35}$$

$$\Delta G\left(n_{\text{A}}, n_{\text{B}}, T\right) = -n_{\text{A}}kT \ln \frac{\Gamma_{\text{A}g}}{\Gamma_{\text{A}\ell}} - n_{\text{B}}kT \ln \frac{\Gamma_{\text{B}g}}{\Gamma_{\text{B}\ell}} + 4\pi r^2\sigma \quad \text{(J)} \tag{2.36}$$

where ψ (J/mol) is the thermodynamic affinity, A_s (nm^2) is the surface area, A and B are the participating species, k (J/K) is the Boltzmann constant (expressed alternatively for clarity), and r (nm) is the nucleus/embryo radius. Note that the surface tension σ (N m^{-1}) is dependent on the aerosol weight composition. The activities Γ_i are defined here according to Seinfeld and Pandis (2016):

$$\Gamma_{\text{A}g} = p_{\text{A}}/p^{\text{s}}_{\text{A}} = \text{activity of A in gas phase}$$
$$\Gamma_{\text{B}g} = p_{\text{B}}/p^{\text{s}}_{\text{B}} = \text{activity of B in gas phase}$$
$$\Gamma_{\text{A}\ell} = p^{\circ}_{\text{A}_{\text{sol}}}/p^{\text{s}}_{\text{A}} = \text{activity of A in the liquid phase}$$
$$\Gamma_{\text{B}\ell} = p^{\circ}_{\text{B}_{\text{sol}}}/p^{\text{s}}_{\text{B}} = \text{activity of B in the liquid phase}$$

with p^{s}_{i} the saturation vapor pressure of component i and $p^{\circ}_{\text{i}_{\text{sol}}}$ the vapor pressure of compound i over a flat surface of a solution with the same composition as the aerosol.

The first two terms on the right side of Eq. (2.36) represent the bulk free energy change that describes the likelihood of a phase change through its thermodynamic affinity ψ and it scales with volume. This term is always negative in the case of condensation (energy gain). The last term on the right is the energy cost to form an interface between the two phases, it scales with surface area and it is always positive. Both contributions are shown in Fig. 2.9 as a function of the nucleus radius. The affinity of a transformation from a gas to a liquid phase depends on the chemical potential of both phases and it is commonly expressed through the theory of supersaturation as shown in Eq. (2.37).

$$\psi = \phi_{i,g} - \phi_{i,\ell} = kT \ln \text{SR}_i = kT \ln \frac{\Gamma_{i,g}}{\Gamma_{i,\ell}} = kT \ln \frac{\gamma_{i,g}N_{i,g}}{\gamma_{i,\ell}N_{i,\ell}} \quad \text{(J/mol)} \tag{2.37}$$

where SR_i denotes the saturation ratio of a species i, which can be expressed through its activities or through the product of the number concentrations and their activity coefficients. The latter approach is taken in Eq. (2.48) from Merikanto et al. (2016). If $\psi < 0$, the process is thermodynamically impossible; $\psi > 0$ corresponds to a spontaneous process; and $\psi = 0$ indicates thermodynamic equilibrium.

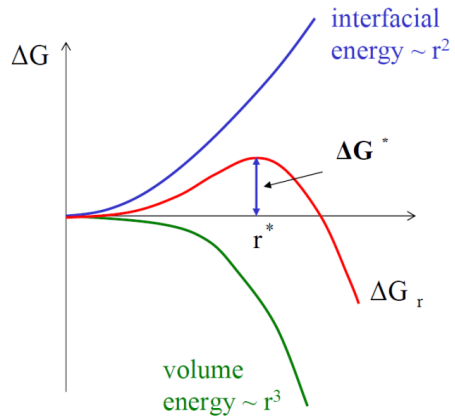

Figure 2.9: Graphical illustration of the free energy change ΔG as a function of the embryo radius (Priezjev, 2020)

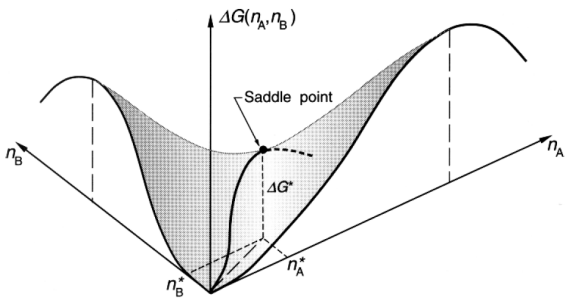

Figure 2.10: Schematic diagram of saddle point in the ΔG surface (Seinfeld & Pandis, 2016)

Figure 2.9 and 2.10 illustrate the physical relevance of the critical embryo radius r^*. It is a point of metastability in the phase transformation and represents the smallest cluster that is at least as likely to grow as to decay (Merikanto et al., 2016). Clusters that have $r < r^*$ will eventually redissolve, but clusters that surpass the critical radius will continue to grow as it is thermodynamically favorable. In the event of BHN, the Gibbs free energy of nucleus formation represent a three-dimensional surface, as seen in Fig. 2.10, which contains a saddle point. The embryo radius r is given by Eq. (2.38), but the critical radius can be obtained through optimization by setting the derivative of Eq. (2.36) with respect to the radius equal to zero.

$$\frac{4}{3}\pi r^3 \rho = n_\mathrm{A} m_\mathrm{A} + n_\mathrm{B} m_\mathrm{B} \tag{2.38}$$

$$\left(\frac{\partial \Delta G\left(r^*\right)}{\partial r}\right)_{x_A = x_A^*, T} = 0 \tag{2.39}$$

where m_i is the mass of molecule i, and $x_A = n_A / (n_A + n_B)$ is the mole fraction of species A.

The boundary condition imposed by Eq. (2.39) results in an expression for r^*, given by Eq. (2.40), which needs to be solved iteratively in conjunction with the critical weight composition. Remark that Eq. (2.40) is an alternate form of Eq. (2.13) (Ostwald-Freundlich). The weight fraction of each species is determined with the Gibbs-Duhem relation, derived earlier in Section 2.1.2, and rewritten here as Eq. (2.41). The critical Gibbs free energy change ΔG^* is then obtained through Eq. (2.42).

$$r^* = \frac{2\sigma(x_A^*)\varsigma_i(x_A^*)}{kT \ln \mathrm{SR}_i} \quad (\mathrm{nm}) \tag{2.40}$$

$$\varsigma_B(x_A^*) \ln \mathrm{SR}_A = \varsigma_A(x_A^*) \ln \mathrm{SR}_B \tag{2.41}$$

$$\Delta G^* = \frac{4}{3}\pi\sigma(x_A^*) r^{*2} \quad (\mathrm{J}) \tag{2.42}$$

wherein ς_i ($\mathrm{m}^3/\mathrm{mol}$) is the partial molar volume of species i.

It turns out that the critical radius is much less sensitive to variations in ambient conditions compared to the weight composition (mole fractions) of the critical embryo and the nucleation rate, in particular the saturation ratios (Määttänen et al., 2017). Next, the pre-exponential factor C needs to be addressed. Its original form, already derived by Reiss (1950), still stands and it is formulated here by Eq. (2.43).

$$C = \frac{\beta_\mathrm{A}\beta_\mathrm{B}}{\beta_\mathrm{A} \sin^2\zeta + \beta_\mathrm{B} \cos^2\zeta} Z \left(N_\mathrm{A} + N_\mathrm{B}\right) A_s^* \quad (1/(\mathrm{cm}^3\,\mathrm{s})) \tag{2.43}$$

where β_i ($1/(\mathrm{cm}^2\,\mathrm{s})$) is the impingement rate of molecules of component i and calculated according to Eq. (2.44); the angle ζ depends on the free energy surface and the impinging rate of both species and is illustrated in Fig. 2.11, a practical expression for ζ according to Määttänen et al. (2007) is Eq. (2.45); Z is the Zeldovich non-equilibrium factor; N_i are the number concentrations of the gas-phase species; and A_s^* is the surface area of the critical cluster.

$$\beta_i = \frac{p_i}{\sqrt{2\pi M_i kT}} \quad (1/(\mathrm{cm}^2\,\mathrm{s})) \tag{2.44}$$

$$\tan\zeta = \frac{n_\mathrm{B}^*}{n_\mathrm{A}^*} \tag{2.45}$$

The impingement rate is also known as the forward rate constant (counter to the reverse rate constant which governs cluster disintegration). It can be accompanied by an accommodation factor which is a measure for the fraction of monomers that collide with the critical cluster and stick (see e.g. the

kinetic model from Yu and Turco (1998)). Here it assumed to equal unity. The Zeldovich factor is the probability that a cluster on top of the nucleation barrier continues to grow instead of redissolving (Zeldovich, 1943). While it is possible to simplify the pre-exponential term for certain limiting cases where one of the solution components is dilute with respect to the other (e.g. Hamill et al. (1982)), this is not possible for the saturation ratios related to an SAI mission and the full expression needs to be evaluated. This can be a tedious process and the model from Merikanto et al. (2016) solves it algebraically through Eq. (2.46), an alternative expression of the nucleation rate, but the principle remains the same.

$$J_{\text{neutral,hom}} = R_{\text{g,av}} Z N^* = |\lambda_1| \frac{1}{\sqrt{|\det G(r^*)|}} N^* \quad (\text{embryos formed}/(\text{cm}^3\text{s})) \tag{2.46}$$

with

$$R_{\text{g,av}} = \frac{\beta_{\text{A}} \beta_{\text{B}}}{\beta_{\text{A}} \sin^2 \zeta + \beta_{\text{B}} \cos^2 \zeta} \quad : \text{Average growth rate due to condensation}$$

$$N^* = (N_{\text{A}} + N_{\text{B}}) A_s^* \exp\left(\frac{-\Delta G^*}{kT}\right) \quad : \text{Number concentration of critical clusters in the vapor}$$

Lastly, to be able to solve the model above, a wide range of experimental data is required on various thermodynamic properties including the surface tension, the density of the aerosol solution, and the equilibrium vapor pressures over a flat surface. The various sources, mainly combined by Vehkamäki et al. (2002), are summarized in Table 1 from Merikanto et al. (2016).

Hydrates

As mentioned in the introduction on particle formation, Merikanto et al. (2016) make use of quantum chemical data to define the activity of sulfuric acid vapor, which depends on the amount of hydrates present in the vapor. The theory behind QC normalized CNT is outside the scope of this work, but the implications on the thermodynamic model are summarized below. The data from the CLOUD experiments provides information about the partitioning of H_2SO_4 into free monomers and hydrated molecules. Only the free monomers take part in particle formation and thus the concentration of free sulfuric acid monomers defines the activity and subsequently the saturation level (Vehkamäki et al., 2002, Merikanto et al., 2016). Suppose H_2SO_4 corresponds to species A and H_2O to species B, then the affinity can be expressed as:

$$\psi = kT \ln \text{SR}_i \approx kT \ln\left(\frac{N_i^{\text{free}}}{N_{i,s}^{\text{free}}(x_A)}\right) \quad (\text{J/mol}) \tag{2.47}$$

where N_i^{free} is the number concentration of free molecules of component i in the nucleating vapor and $N_{i,s}^{\text{free}}$ is the number concentration of component i in saturated vapor above a solution with sulfuric acid mole fraction x_A. This new definition needs to be included in all equations that rely on the saturation ratio, e.g. Eq. (2.48) for the Gibbs free energy of formation.

$$G(r, x_A) = -n_{A,\text{tot}} kT \ln\left(\frac{N_A^{\text{free}}}{N_{A,s}^{\text{free}}(x_A)}\right) - n_{B,\text{tot}} kT \ln\left(\frac{N_B^{\text{free}}}{N_{B,s}^{\text{free}}(x_A)}\right) + 4\pi r^2 \sigma(x_A) \quad (\text{J}) \tag{2.48}$$

where the total numbers of sulfuric acid and water molecules $n_{A,\text{tot}} = n_{A,\text{c}} + n_{A,\text{s}}$ and $n_{B,\text{tot}} = n_{B,\text{c}} + n_{B,\text{s}}$ include both bulk liquid ($n_{A,\text{c}}$, $n_{B,\text{c}}$) and surface excess ($n_{A,\text{s}}$, $n_{B,\text{s}}$) contributions.

A word of caution, Merikanto et al. (2016) assume that the concentrations of hydrates with more than one acid molecule are negligible, so only clusters with one sulfuric acid molecule are significant and the hydrate distribution is truncated after four water molecules. This assumption stems from the fact that they expect higher orders of H_2O concentrations compared to H_2SO_4, but this is not necessarily true

for an SAI application. Remark that the concentration of water vapor molecules is not really affected by hydration in humid conditions and therefore $N_B^{\text{free}} = N_B^{\text{total}}$ (Vehkamäki et al., 2002).

2.4.2. Extensions of Classical Nucleation Theory

So far, the only gas-to-particle conversion process that has been discussed is binary homogeneous nucleation where the homomolecular nucleation of H_2SO_4 is only considered feasible under conditions where BKPF is applicable. BHN is very temperature sensitive and occurs only in areas of relatively low temperature and high ambient sulfuric acid or water vapor concentration (Yue and Deepak, 1982, Weisenstein et al., 1997). As became apparent in the introduction to particle formation, several other pathways that lead to nucleation of volatile particles exist. They are introduced below and naturally extent on the CNT framework that has been covered in Section 2.4.1.

Heteromolecular Heterogeneous Nucleation

Heteromolecular heterogeneous nucleation is the formation of multi-component solution droplets onto the surface of foreign pre-existing particles, e.g. the creation of mixed particles through nucleation of the H_2SO_4-H_2O binary system on soot particles. Once they are covered by an initial layer, they are activated for subsequent growth through condensation, at which point they are classified as condensation nuclei (please see the discussion on soot in Section 2.3.1). Accumulation of gaseous vapor onto foreign particles either happens through adsorption or absorption. The former process is the event where gas molecules collide with a solid surface and reside on the exterior face for a limited amount of time. The latter process requires the CN to be soluble, such as a salt, which results in ternary systems, but not a lot is known about their properties (Hamill et al., 1982). To the author's knowledge, there are no significant constituents in the wake that allow for absorption. As mentioned earlier, the fresh soot particles that exit the jet engine are usually small and hydrophobic. Yet, a small fraction is viable for heterogeneous nucleation through adsorption if they are large enough ($d_p > 15$ nm). On top of that, if the soot clusters are charged, heterogeneous nucleation will happens much faster (Starik, 2007).

To calculate the heterogeneous nucleation rate, the effect of the foreign surface on the Gibbs free energy of nucleation has to be considered. In the case of homogeneous nucleation, the surface area that needs to be formed is that of a sphere, but in the presence of a foreign object, part of that surface area is accounted for and this lowers the nucleation barrier (Zhao & Turco, 1995). This is illustrated in Fig. 2.11. The lower nucleation barrier is implemented by multiplying the required ΔG^* for homogeneous nucleation from Eq. (2.42) with a correction factor $f_{\text{h}}(\theta, R_{\text{CN}})$ that depends on the contact angle and the radius of the CN, as shown in Eq. (2.49). The correction factor can be estimated with Eq. (2.50) for a spherical impurity from Fletcher (1958).

$$\Delta G^*_{\text{het}} = \Delta G^*_{\text{hom}} f_{\text{h}} \quad \text{(J)} \tag{2.49}$$

$$f_{\text{h}}(b_1, b_2) = \tfrac{1}{2}\left\{1 + \left(\tfrac{1-b_1 b_2}{b_3}\right)^3 + b_2^3\left[2 - 3\left(\tfrac{b_2-b_1}{b_3}\right) + \left(\tfrac{b_2-b_1}{b_3}\right)^3\right] + 3b_1 b_2^2\left(\tfrac{b_2-b_1}{b_3} - 1\right)\right\} \tag{2.50}$$

with

$b_1 = \cos\theta = \dfrac{\sigma_{SV} - \sigma_{SL}}{\sigma_{LV}}$: An expression for the contact angle based on the interfacial tensions

$b_2 = \dfrac{R_{\text{CN}}}{r^*}$: Ratio of radii

$b_3 = \left(1 + b_2^2 - 2b_1 b_2\right)^{1/2}$: Substitution parameter

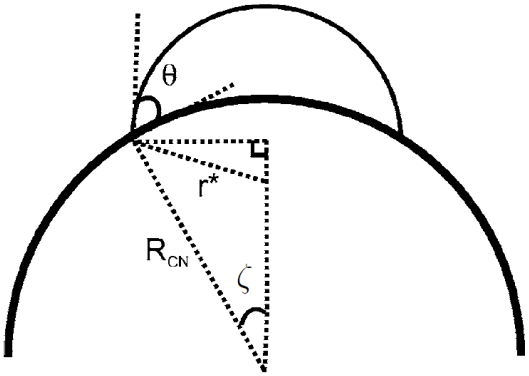

Figure 2.11: The geometry of heterogeneous nucleation: a critical cluster of radius r^* on the surface of a pre-existing particle of radius R_{CN}. θ is the contact angle. Angle ζ is related to Eq. (2.43) and (2.45). Adapted from Määttänen et al. (2007).

The contact angle θ is a measure for the wettability of a surface. Depending on the material and roughness of the CN, this angle may range anywhere between 0° and 180°. The difference in heterogeneous nucleation rate for a case where $\theta = 0°$ (perfectly wettable surface) and $\theta = 180°$ (non-wettable surface) can span 50 orders of magnitude. A correct estimation of the contact angle is thus vital to assess the impact of heterogeneous nucleation. In the past, contact angles of 70° have been assumed based on a case where sulfuric acid is formed on solid sulfur. For comparison, the contact angle for water on ice is very close to zero (Hamill, Kiang, et al., 1977, Hamill et al., 1982).

The reader should be careful to apply the extension for heterogeneous nucleation in practice, as it does not take into account the presence of hydrates nor charged CN explicitly, and foreign particles are most definitely not always perfectly spherical. Moreover, the extensive bookkeeping that is required to follow the growth evolution of a mixed particle (a liquid aerosol with a solid core) can increase the computational load significantly. This is related to the issue with fixed particle bins and the inherent numerical diffusion as discussed earlier in Section 2.1.1.

Ion-induced Nucleation

In the proximity of (chemi)ions, an alternate pathway to particle formation is possible through a combination of heterogeneous nucleation and electrostatic effects. The various contributions of chemiions to particle mechanics in the engine wake were discussed previously in Section 2.3.2. This section introduces the framework behind the implementation of IIN as an extension of CNT but without the inclusion of dipole effects and charge sign dependence (e.g see Yu (2005)). The classical version of IIN includes the addition of a fourth term to the Gibbs free energy of formation that takes the electrical potential of the ion into account, as shown in Eq. (2.51). This modified version of ΔG results in a new expression for the critical cluster size r^*, given by Eq. (2.52) and often referred to as the Kelvin-Thomson equation (although he did not derive it).

$$\Delta G_{\text{IIN}} = \Delta G_{\text{neutral}} + \frac{q^2}{8\pi\varepsilon_0}\left(1 - \frac{1}{\varepsilon_r}\right)\left(\frac{1}{r} - \frac{1}{r_{\text{ion}}}\right) \quad \text{(J)} \tag{2.51}$$

$$r^* = \frac{2\sigma(x_A^*)\varsigma_i(x_A^*)}{kT \ln \text{SR}_i}\left[1 - \frac{q^2}{64\pi\varepsilon_0\sigma\left(x_A^*\right)}\left(1 - \frac{1}{\varepsilon_r}\right)\frac{1}{r^{*4}}\right] \quad \text{(nm)} \tag{2.52}$$

where q (C) is the net electrical charge of the ion and ε_i (F/m) is the permittivity of the solution (r) and the vacuum (0).

The last term of Eq. (2.51) is proportional to $1/r$ and always negative when the radius of the ion is smaller than the critical embryo $r_{\text{ion}} < r$. As a result, the nucleation barrier falls off more rapidly and smaller critical clusters can be obtained. Apart from the electrostatic effect, the ion also provides a

surface to condense on which is the heterogeneous effect (Merikanto et al., 2016, Hamill et al., 1982). Because of the added term between brackets, Eq. (2.52) has two possible real solutions (instead of one in the neutral case). This is best explained by looking at Fig. 2.12, where the Gibbs free energy of formation now has a local minimum next to a local maximum. This graph clearly shows that the impact of the ion, embedded in the cluster, on the arrival rate of vapor molecules is considerably weaker than that on the evaporation rate. Above all, it stabilizes the cluster and prevents disintegration of smaller clusters through the local minimum (Seinfeld & Pandis, 2016).

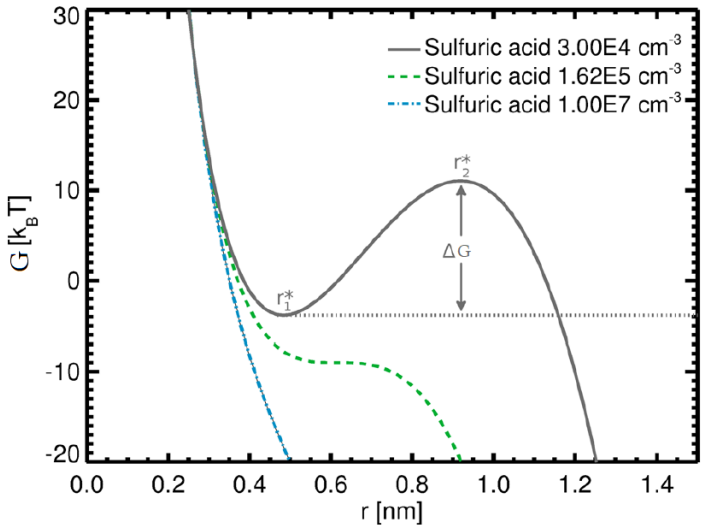

Figure 2.12: Work of formation as a function of cluster geometric radius with fixed composition x_A^* for the ion-induced sulfuric acid-water particle formation. The cluster at r_1^* contains the core ion with some sulfuric acid and water attached, and r_2^* cluster contains the ion at the core as well as additional sulfuric acid and water attached into it. Adapted from Merikanto et al. (2016).

The green dashed line in Fig. 2.12 indicates the onset of barrierless kinetic particle formation (BKPF) at increased saturation levels (concentrations) which is the final extension to CNT and discussed hereafter. It is the restricting case where the particle formation rate becomes kinetically inhibited by the arrival rate of gas molecules.

Note that the IIN theory above does account for sign preferences, but there is strong evidence that suggests that certain gases nucleate faster depending on the charge sign. To give an example, it has been known for more than a century that water molecules prefer to bind with anions due to their polarity and this is also the case for sulfuric acid molecules. This sign preference stems from the dipole interactions that are relevant on microscopic scale of clusters (Yu, 2005). Chemical polarity is the concept of asymmetrical charge distribution over a molecule, creating a permanent dipole moment (PDM) with a negatively and positively charged end. Although the inclusion of these PDMs is theoretically more grounded, the implementation still leads to the same degrees of uncertainty as the original model (see the discussion on ion interactions by Benduhn (2008)). Secondly, classical IIN implicitly assumes that the size of the ion does not influence the energetics of nucleation. Mathematically, this means that the radius of the bare ion should be smaller than the lower critical cluster radius: $r_{\text{ion}} < r_1^*$. This is the case for the small molecular-sized ions that exit the engine such as NO^+, H_3O^+, SO_3^-, HSO_4^-, and NO_3^- which are mostly conjugate bases of acids. However, should the ions be part of large organic clusters through charging of soot, the classical IIN approach is not suitable anymore (Määttänen et al., 2017). Common molecular-sized ion radii are $\sim$ 0.5 nm and all clusters treated by IIN consist of only one ion. Lastly, the linear dependence of the nucleation rate on the ion density might not hold for increasing concentrations as pointed out by Yu (2002). This is the consequence of increased recombination rates and leads to shorter lifetimes. The leftover concentration of ions can be estimated with the use of Eq. (2.53) that incorporates the effect of dilution, coagulation/scavenging by pre-existing particles and

ion-ion recombination (Dunne et al., 2016).

$$N_{\text{ion}}(t) = N_{\text{ion,exit}} - \left[\left(\frac{dN_{\text{ion}}}{dt} \right)_{\text{dilution}} + \text{Coag}_{\text{sc}}\, N_{\text{ion}} + \alpha N_{\text{ion}}^2 + J_{\text{ion}} \right] t \quad (1/\text{cm}^3) \tag{2.53}$$

with the operator Coag_{sc} $(1/\text{s})$ that represent the scavenging rate due to coagulation with pre-existing particles, α (cm^3/s), the ion-ion recombination rate and J_{ion} $(1/(\text{cm}^3\,\text{s}))$, the ion-induced nucleation rate. The dilution rate can be calculated explicitly with an advection-diffusion scheme.

Barrierless Kinetic Particle Formation

The final extension to CNT follows from the necessity to be able to simulate the limit of particle formation where the nucleation barrier ΔG^* vanishes. Mathematically, this corresponds to the case where the exponential term in Eq. (2.34) equals zero and the nucleation rate becomes limited by the kinetic prefractor C. This barrierless kinetic particle formation (BKPF) limit is obtained for high concentrations of gas-phase molecules, as is the case for SAI where large amounts of H_2SO_4 are injected into the engine plume. Critical embryos become extremely stable, containing only one sulfuric acid molecule. Määttänen et al. (2017) created a parameterization to calculate the threshold concentration for the onset of BKPF depending on temperature and RH. The neutral and ion-induced kinetic particle formation rates are then given by Eq. (2.54) and (2.55), which are analytical expressions presented by Merikanto et al. (2016). A discussion on their origin is outside the scope of this work.

$$J_{\text{kin,neutral}} = \frac{C_{\text{BKPF}}}{2} \sqrt{T} \left(N_A^{\text{total}} \right)^2 \quad (\text{embryos formed}/(\text{cm}^3\text{s})) \tag{2.54}$$

$$J_{\text{kin,ion-induced}} = C_{\text{BKPF}} N_{\text{pre}} \sqrt{T} \left(N_A^{\text{total}} \right) \quad (\text{embryos formed}/(\text{cm}^3\text{s})) \tag{2.55}$$

with

$$C_{\text{BKPF}} = (r_A + r_{\text{ref}})^2 \sqrt{8\pi k \left(\frac{1}{m_A} + \frac{1}{m_{\text{ref}}} \right)} \quad (\text{cm}^3/(\text{sK}^{0.5})) \tag{2.56}$$

where

$$r_{\text{ref}} = r_A = 0.3 \cdot 10^{-9}\ \text{m} \quad \text{and} \quad m_{\text{ref}} = m_A = 98.07 \cdot 1.661 \cdot 10^{-27}\text{kg} \quad : \text{in case of Eq. (2.54)}$$

$$r_{\text{ref}} = r_{\text{ion}} = 0.487 \cdot 10^{-9}\ \text{m} \quad \text{and} \quad m_{\text{ref}} = m_{\text{ion}} = 98.07 \cdot 1.661 \cdot 10^{-27}\text{kg} \quad : \text{in case of Eq. (2.55)}$$

Note that species A corresponds to H_2SO_4 and the pre-existing cluster concentration N_{pre} is the negative ion concentration N_{anion}. The reference clusters are relics from normalized CNT and it suffices here to treat them as constants. If nucleation takes place in the kinetic regime, the neutral particle formation rate becomes a function of the collision rate between a free sulfuric acid molecule or hydrate with another free sulfuric acid molecule or hydrate, while the ion-induced nucleation rate depends on the collision frequency involving ions.

Remark that the kinetic neutral rate is proportional to the concentration of sulfuric acid squared, yet the kinetic ion-induced rate only to the first power. Literature calls the former ‘kinetic-type’ particle formation and the latter ‘activation-type’, but in this study they are both denoted as BKPF processes. In addition, both rates are weakly dependent on temperature ($\sqrt{T}$) and have an almost negligible dependence on relative humidity (through collisions involving hydrates). BPFK is always the upper limit to nucleation and this is shown in Fig. 2.13 where the formation rates (solid lines) converge towards the kinetic limit (dotted lines). Notice the restriction (black striped line) where the amount of available ions limits the formation rate.

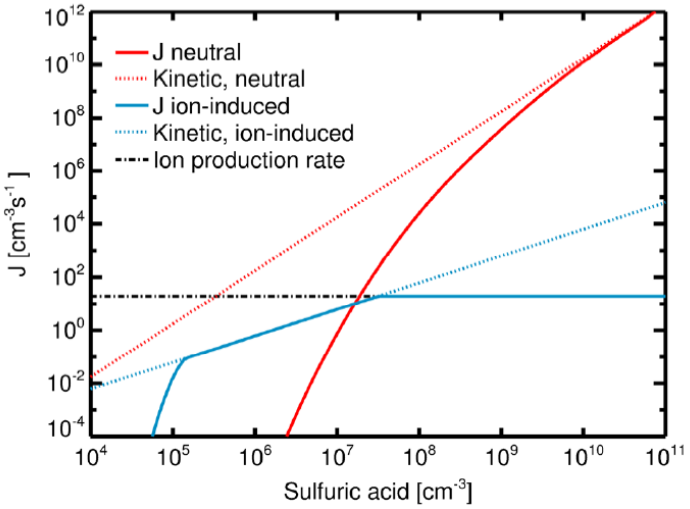

Figure 2.13: Neutral (red line) and ion-induced (blue line) particle formation rates as a function of sulfuric acid concentration. Dotted red and blue lines illustrate the kinetic limits for the neutral and ion-induced particle formation rates, respectively. The black dash-dotted line represents the ion production rate, which poses an upper limit for the ion-induced particle formation rate (Merikanto et al., 2016).

On a final note, whenever a binary system resides in the kinetic regime, the nucleation is likely not affected by the presence of a third chemical species because there is no free energy barrier that normally impedes formation. This was mentioned already in this section's introduction but it is worth repeating (Merikanto et al., 2016).

2.5. Condensation and Evaporation

The previous section introduced nucleation, the initial stage of volatile particle formation where stable particle diameters can range from $\sim$ 1 to 10 nm. Once a particle is stable, the process of particle growth continues either through condensation (2nd stage) or coagulation (3rd stage). Although both growth processes can exist simultaneously, condensation is usually dominant for the early lifetime of a particle. Condensation, in the way that it is treated here, is defined as the phase transformation of a gas-phase substance to its liquid form when in contact with an 'activated' pre-existing particle, otherwise called 'condensation nuclei' (CN). The reverse process is called evaporation. Note that some authors use terms like condensation rate to denote collision frequencies when dealing with nucleation, but this can lead to confusion. This work uses the term in its traditional sense to refer to the second stage of particle growth. Once again, it is possible to differentiate between homo- and heteromolecular, as well as homo- and heterogeneous processes (see the introduction of Section 2.4). As shown earlier, sulfuric acid vapor can condense onto activated soot clusters next to pure H_2SO_4 droplets. This discussion only focuses on heteromolecular condensation and does not discriminate between homo- or heterogeneous condensation because it does not affect the growth process on the level of abstractness that is considered here. In reality, the nature of the particle core (foreign or pure material) does have an influence on the energetics of formation, especially in the presence of charge.

Nucleation mode particles evolve into Aitken mode particles through the act of condensation (see also Section 2.1 on particle properties). Aitken particle diameters range anywhere between 10 - 100 nm, and at 50 nm coagulation already starts to become dominant (Seinfeld & Pandis, 2016). In the undisturbed stratosphere, condensation is usually the biggest contributor of the vapor-to-particle conversion, but Section 2.7.2 will show that coagulation is the dominant growth process in an aircraft plume (Weisenstein et al., 1997). The primary effect of condensation is the shift of the PSD to larger particle sizes over time where the total condensed volume only depends on the available amount of condensable vapor. A secondary (indirect) effect of condensation is its influence on the total number

concentration of particles through the coagulation kernel, which is dependent on the particle size distribution. Larger particles are less prone to merge upon coagulation than smaller particles (Turco & Yu, 1999). This is discussed in Section 2.6.

This study will use Eq. (2.59), a one-dimensional expression, to calculate particle growth based on the approach by Hamill (1975) and Hamill, Toon, et al. (1977). Alternatively, one could regard condensation as a coagulation process and use a kinetic approach, e.g. Yu and Turco (1998), Benduhn (2008). It is left to the reader to study this method on their own initiative. The original from of the growth equation is Eq. (2.57). Under the assumption that the average volume per molecule and the mole fraction of sulfuric acid in the aerosol droplet remains the same, this can be reshaped into Eq. (2.59) following Fuchs and Sutugin (1971). Note that the subscript s refers to the sulfuric acid fraction.

$$\frac{dr_p}{dt} = \frac{dr_p}{dn_s}\frac{dn_s}{dt} \tag{2.57}$$

$$\frac{dr_p}{dt} = \frac{\bar{v}}{4\pi r_p^2 x_s}\frac{4\pi r_p D_M N_s}{1 + f_{co}\mathrm{Kn}} \tag{2.58}$$

$$\frac{dr_p}{dt} = \frac{\bar{v} D_M \left(p_s - p_s^\dagger\right)/(kT)}{r_p x_s \left(1 + f_{co}\mathrm{Kn}\right)} \quad (\mu\mathrm{m/s}) \tag{2.59}$$

where $\bar{v}$ (nm^3) is the average volume per molecule in the droplet, D_M is the molecular diffusion coefficient, x_s is the mole fraction of H_2SO_4 in the droplet, f_{co} is the correction factor, Kn is the Knudsen number, p_s is the partial vapor pressure of ambient sulfuric acid, and $p_s^\dagger$ the partial vapor pressure of sulfuric acid over the droplet surface. If $\left(p_s - p_s^\dagger\right) > 0$, growth by condensation occurs. If $\left(p_s - p_s^\dagger\right) < 0$, evaporation occurs.

Note that the diffusion coefficient D_M in the gas-like molecular regime is now given by Eq. (2.60), which is exactly the same as Eq. (2.24) for the kinematic viscosity predicted by kinetic theory of gases (Trachenko & Brazhkin, 2020). This is a different process than Brownian diffusion and Eq. (2.23) from earlier does not apply. Similarly, the Knudsen number was introduced by Eq. (2.14) but is calculated slightly different using an "effective" mean free path λ_{eff} for sulfuric acid molecules in air, given by Eq. (2.61). Lastly, the correction factor f_{co} to account for non-continuum effects and imperfect surface accommodation can be approximated with Eq. (2.62) (Fuchs & Sutugin, 1971)(Seinfeld & Pandis, 2016).

$$D_M = \frac{1}{3}\lambda\bar{c} \approx \frac{1}{3}\left(\frac{8kT}{\pi m_s}\right)^{\frac{1}{2}}\lambda_{\text{eff}} \quad (\mu\mathrm{m}^2/\mathrm{s}) \tag{2.60}$$

$$\lambda_{\text{eff}} = \left(\pi N_{\text{air}} d_{\text{av}}^2 \sqrt{\frac{M_{\text{air}}}{M_{\text{air}} + M_s}}\right)^{-1} \quad (\mu\mathrm{m}) \tag{2.61}$$

$$f_{co} = \frac{1.333 + 0.71\mathrm{Kn}^{-1}}{1 + \mathrm{Kn}^{-1}} + \frac{4(1 - b_a)}{3b_a} \tag{2.62}$$

in which N_{air} is the number density of air molecules, $d_{\text{av}} = \frac{1}{2}(d_{\text{air}} + d_s)$ and b_a is the accommodation coefficient.

Now, the expression for particle growth in Eq. (2.59) is problematic in more than one way. To start, it explicitly assumes that the aerosol particle is activated with respect to the sulfuric acid vapor because the acid vapor is supersaturated (SR $>$ 1) and the RH of water vapor is below 100%. As a result, the aerosol is in equilibrium with the water vapor and the growth depends on the impingement rate β of H_2SO_4 molecules. When a sulfuric acid molecule condenses onto the aerosol, its molality changes and it moves away from its equilibrium radius determined by the path of minimum Gibbs free energy (see also Section 2.4.2 on nucleation). Yet, if it absorbs extra H_2O molecules it falls back to its

equilibrium state or local minimum. This is illustrated in Fig. 2.14. It is assumed here that the water vapor concentration is multiple orders larger than the sulfuric acid concentration and that the water vapor equilibrium is obtained instantaneously. At this local minimum in ΔG, any water molecule that impinges onto the aerosol, re-evaporates immediately (Hamill, 1975)(Weisenstein et al., 1997). Note that the aerosol can still grow or shrink when the RH of the surrounding system changes as shown in Fig. 2.15. In case $N_{H_2SO_4} > N_{H_2O}$ or when the RH is above 100%, this theory requires modifications.

Secondly, the expression for dr_p/dn_s in Eq. (2.57) assumes that the average volume per molecule and the mole fraction of sulfuric acid in the aerosol is constant. The evaluation of Eq. (2.59) requires small increments over the radius to limit the error, thus small time steps. A third shortcoming of the growth equation above is the omission of several other influential factors such as the effect of dissolved impurities (core material) on the vapor pressures, the influence of latent heat released by vapor condensation on the temperature of the droplet (thermal diffusion), and the attachment of H_2O clusters to H_2SO_4 molecules through the diffusion of water (Turco et al., 1979).

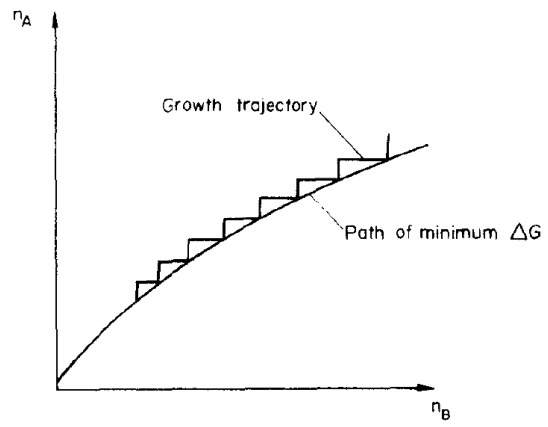

Figure 2.14: Growth trajectory for a solution droplet in the n_A, n_B plane (Hamill, 1975)

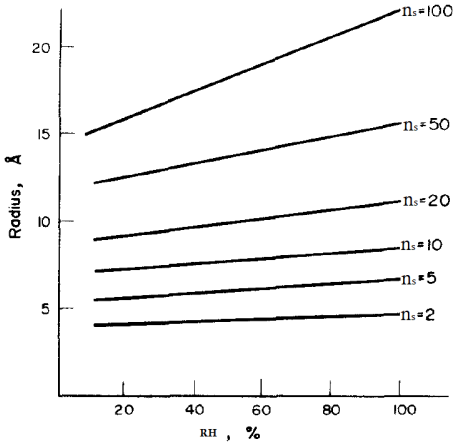

Figure 2.15: Equilibrium radius of embryo as a function of relative humidity for droplets containing 2 to 100 molecules of H_2SO_4 (Hamill, 1975)

Ultrafine particles grow less fast than bigger particles because of the Kelvin effect (see Section 2.1.2). At larger sizes, the surface tension is less influential and the amount of water molecules that can be absorbed for every sulfuric acid molecule increases (Hamill, 1975). The same effect can also create a peculiar situation where smaller particles evaporate while larger particles continue to grow (Hamill & Yue, 1979). However, for radii larger than 0.1 µm the growth rate slows down as more molecules are required to cause a significant change in size. Consequently, PSDs tend to 'squeeze' over time, creating a smaller size range (Seinfeld & Pandis, 2016). Logically, the time of growth is inversely proportional to the number concentration of H_2SO_4. Furthermore, the accommodation coefficient b_a for the condensation of H2SO4 molecules on particle surfaces remains a point of uncertainty. It can range anywhere between 0.1 - 1. Most authors assume that the coefficient equals unity but Yu and Turco (1998) warn that it might be significantly lower for particles between 0.05 - 0.5 µm. They predict values closer to 0.1 for submicroscopic particles.

Remark that the condensation rate, and correspondingly aerosol growth, is heavily influenced by the nucleation process as they both compete for the same vapor source. Therefore, depletion of acid vapor over time should be accounted for.

2.6. Coagulation

The third and final stage of aerosol growth is called coagulation and involves the collision and coalescence of stable aerosol particles. It continues long after the vapor source has been depleted until it is

eventually quenched by dilution of the plume. The interaction between the dilution rate of the plume (increase in volume) and coagulation is discussed in Section 2.7.2. The relative motion between two particles that forgoes collision can be induced through Brownian motion (thermal agitation), gravitational sedimentation or turbulent motion and it is further influenced by hydrodynamics (viscous forces), the presence of electric charge, the size of a particle and its fractal geometry. All this phenomena can be accounted for by specifying specific coagulation rate coefficients, or kernels, which are commonly superimposed although this theoretically leads to erroneous results due to interdependencies. For a complete summary on coagulation mechanics, the reader is referred to the works from Fuchs (1964), Jacobson (2005) and Seinfeld and Pandis (2016). The primary effect of coagulation is that it limits the particle number density n_N whereas the amount of condensable vapor predominantly governs the obtained particle size or total aerosol mass in the system (Turco and Yu, 1997, Rasch et al., 2008). Yet, as will become clear in Section 2.7.2, the comparatively short time frames of the nucleation and condensation stages cannot compete with the long-lasting coagulation stage which makes coagulation the dominant particle growth process under elevated concentrations in an engine plume (Turco and Yu, 1999, Pierce et al., 2010). The timewise variation of the particle size distribution of a coagulating aerosol can be described by Eq. (2.63), which is a version of the aerosol continuity equation (Yue & Deepak, 1979).

$$\begin{aligned}\frac{\partial n(r,t)}{\partial t} = &- n(r,t)\int_0^\infty K\left(r,r'\right) n\left(r',t\right) dr' \\ &+ \frac{1}{2}\int_0^\infty \int_0^\infty K\left(r_i,r_j\right) n\left(r_i,t\right) n\left(r_j,t\right) dr_i dr_j\end{aligned} \tag{2.63}$$

where $n(r,t)\ dr$ is the continuous number distribution of the particles that participate in coagulation and K (cm^3 particle^{-1} s^{-1}) is the coagulation kernel. The first term on the right describes the reduction in number of particles of radius r as they collide with other particles, while the second term on the right accounts for the production of newly sized particles with radius r through coalescence of two particles with radius r_i and r_j. The method is volume-conserving such that the radii are related through Eq. (2.64).

$$r_i^3 + r_j^3 = r^3 \tag{2.64}$$

It is possible to include more terms in the continuity equation that account for condensational growth and the scavenging of newly formed aerosol by ambient aerosol in the atmosphere. The former has been treated separately in Section 2.5 and the latter is neglected for now. For those who wish to know more, Turco and Yu (1997, 1998, 1999) have derived some powerful analytical solutions to the aerosol continuity equation that include the effects of condensation, and aerosol scavenging by soot under certain limiting conditions. Now, because the evaluation of Eq. (2.63) over time in continuous radius space is an impossible task due to its large range (easily 4 orders in magnitude), the continuous coagulation equation can be expressed in logarithmic space using particle size bins. Please see Section 2.1 where the effects of this mathematical transformation are discussed. Following the approach from Yue and Deepak (1979), one can obtain the discrete coagulation equation for a polydisperse population which is given here by Eq. (2.65) from Weisenstein et al. (1997).

$$\begin{aligned}\frac{\partial N_i}{\partial t} = &-N_i \sum_{j\neq i} K_{ij} N_j - \frac{1}{2} K_{ii} N_i^2 \\ &+ \frac{1}{2} K_{i-1,i-1} N_{i-1}^2 + N_i \sum_{j<i} \left(1 - \frac{V_j}{V_i}\right) K_{ij} N_j \\ &+ \sum_{j<i-1} \frac{V_j}{V_{i-1}} K_{i-1,j} N_{i-1} N_j\end{aligned} \tag{2.65}$$

where the subscripts now denote particle bins with size indices i and j. Note that the particle number

concentration of a bin i can only increase through collisions between particles of bin $i-1$ and bin $i-1$, bin i and bins smaller than bin i, or bin $i-1$ and bins smaller than $i-1$.

The rate at which coagulation happens is governed by the coagulation kernel K_{ij}, or the collision frequency per unit volume. This kernel is often a superposition of individual kernels that simulate a multitude of microphysical processes. The size and shape of the particles that partake in coagulation can have an impact on the coagulation/collection/coalescence efficiency E_{coag} (among other factors), especially in the kinetic regime where not all collisions result in coalescence. This efficiency needs to be multiplied with the kernel. Note that this study assumes all particles are spherical and only considers two-body collisions, but in theory more bodies could be involved in a single collision.

An intuitive way to quantify the impact of several microphysical effects is to compare their coagulation kernels. Figure 2.16(a) indicates that Brownian motion is the dominant coagulation mechanism for particles below 1 µm or the kinetic regime, which is supported by Yu and Turco (1998) and Golja et al. (2021). Diffusion enhancement, the second biggest contributor to the kernel, is an indirect effect of Brownian motion and the eddies that particles create in their wake. Remark that for sub-micrometer particles the contributions by other processes pale in comparison with the Brownian coagulation kernel as they are 4 to 8 orders in magnitude lower. However, the author expects that the presented kernels related to turbulence use standard atmospheric turbulence dissipation rates ($\epsilon_k \sim 10^1 - 10^3$ cm^2 s^{-3}) which are non-representative of the conditions found in a jet engine plume ($\epsilon_k \sim 10^4 - 10^8$ cm^2 s^{-3}). The difference could amount up to 4 - 6 orders of magnitude, increasing the contribution of turbulent shear and acceleration, but still not surmounting the effect of Brownian motion. In addition, the presence of electrical charge in the form of ions can significantly enhance the collision rate and sticking probability of two colliding particles and is not shown here. The nature of the particle (liquid, solid or mixed) can also play a role, but this is outside the scope of this research.

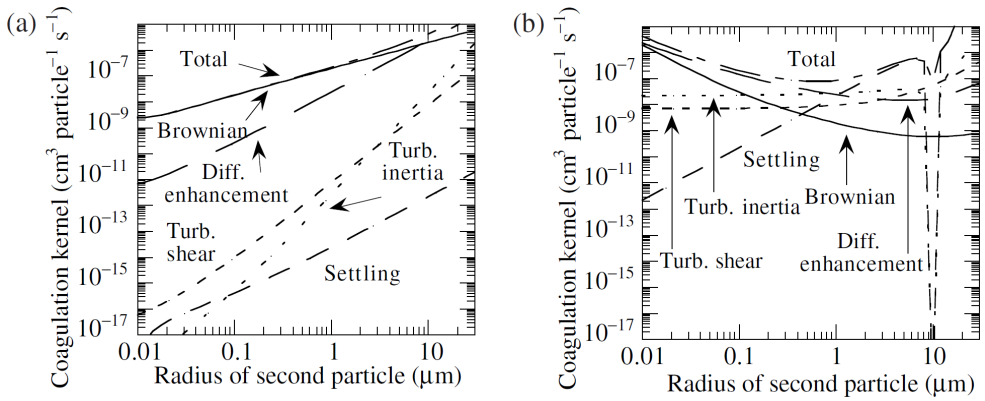

Figure 2.16: (a) Coagulation kernels for five processes when a particle 0.01 µm in radius coagulates with particles of different size at 298 K. (b) Coagulation kernels for five processes when a particle 10 µm in radius coagulates with particles of different size at 298 K. The dip at 10 µm results because the difference in fall speed is zero at that point. The real width of the dip is narrower, but the resolution of the size bins used for the graph was coarse (Jacobson, 2005).

2.6.1. Brownian Coagulation

The introduction to Section 2.6 introduced the concept of coagulation kernels and showed that the collision rate of aerosol particles as the result of Brownian motion are the dominant contribution to particle aggregation. Brownian coagulation is fairly well understood and the uncertainty is much smaller compared to nucleation and condensation rates (Pierce et al., 2010, Seinfeld and Pandis, 2016). This study follows the formulation of the coagulation kernel from Eq. (2.66) as derived by Fuchs (1964), which is applicable in all three regimes of fluid-particle interactions: continuum, transition and free

molecular flow.

$$K_{ij} = 4\pi \left(r_i + r_j\right)\left(D_{B_i} + D_{B_j}\right) \times \left[\frac{r_i + r_j}{r_i + r_j + \sqrt{\delta_i^2 + \delta_j^2}} + \frac{4\left(D_{B_i} + D_{B_j}\right)}{\sqrt{\bar{c}_i^2 + \bar{c}_j^2}\left(r_i + r_j\right)}\left(\frac{1}{b_s}\right)\right]^{-1} \quad (\text{cm}^3\,\text{particle}^{-1}\,\text{s}^{-1}) \tag{2.66}$$

where D_{B_i} ($\text{cm}^2\,\text{s}^{-1}$) is the Brownian diffusion coefficient given by Eq. (2.23), $\bar{c}_i$ is the average kinetic velocity of a particle from Eq. (2.25) and b_s is the sticking coefficient. For more information on the origin of Brownian motion, please consult Section 2.2.2. Note that in the calculation of the diffusion coefficient and the Knudsen as part of the Cunningham correction factor, you need to use the 'effective' mean free path defined as Eq. (2.67). The correction factor δ_i is given by Eq. (2.68) and corresponds to the mean distance from the center of a sphere reached by particles leaving the sphere's surface and traveling a distance of particle mean free path λ_i (Jacobson, 2005).

$$\lambda_{\text{eff}} = \left(\pi N_{\text{air}} d_{\text{av}}^2 \sqrt{\frac{M_{\text{air}}}{M_{\text{air}} + M_{\text{aerosol}}}}\right)^{-1} \quad (\mu\text{m}) \tag{2.67}$$

in which N_{air} is the number density of air molecules and $d_{\text{av}} = \frac{1}{2}(d_{\text{air}} + d_{\text{aerosol}})$.

$$\delta_i = \frac{1}{6 r_i \lambda_i}\left[\left(2r_i + \lambda_i\right)^3 - \left(4r_i^2 + \lambda_i^2\right)^{3/2}\right] - 2r_i \tag{2.68}$$

where

$$\lambda_i = \left(8 D_{B_i}\right) / \left(\pi \bar{c}_i\right) \tag{2.69}$$

The Brownian coagulation kernel is visualized in Fig. 2.17 for particles of different sizes as a function of their diameter d_p.

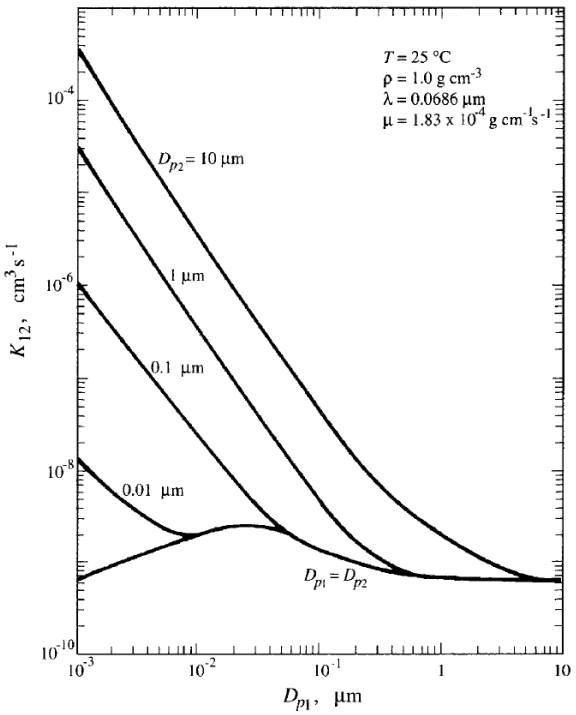

Figure 2.17: Brownian coagulation coefficient K_{12} for coagulation in air at 25 °C of particles of diameters d_{p1} and d_{p2}. To use this figure, find the smaller of the two particles as the abscissa and then locate the line corresponding to the larger particle (Seinfeld & Pandis, 2016).

It is clear that the collision kernel increases with the ratio of particle diameters which is indicative of the increasing synergy between the two particles. For equally-sized particles, a maximum is reached around 0.02 µm. Large particles coagulate relatively slowly compared to smaller particles, but they on the other hand tend to miss each other more often because of their smaller cross-sectional area. A large and small particle combine the advantages of a large target area and a large relative speed difference which results in a larger collision rate. One can show that in the continuum limit Kn $\rightarrow 0$ the coagulation kernel is independent of the particle size, while the kernel in the kinetic regime Kn $\rightarrow \infty$ is proportional to the square root of the particle size (Turco and Yu, 1998, Seinfeld and Pandis, 2016).

As noted in the introduction to this section, not all collisions results in coalescence and this is accounted for via a general coagulation efficiency E_{coag} or in this case a sticking coefficient b_s. While many models simply assume this coefficient is equal to unity, this is probably an overestimate of the coalescence of ultrafine particles (< 0.1 µm) according to Yu and Turco (1998). By looking at Eq. (2.66), one can see that K_{ij} is only sensitive to variations in b_s when $r_i + r_j \ll \lambda_i$. Thus, when bigger particles collide, they can be seen as permanently aggregated. Yu and Turco (1998) propose a semi-empirical relation to estimate the dependence of b_s on the particle sizes which is shown here under Eq. (2.70).

$$b_s(r_i, r_j) = \text{Min}\left[b_0^{\log\left(r_{\text{ref}}/\sqrt{r_i r_j}\right)/\log(r_{\text{ref}}/r_{\text{molecule}})}, 1\right] \tag{2.70}$$

where $b_0 = 0.01$, $r_{\text{ref}} = 10$ nm and $r_{\text{molecule}} = 0.277$ nm.

2.6.2. Ion-induced Coagulation

The presence of an electrostatic field normally does not have a big impact on aerosol coagulation kernels under standard atmospheric conditions because there needs to be a significant charge difference between the two colliding bodies. Clouds can contain charged ice crystals which leads to enhanced coagulation with aerosol particles, but self-coagulation of aerosol is usually not significantly affected (Jacobson, 2005). Yet, Section 2.3.2 explained that copious amounts of molecular-sized ions can be found in the wake of a jet engine as the result of chemi-ionization processes during combustion and Section 2.3.1 revealed that a significant amount of soot particles are present in wake as well which may lead to persistent cloud/contrail formation under the right conditions. The discussion thus far focused on the role of chemiions during particle formation/nucleation and their role in the activation of soot particles. For more information, consult Section 2.4. Once charged particles clusters have formed, the presence of ions at their core core leads to enhanced attraction/repulsion during coagulation, increasing the overall collision rate and the probability that particles coalesce upon impact. Incorporating this effect in a theoretically consistent way at low computational expense is still a work in progress and requires further investigation (Benduhn, 2008).

A relatively inexpensive approach is the one from Fuchs (1964) which uses a semi-empirical formulation for the potential energy Ψ that exists between two charged particles corresponding to the central electrostatic force F. This base form does not take into account the asymmetric charge distribution of molecular scale clusters, which becomes important when a charged particle interacts with a polarizable molecule. To generalize the base equation, Yu and Turco (1998) include a permanent dipole moment (PDM), which is an uneven distribution of charge, where the final formulation is given as Eq. (2.71).

$$\begin{aligned}\Psi\left(\frac{r_i + r_j}{x}\right) = \frac{1}{r_t + r_j}\Bigg[q_i q_j\left(x + \frac{15}{448}x^7 + \ldots\right) \\ - \left(q_i^2 + q_j^2\right)\left(\frac{1}{16}x^4 + \frac{1}{64}x^6 + \ldots\right)\Bigg] - \frac{q_t^2 + q_j^2}{\left(r_i + r_j\right)^2}\left(\frac{L_0}{q_0}x^2\right)\end{aligned} \tag{2.71}$$

where q_i and q_j (C) are the charges located at the center of the particle clusters, q_0 (C) is the elementary charge and L_0 (C m) is the PDM of the condensing molecular species (in this case H_2SO_4). The first

term on the right represents the Coulomb force, the second are the inductive forces and the third is the PDM correction for molecular sizes. The corresponding electrostatic enhancement factor f_{ee} is calculated via Eq. (2.72).

$$f_{ee} \equiv \left(\int_0^1 \exp \left[\frac{\Psi \left(\frac{r_i + r_j}{x} \right)}{kT} \right] dx \right)^{-1} \tag{2.72}$$

By solving Eq. (2.72) numerically for equally-sized particles with charge $q_i = q_0$ and possible combinations of $q_j = sq_i$ ($s = -1, 0, 1$), you obtain the curves depicted in Fig. 2.18.

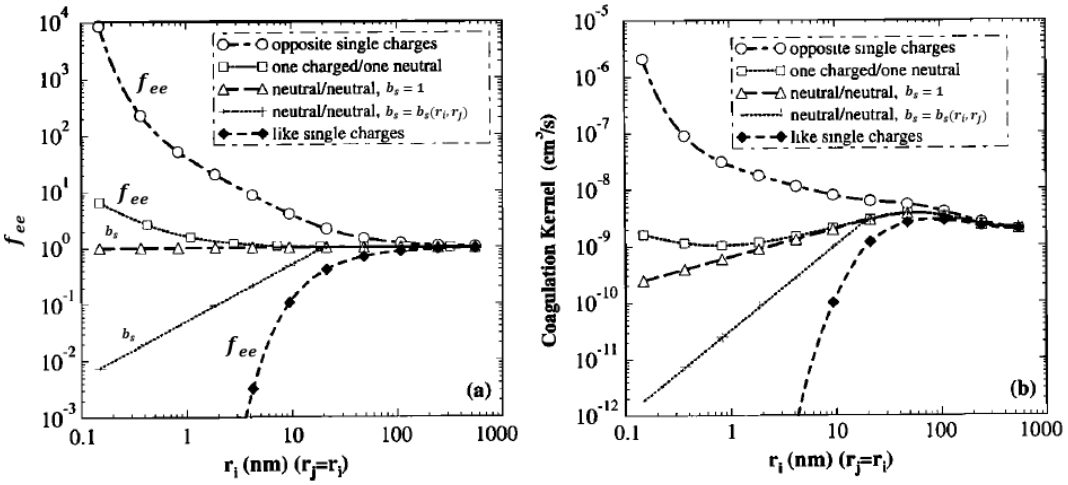

Figure 2.18: Dependence on particle size of (a) the coagulation enhancement factor and sticking coefficient and (b) the coagulation kernel, with and without the effects of electrical charge. Adapted from Yu and Turco (1998).

The impact of electrostatic enhancement on the collision rate of small particles is striking as the enhancement factor for oppositely charged particles can be larger than a factor 100 for the smallest aerosol droplets with radii of approximately 0.3 nm. Similarly, charge-like particles result in repulsion and notice that the effect is stronger than attraction because it is more difficult to achieve collision than merely repelling any particles in the vicinity. Charge-neutral interactions also enhance coagulation, although be it less profound with a factor closer to 1 - 2. This is because charged particles induce temporary image forces (polarization) in neutral particles (Starik, 2007). Once particles grow beyond radii of 10 nm, the charge effects become negligible. The electrostatic force field induced by an ion decays relative rapidly with increasing radius. As a result, larger particles can't use it to their advantages to stabilize growth and increase the sticking probability. This is based on the assumption that a single ion charge is located at the center of the aerosol and this approach should not be used for multi-charge distributions. Typically, the initial size of soot and mixed solid-liquid aerosols is about 20 nm and because they are additionally sparsely distributed, they do not experience strong electrostatic effects during growth (Yu & Turco, 1998). The observant reader will also notice two curves for the neutral case (without electrostatic enhancement) where two different sticking coefficients are used. One assumes all collisions result in coalescence (b_s = 1), the other applies the scaled sticking coefficient $b_s(r_i, r_j)$ from Eq. (2.70) which results in a retarded collection rate for smaller particles. When charge effects are present, b_s is equal to unity because the electrostatic potential is much larger than the kinetic energy of colliding mono- and dimers. Understanding the role of chemiions in an aircraft plume remains a complex issue with various uncertainties about its mechanics. According to Yu and Turco (1998), they have a profound impact on the PSD from the start as large concentrations of ultrafine aerosol clusters form upon the ions themselves in the milliseconds after ejection. Subsequently, these ionized particles are much more efficient at scavenging sulfuric acid than neutral clusters and coagulate at a faster rate among themselves. This inhibits the growth of the neutral part of the nucleation mode particles and results in accelerated growth of ionized segment. The result is a bimodal-shaped PSD (see Fig. 2.8)

as opposed to the recurring log-normal distribution for atmospheric aerosol. While laboratory observations (e.g. Arnold (2006)) seem to confirm this trend, in-situ measurements of aircraft plumes failed to provide clear evidence in the past due to the limited sampling range of its acquisition probes.

2.7. The Aircraft Plume

Up until now the discussion mostly ignored the influence of the plume domain on aerosol mechanics, but it is an important part of the aerosol growth process because it leads to non-linearity in the chemical rates (e.g. nucleation). Non-linear effects or plume-scale effects are conditions where the chemistry behaves differently than the surrounding atmosphere (Fritz, 2018). This is the result of elevated saturation levels of vapor sources such as H_2O and H_2SO_4, the presence of chemiions in high concentrations, and the evolution of jet wake turbulence among others. A good example is the discussion in Section 2.4.1 on the failing linear dependence of the ion-induced nucleation rate on the ion concentration under elevated conditions (Yu, 2002). Injecting high H_2SO_4 concentrations as part of SAI may further aggravate these effects or conversely reduce them. Therefore, it is essential to have a good understanding of plume dynamics.

As part of the Climatic Impact Assessment Program (CIAP), plume dynamics were reviewed extensively in the early 1970s (Yu & Turco, 1998) and not much progress has been made in the field of plume morphology hereafter apart from some more advanced large-eddy simulations (LES) (e.g. Unterstrasser et al., 2014, Paoli and Shariff, 2016) to investigate the mixing mechanics in the exhaust plume. This is the topic of Section 2.7.1. Then, around the turn of the century, increasing concern about the possible impact of aircraft emissions on the climate lead to a new series of in-situ measurements involving sub- and supersonic aircraft flying in the tropo- and stratosphere. Famous examples are the AEAP project by NASA in North-America (e.g. Friedl et al., 1997, Fahey et al., 1995) and the POLINAT, SULFUR experiments by DLR in Western-Europe (Schumann et al., 2002). In the follow-up of these experiments, multiple PDMs with varying complexity were created to simulate the dispersion of engine emissions and investigate aerosol growth to gain insight in the dominant formation mechanics. Therefore, Section 2.7.2 focuses on the contribution of individual microphysical processes to aerosol growth in an expanding plume that undergoes mixing.

2.7.1. Plume Morphology

In order to understand the following discussion, it is helpful to explain some terminology which is commonly used to describe an aircraft plume. There is no exact definition of an aircraft plume and this study chooses to define it from an emissions standpoint, it being the temporary volume created by the passing of an aircraft that contains elevated concentrations of pollutants above ambient conditions. The morphology of a plume refers to its structure or shape which is dependent on the turbulence intensity and stratification of the atmosphere as well as the influence of the aircraft through wake turbulence of which the jetwash and wingtip vortices are main contributions. A plume degrades over time, it dilutes through the act of dispersion where the particles of a substance scatter in the air, reducing pollutant concentrations and weakening plume-scale effects. In literature, the terms dilution and dispersion after often used alternately to describe the same process. However, this study would like to stress that dispersion is one cause of dilution (next to advection for example). Dispersion is synonymous to diffusion, a process of spreading, but diffusion comes in many forms: molecular or spontaneous diffusion, Brownian or thermal diffusion and turbulent diffusion. The reader is referred to Section 2.2.3 to learn more about their differences.

The evolution of the aircraft plume can be categorized in four dynamical regimes based on time and mixing intensity (ratio of entrainment). They are illustrated in Fig. 2.19. The jet regime, a momentum-driven axisymmetric flow, is the earliest stage of the plume and initially undergoes free expansion. It

experiences strong diffusion through turbulent entrainment of the ambient air as a result of the jetwash, which is the turbulence associated with the rapid expulsion of hot gases from the engine. At the same time, due to the spanwise variation in circulation along the wing wing, a trailing vortex sheet is created which rolls up in a pair of counter-rotating vortices that are shed at the wingtips and interact with the jet wake. After a few seconds ($t \sim 10$ s), the evolving vortices eventually trap the engine exhaust in their core forming the primary wake. This marks the start of the vortex regime, a period of slow mixing and low dilution. The vortex pair sinks in the vertical direction as the result of their mutual downward velocity induction and warms up. At that stage, a secondary wake is created as the result of baroclinic instability (density difference). A small part of the exhaust mass, temperature, and momentum is detrained from the primary wake and rises upward, connecting the primary wake to the cruise altitude. As a result, it experiences a different dynamic and microphysical evolution. This stage lasts up to 3 min ($t \sim 100$ - 200 s) depending on the vortex strength until the primary vortex pair and secondary vorticity start to disintegrate. This is the start of the vortex-dissipation regime where the organized vortical motion breaks up in turbulence and its energy subsequently dissipates into the background. This stage ends after about 3 hours ($t \sim 1000$ s) once the aircraft-induced diffusion has become negligible. Atmospheric turbulence and sedimentation will continue to disperse the plume in the diffusion regime until full mixing is obtained, usually within a few hours. Aircraft plumes can last up to 12 hours and reach up to 100-200 km horizontally while only growing 200-400 m vertically. This is especially true for the lower stratosphere which has stable stratification and does not experience a lot of convection. (Yu and Turco, 1998, Gerz et al., 1998, Tait et al., 2022)

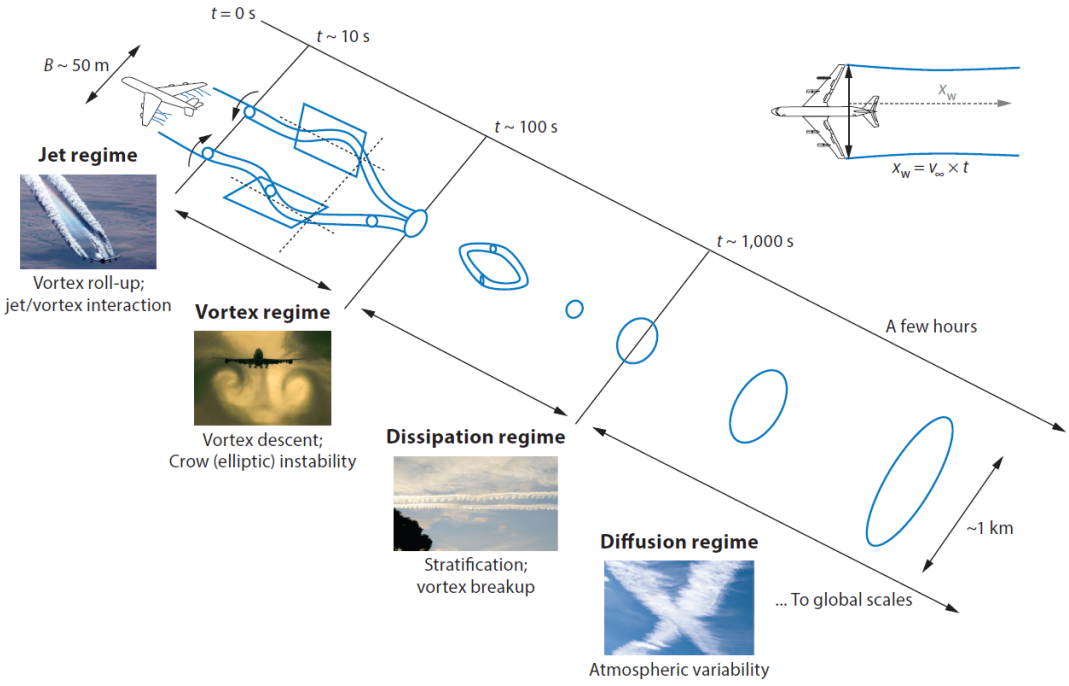

Figure 2.19: Classification of aircraft wake evolution into four regimes (Paoli & Shariff, 2016).

Plume dynamics and their influence on emissions have been studied in the past both empirically (e.g. Schumann et al., 1998) and with the use of high-resolution large-eddy simulations (e.g. Dürbeck and Gerz, 1995, Paoli et al., 2008) to determine the dilution ratios and diffusivity coefficients associated with each dynamical regime. Well-constructed LES can provide highly accurate flow fields mapping out the inhomogeneity of the flow and revealing the strong fluctuations that exist among the pressure, temperature and humidity levels. However, the high computational cost of LES still limits its application to specific case studies rather than any fully-fledged sensitivity study of particle formation in the wake. Only a handful of studies have tried to couple simplified microphysical models with LES. Paoli et al.

(2008) concluded that inhomogeneity in the plume can lead to strong alterations of the PSD compared to a plume where thermodynamic quantities are averaged across the plume. This is the result of turbulent entrainment of cold ambient air and the transport of fluid particles from the hot center of the plume to the colder outer edges of the plume. In the past, researchers have simplified plume morphology considerably by creating quasi-one-dimensional representations of the wake with a single circular streamtube behind the aircraft and a constant expansion rate as is shown in Fig. 2.20. The low-cost Gaussian plume model (GPM) is very popular among literature to simulate plume cross-sectional areas and concentrations and makes use of empirical or LES-calibrated diffusion coefficients to account for each regime. Yet, it is not applicable to simulate the dispersion of chemically active species which can result in non-uniform concentration distributions as mentioned previously in Section 1.1 (Kraabøl et al., 2000). To alleviate this problem and bridge the gap between simple GPMs and costly LES, Fritz et al. (2020) created APCEMM, a multi-layered microphysical plume model, which starting from the dissipation regime, accounts for radial variations in emission concentration levels and asymmetry of the plume. Still, they choose to model the jet and vortex regime as an expanding box with cross-sectional homogeneity in accordance with the approach of Kärcher (1995), because the entrainment rates are low and mixing is relatively consistent across the plume. Figure 2.21 shows a depiction of a multi-layered plume. As mentioned in Section 1.2, one of the key objectives of this study is to investigate whether spatial fluctuations in temperature and concentrations heavily affect the non-linear microphysical processes early on in the plume. Therefore this study does investigate the jet regime and tries to simulate the flow field more accurately with a decoupled RANS simulation, which is explained in more detail in Section 4.1.

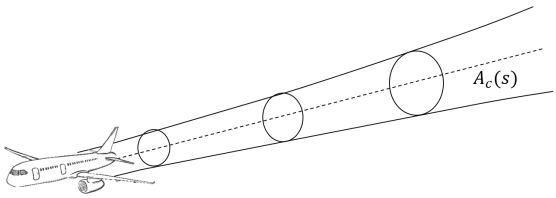

Figure 2.20: Quasi-one-dimensional single plume representation of aircraft wakes.

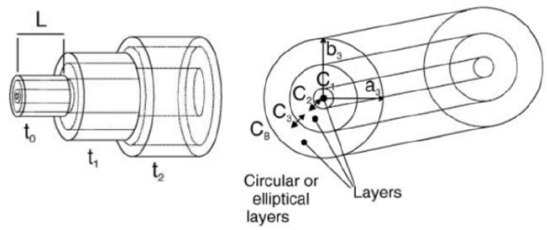

Figure 2.21: The multi-layered plume (Kraabøl et al., 2000).

2.7.2. Plume-scale Aerosol Microphysics

This literature review has now covered binary H_2SO_4-H_2O aerosol thermodynamics, fluid-particle interactions, processes related to aerosol formation and growth, engine emissions, and aircraft plume dynamics. To end the discussion, it is only natural that the impact of plume-scale effects on aerosol microphysics and the interdependence of individual microphysical processes is elucidated. Past research has shown that the steady-state PSD of secondary aerosol, formed in the aircraft engine wake, is highly insensitive to variations in nucleation and condensation rates. Nucleation and condensation act on remarkably short timescales compared to coagulation, as illustrated in Fig. 2.22. Within seconds after emissions, almost no H_2SO_4 vapor remains in the system and further growth of the aerosol purely happens through self-coagulation. The dominant role of coagulation in the aerosol growth process cannot be understated as it continuous to reduce the aerosol particle concentration long after the formation of new particles has seized, shifting the PSD to larger particle sizes. Any differences in the freshly nucleated aerosol population are quickly damped by coagulation as it is proportional to the square of the particle concentration (Benduhn et al., 2016; Pierce et al., 2010; Turco & Yu, 1999). The

only countermeasure to coagulation is particle dispersion or diffusion and in the jet regime this happens predominantly through turbulent entrainment of ambient air which increases the plume volume and reduces the concentration of aerosols as well as condensing vapor. This competitive interplay between coagulation and dilution quickly became the focus of research at the end of the 20th century as various PDM were built to analyze the dispersion of aircraft emissions. It was believed that the PSD might be invariant to the early growth stage and could purely be modeled through asymptotic solutions to the coagulation equation.

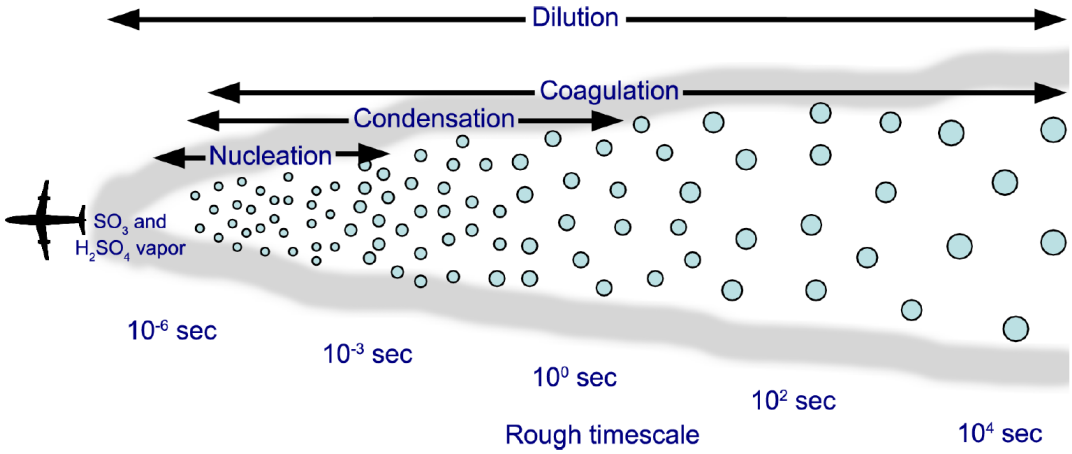

Figure 2.22: Schematic showing the rough timescales where various processes are important within the aircraft plume following H2SO4 emission. The timescales for the processes vary from the values shown here depending on the nucleation, condensation and dilution assumptions tested in the plume model (Pierce et al., 2010).

It was Friedlander and Wang (1966) who showed that a lognormal PSD is a self-preserving spectrum under Brownian coagulation. This also holds for processes that involve nucleation and condensation as long as Brownian coagulation is dominant (Picht et al., 1970). Lai et al. (1972) expanded on this theory by proving that it holds in both the continuum and free-molecular regime. Based on this approach, Turco and Yu (1997, 1998, 1999) showed analytically that, beyond a initial concentration threshold, the steady-state aerosol particle population inside an expanding jet plume is independent of its formation rate and instead governed by the dispersion/mixing rate of the plume and self-coagulation of the aerosol. They even formulated an expression for the invariant aerosol population analogous to the self-preserving log-normal PSD for Brownian coagulation derived by Friedlander and Wang (1966). Their approach fully determines the time evolution of the aerosol and provides an estimate for the total number concentration of the aerosol after reaching atmospheric background conditions. However, the theory assumes some stringent conditions and this makes it highly unlikely that this method is an accurate representation of reality. The problem with this theory is threefold, it assumes a uniform aerosol population (in size and concentration) across the plume, uniform mixing and a size-averaged coagulation kernel. While Wang and Friedlander (1967) already showed that under a size-dependent coagulation kernel (Knudsen number dependence) the self-preserving property of PSD does not hold, the previously-mentioned authors also recognize that in the presence of turbulence, spatial and temporal inhomogeneity in concentration levels might lead to variations in the PSD. Likewise, the presence of soot and ions can result in unforeseen alterations to the PSD as the initial population consists of different aerosol types and sizes (F. Yu, personal communication, November 10, 2022).

Although self-limited growth seems unlikely in the wake of an engine aircraft, it did lead to insights in the competitive effect of dilution/mixing and coagulation. The influence of self-coagulation and dilution can be evaluated through their characteristic time constants. Based on empirical data, the time evolution of the plume volume (or its cross-sectional area at that time instant) can be estimated with

Eq. (2.73) (Rasch et al., 2008).

$$V(t)/V_0 = (1 + t/\tau_{\text{mix}}) \approx 100t^{0.8} \quad \text{where} \quad t \geq 0.0032\text{s} \tag{2.73}$$

where V_0 is the initial plume volume and τ_{mix} (s) is the characteristic mixing time scale. In the case of a jet engine, τ_{mix} is anywhere between 0.1 and 10 s based on Schumann et al. (1998). The characteristic time constant for coagulation τ_{co} is given by Eq. (2.74).

$$\tau_{\text{co}} = \frac{2}{N_{\text{p0}} K_{\text{c0}}} \tag{2.74}$$

where N_{p0} is the initial aerosol concentrations and K_{c0} is the initial coagulation kernel.

Rasch et al. (2008) visualize the effect of the rate of mixing on self-coagulation in Fig. 2.23 by defining a scaled time parameter, $f_t = t/\tau_{\text{co}}$, and scaled mixing parameter $f_m = \tau_{\text{mix}}/\tau_{\text{co}}$. When mixing is comparatively slow compared to coagulation (high values of f_m), the aerosol concentrations in the volume are preserved longer which results in more collisions, thus bigger growth of the average particle radius and a decline in aerosol numbers. Conversely, for fast mixing rates, dilution of the plume quenches coagulation and you end up with more particles of smaller size which is desirable for SAI applications. Prompt self-coagulation under slow dilution/mixing rates is difficult to compensate for. Only reducing the initial particle concentration would help, but this would require lower injection rates and lead to additional flight activity which then again affects payload and/or infrastructure (Rasch et al., 2008; Turco & Yu, 1999). Luckily, prompt coagulation should normally not be an issue in jet engine wakes as the mixing rate is sufficiently high. Another factor that might lead to a reduction in aerosol particle numbers is the entrainment of larger background particles which scavenge freshly nucleated particles before they grow to size. Turco and Yu (1999) estimate their influence to be low, but Benduhn et al. (2016) advise to keep the early plume growth period as short as possible such that particles are large enough by the time background interaction becomes dominant.

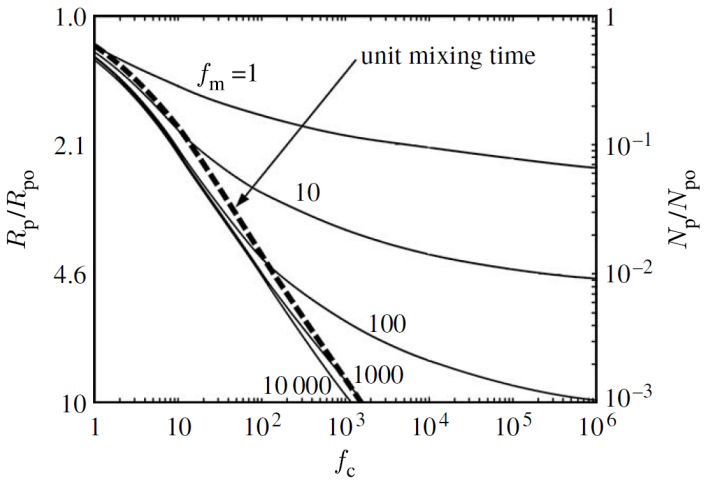

Figure 2.23: Evolution of the total concentration of particles N_p and the mass-mean particle radius R_p in an expanding injection plume. Both variables are scaled against their initial values in the starting plume. The time axis ($f_t = t/\tau_{\text{co}}$) is scaled in units of the coagulation time constant tco. Each solid line, corresponding to a fixed value of f_m, gives the changes in N_p and R_p for a specific mixing time scale tmix measured relative to the coagulation time scale τ_{co} or $f_m = \tau_{\text{mix}}/\tau_{\text{co}}$. The heavy dashed line shows the changes at the unit mixing time, for which $f_t = f_m$ when the plume cross-sectional area has roughly doubled; the longer the mixing time scale, the greater the reduction in particle abundance and particle radius (Rasch et al., 2008).

3

Methodology

This chapter provides a comprehensive and transparent account of the research process. It starts by recapitulating Chapter 2, summarizing the known microphysical pathways that lead to the formation and growth of sulfate aerosol in a jet engine wake in Section 3.1. This preludes the explanation of the research approach in Section 3.2, including the research questions, and what cases were considered in the verification process and the sensitivity study. Lastly, Section 3.3 elaborates on the modeling framework and the new features that were implemented, i.e. the implementation of the local distribution of temperature and water vapor in the domain, and the entirely new nucleation module that includes ion-induced nucleation.

3.1. Pathways to Sulfate Aerosol Formation and Growth

The possible pathways to sulfate aerosol formation and growth are numerous because there are other compounds present in a jet engine wake besides gaseous H_2SO_4 and H_2O. The schematic in Fig. 3.1 depicts most of the known pathways that were identified as part of the literature review on aerosol mechanics in Chapter 2, focusing on the predominant channels. This study will only consider secondary aerosol, i.e. particles that form from condensable vapor in subsequent stages of the plume.

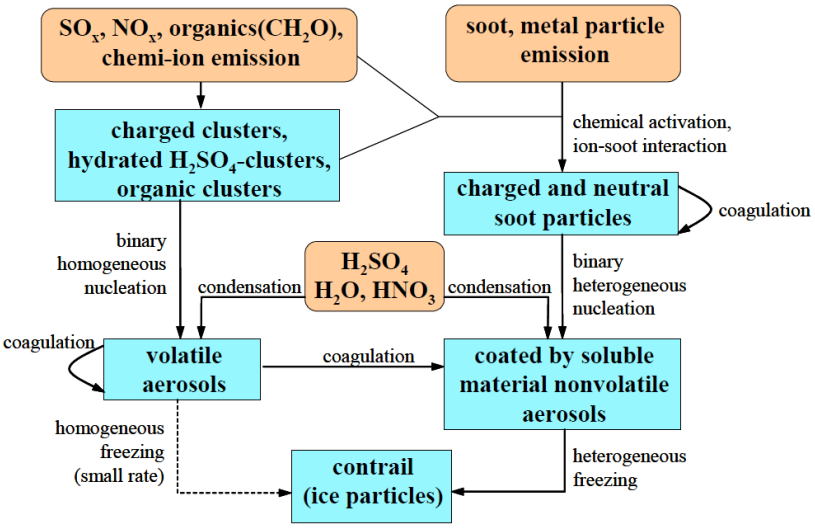

Figure 3.1: Responsible processes for aerosol particle formation in a jet engine wake (Starik, 2007).

The first stage of particle formation is usually nucleation which serves two functions, it creates new liquid particles from the vapor phase through homogeneous nucleation and it activates pre-existing particles, like soot, through heterogeneous nucleation such that they become condensation nuclei. If the process involves multiple species, it is called heteromolecular, or in this case, a 'binary' process because pure sulfate aerosol only contains H_2SO_4 and H_2O (Yu & Turco, 1998). For the particular case of SAI and the buildup of large vapor concentrations, the nucleation barrier (a probability function that governs the formation of clusters against the trend of cluster decay) can vanish and particle formation becomes kinetically limited. Then we speak of barrierless kinetic particle formation as opposed to nucleation (Merikanto et al., 2016). Nucleation can be aided through external factors such as a third compound which acts as a catalyst by participating in the formation process (e.g. HNO_3) or through electrostatic attraction in the presence of charged particles (ions).

Once a stable aerosol embryo has been formed, the process of particle growth continues either through condensation (2nd stage) or coagulation (3rd stage). Although both growth processes can exist simultaneously, condensation is usually dominant for the early lifetime of a particle. Condensation, in the way that it is treated here, is defined as the phase transformation of a gas-phase substance to its liquid form when in contact with an 'activated' pre-existing particle, otherwise called 'condensation nuclei' (CN). The reverse process is called evaporation. In the undisturbed stratosphere, condensation is usually the biggest contributor of the vapor-to-particle conversion, but coagulation is undoubtedly the dominant growth process in an aircraft plume (Pierce et al., 2010; Weisenstein et al., 1997). Coagulation is a mechanical process where two particles collide and fuse because of their relative motion, induced by either Brownian motion, gravitational settling, ions, or turbulence (Yu & Turco, 1998). In the end, the aerosol population consists of volatile particles (no solid core upon evaporation) and non-volatile particles covered in a soluble (mixed).

A word of caution, throughout this study it has been mentioned several times that the presence of non-volatile material (mostly soot) and chemiions in the wake can significantly alter the aerosol formation process. Activated soot provides a grow bed for H_2SO_4 droplets to nucleate onto. While it is very rare for pure sulfuric acid particles to freeze, mixed H_2SO_4-soot particles also tend to freeze more easily and create contrails. Condensation rates are heavily affected by ice forming and this should be accounted for. If the ice supersaturation is persistent, this leads to cloud formation. A good indicator for the formation of contrails is the Schmidt-Appleman criterion (Appleman, 1953; Tait et al., 2022). Yet, the stratosphere is relatively dry and the atmospheric temperature usually does not allow contrails to appear (Zhao & Turco, 1995). Moreover, given the comparatively low concentrations of soot in the engine wake in the case of SAI, it is believed that soot does not have a significant impact on the particle size distribution of H_2SO_4-H_2O aerosol in the stratosphere (Turco and Yu (1998); F. Yu, personal communication, November 10, 2022). Chemiions on the other hand could play a significant role in the early formation process, and should be accounted for, based on their ability to stabilize early cluster formation, and to enhance neutral coagulation. Remember that ion-induced particle formation is always energetically preferred to neutral particle formation (Merikanto et al., 2016).

3.2. Research Approach

This research started out as a logical continuation of the work from Golja et al. (2021) on aerosol dynamics in the near field of the SCoPEx stratospheric balloon experiment. The aim of this study is to act upon their recommendation to identify any weaknesses in the modeling of high-density aerosol nucleation, condensation and coagulation in an aircraft wake. The literature review on aerosol mechanics revealed that (1) the role of chemiions in particle formation is considerable, and should not be excluded from the modeling framework; (2) while non-volatile particulate matter (of which soot comprises the biggest share) will not be able to significantly influence the particle formation process given their low number densities in the plume; (3) large uncertainties are involved with the modeling of high-density nucleation

and condensation, especially in hot environments given the limited temperature range of the parameterizations in Table 4.1; (4) Previous studies have pointed out that the PSD is remarkably insensitive to strong variations in nucleation and condensation rates given the short timescales they are allowed to continue, as opposed to coagulation which spans several time decades (see also Section 2.7.2 on self-limited growth). Yet, there are concerns that the adopted modeling approaches, which lead to this conclusion, are based on too stringent conditions (e.g. uniform population across the plume, uniform mixing, and a size-averaged coagulation kernel); (5) the high injection concentrations that are required to make an SAI mission economically/logistically viable impose a serious risk of prompt self-coagulation, and overshooting the target particle size by the end of the early growth period. As a result, the choice of where to inject, and the associated diffusion/dispersion rates, may have a significant impact on the steerability of SAI.

Based on these findings, the choice was made to expand on the modeling approach of Golja et al. (2021), and replace the flow field with a RANS simulation of the jet engine wake. The microphysical routines were adapted to improve the fidelity of the simulation: the existing nucleation routine was replaced entirely, to improve the validity range and allow for the modeling of ion-induced nucleation; the thermodynamic parameterization for the equilibrium vapor pressure over a flat surface of liquid water was replaced; and the entire microphysical module was adapted to work with local (gridded) temperature and water vapor concentrations instead of a global uniform value. The plume dispersion model is discussed in its entirety in Chapter 4, but the implementation of the gridded distribution of temperature and water vapor, as well as the ion nucleation module, is explained in Section 3.3.

3.2.1. Research Questions

To formulate the research questions, let us return to the research objective in Section 1.2 which expresses the intend to gain insight in the growth process of Accumulation-Mode H_2SO_4-H_2O aerosol in a jet engine plume after injection of condensable sulfuric acid vapor by realistically simulating the jet regime using the RANS equations. Therefore, the main question this investigation aims to answer is: **"What are the mechanisms within the near-field of a jet engine wake that lead to the creation of aerosols and subsequent growth, when accounting for local variations in temperature and relative humidity?"**

The first steps to address this problem have been undertaken by reviewing relevant aerosol models and their validity range. To investigate the interaction among different aerosol growth processes further, some important sub-questions could be: At what stage do certain processes become significant and what time intervals do they span? How do they compete for the same vapor resource by looking at the H_2SO_4 depletion rates? This might prove insightful to establish a correct injection strategy that incorporates factors like engine settings, injection rates, and locations. Based on the answer to the first research question, a second research question is addressed: **"How can classical thermodynamic approaches to nucleation and condensation be improved to better model high-density aerosol formation from condensable vapor?"**

The goal is to identify the modeling errors that are most impactful on the growth process of the aerosol, and the final particle size distribution. If possible, alternative approaches will be considered to increase the model's fidelity. In general, the literature review revealed several assumptions and limitations in modeling aerosol mechanics in a jet engine wake. Yet, their impact is uncertain, or not quantifiable. Therefore, a third research question is formulated: **"What are the key uncertainties in modeling aerosol mechanics in a jet engine wake and how do they impact our understanding of the microphysics?"**

The answer to the third question will enable us to improve on the right areas in the modeling approach, and to perform targeted sensitivity studies in subsequent stages to quantify their relative impact on the microphysics.

3.2.2. Study and Verification Cases

In order to formulate an all-inclusive answer to the research questions from Section 3.2.1, a series of sensitivity studies is to be carried out by varying several key parameters such as temperature and the initial concentrations of H_2SO_4, H_2O, or chemiions at the engine exit; injecting into the core, bypass or further downstream; or variations in the turbulence parameters such as the Schmidt number are also among the possibilities. However, the first step is to verify the trustworthiness of the simulation. As mentioned in the the introduction, there is is a need for in-situ observations of near-field plume aerosol dynamics for SAI applications in order to truly validate the model output because no experimental datasets exist that cover any realistic recreation of a SAI scenario that employs aircraft as a distribution platform (Floerchinger et al., 2020). To the author's knowledge, no simulations have been reported on SAI studies in the early-plume regime. It is possible to circumvent part of the problem by looking at the experimental investigations from e.g. Fahey et al. (1995), Friedl et al. (1997) & Schumann et al. (2002) that were conducted to map out aircraft emissions at the start of the 21st century. They provide a wide range of aircraft wake measurements for various sub- and supersonic aircraft at both tropo- and lower stratospheric altitudes, but serious concerns were raised on the detection limit of the measurement equipment as it struggled to detect the nanoscale (below 5 nm) aerosol population under plume conditions (Kärcher, 1998; Schumann et al., 2002). The most common approach to compare a polydisperse aerosol population is to visualize the particle size distribution (PSD) over time. Key variables are the particle radius r (or the diameter) and the particle number distribution $dn/d\log(r)$ which is distributed logarithmically to allow for better visualization of the size range. Figure Fig. 3.2 shows an excellent example of a PSD of the various aerosol types in an exhaust plume 1 sec after emission (or roughly 250 m in plume distance). Remark the large estimated ranges of variability of both number and sizes due to variations of key parameters (e.g. fuel sulfur content, conversion fraction of H_2SO_4, engine emission parameters, ambient conditions), making it difficult to compare individual cases (Kärcher, 1998; Penner et al., 1999). Yet, together with the in-situ measurement data from the SULFUR-7 experiments (Schumann et al., 2002) for a plume of young age (0.4 - 0.8 s after emission), it is possible to validate volatile and non-volatile particle number predictions under 'normal' conditions (meaning no artificially-increased concentrations of sulfuric acid vapor or other emissions). However, the model that is used for the purpose of this study, is still under development, and currently unable to simulate different aerosol types (pure, binary, or mixed with a solid core). While ion-assisted nucleation has been implemented, further adaptation of the coagulation routine by including electrostatic enhancement is required before the model can predict ion modes correctly. This would demand additional computation time, because instead of self-coagulation among one aerosol type, one needs to account for positively- and negatively-charged clusters as well as neutral clusters, and the possibility to recombine/neutralize. Therefore, the first step is to verify particle formation of binary sulfate aerosol without the inclusion of ions. Yu and Turco (1998) did a sensitivity study on the differences between ion-mediated nucleation and neutral nucleation, and presented a neutral particle size distribution for $\sim$ 1.5 s and 16 min after exhaust emission, as illustrated in Fig. 3.3. This will form the base of the verification process, and from there sensitivity studies can be conducted on the parameters that were mentioned at the start of this section. In the future, individual microphysical processes and their effect on the PSD could be verified by comparing them to other models from e.g. Brown et al. (1996), Yu and Turco (1998), Kärcher (1998), Paoli et al. (2008), and Fritz et al. (2020).

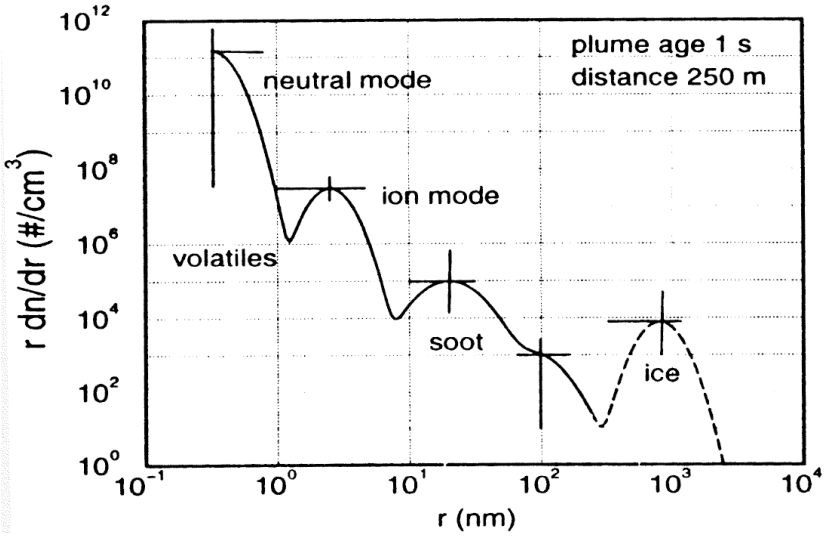

Figure 3.2: Schematic of the various aerosol types present in a young jet plume. Shown are approximate number size distributions versus aerosol radius for volatile aerosols (neutral and ionized modes), black carbon soot (primary and secondary modes), and primary contrail ice particles (dashed line). Exhaust metal particles are not shown. Horizontal and vertical bars indicate the estimated ranges of variability of both number and sizes due to variations of key parameters (e.g., fuel sulfur content, engine emission parameters, ambient conditions). In the presence of contrail crystals, the spectra of the other components may be subject to changes (not shown) (Kärcher, 1998).

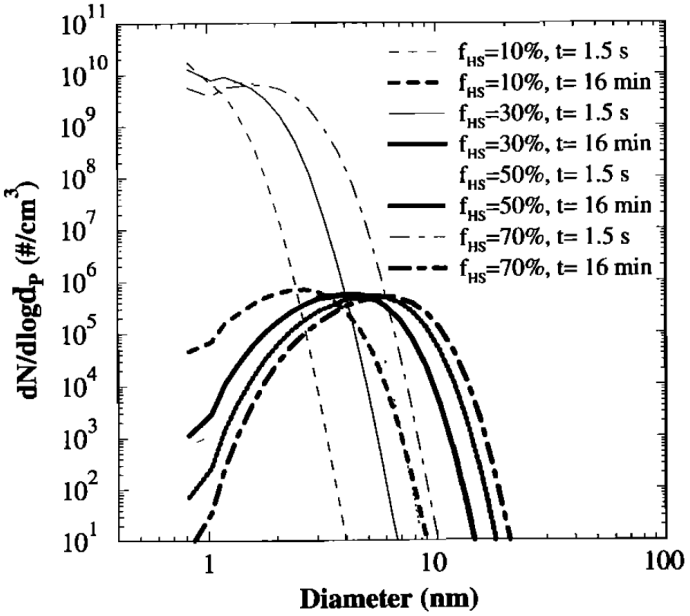

Figure 3.3: Size distributions of the acid (volatile) particles at two times during the evolution of the plume ($\sim$ 1.5 s and 16 min after exhaust emission) for the classical model, without ions nor soot present, and with ideal "sticking coefficients" for all particle collision processes (Yu & Turco, 1998).

3.2.3. Research Setup

Because of the uncertainty on potential harmful effects of SAI to nature (see Chapter 1), this research is done purely by means of numerical simulations. The faculty of Aerospace Engineering at TU Delft has a strong expertise in numerical flow simulation along side good turbofan jet engine models as well as a dedicated research group ACNE for aircraft noise and emissions. The engine model is based on the mission design from Janssens et al. (2020) and built with the Royal Netherlands Aerospace Centre's in-house turbine simulation tool GSP 12[1]. This tool provides the initial conditions for the computational fluid dynamics (CFD) and constrains the problem. The CFD mesh is constructed in Ansys FLUENT,

[1] https://www.gspteam.com/index.html

a commercial software program available to TU Delft students, mainly for ease of adaptation should the need arise to try out different solver types or turbulence models. The results are then interpolated with tools available in ANSYS to match the grid that is used to solve the microphysical equations. The additional microphysical routines will be written in MATLAB, and build further on the code that was developed for the research of Golja et al. (2021). A different possibility would have been to use the APCEMM microphysical model from Fritz et al. (2020) which was developed in C++ and is made publicly available through GitHub[2]. While an argument can be made about better achievable performance with C++, MATLAB has the preference because of its good data visualization options, mathematically robust build-in routines and toolboxes as well as good debugger functionality. It is a commercial software which limits its widespread use, but it is generally accessible for the scientific community. Thus, for the early development stage and the implementation of new microphysical processes, MATLAB will be the main coding language.

3.3. Modeling Framework

The full description of the decoupled plume dispersion model is the topic of Chapter 4. This section focuses on the specific contributions that were made to the microphysics module of the PMD to increase its fidelity in simulating aerosol formation and growth in a jet engine wake. Consider Fig. 3.4, which depicts the structure of the aerosol microphysics module.

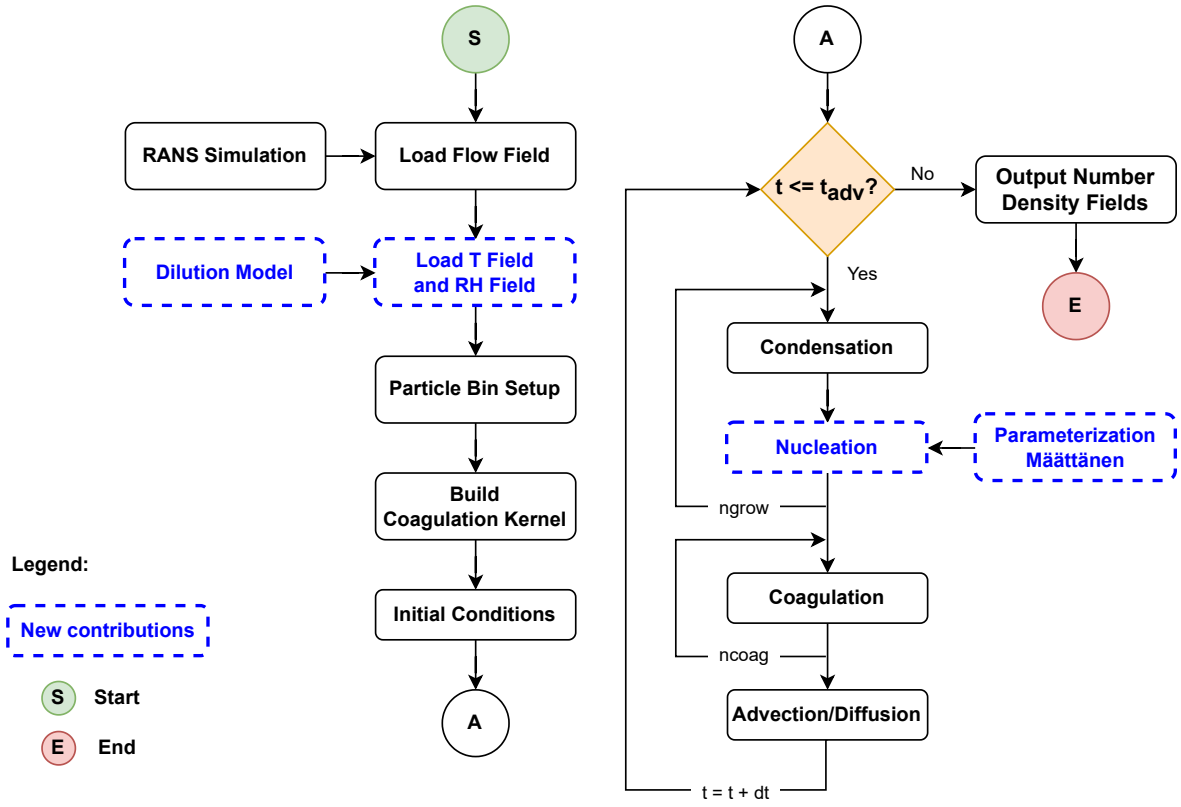

Figure 3.4: Flowchart of the microphysics module, including new contributions.

The new features are indicated by the blue-dashed blocks. The biggest contribution is the inclusion of a gridded temperature and RH field. This required the addition of a new plume dilution model, which is the topic of Section 3.3.1. In the end, this affected almost all elements of the microphysics module because they had to be adapted to work with local field variables instead of a constant value for T

[2] https://github.com/MIT-LAE/APCEMM

and RH. A second contribution is the full replacement of the nucleation routine, and the addition of a ion-nucleation module which is discussed in Section 3.3.2.

3.3.1. Plume Dilution

The dilution rate of the exhaust plume is a crucial factor in the microphysical processes that promote aerosol growth, but the dilution rate varies widely over the course of a plume's lifetime depending on the stage, engine specifications, and ambient conditions. Therefore, the entrainment and mixing of ambient air, resulting in the expansion of the plume and dispersion of exhaust emissions, has been the subject of investigation alongside the development of microphysical models. A correct estimation of the time evolution of emission concentration levels and local temperature is key in simulating early-plume aerosol microphysics. Technically, all this information can be provided by an accurate numerical simulation of the flow field and the necessary boundary condition, e.g. the LES investigation from Gerz et al. (1998) on transport and diffusion of aircraft emissions. Because only the early jet regime is considered in this study, the RANS simulation should be able to provide the necessary information on the temperature and mass diffusion rates in the domain. Yet, as the simulation of the flow field was still under development as part of another study from Tluk (2023), and some information was still missing, it was desirable to compare the RANS case to other (empirical) studies, given the large dependence of aerosol microphysics on local concentration, temperature and relative humidity. An excellent source is the empirical investigation by Schumann et al. (1998) who created a timewise interpolation of the "bulk" plume dilution ratio, which is the amount of air mass with which the exhaust resulting from a unit mass of burned fuel mixes per unit flight distance within the bulk of the plume. This curve, shown in Fig. 3.5, is based on in-situ measurements of CO_2, NO, NO_x, SO_2, H_2O, temperature, and contrail diameters behind subsonic and supersonic aircraft in the upper troposphere, tropopause, and lower stratosphere, for plume ages of seconds to hours, and sampled from over more than 70 plume encounters.

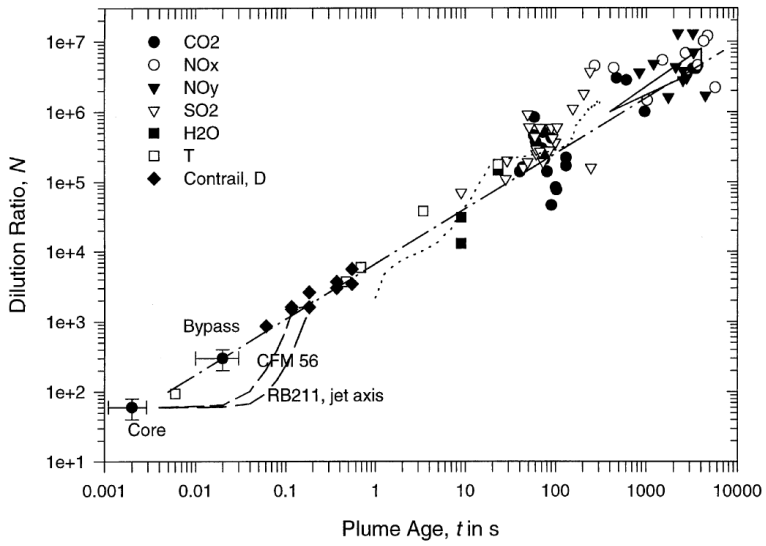

Figure 3.5: Dilution ratio versus plume age. The symbols without error bars are derived from measurements. The dots with error bars denote characteristic values for the engine core and bypass exits. The dilution on the jet axis computed for two engines of type CFM56 and RB211 is shown by short and long dashed curves. For more information, see Schumann et al. (1998).

However, the fit is best for young plumes between 1 to 50 seconds, as it fails to capture the early-jet regime (< 1 s) and the region of slow-mixing during the vortex regime (10 - 180 s) where mixing with ambient air is almost entirely suppressed (see Fig. 3.6, and also the discussion on plume morphology in Section 2.7.1). Secondly, and more importantly, the fit is based on averaged plume measurements while the early plume concentrations are highly non-uniform with a strong Gaussian distribution in radial

direction. This is confirmed by a two-dimensional mixing model for two separate engines (long-dashed curves on the bottom) in the core region along the jet axis, which indicate that the concentration on the plume axis stays about constant until 0.02 s, and then approaches the bulk mean after about 0.3 s Schumann et al. (1998). This study will follow the box-model approach from Kärcher (1995) instead, which puts special emphasis on modeling the relaxation of temperature and peak exhaust chemical species concentrations in the innermost part of the plume (the core) for the early jet regime. Because the rate of diffusion in the jet regime is largely the result of turbulent mixing of the wake with the ambient air, they model the rate of change of temperature and species concentrations through a first-order decay term with a turbulent entrainment rate ω, as shown in Eq. (3.1) and Eq. (3.2).

$$\frac{dT}{dt} = -\omega_T \left(T - T_{\text{amb}}\right) \tag{3.1}$$

$$\frac{dN}{dt} = -\omega_N \left(N - N_{\text{amb}}\right) \tag{3.2}$$

where the subscript 'amb' denotes ambient conditions.

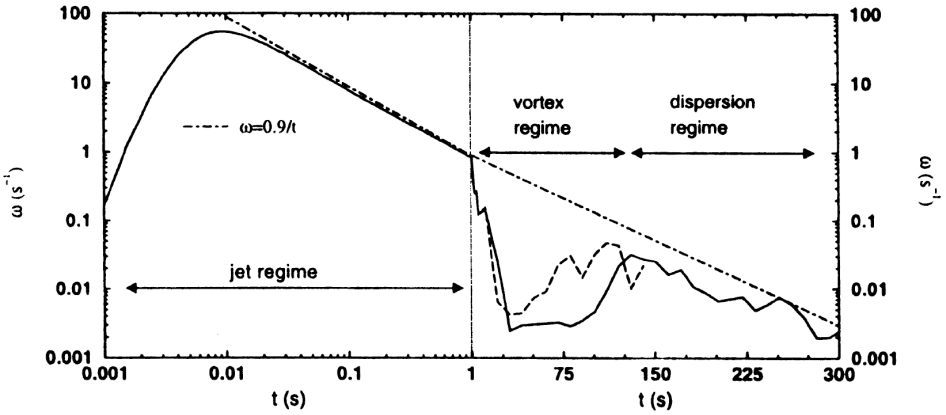

Figure 3.6: Simulated entrainment rate ω_N of the plume and wake of a commercial airliner versus time t after passage of the aircraft without (solid line) and with (dashed line) weak atmospheric turbulence. The rate is based on the maximum value of the concentration of a tracer in the flow field. Taken from Gerz et al. (1998) and adapted by Kärcher (1999).

The concentration entrainment rate, depicted in Fig. 3.6 for the case of a high-bypass B747-400 jet engine operating at subsonic speeds (0.8 Mach), varies significantly depending on the plume regime. The plume entrains little to no air until $\sim$ 0.01 s after emission, when the mixing process which starts at the shear line of the axisymmetric jet, has reached the jet axis. At that point, the entrainment rate reaches its maximum and subsequently decays with $\sim 1/t$ for the time period of the jet regime (Gerz et al., 1998). The jet entrainment rates between 0.001 and 1 s are taken from Kärcher (1995), who extracted them from a two-dimensional turbulent mixing model of a single jet of hot exhaust gas with the atmosphere. The curve fits of the entrainment rates are shown in Fig. 3.7a. The integration of Eq. (3.1) and Eq. (3.2) is done in MATLAB with standard "ode15s" functionality for ordinary differential equations, given appropriate initial and ambient conditions (see Table 3.1).

Table 3.1: Aircraft parameters and ambient conditions for the tropopause and stratosphere study cases.

	T_0 (K)	T_{amb} (K)	N_0 (#/cm^3)	N_{amb} (#/cm^3)	u_0 (m/s)	u_{amb} (m/s)	P_{amb} (hPa)
B747[a]	590	224	n.a.	n.a.	473	237	239
Case study[b]	570	216	3.5e16	1.0e13	450	210	48

[a] Data from the original model case of the high-bypass B747-400 engine flying at cruise conditions in the tropopause (Kärcher, 1995), but it was not possible to extract bypass parameters.

[b] Conditions for the study case in the lower stratosphere. Biggest discrepancy is the ambient pressure. Water vapor concentrations are retrieved from Zhao and Turco (1995).

For the case study in the lower stratosphere, the evolution of peak temperature and water vapor concentration in the core of the plume are shown in Fig. 3.8a and Fig. 3.8b. The normalized flow variables are shown in Fig. 3.7b, in line with figure 3b from Kärcher (1995), and clearly indicate slower mixing of temperature compared to water vapor as a result of the bypass flow temperature surpassing ambient conditions.

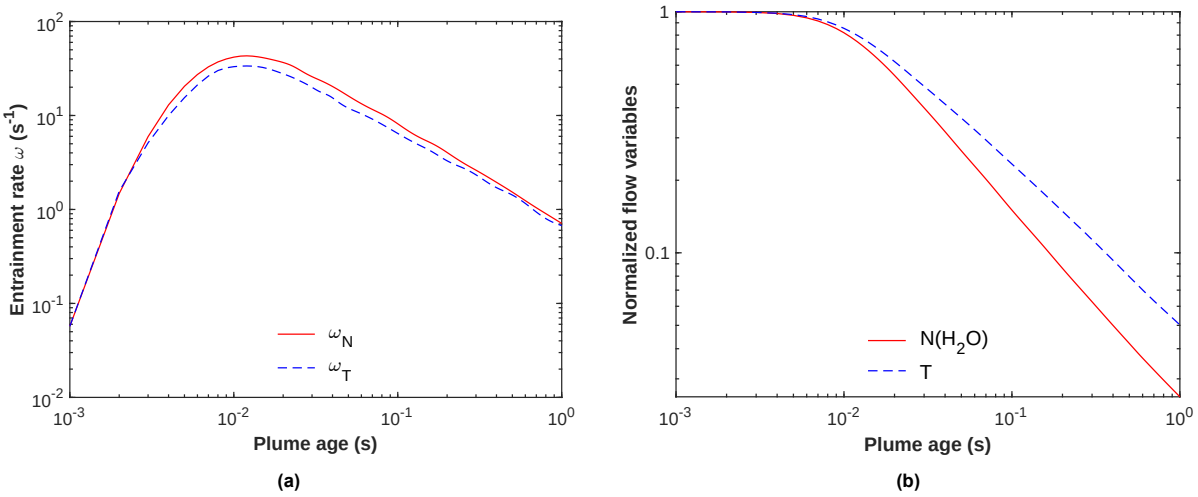

Figure 3.7: (a) Entrainment rates for the B747-400 engine versus plume age. Due to the presence of a bypass, ω_T is different from ω_N in the jet regime. (b) The temporal evolution of the normalized peak temperatures and water vapor mixing ratios.

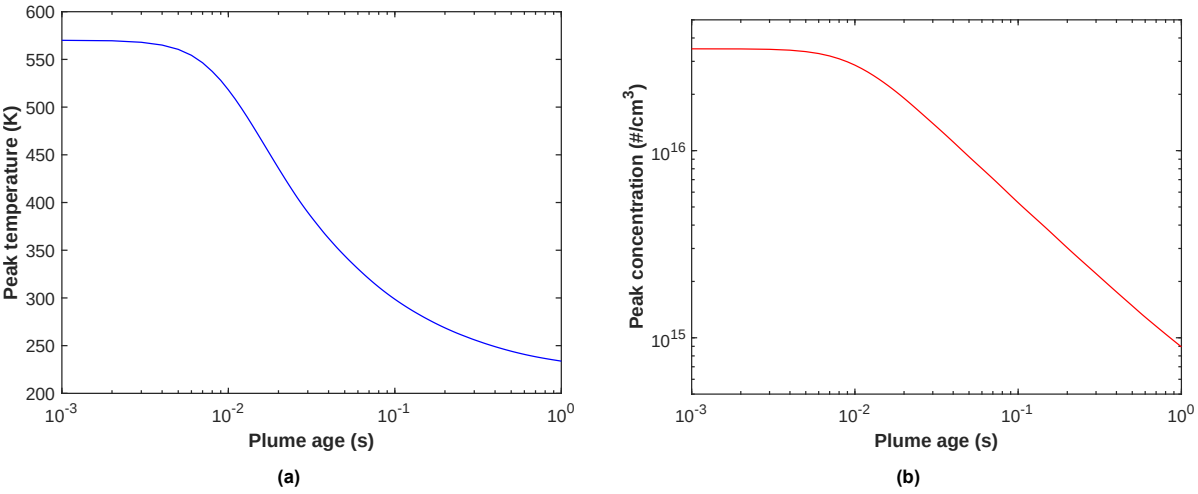

Figure 3.8: Temporal evolution of the peak (a) temperature, and (b) water vapor concentration in the plume core as a result of turbulent diffusion. Initial and ambient conditions are reported in Table 3.1.

The next step is to convert the temporal dependence of Fig. 3.8a and Fig. 3.8b to a spatial dependence, such that it can be used with the three-dimensional microphysical grid. This is achieved with the substitution $t = x/u$, giving us the spatial evolution of the peak temperature and concentration along the plume axis. The final step is to replicate the Gaussian distribution in radial direction, for which we look at the resolved radial temperature distribution from our RANS simulation. This is arguably the biggest discrepancy in the modeling approach as we implicitly assume that the radial diffusion does not depend on the engine exit conditions, and ignore the shortcomings from the k-ϵ_k turbulence model (see Section 4.1.2). This is only considered acceptable given that the first and foremost goal of this research is to perform an early sensitivity study of the effect of temperature and relative humidity. It is now possible to combine the information from Fig. 3.9a and Fig. 3.9b, and create a three-dimensional temperature distribution with the scaling operation described by Eq. (3.3), under the assumption that

the Lewis number in radial direction is equal to 1. The procedure for the water vapor concentration in the domain is performed in the same way.

$$\frac{T_R(x,y,z) - T_{\text{amb}}}{T_{R,\text{max}}(x) - T_{\text{amb}}} = \frac{T_K(x,y,z) - T_{\text{amb}}}{T_{K,\text{max}}(x) - T_{\text{amb}}} = \frac{N_K(x,y,z) - N_{\text{amb}}}{N_{K,\text{max}}(x) - N_{\text{amb}}} \tag{3.3}$$

$$T_K(x,y,z) = \left(\frac{T_R(x,y,z) - T_{\text{amb}}}{T_{R,\text{max}}(x) - T_{\text{amb}}} \cdot \frac{T_{K,\text{max}}(x) - T_{\text{amb}}}{1} \right) + T_{\text{amb}} \tag{3.4}$$

where $T_K(x,y,z)$ is the *unknown* radial distribution of temperature along the plume axis for the temperature evolution described by Kärcher; $T_R(x,y,z)$ is the *known* radial distribution of temperature along the plume axis from the RANS simulation; $T_{K,\text{max}}(x)$ is the *known* one-dimensional peak temperature evolution along the plume axis described by Kärcher; and $T_{R,\text{max}}(x)$ is the *known* one-dimensional peak temperature evolution along the plume axis from the RANS simulation.

The resulting (three-dimensional) temperature field based on the temperature evolution from Kärcher (1995) is shown in Fig. 3.10, the RANS-resolved temperature field is shown for comparison in Fig. 3.11. Because the domain is axisymmetric, a section cut at the core of the plume ($z = 0$ m) suffices to visualize the entire domain.

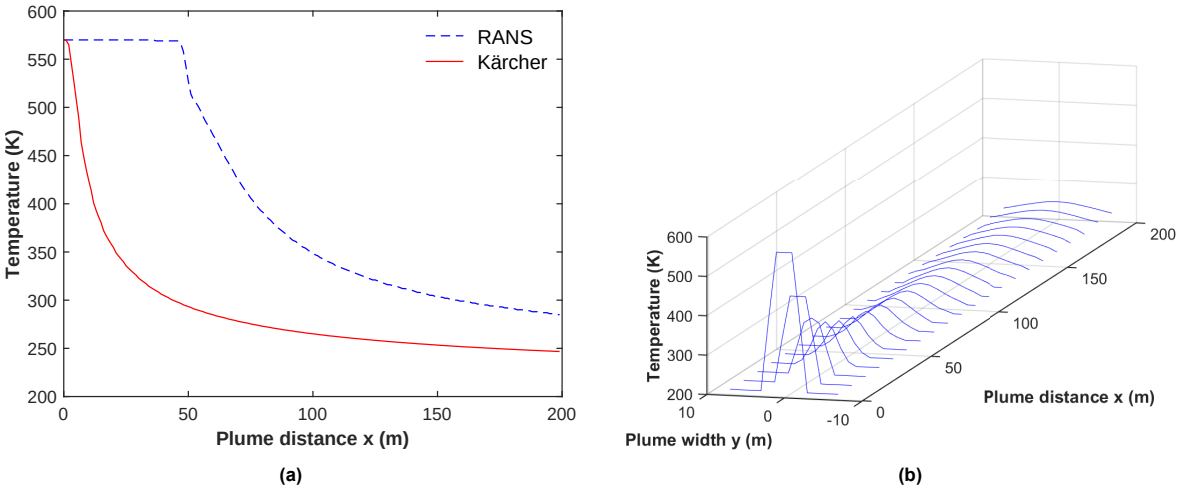

Figure 3.9: (a) Evolution of the peak temperature versus plume distance for both the RANS simulation and box-model equation from Kärcher (1995). (b) The RANS-resolved radial temperature profile in one dimension along the plume axis.

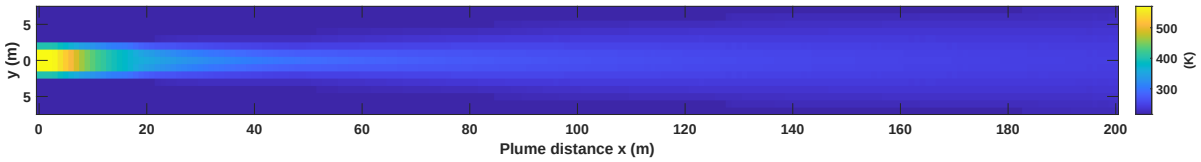

Figure 3.10: A 2D section cut of the temperature distribution of an axisymmetric plume based on the peak temperature evolution from Kärcher (1995), and radial profile from RANS, section cut at $z = 0$ m.

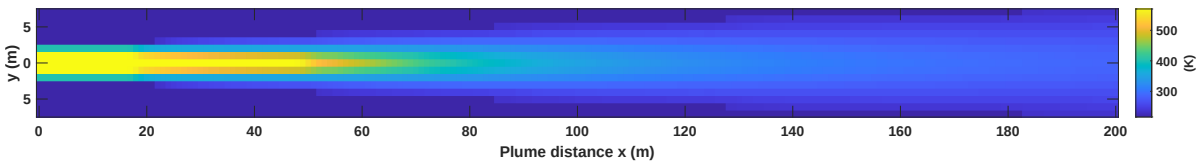

Figure 3.11: A 2D section cut of the RANS-resolved temperature distribution of an axisymmetric plume, section cut at $z = 0$ m.

Notice the distinct difference between both temperature profiles in Fig. 3.9a. The RANS-resolved plume core temperature remains constant until about 45 m behind the engine exit ($\sim$ 0.1 s), as opposed to

the mixing model from Kärcher which predicts a much faster breakdown of the core after roughly 5 m ($\sim$ 0.01 s). Consequently, the 3D temperature distributions in Fig. 3.10 and Fig. 3.11 also look vastly different. Further analysis will have to confirm what the reason is for this discrepancy, but both models can be used to perform a sensitivity study and assess the impact of temperature and relative humidity on the microphysical processes. The axial evolution profile, and 3D-distributions of the water vapor concentration are included in Appendix A. Finally, take a look at the relative humidity distributions which are an overlay of the water vapor concentration and its saturation vapor pressure based on the temperature distribution. They are shown in Fig. 3.12 and Fig. 3.13, note that the values are scaled logarithmically to improve the resolution of the image. The faster rate of dilution predicted by Kärcher also shows in the evolution of relative humidity. Both models predict extreme dry conditions just beyond the engine exit (RH < 0.01 %), and the relative humidity increases gradually in the core of plume albeit at a faster rate in the case of Kärcher. Similar humid conditions in the jet shear line are witnessed after approximately 20 m with relative humidities reaching maxima of just above 20 %. This is significantly larger than the standard relative humidity levels of approximately 1 % for lower stratospheric atmosphere.

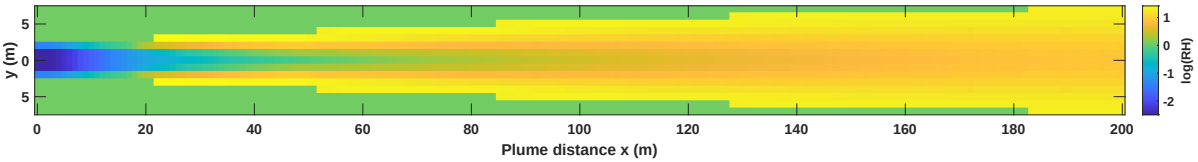

Figure 3.12: A 2D section cut of the RH distribution of an axisymmetric plume based on the peak temperature evolution from Kärcher (1995), section cut at $z = 0$ m. Values are log-scaled for illustrative purposes.

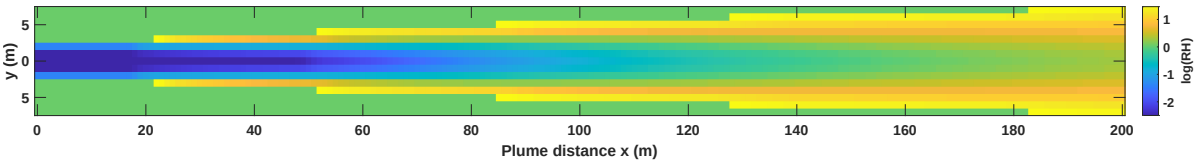

Figure 3.13: A 2D section cut of the RH distribution of an axisymmetric plume based on a RANS-resolved temperature distribution and $Le_t = 1$, section cut at $z = 0$ m. Values are log-scaled for illustrative purposes.

3.3.2. Ion-induced Nucleation

To improve the functionality of the nucleation routine, the parameterization from Vehkamäki et al. (2002) was replaced by the one from Määttänen et al. (2017) (see also Section 4.2.2). This increased the temperature validity range, and provided the possibility to simulate ion-induced nucleation based on an experimentally-validated parameterization. The architecture of the new routine closely resembles the old nucleation routine as the methodology remains the same. First, the critical cluster composition, and size, is determined based on the local temperature, local relative humidity, and the gas phase concentration of sulfuric acid. Then, the nucleation rate is determined. The next step is to scale the fresh nucleus to match the sectional bin composition, and categorize them according to their size. Finally, the metrics to track the population of vapor and aerosol are updated, and safety checks are in place to verify that no negative nucleation rates nor negative population counts are witnessed. The inclusion of charged particle formation requires all of this steps to be performed twice with different model parameters and coefficients, but the principle remains the same. As mentioned before in Section 3.2, the ion module is still in development and ion-assisted coagulation is not available yet. Therefore, all clusters (neutral or charged) are treated equally, and a charged aerosol particle does not posses any physical advantages over their neutral siblings. They may have a different composition and/or size though, depending on the conditions.

In addition, a new population metric for ions was created to track the concentration of ions in the plume. Their movement is governed by the same advection-diffusion equation as the aerosol, and vapor, but ions do neutralize over time (the process where two oppositely charged ions recombine). The evolution of the ion concentration is tracked using Eq. (2.53), but the scavenging rate due to coagulation with pre-existing particles is neglected at this stage. The ion-ion recombination rate is estimated based on a parameterization from Dunne et al. (2016), and given by Eq. (3.5).

$$\alpha = \left(6 \times 10^{-8}\right) \sqrt{(300/T)} + \left(6 \times 10^{-26}\right) N_{\text{air}} \left(\frac{300}{T}\right)^4 \quad (\text{cm}^3/\text{s}) \tag{3.5}$$

The predicted nucleation rates of the ion module were verified by replicating the graphs from Määttänen et al. (2017) in a simple box-model.

4

Plume Dispersion Model

The problem statement in Section 1.1 briefly introduced the necessary modules to create a hybrid PDM that is able to realistically simulate the flow behind a jet engine with the inclusion of aerosol particles: (1) a 3D flow solver which resolves the Navier-Stokes equations to some extent; (2) a chemistry module which includes all the relevant microphysical processes that affect aerosol growth; and (3) a diffusion-advection module which calculates the displacement of mass in the flow field. Ideally, they are fully integrated in one cohesive physical model that takes all inter-dependencies into account, but the computational load to perform only a simple sensitivity study among its variables would be insurmountable. Instead, a decoupled modeling approach is followed where some variables are solved independently of others. The velocity field and turbulent diffusion of the wake are computed on a meshed domain with the use of ANSYS, a commercial CFD package, as described in Section 4.1. The aerosol dynamics are resolved separately on a different grid, meaning that the flow does not perceive the presence of particulate matter nor chemical reactions between different species. Consequently, an interpolation method is established to transfer knowledge of the flow field to the microphysics solver. Aerosol mechanics were described extensively under Chapter 2, and Section 4.2 explains what microphysical relations were used to simulate aerosol formation and growth, and shows the validity ranges for several parameterizations of important thermodynamic parameters. Lastly, Section 4.3 elaborates on the advection-diffusion scheme, which models the transport of aerosol, vapor, and ions throughout the plume, and is also written in MATLAB.

4.1. Numerical Flow Solver

The flow field in the wake of a jet is highly turbulent and complex. To predict the resulting velocity field, we need to solve the Navier-Stokes equations, which is often times not pragmatic as discussed in Section 4.1.1. To reduce the complexity of the problem, the equations are filtered, and separated in their low- and high-frequency components. This process is discussed in Section 4.1.2. Lastly, Section 4.1.3 outlines the exact specifications of the RANS simulation that was conducted for the purpose of this research.

4.1.1. The Navier-Stokes Equations

Fluid motion has to obey the laws of mass, momentum, and energy conservation (Eq. 4.1 - 4.3). They are shown below in their conservation (Eulerian) form, but often appear in their convective (Lagrangian) form elsewhere by introducing the substantial derivative. To obtain the velocity field of a jet engine wake,

this set of equations needs to be solved simultaneously for given boundary conditions. Note that they are derived for a Newtonian fluid, where the fluid is treated as a continuum (see also Section 2.2.1). In addition, the fluid is assumed to be isotropic and isobaric. A short overview is given below, for full derivations the reader is referred to Anderson (2017).

The differential form of the continuity equation is a mathematical expression of the fundamental principle that 'mass can neither be created nor destroyed':

$$\frac{\partial \rho}{\partial t} + \nabla \cdot (\rho \mathbf{u}) = 0 \tag{4.1}$$

where the bold font represents the three-dimensional velocity vector $\mathbf{u} = [u_x, u_y, u_z]$.

The momentum equation, consisting of three equations in total, embodies Newton's second law which states that 'a force acting a (fluid) body equals its time rate of change of momentum':

$$\frac{\partial}{\partial t}(\rho \mathbf{u}) + \nabla \cdot (\rho \mathbf{u} \otimes \mathbf{u}) = -\nabla P + \nabla \cdot \boldsymbol{\tau}_{\text{visc}} + \rho \mathbf{f} \tag{4.2}$$

where $\nabla\cdot$ is the divergence, $\otimes$ is the outer product, $\boldsymbol{\tau}_{\text{visc}}$ ($\mathrm{N\,m^{-2}}$) is the viscous stress tensor, and $\mathbf{f}$ ($\mathrm{N\,kg^{-1}}$) are any net body forces per unit mass acting on the fluid.

The energy equation, derived from the first law of thermodynamics, which embodies the physical concept that 'energy can neither be created nor destroyed, but only change form':

$$\frac{\partial}{\partial t}\left[\rho\left(U + \frac{\|\mathbf{u}\|^2}{2}\right)\right] + \nabla \cdot \left[\rho\left(U + \frac{\|\mathbf{u}\|^2}{2}\right)\mathbf{u}\right] = \rho\dot{q} - \nabla \cdot (P\mathbf{u}) + \rho(\mathbf{f} \cdot \mathbf{u}) + \dot{Q}'_{\text{visc}} + \dot{W}'_{\text{visc}} \tag{4.3}$$

where U ($\mathrm{J\,kg^{-1}}$) is the internal energy per unit mass, $\dot{q}$ ($\mathrm{J\,kg^{-1}\,s^{-1}}$) the rate of volumetric heat addition per unit mass. $\dot{Q}'_{\text{visc}}$ and $\dot{W}'_{\text{visc}}$ ($\mathrm{N\,m^{-2}\,s^{-1}}$) are dummy variables that represent the energy fluxes of heat and work due to viscous forces.

The system of five equations, shown above, is under-determined as it contains six dependent values $(\rho, P, u_x, u_y, u_z, U)$. It needs an additional sixth equation of state to relate pressure, temperature, and density of the fluid to each other. One could for example use the perfect gas law (Eq. 4.4) and the assumption that the gas is calorically perfect:

$$P = \rho \frac{R}{M} T \tag{4.4}$$

$$U = c_v T = \frac{c_v P M}{\rho R T} \tag{4.5}$$

where c_v ($\mathrm{J\,kg^{-1}\,K^{-1}}$), the specific heat capacity at constant volume, is assumed to be a constant. This is only valid for air in subsonic and low supersonic conditions.

The last step is to include expressions for the viscous terms in the momentum and energy equation. The multi-dimensional viscous stress tensor $\boldsymbol{\tau}_{\text{visc}}$ has nine components that are linearly proportional to the time rate of strain or the spatial derivative of the velocity vector:

$$\boldsymbol{\tau}_{\text{visc}} = \begin{bmatrix} \tau_{xx} & \tau_{xy} & \tau_{xz} \\ \tau_{yx} & \tau_{yy} & \tau_{yz} \\ \tau_{zx} & \tau_{zy} & \tau_{zz} \end{bmatrix} \quad (\mathrm{N\,m^{-2}}) \tag{4.6}$$

with the normal stresses τ_{ii} on the diagonal and tangential shear stresses τ_{ij}:

$$\tau_{xx} = \mu_b(\nabla \cdot \mathbf{u}) + 2\mu\frac{\partial u_x}{\partial x} \tag{4.7}$$

$$\tau_{xy} = \tau_{yx} = \mu\left(\frac{\partial u_y}{\partial x} + \frac{\partial u_x}{\partial y}\right) \tag{4.8}$$

where μ_b (N s m^{-2}) is the bulk (or second) viscosity coefficient, often modeled as $\mu_b = -\frac{2}{3}\mu$.

Likewise, it can be shown that:

$$\dot{Q}'_{\text{visc}} = \frac{\partial}{\partial x}\left(q_T\frac{\partial T}{\partial x}\right) + \frac{\partial}{\partial y}\left(q_T\frac{\partial T}{\partial y}\right) + \frac{\partial}{\partial z}\left(q_T\frac{\partial T}{\partial z}\right) \tag{4.9}$$

wherein q_T (N s^{-1} K^{-1}) is the thermal conductivity.

$$\begin{aligned}\dot{W}'_{\text{visc}} = &\frac{\partial\left(u_x\tau_{xx}\right)}{\partial x} + \frac{\partial\left(u_x\tau_{yx}\right)}{\partial y} + \frac{\partial\left(u_x\tau_{zx}\right)}{\partial z}\\ &+ \frac{\partial\left(u_y\tau_{xy}\right)}{\partial x} + \frac{\partial\left(u_y\tau_{yy}\right)}{\partial y} + \frac{\partial\left(u_y\tau_{zy}\right)}{\partial z}\\ &+ \frac{\partial\left(u_z\tau_{xz}\right)}{\partial x} + \frac{\partial\left(u_z\tau_{yz}\right)}{\partial y} + \frac{\partial\left(u_z\tau_{zz}\right)}{\partial z}\end{aligned} \tag{4.10}$$

Insert Eq. (4.6) - (4.8) into Eq. (4.2), and insert Eq. (4.9) - (4.10) into Eq. (4.3), to obtain the complete set of parameters that govern fluid dynamics (ignoring body forces here):

$$\begin{aligned}\rho\frac{\partial u_x}{\partial t} + \rho u_x\frac{\partial u_x}{\partial x} + \rho u_y\frac{\partial u_x}{\partial y} + \rho u_z\frac{\partial u_x}{\partial z} = &-\frac{\partial p}{\partial x} + \frac{\partial}{\partial x}\left(\mu_b\nabla\cdot\mathbf{u} + 2\mu\frac{\partial u_x}{\partial x}\right)\\ &+ \frac{\partial}{\partial y}\left[\mu\left(\frac{\partial u_y}{\partial x} + \frac{\partial u_x}{\partial y}\right)\right] + \frac{\partial}{\partial z}\left[\mu\left(\frac{\partial u_x}{\partial z} + \frac{\partial u_z}{\partial x}\right)\right]\end{aligned} \tag{4.11}$$

$$\begin{aligned}\rho\frac{\partial u_y}{\partial t} + \rho u_x\frac{\partial u_y}{\partial x} + \rho u_y\frac{\partial u_y}{\partial y} + \rho u_z\frac{\partial u_y}{\partial z} = &-\frac{\partial p}{\partial y} + \frac{\partial}{\partial x}\left[\mu\left(\frac{\partial u_y}{\partial x} + \frac{\partial u}{\partial y}\right)\right]\\ &+ \frac{\partial}{\partial y}\left(\mu_b\nabla\cdot\mathbf{u} + 2\mu\frac{\partial u_y}{\partial y}\right) + \frac{\partial}{\partial z}\left[\mu\left(\frac{\partial u_z}{\partial y} + \frac{\partial u_y}{\partial z}\right)\right]\end{aligned} \tag{4.12}$$

$$\begin{aligned}\rho\frac{\partial u_z}{\partial t} + \rho u_x\frac{\partial u_z}{\partial x} + \rho u_y\frac{\partial u_z}{\partial y} + \rho u_z\frac{\partial u_z}{\partial z} = &-\frac{\partial p}{\partial z} + \frac{\partial}{\partial x}\left[\mu\left(\frac{\partial u}{\partial z} + \frac{\partial u_z}{\partial x}\right)\right]\\ &+ \frac{\partial}{\partial y}\left[\mu\left(\frac{\partial u_z}{\partial y} + \frac{\partial u_y}{\partial z}\right)\right] + \frac{\partial}{\partial z}\left(\mu_b\nabla\cdot\mathbf{u} + 2\mu\frac{\partial u_z}{\partial z}\right)\end{aligned} \tag{4.13}$$

$$\begin{aligned}\frac{\partial}{\partial t}\left[\rho\left(U + \frac{\|\mathbf{u}\|^2}{2}\right)\right] + \nabla\cdot\left[\rho\left(U + \frac{\|\mathbf{u}\|^2}{2}\right)\mathbf{u}\right] = &\rho\dot{q} + \frac{\partial}{\partial x}\left(k\frac{\partial T}{\partial x}\right) + \frac{\partial}{\partial y}\left(k\frac{\partial T}{\partial y}\right)\\ &+ \frac{\partial}{\partial z}\left(k\frac{\partial T}{\partial z}\right) - \nabla\cdot p\mathbf{u} + \frac{\partial\left(u_x\tau_{xx}\right)}{\partial x} + \frac{\partial\left(u_x\tau_{yx}\right)}{\partial y}\\ &+ \frac{\partial\left(u_x\tau_{zx}\right)}{\partial z} + \frac{\partial\left(u_y\tau_{xy}\right)}{\partial x} + \frac{\partial\left(u_y\tau_{yy}\right)}{\partial y} + \frac{\partial\left(u_y\tau_{zy}\right)}{\partial z}\\ &+ \frac{\partial\left(u_z\tau_{xz}\right)}{\partial x} + \frac{\partial\left(u_z\tau_{yz}\right)}{\partial y} + \frac{\partial\left(u_z\tau_{zz}\right)}{\partial z}\end{aligned} \tag{4.14}$$

Equations (4.11) to (4.13) are the infamous Navier-Stokes equations, which are seemingly impossible to solve analytically. They are a coupled system of nonlinear, second-order partial differential equations. In combination with Eq. (4.1) and Eq. (4.14), they describe unsteady, compressible, three-dimensional viscous flow (Anderson, 2017). The complexity of the system (attributed to its non-linearity) demands

for a numerical approach to obtain an approximative solution. While its technically possible to solve the Navier-Stokes equations with a Direct Numerical Simulation (DNS), the computational effort for turbulent flows such as a jet is very high, and often not pragmatic. This is caused by the need to resolve the smallest turbulent scales in the flow, which requires a very refined computational grid (small cells) and small time steps. The way to overcome this problem is to filter the Navier-Stokes equations and divide the flow field in its low- (mean) and high-frequency (turbulent) values. This is the topic of Section 4.1.2 on RANS simulations.

4.1.2. The RANS Equations

The most common and pragmatic approach to model a turbulent flow is a RANS simulation which solves the Reynolds-averaged Navier-Stokes equations (or Favre-averaged in case of compressible flows). This gives a time-averaged (steady-state) representation of the fluid dynamics where the effects of turbulence (temporal fluctuations in the flow) are approximated through turbulence models. The RANS equations are obtained after inserting Eq. (4.15), the Reynolds decomposition (Reynolds, 1895), into Eq. (4.2). Favre formulated an alternative filtering step to account for the variable density and simplified the notation, as seen in Eq. (4.16). The final form of the RANS equations is then given by Eq. (4.17).

$$\mathbf{u}(x,y,z,t) = \overline{\mathbf{u}(x,y,z)} + \mathbf{u}'(x,y,z,t) \tag{4.15}$$

where $\overline{\mathbf{u}}$ denotes the expectation (steady-state) value of the velocity, and $\mathbf{u}'$ the turbulent fluctuations.

$$\widetilde{u_i} = \overline{u_i}\left(1 + \frac{\overline{\rho' u_i'}}{\overline{\rho u_i}}\right) \tag{4.16}$$

$$\frac{\partial\left(\bar{\rho}\tilde{\mathbf{u}}\right)}{\partial t} + \nabla\cdot\left(\rho\tilde{\mathbf{u}}\otimes\tilde{\mathbf{u}}\right) + \nabla\cdot\left(\overline{\rho\mathbf{u}''\otimes\mathbf{u}''}\right) = -\nabla P + \nabla\cdot\boldsymbol{\tau}_{\text{visc}} \tag{4.17}$$

where $\bar{\rho}$ is the Reynolds-averaged density, $\tilde{\mathbf{u}}$ is the Favre-averaged velocity vector. For the Favre-averaged versions of the continuity equation and the energy equation, please see Rumsey (2017).

The terms on the left of Eq. (4.17) are convection terms (field properties), while the ones on the right resemble diffusion processes (material properties). The specific terms that need additional modeling are the nonlinear Reynolds stresses (turbulent accelerations): $\nabla\cdot\left(\overline{\rho\mathbf{u}''\otimes\mathbf{u}''}\right)$. As mentioned earlier in Section 2.2.3, the observation that turbulence leads to exchange of momentum, has resulted in it being modeled as a linear diffusion process, comparable to the viscous stress tensor $\boldsymbol{\tau}_{\text{visc}}$ as shown by Eq. (4.18). This is called the Eddy Viscosity Model (EVM), which assumes the mechanics of turbulence are analogous to molecular stresses and thus the mean shear rate. This is an effective but inadequate representation of turbulence because it neglects its anisotropic nature (Franke et al., 2004).

$$\overline{\mathbf{u}''\otimes\mathbf{u}''} \cong 2\nu_t S_{ij} - \frac{2}{3}\delta_{ij}k_t \tag{4.18}$$

where the dynamic viscosity is replaced by a different proportionality factor, dubbed the 'eddy viscosity' ν_t ($\mathrm{m^2\,s^{-1}}$); S_{ij} ($\mathrm{s^{-1}}$) is the mean shear rate, δ_{ij} is the Kronecker delta, and k_t ($\mathrm{m^2\,s^{-2}}$) is the turbulent kinetic energy. It is important to stress that the eddy viscosity is a field property, it is determined empirically, and does not represent a material property even though it is modeled as such. Multiple expressions exist that try to quantify the eddy viscosity. A popular method, and the one used for this study, is the k-ϵ turbulence model (Jones & Launder, 1972), where two additional transport equations are solved to compute the turbulent kinetic energy k_t and dissipation rate of the turbulent kinetic energy ϵ_t. It is likely the most widely used model in engineering applications because of its low computational cost and good applicability to external flows, but it is known for its inaccuracy to predict the spreading

rate of round jets[1]. The value of the eddy viscosity then follows from Eq. (2.27), shown earlier as part of the discussion on turbulent diffusion.

4.1.3. CFD Simulation

This section describes the work that was carried out as part of another investigation (Tluk, 2023). Permission was given to use the outcome of that study for the purpose of this research. The computational domain has been constructed with the use of ANSYS Meshing. As a first step in the design and analysis of a jet engine wake, the mesh is shaped into cylinder, with a radius of 12 m and a length of 200 m. This reduces the complexity of the simulation since the axisymmetric assumption can be applied. Instead of solving the RANS equations in three dimensions, an axisymmetric simulation only requires solving the equations in two dimensions, which greatly simplifies the computation. Additionally, the axisymmetric geometry often results in fewer boundary conditions, and makes the simulation faster and more efficient[2]. The meshed domain comprises 35,000 cells in total, which are tailored by sizing the edges according to the number of divisions, and bias factor (the ratio of the largest edge to the smallest edge). This results in cell expansion towards the boundaries of the domain. The number of divisions in axial direction is 1000, and the radial direction has 25 divisions. The bias factor in both dimensions is equal to 10. The jet exit is modeled as an inflow condition at the left boundary of the domain. This is a (Gaussian) velocity profile ranging from y = 0 m (the core) up to y = 2.25 m, including the bypass, and the shear line which is 0.25 m wide. The maximum exit velocity is determined with GSP (see Section 3.2.3 on the research setup), and the turbulence intensity is set at 10 %. The exit temperature is equal to 570 K, and the exit pressure is equal to about 1.2 $\times P_{\text{amb}}$. The boundaries of the domain are modeled as free-stream inflow conditions, except for the core axis (y = 0) which is the axis of the symmetry, and the right boundary which has an outflow condition based on the static pressure.

The RANS simulation was conducted with the finite-volume solver ANSYS Fluent, and the standard k-ϵ turbulence model. The Semi-Implicit Method for Pressure-Linked Equations (SIMPLE) algorithm is used for pressure-velocity coupling in conjunction with Roe flux-difference splitting. The Least Squares Cell Based method is used for discretization of gradients, the Second Order Upwind scheme is used for discretization of momentum, and the First Order Upwind scheme for turbulent kinetic energy and turbulent dissipation rate.

4.2. Aerosol Microphysics Module

The microphysical model is an adaptation of the nucleation, condensation and coagulation subroutines of the Atmospheric and Environmental Research (AER) 2-D chemical transport model (Weisenstein et al., 2015) that were translated from Fortran to MATLAB as part of Golja et al. (2021)'s research on aerosol dynamics in the near field of the SCoPEx stratospheric balloon experiment. It makes use of a number of thermodynamical properties of a substance that are not calculated explicitly, but parameterized instead, and they might not always be valid for the conditions inside a jet engine plume (and for high H_2SO_4 saturation ratios). They are listed in full in Table 4.1, and mentioned throughout this section with the acronym PARAM.

4.2.1. Sectional Particle Bins

The sulfate aerosol size distribution is subdivided into 40 geometrically progressive bins based on particle radius, where the volume ratio between adjacent bins is equal to two. The particle radii range from 0.39 nm to 3.2 µm. The smallest bin should therefore be able to accommodate the smallest of liquid particles that originate from homogeneous nucleation, consisting of pure sulfuric acid, i.e. aerosol

[1] https://imechanica.org/files/fluent_13.0_lecture06-turbulence.pdf (Accessed on 16-01-2023)
[2] https://help.solidworks.com/2021/english/SolidWorks/cworks/c_2D_Simplification_Overview.htm (Accessed on 16-01-2023)

containing only 2 H_2SO_4 molecules and no water (see Section 2.4 on BKPF and the one-component limit). It is bound by a number of limitations. To start, the particle bins do not make a distinction between aerosol types (pure, mixed, charged etc.), which is a point of improvement for future studies on different aerosol modes. Because it is a sectional model, it also suffers from numerical diffusion during the condensation and coagulation stages, as discussed in Section 2.1.1. While a volume ratio of 1.5 would give better accuracy, this also increases the number of bins that need to be tracked, and consequently the computational load. Moreover, the code (and the coagulation stage in particular) would require modifications because particles would be able to skip particle bins as their volume increase surmounts the bin width. Both studies from Turco and Yu (1998) and Debra Weisenstein (personal communication, December 02, 2022) showed that a volume ratio of two is sufficient for modeling nanoscale particles, as they predominantly grow by coagulation, and the PSD is largely unaffected by even lower volume ratios. Although the size of (sub)microscopic particles can still differ by a factor two, since they grow through both condensation and coagulation. In addition, the PSD is based on the wet mass of the aerosol (particle radius), instead of dry mass (# of H_2SO_4 molecules/particle), so it is required to specify the weight composition (and resulting density) of each bin. The particle composition is calculated with PARAM (1) (Tabazadeh et al., 1997) based on the assumption that the equilibrium vapor pressure of water over the aerosol solution is equal to the water partial vapor pressure, thus setting the liquid phase water activity equal to the gas phase water activity. However, the model does not incorporate the Kelvin effect (see Eq. (2.13)), thus all bins have the same composition, while in reality, particles with radii less than $\sim$ 0.01 µm have different weight percentages. This would result in less particles in the lower sizes, but the impact should be minimal on integrated aerosol quantities, as very little mass resides in these small particles (D. K. Weisenstein, personal communication, November 17, 2022). Once the composition is known, the density of the sulfuric acid-water solution is calculated with PARAM (2), a fit from Vehkamäki et al. (2002). For standard lower stratospheric background conditions, i.e. 216 K and 48 hPa, the aerosol inside the particle bins would have a sulfuric acid mole fraction $x_{a,\text{bin}}$ of 0.3255 (thus 1/3 acid, 2/3 water), and a density ρ_{bin} of 1.7177 g/cm^3.

4.2.2. Nucleation

Originally, the nucleation routine was almost fully modeled through the parameterized equations from Vehkamäki et al. (2002), which is a thermodynamic model based on QC-normalized CNT. The strengths and limitations of this theory were discussed elaborately in Section 2.4. The nucleation routine only considers binary homogeneous nucleation of liquid aerosol, and is not able to simulate the formation of mixed aerosol (with a solid core) through heterogeneous nucleation, nor charged particle formation and electrostatic enhancement through ions. Besides, it is only valid at temperatures between 230.15 K and 305.15 K, relative humidities between 0.01% and 100%, and sulfuric acid concentrations from 10^4 to 10^{11} cm^{-3}. Its inability to work with high number densities of gaseous H_2SO_4, motivated Golja et al. (2021) to implement a new routine capable of identifying and simulating regions where barrierless kinetic particle formation could occur (see Section 2.4.2 on BKPF). The analytical relations are provided by the parameterization from Määttänen et al. (2017), building on the model from Merikanto et al. (2016). Based on more recently obtained experimental data from the CLOUD project in CERN, the parameterization from Määttänen presents itself as an overall update on Vehkamäki's parameters, and it was decided to fully implement the thermodynamic equations from Määttänen et al. (2017) for this study. Although they deviate slightly more from the theoretical nucleation rates compared to Vehkamäki et al. (2002) at low or high nucleation rates, it is still a significant improvement over their predecessor due to its larger validity range. They prescribe wider temperature and sulfuric acid concentration ranges, extend to very low relative humidities, and above all, include a new routine that allows for the prediction of ion-induced nucleation, which is an important aerosol growth factor in a jet engine wake. The fit for IIN is valid for temperatures between 195 and 400 K, sulfuric acid concentrations ranging from 10^4 to 10^{16}

molecules/cm^3, and relative humidities of 10^{-5} - 100 %. For neutral particle formation, however, the validity range of RH shrinks to 10^{-3} - 100 %, and the maximum verifiable H_2SO_4 vapor concentration is lowered to 10^{13} molecules/cm^3.

This brings us to the distribution of temperature and relative humidity throughout the plume domain. Whereas the assumption of constant pressure, temperature, and relative humidity, would suffice in the case of a propeller, such as the one described in Golja et al. (2021), this no longer works for a jet engine wake. It is the local temperature, relative humidity, and gas phase concentration of sulfuric acid that determine the weight composition of nucleating aerosol in the wake. Although the engine ejects highly concentrated volumes of water, the temperature at the engine exit is typically equal to about 600 K or more, initially leading to an extreme dry environment which delays nucleation in the plume core. This needs to be accounted for, in conjunction with a dilution mechanic prescribing the diffusion of mass and temperature in the plume as a function of time, discussed in Section 3.3.1. The relative humidity is determined as the ratio of the partial pressure of water vapor to the saturation vapor pressure of water at the same temperature. The saturation vapor pressure, or the equilibrium vapor pressure over a flat surface of (possibly supercooled) pure liquid water, is calculated with PARAM (3), a combination of two fits by Wexler (1971) and Murphy and Koop (2005). They replace an older fit by Preining et al. (1981). Once the plume conditions are determined, the composition of the freshly formed nucleus can then be used to calculate the corresponding nucleation rate (# particles/cm^3 s) and the radius of the critical cluster. This is done separately for every grid point, resulting in wide variety of clusters with different compositions and sizes, but this creates a conflict with the fixed aerosol weight composition of the particle bins. To resolve the issue, and conserve the number of H_2SO_4 molecules in the critical cluster, water is added or subtracted from the cluster until its composition matches the one from the bins. By setting the total mass of H_2SO_4 inside the critical cluster equal to the total mass of H_2SO_4 inside an aerosol bin particle, one is able to derive the corresponding radius of a particle with the fixed bin composition. The mass relation is shown in Eq. (4.19).

$$\begin{aligned} x_{a,\text{crit}} \cdot \rho_{\text{crit}} \cdot r_{\text{crit}}^3 &= x_{a,\text{bin}} \cdot \rho_{\text{bin}} \cdot r_{\text{scaled}}^3 \\ \leftrightarrow r_{\text{scaled}} &= r_{\text{crit}} \cdot \sqrt[3]{\frac{x_{a,\text{crit}} \cdot \rho_{\text{crit}}}{x_{a,\text{bin}} \cdot \rho_{\text{bin}}}} \end{aligned} \tag{4.19}$$

Note that the scaled radius is not the final size of the cluster, it is readjusted once more to fit the nearest bin size. Again, the number of H2SO4 molecules that transform from gas into liquid aerosol is conserved, by increasing/reducing the amount of aerosol particles that are formed. Should the particle nucleation rate exceed the total vapor density in a given spatial location, all vapor is forced to condense and the aerosol number is adjusted based on the available vapor.

4.2.3. Particle Growth

The subsequent growth or decline of stable particle clusters via condensation or evaporation is modeled with a one-dimensional equation (Eq. 2.59) from Hamill, Toon, et al. (1977), but the expressions for the mean free path of a gas molecule (Eq. 2.61) and the molecular diffusion coefficient (Eq. 2.60) were replaced by the ones from Jacobson (2005) for a trace-gas in a dilute mixture (see Eq. 16.17 and Eq. 16.22). This assumption only holds when $N_{H_2SO_4} \ll N_{\text{air}}$. The growth rate depends on the aerosol sulfur content and the equilibrium vapor pressure of sulfuric acid vapor over a flat surface (the level of supersaturation), with the inclusion of a curvature correction based on the Kelvin effect (see Eq. (2.13)). The saturation vapor pressure of sulfuric acid is determined with PARAM (4), a fit by Kulmala and Laaksonen (1990) and Noppel et al. (2002). The composition-dependent surface tension for a liquid solution is required to calculate the curvature correction and is provided by PARAM (5), a fit from Vehkamäki et al. (2002). The growth rate of particles within a particular bin k is expressed

as change in particle volume per second per unit surface area. By multiplying the growth rate with the surface area of a bin k particle, and dividing by its volume, the relative mass increase/reduction is obtained, expressed in number of particles per second. This value is multiplied with the bin population to get the total amount of condensed/evaporated mass. If the amount of mass is sufficient to grow into a particle of bin $k+1$ (which is twice the mass of bin k for a volume ratio of two), this mass is moved to the next bin together with a particle of bin k; and vice versa in the case of evaporation. Ideal conditions are assumed, where the accommodation coefficient b_a is equal to one.

The coagulation routine solves the discrete coagulation equation with an explicit scheme based on the approach by Yue and Deepak (1979) (see Section 2.6.1). At this stage, only Brownian coagulation is considered, but future work might include the effects of turbulence and electrostatic enhancement through ions. While the explicit scheme is volume-conserving, it suffers from instability for larger time steps, and iterative procedures are in place to prevent this. The scheme cannot work with volume ratios below two, which would require additional modification. Furthermore, it assumes all particles are spherical and two-body collisions only. Ideal conditions are assumed once again, so all collisions results in coalescence ($b_s = 1$), and particle breakup is not possible.

4.2.4. Thermodynamic Parameterizations

A list of thermodynamic parameters and their parameterizations for a system containing sulfuric acid and water is presented in Table 4.1. For a reference list on the various experiments mentioned in this table, please consult Merikanto et al. (2016).

Table 4.1: Thermodynamical data for the sulfuric acid-water system. Adapted from Merikanto et al. (2016).

n°	Parameter	Experiments	Fit	T Range
(1)	x_a		Tabazadeh et al. (1997)	185 - 260 K
(2)	$P_w(T)$		Wexler (1971)	273 - 373 K
			Murphy and Koop (2005)	< 273 K
(3)	$P_a(T)$	Ayers et al. (1980)		338 - 445 K
			Kulmala and Laaksonen (1990)	153.15 - 363.15 K
			Noppel et al. (2002)	
(4)	$\sigma(x_a, T)$	Sabinina and Terpugow (1935)	Vehkamäki et al. (2002)	233 - 323 K
		Morgan and Davies (1916)		
		Suggitt et al. (1949)		
		Hoffmann and Seeman (1960)		
		Myhre et al. (1998)		
(5)	$\rho(x_a, T)$	National Research Council (1928)	Vehkamäki et al. (2002)	273 - 373 K
		Myhre et al. (1998)		220 - 300 K

* Part of the data have been extrapolated below their temperature ranges, as mentioned also in Vehkamäki et al. (2002)

4.3. Advection-Diffusion Module

The motion of trace gasses and particulate matter in the plume relies on the processes of advection and diffusion, which are determined based on the steady-state velocity and turbulent viscosity fields from the RANS simulation. Section 4.3.1 shows the advection-diffusion equation and discusses the numerical schemes that are used to solve it. Section 4.3.2 explains the dimensions of the microphysical grid and what initial condition were used.

4.3.1. Numerical Scheme

The dispersion of aerosol, vapor, and ions within the plume is governed by Eq. (4.20), which models the concentration of a substance N as a function of time while under the influence of advective and diffusive processes. This is a second-order hyperbolic partial differential equation that needs to be solved numerically (Stocker, 2011).

$$\frac{\partial N}{\partial t} = -\nabla \cdot (\mathbf{u}N) + \nabla \cdot (D \nabla N) + I \tag{4.20}$$

where D ($\mathrm{cm^2\,s^{-1}}$) is the effective diffusion coefficient and I ($\mathrm{cm^{-3}\,s^{-1}}$) stands for sources or sinks of aerosol such as nucleation processes, the scavenging of fresh aerosol by large background particles, or the injection of condensable vapor in the wake.

The diffusion coefficient only includes the effects of jet-induced turbulence for now, as it is by far the dominant diffusion process in the jet regime (with D_T exceeding 10 $\mathrm{m^2\,s^{-1}}$ after 0.1 s, compared to $\sim$ 1 $\mathrm{cm^2\,s^{-1}}$ for molecular or Brownian diffusion. In later stages of the plume, aircraft-induced turbulence should be accounted for (vortex and dissipation regime), and molecular/Brownian diffusion as well as atmospheric turbulence and sedimentation (diffusion regime). For more information on plume morphology, please consult Section 2.7.1. Unless otherwise specified, the ANSYS standard Schmidt number of 0.7 is used to relate turbulent viscosity to turbulent diffusion through Eq. (2.27), which is in line with Forstall Jr. and Shapiro (1950).

To evaluate Eq. (4.20), we copy the approach from Golja et al. (2021) and solve for convection and diffusion separately, using operator splitting. The advection term is solved with a high-resolution Lax-Wendroff method, which is a second-order accurate central-differencing scheme, with the inclusion of a Superbee flux limiter. The use of a second-order scheme prevents excessive numerical diffusion of sharp particle size distributions which easily span multiple orders of magnitude. The Superbee flux limiter is included to prevent oscillations in areas with strong velocity gradients, while also preventing numerical dispersion in areas with strong discontinuities in the aerosol/vapor concentrations such as the injection location or nucleation region. The diffusion term is solved with a second-order finite difference scheme from Hyman et al. (1997). Note that the quantity of interest in Eq. (4.20) is the number density, but the number density is converted to mass in the numerical schemes.

4.3.2. Microphysical Grid and Initial Condition

The microphysical grid is the domain that is used to perform all microphysical calculations, and model the dilution mechanics of the plume constituents. It differs from the flow solver domain, as it is significantly more coarse to keep the computational load manageable. The size of the domain, measured from the engine exit, is equal to -1 to 199 m in X-direction (axial), and - 7 to 7 m in both Y- and Z-direction, with a resolution of 1 m. The required wall time to simulate 1 second of aerosol formation and advection is just above 48 hours. Velocities and diffusion coefficients are interpolated onto the nodes as detailed in Section 4.1.3. Given the maximum axial velocity of 450 m/s, and a constant time step of 1e-5, the maximum Courant-Friedrichs-Lewy (CFL) number in the domain becomes:

$$CFL = u_x \frac{\Delta t}{\Delta x} = 450 \frac{10^{-5}}{1} = 0.0045 \tag{4.21}$$

where Δt is the time step size, Δx is the spatial scale of the domain.

This is substantially smaller than what is required to ensure convergence, but the numerical stability of the advection-diffusion scheme is not what limits the time step. The coagulation routine becomes unstable for larger time steps, and in the future, it might be beneficial to replace the explicit coagulation scheme by a semi-implicit scheme such as the one from Jacobson (2011). In addition, the microphysical domain and its initial condition could greatly benefit from an increased resolution in Y- and Z-direction, to

increase the fidelity of injection scenarios in the future. To better understand how the injection scenario is represented by the initial condition of the microphysical grid, consider the 2D representation of the microphysical domain in Fig. 4.1.

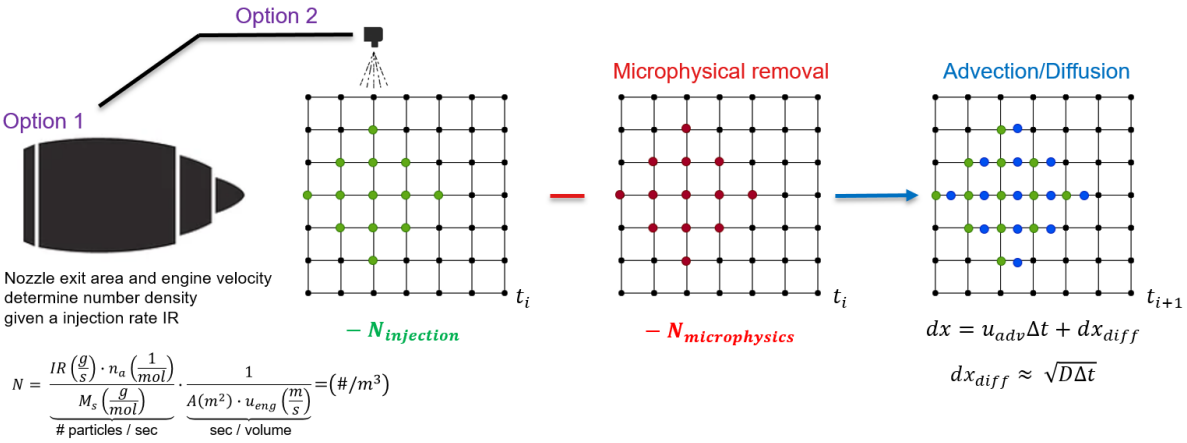

Figure 4.1: Illustration of the initial condition and injection scenarios.

The injection of condensable vapor into the jet engine wake can either be done externally through means of a boom, or internally (either in the hot engine core or cold by-pass area). Both methods will probably have to use a nozzle to spray the vapor from a heated reservoir into the jet stream. The objective is to determine the required mass rate to maintain a constant concentration of condensable vapor at the injection location, and fix the aerosol growth processes, resulting in steady-state particle distribution at later stages in the plume. Yet, this proofs to be challenging given two reasons: (1) The microphysical routines in the model require the specification of a number density (or concentration) on each node. Therefore, it is not sufficient to solely prescribe a mass rate (# molecules/s) and time step, but one has to define an associated volume to set the number density. In the numerical grid, this volume is fixed, and defined by the spatial resolution. While in reality, the associated volume depends on the flow velocity and cross-sectional area of the engine exit. Thus, there is a mismatch between grid cell volume and injection volume per time step. Unless the spatial resolution is sufficiently small (injected volume per time step = grid cell volume), this will lead to dilution of the number densities at individual nodes if mass is to be conserved. As a result, the microphysics will behave differently as the perceived concentration levels are lower than in reality. (2) If the injection pattern of a nozzle is to be replicated, a 3D Gaussian distribution would be a likely candidate, and the initial mass distribution would have a diamond pattern (2D) such as the green nodes in Fig. 4.1 with a higher number density at the center. If the mass distribution of condensable vapor is to be replenished by the next time step, the substance removal rate must be determined based on the amount that is consumed by microphysical processes (which is highly location-specific), and the amount of vapor that is transported by advection and diffusion per time step. However, if the spatial resolution is too crude, the injected mass will not have exited the area of injection by the next time step leading to difficult accounting of what additional mass is required at each node to maintain a constant number density. The result is that a simple arithmetic operation of vapor addition per time step would significantly alter the initial condition over time as there is a build up of concentrations. In addition, a smooth 3D Gaussian distribution is difficult to achieve if the numerical grid only has 9 nodes to represent the entire exit area of the engine core (such as is the case for our grid), leading to errors in the advection routine.

All the aforementioned limitations eventually boil down to the same problem, which is the resolution of the numerical grid. Trying to predict the required injection rate to maintain a constant concentration at the initial condition is essentially meaningless for large spatial steps given the large errors in the

resulting microphysics. This is why the author will not make an attempt to calculate the injection rate. Instead, the microphysical evolution of aerosol is to be conserved for the entirety of the simulation by prescribing a constant number density distribution at the injection location. A possible solution in the future might be to expand upon the domain and subdivide it into multiple grids, following the example from Golja et al. (2021). This way, the starting grid can be refined to better represent injection conditions, while additional grids with a coarser resolution extend the domain to simulate longer plumes ages. An example of what that would look like is given by Fig. 4.2 (courtesy of Dr. Colleen Golja). The velocity and diffusivity fields for the larger grids don't necessarily have to be computed with a 3D numerical flow solver, as the 3D microphysical grid can be replaced with a simpler 2D model such as a multi-layered plume (Fritz, 2018; Fritz et al., 2020).

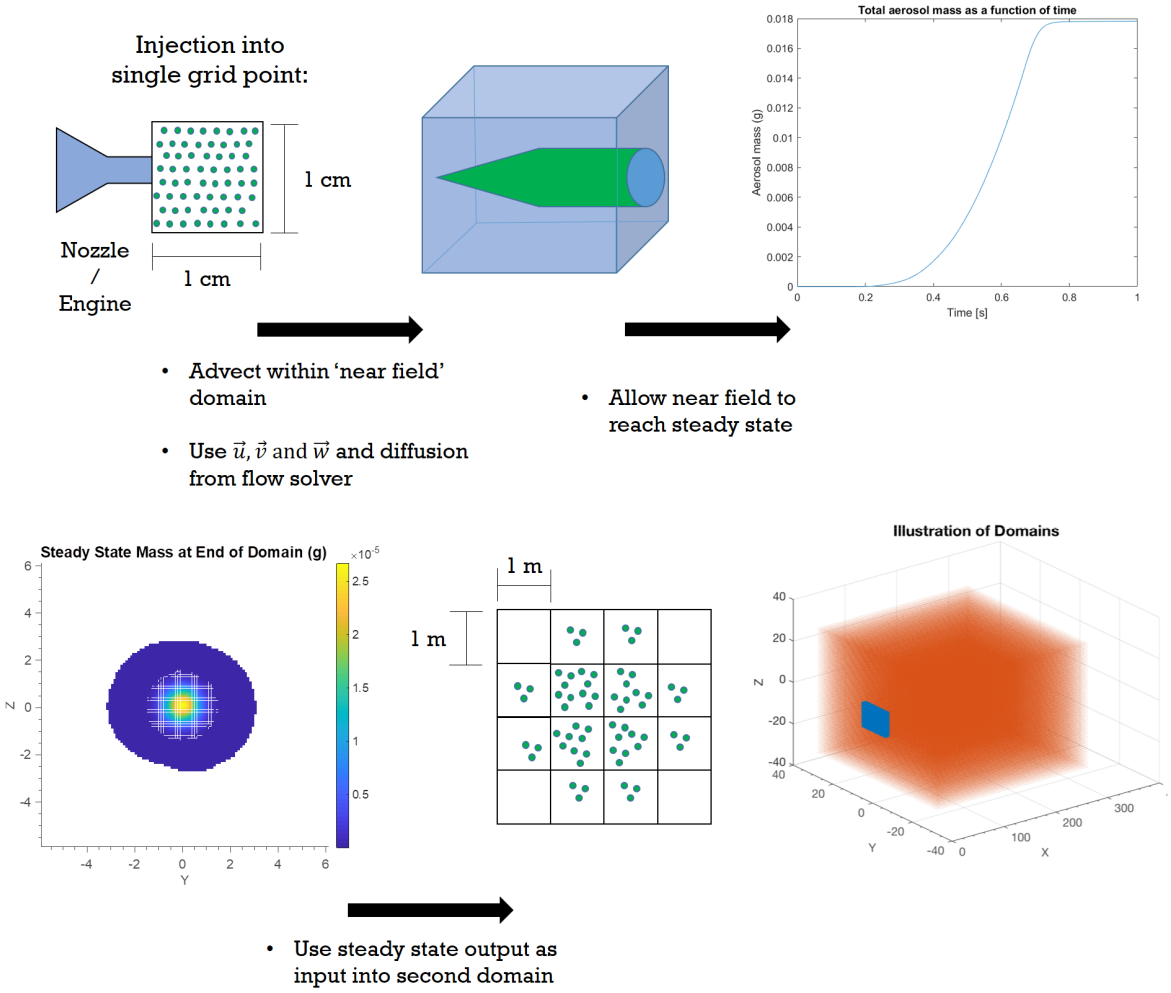

Figure 4.2: The practice of multi-domain simulations (Reproduced and adapted by permission of Dr. Colleen Golja).

4.4. Assumptions and Limitations

The models that simulate the aerosol microphysics and flow physics are based on some substantial assumptions that might lead to a limited representation of reality in certain cases. All of them have been discussed as part of the literature review in Chapter 2 and throughout this chapter on the plume model. This would like to repeat/highlight those that are most impactful or problematic, such that they are not overlooked and might possibly become the topic of investigation in the future. Assumptions are grouped according to their applicable field.

Particle size distribution - Section 2.1.1
When a particle size distribution is discretized into bins, there is unavoidably a loss of detail in the population. The discretization can be done according to aerosol volume (wet mass) or number of H_2SO_4 molecules/monomers per particle (dry mass). In both cases, care should be taken that mass or concentration is conserved during growth as numerical diffusion sets in. This leads to artificial abundances of particles in the lower and higher size categories. This was investigated by Jacobson and Turco (1995) who proposed the concept of flexible bin sizes to accommodate for this discrepancy. While its theoretically possible to reduce the numerical error by reducing the bin range (step size), this ultimately results in an insurmountable computational cost.

Aerosol thermodynamic parameters - Section 2.1.2
All models that incorporate aerosol physics inevitably need to incorporate some thermodynamic properties of the substance that makes up the aerosol based on its molar composition. This is usually obtained from parameterizations that are based on laboratory experiments, but this has its limitations. This is usually done in steady-state conditions where flow dynamics have settled down, while the plume environment shortly after emission is highly dynamic. Secondly, almost all parameterizations for H_2SO_4 are not valid for the high temperature levels that arise early in the plume nor the local relative humidity which can be extremely dry. Lastly, the parameterization from Tabazadeh et al. (1997) to calculate the molar fraction of H_2SO_4 in the aerosol, but this model explicitly assumes the aerosol is in equilibrium with the surrounding water vapor. This is only true if the water vapor is present in relatively large concentrations compared to gaseous H_2SO_4 which is questionable in the case of elevated conditions for SAI. A more accurate approach is to compute the weight composition using the Gibbs-Duhem relation from Eq. (2.10).

Turbulent diffusion - Section 2.2.3
The approach to model turbulent mass diffusion through a quantity called the eddy viscosity is not based on a solid physical basis. In addition, it explicitly assumes the turbulence in the wake is isotropic, which is doubtful. The fact that the turbulent Schmidt number needs to retrieved from experimental data while the nature of turbulence is very case specific, does not add to its reliability.

Chemiions - Section 2.3.2
The largest uncertainty or limitation related to chemiions in the engine wake is that not much is known about their size and the amount of charge they carry. At the time of writing, experimental investigations are ongoing at the French Aerospace Lab ONERA to gain more insight about the population at the engine exit (I.K. Ortega, personal communication, July 26, 2022). The model for ion-induced nucleation from Määttänen et al. (2017) is only valid for ions that are smaller than the critical embryo itself, because they assume the ion does not influence the energetics of nucleation. This means the ion should be molecular-size and it is not certain what percentage of chemiions actually meets this criterion. There are also some problematic assumptions in the modeling of ions as part of CNT, but this is discussed below.

Classical Nucleation Theory - Section 2.4.1
CNT remains an approximative theory and it has a range of shortcomings which were discussed extensively as part of a discussion on its limitations in Section 2.4.1. Please read that part for the full explanation. To start, it assumes thermodynamic equilibrium, particles are either stable or not and there is no unstable growth phase before the critical radius is obtained. Yu (2006b) believes the formation process should be modeled as a kinetic process of coagulation that includes an unstable size range. Evaporation of non-mature embryos during nucleation is the mechanism that is the least understood by scientists. Secondly, it applies the capillarity approximation which is the premise that the surface

tension of nano-size critical clusters is equal to that of a flat interface which is shown to be false. Yet, Merikanto et al. (2007) believes this is correctable. Moreover, the parameterization by Määttänen et al. (2017) makes use of hydrate theory to estimate its chemical activity coefficients, but here it is assumed that the concentration of water vapor is a few orders bigger than sulfuric acid vapor which is not the case for SAI concentration levels. In the presence of ions, it applies the Kelvin-Thomson equation to estimate the electrostatic influence, but it has been shown to perform poorly on nanoscale clusters due to enhanced dipole interaction (Yu, 2005). Lastly, the linear dependence of the ion-induced nucleation rate on ion concentration is questionable, because elevated concentrations will eventually result in a higher ion-ion recombination rate which eventually offsets the electrostatic enhancement effect (Yu, 2006b).

Condensation/Evaporation - Section 2.5

The model for condensation and evaporation is based on an one-dimensional growth equation where it is assumed that the molar fraction of H_2SO_4 remains constant in the particle. This is acceptable as long as the growth equation is evaluated for small time steps to limit the error. A second problem is the assumption that the aerosol is in equilibrium with the water vapor and the growth depends on the impingement rate of H_2SO_4 molecules which is possibly not the case for SAI conditions. As a consequence, Eq. (2.59) might need to be reformulated. Likewise, this formula needs adaptation if RH exceeds 100%. Several other influential factors are neglected as well such as the effect of dissolved impurities (core material) on the vapor pressures, the influence of latent heat released by vapor condensation on the temperature of the droplet (thermal diffusion), and the attachment of H_2O clusters to H_2SO_4 molecules through the diffusion of water.

Coagulation - Section 2.6

The main assumptions related to coagulation are that the particles are all spherical and only two-body collisions occur. In addition, the possibility of particle breakup is not considered. A point of interest is the probability that a collision of two ultrafine particles results in coalescence. While Jacobson (2011) argues the coalescence efficiency is close to unity, Yu and Turco (1998) believe the sticking probability is significantly lower for ultrafine particles. The nature of the particle (liquid or mixed) can also play a role, but is ignored at this stage.

Plume Dynamics - Section 2.7.1

This research chooses to focus on the early jet regime, so the interaction with wingtip vortices and all subsequent stages of the plume are ignored. The flow field is resolved by means of RANS simulation which provides a an averaged depiction of the flow field, but very little information about turbulent entrainment of ambient air. Ideally, the flow field is studied by means of an LES which would allow for a detailled study of turbulent transport of aerosol parcels throughout the plume and provide accurate estimates of the local temperature and relative humidity which influences aerosol growth significantly. The possibility of ice formation and the creation of contrails is ignored based on the discussion in Section 3.1.

5

Results

What follows are the results of the simulations and analyses conducted on the formation of aqueous sulfate aerosol from gaseous sulfuric acid and water in the early jet-regime of an aircraft engine wake. This research was performed as part of a study on stratospheric aerosol injection through the distribution of condensable vapor from aircraft. The purpose of this study was to elucidate the intricacies of the aerosol formation process in the early stages of the wake by increasing the resolution of the domain. To this end, a decoupled approach was followed where the flow field is resolved through an axisymmetric RANS simulation of an aircraft engine wake, and particle thermodynamics/mechanics are solved independently on a separate microphysical grid. The inclusion of a plume dilution mechanic for water vapor, and temperature, allowed for the creation of a realistic distribution of temperature and relative humidity throughout the wake. This approach provides new insights in the processes that steer aerosol growth on a 'local' scale, and the limitations of classical thermodynamic approaches to modeling high-density aerosol formation. The results are organized into four sections, starting with Section 5.1 on the output of the RANS simulation, which was constructed as part of another study (Tluk, 2023), and remained unaltered throughout this entire study. Section 5.2 presents the verification results of the model where we replicate the sulfate aerosol population that forms after emission of standard H_2SO_4 concentrations by a civil transport aircraft under cruise conditions. Subsequently, the sensitivity of the microphysical processes to variations in local temperature and relative humidity is presented in Section 5.3. Lastly, Section 5.4 examines the effects of increased injection concentrations of H_2SO_4 vapor on aerosol growth as part of a larger effort to simulate a realistic SAI scenario.

5.1. Velocity and Turbulent Viscosity Fields

The computational domain, flow solver settings, and boundary conditions that resulted in the resolved flow fields below, are described in Section 4.1.3. The primary variables of interest are the local axial flow speeds, shown in Fig. 5.1, and the local 'kinematic' eddy viscosity (or rate of turbulent momentum-diffusivity), shown in Fig. 5.2. Note that the grids below are interpolated/coarsened to fit the microphysical domain of $7\times201\times7$ cells. Be aware that the heat map representation of the flow fields colors the cells, but the velocities are stored at the cell vertices instead of the cell center.

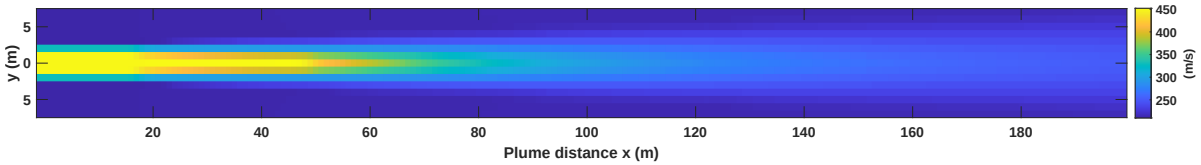

Figure 5.1: A 2D slice of the 3D domain describing the axial velocity component in the wake of a round jet based on an axisymmetric RANS simulation, section cut at $z = 0$ m.

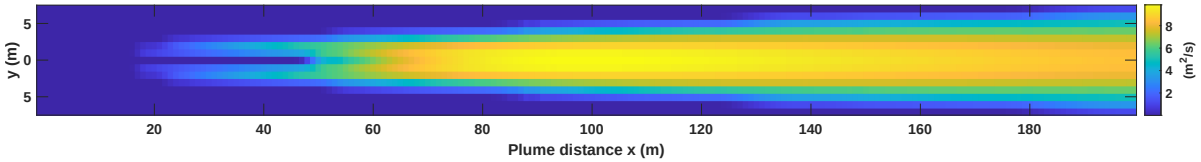

Figure 5.2: A 2D slice of the 3D domain describing the kinematic turbulent viscosity in the wake of a round jet based on an axisymmetric RANS simulation, section cut at $z = 0$ m.

The engine is positioned at the left of the domain and the flow moves from left to right. The engine exit diameter, including the bypass, is equal to 3.5 m, which amounts to an initial plume cross-section of 9.6 m^2. The exit area is visible on the left of Fig. 5.1 as the area of constant velocity at the start which spans 5 nodes or 4 m in width and lasts for approximately 17 m. The inner 3 nodes represent the core exit velocity, while the outer 2 nodes resemble the shear line and the mixing region of the core with the bypass, and the ambient air. The average initial velocity in the core is equal to 450 m/s, while the average velocity in the vicinity of the shear line is equal to about 330 m/s. After roughly 20 m, the wake starts to grow due to mixing with the ambient air as the result of turbulence in the shear line, as indicated by the fork-like shape in Fig. 5.2 (more like a diamond-shape with higher resolution). While the turbulent diffusion of momentum is initially confined to the shear line, the mixing processes eventually reach the wake's core after 50 m, which is also the start of the decline in velocity along the plume axis in Fig. 5.1. The kinematic eddy viscosity reaches its maximum intensity of nearly 10 m^2/s in the wake's core after about 100 m, and stays above 1 m^2/s in the plume interior until the end of the domain.

5.2. Verification Case for Standard Cruise Emissions

To verify the microphysical model's credibility and quality of output, the model is compared to the microphysical study of Yu and Turco (1998), using standard emission indices of a civil transport aircraft flying at cruise conditions in the lower stratosphere. Although they consider supersonic flight, and this study deals with subsonic conditions, this is considered acceptable for lack of a better test case in the near-field with similar microphysical detail. It is assumed that the biggest discrepancy lies in the diffusion rates following emission, even though Kärcher (1995) does not report large differences in entrainment rates. The full discussion on methods of verification and validation can be found in Section 3.2.2. The microphysical model was initialized under the conditions listed in Table 3.1 for the stratospheric case study, with the initial acid vapor number density depending on the fuel sulfur conversion fraction f_{HS}. We consider three conversion fractions ($f_{HS} = 10 - 30 - 100\%$) based on the approach from Yu and Turco (1998), and explained in Section 2.3.1, which gives initial concentrations of roughly 1e11 - 3e11 - 1e12 molecules/cm^3. However, the level of similarity with Yu and Turco (1998) is probably low as it was not possible to extract the exact initialization conditions that were used for the fuel sulfur content and flow rates. In addition, the choice was made to replace the RANS temperature and RH fields by replicating the dilution approach of Kärcher (1995) as described in Section 3.3.1. The location of injection is 5 m behind the engine exit, to fully insert the Gaussian distribution.

The results of the verification process are discussed below, starting with the aerosol size distributions in Fig. 5.3 - 5.5, which are logarithmically distributed. Because most microphysical models adopt a Lagrangian framework to track the aerosol evolution inside a plume, the age or maturity of an aerosol population is usually expressed by using the plume age, but this is a rather arbitrary when working in a Eulerian framework, were the often-used metric is the plume distance. Matching the age of different PSDs is therefore difficult, but the populations below are all assumed to appear between 0.5 - 1.5 s of plume age, or 200 - 300 m of plume distance. A word of caution, the particle size distribution of Kärcher (1998) is all-inclusive picture of the aerosol population (including soot, ions, and ice). It should not be used to evaluate the model's capacity to predict the characteristics of the sulfate aerosol population inside a jet engine plume, as the current state of the model does not incorporate electrostatic enhancement nor heterogeneous nucleation. Yet, it provides valuable insights on ion- or soot-assisted particle formation. The PSDs of Yu and Turco (1998) are based on thermodynamical model which only includes soot (not included here) and neutral particles, and therefore better suited to evaluate the trustworthiness of the simulation. To facilitate the comparison, a close-up of the neutral pure volatile particle size distribution is included in Fig. 5.4 for different sulfur conversion fractions and corresponding predictions by Yu and Turco.

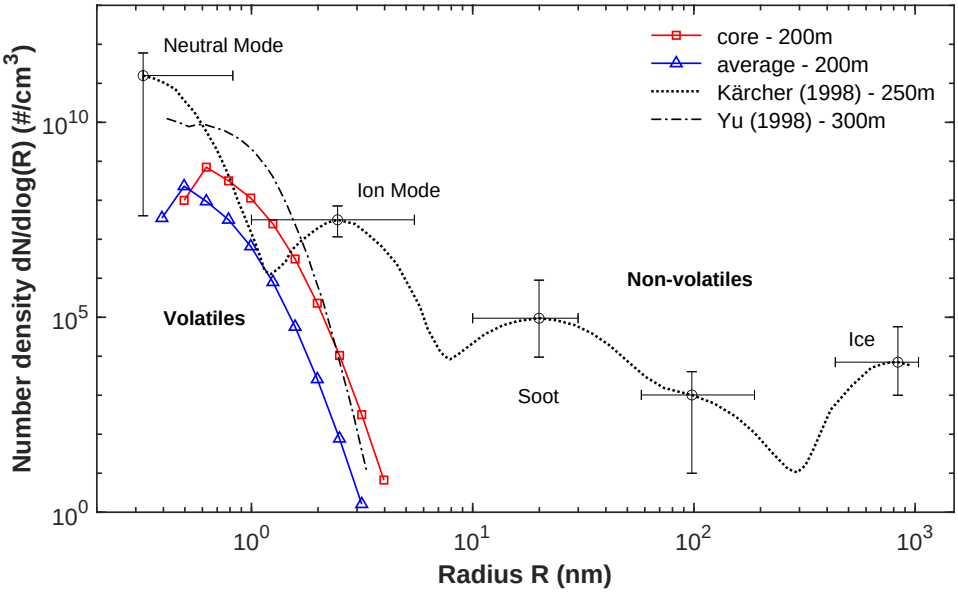

Figure 5.3: (a) Approximate number densities versus radius of volatile and non-volatile aerosol particles in the early jet regime between 200 to 300 m of plume distance. Model output for a conversion fraction f_{HS} of 30 %.

Figure 5.3 shows that the model predicts large abundances of the smallest of particles, followed by a swift decline in number densities with increasing size. This is stereotypical of a population which recently experienced a nucleation event, and in line with the predicted trend of the box models. Furthermore, the lower bound of the particle radii matches the other models almost perfectly, and the associated number densities fall within the uncertainty range of Kärcher (1998) related to engine specifics, the fuel sulfur content, and ambient conditions. Yet, both the distributions in the core and the plume average fall short of the predictions of Yu and Turco (1998) for the smaller particle sizes by one to two orders of magnitude. This is clearly visible in Fig. 5.4, which illustrates the effect of varying the initial vapor concentration at the engine exit. Increasing abundances of condensing vapor clearly lead to accelerated growth. If the density is increased by a factor ten, the radii of the largest particles are more than tripled, leading to ten times more mass per particle. The model follows the increasing trend of Yu and Turco (1998) nicely, even predicting flattening of the curve towards larger injection concentrations.

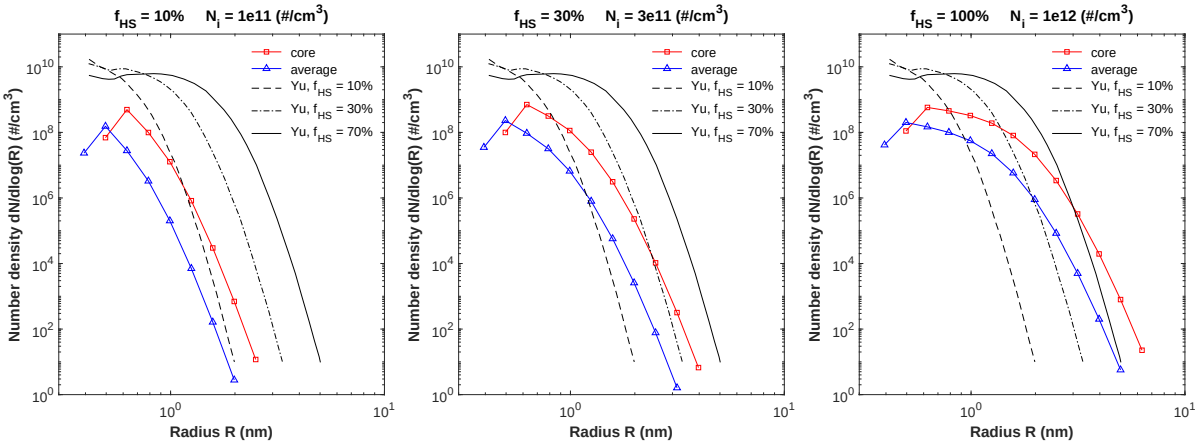

Figure 5.4: Approximate number densities versus radius of neutral pure volatile aerosol particles for different fuel conversion fractions f_{HS} at 200 m of plume distance.

For the remainder of the verification study, we use the results from the simulation with a conversion fraction of 30%. To investigate if the discrepancy in particle count is the result of variations in the onset of particle formation and growth throughout the plume, it is insightful to look at the particle size distribution earlier on in the plume. Figure 5.5 illustrates the evolution of PSD at different distances along the plume axis.

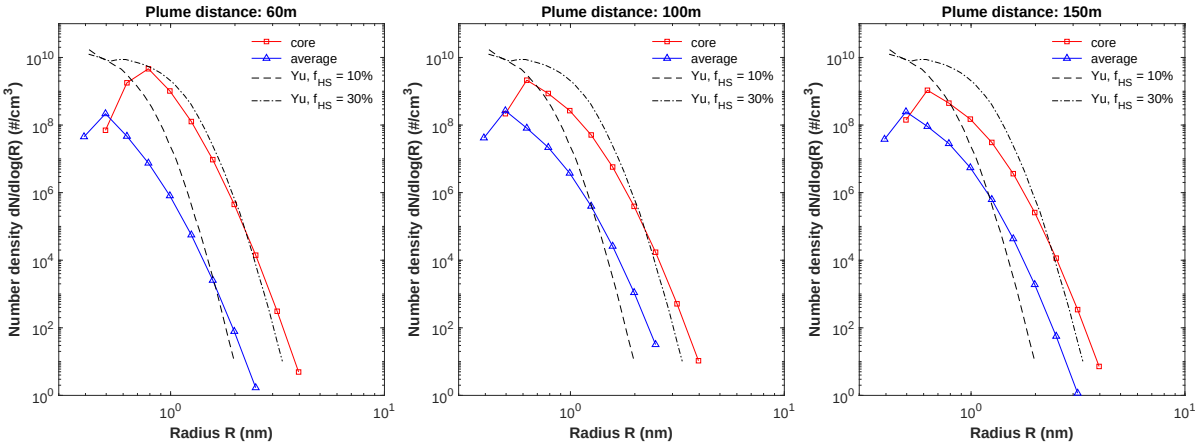

Figure 5.5: Evolution of the volatile particle size distribution as a function of plume distance (or age) for a conversion fraction f_{HS} of 30 %.

With decreasing distance from the engine exit, the particle counts in the core increase significantly, matching the prediction from Yu and Turco (1998) remarkably well. However, the predicted number densities of the smallest clusters below a radius of 0.79 nm lie even lower at 60 m. Snapshots at later instances show a gradual increase in number densities of the smallest clusters, and a decrease in the amount of bigger particles. This behavior eventually stabilizes to a point where the PSD at 150 m looks almost indistinguishable from the one at 200 m, imploring that the plume has reached a more homogeneous distribution, or the microphysical processes have reached a more stable state.

Figure 5.6a describes the variations in gas-to-particle conversation rates due to nucleation and due to condensation versus plume distance at 2 radial locations in the plume, the core and at distance of 4m from the center. Figure 5.6b presents the associated radii of the critical clusters that form under nucleation in the plume's core. Notice that there are three curves that describe three different radii. This is related to the discussion in Section 4.2.2 on the need to match the composition of freshly nucleated clusters with the fixed particle bin composition.

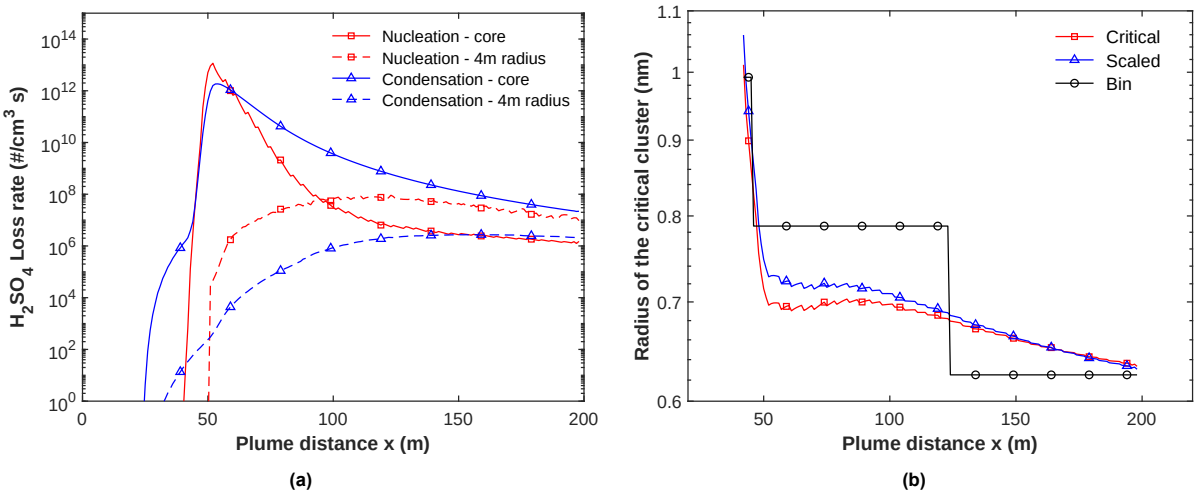

Figure 5.6: (a) Loss rate of H_2SO_4 vapor molecules due to nucleation and condensation at two radial locations. (b) Radii of the critical and scaled cluster resulting from nucleation in the plume's core, and the radius of the assigned bin.

Figure 5.6a confirms that there is a significant difference in the microphysical rates in the core (where almost the entire population resides) at the start and the end of the plume domain. There is a strong surge in both nucleation and condensation rates at 45 m from the engine exit with loss rates exceeding 1e12 molecules/cm^3 s. The peak in the nucleation rate dampens quickly, in contrast to the condensation rate which remains relatively high for most of the simulated plume distance. After roughly 150 m, or 0.3 - 0.5 s, the loss rate of vapor to nucleation starts to stabilize. Interestingly enough, condensation also commences earlier than nucleation in the plume's core, indicating that there is already particulate matter present at that stage. The onset of nucleation happens roughly at the time that the peak temperature in the plume has decreased to about 300 K (see Fig. 3.9a), which is comforting given the fact that all parameterizations from Table 4.1 are within their validity range. Lastly, it is noticeable that the microphysics further away from the core do not show such extreme behavior. While nucleation still occurs almost instantaneously, the overshoot is absent and the rates are relatively stable.

Looking at Fig. 5.6b, we see that the radii of critical clusters (red) vary along the plume, but this continuous distribution is lost when they are sampled, and assigned to a particular bin size (black). More importantly, the scaled radius of the particle with the weight composition of the bins (blue) does not differ much from its original radius, which is good news because this ensures that there is no mismatch during the assignment of a cluster to a bin (Figure B.1 in the appendix shows the percentage of mass that is added or subtracted from the nucleus for the entire plume, not exceeding 20% at any point). The majority of the particles that form in the core are assigned to either particle bin 3 or 4, with radii of 0.63 nm and 0.79 nm, respectively. Yet, in the first few meters, slightly larger particles are created with radii of 0.99 nm (bin 5). This explains why the PSD at 50 m plume distance in Fig. 5.5 shows the highest number densities for the population of 0.79 nm particles, but this also means that particles with radii below 0.63 nm are formed elsewhere in the plume. This notion is further strengthened by the area-averaged PSD in Fig. 5.5, which is shifted to the left. To understand the growth process of the freshly nucleated particles, the individual contributions of condensation and coagulation are plotted next to the nucleation rate in Fig. 5.7. The rates are expressed in the amount of new aerosol particles/(cm^3 s) that are added to a particular bin, in this case bin 6 because it is the first bin size that solely gains new particles through condensation and coagulation.

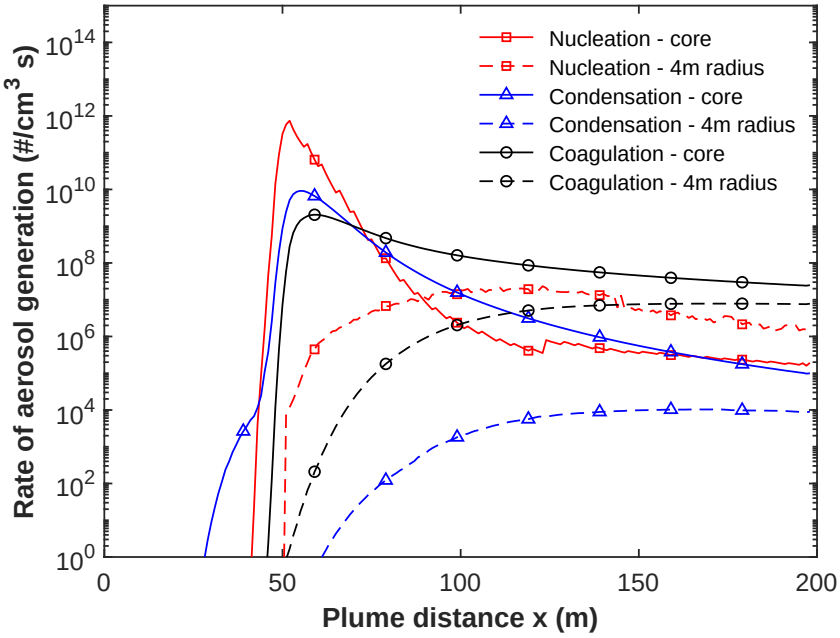

Figure 5.7: Rates of binary homogeneous nucleation, homogeneous condensation, and Brownian self-coagulation versus plume distance at two radial locations. The condensation and coagulation rates are for particles with radii of 1.3 nm (bin 6), while the initial radii of the nucleated particles vary depending on the location.

What is striking, are the almost identical surges in condensation and coagulation even though their maxima lie below the nucleation peak. As a result, a large part of the newly formed aerosol outgrows their cradle bin almost instantaneously, pushing the PSD to larger radii early on in the plume's lifetime as witnessed in Fig. 5.5. In addition, it is apparent that the nucleation rate and condensation rate rapidly decrease in magnitude, while the coagulation rate shows a relatively slow decline. The coagulation and condensation rates in the core, and at at radius of 4 m, can also been to converge towards the end of the plume. This is characteristic of an increasingly mixed wake, and implies more homogeneous ambient conditions across the plume. The trends that stand out in Fig. 5.7 are further substantiated by Fig. 5.8a, which depicts the evolution of the number density of sulfuric acid vapor, and total number density of aerosol along the plume axis.

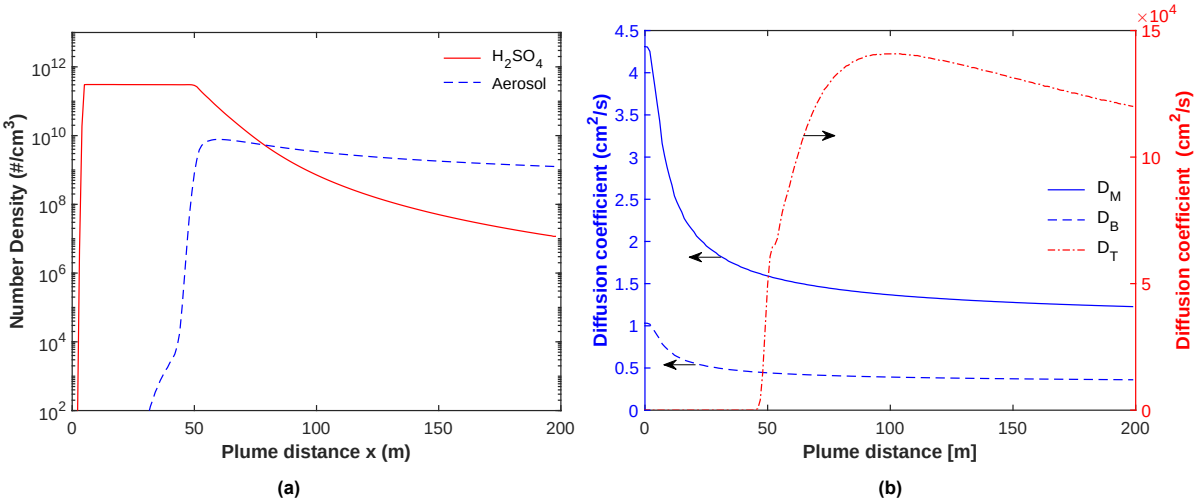

Figure 5.8: (a) Concentration of sulfuric acid vapor and aerosol in the plume's core versus plume distance. (b) Magnitudes of several diffusion coefficients versus plume distance.

The H_2SO_4 vapor concentration remains roughly constant until the onset of heavy nucleation at 45 m, and starts to drop continuously thereafter as gas is converted to liquid particles through nucleation and

prolonged condensation, and vapor is transported out of the core towards the edges of the plume as the result of turbulent mixing. By the end of the domain, a number density 1e7 molecules/cm^3 rests in the core. The concentration of aerosol, on the other hand, experiences a strong rise in numbers between 45 to 50 m where the sulfuric acid vapor is heavily supersaturated. The number densities remain fairly high and only experience a small decline towards the end of the plume even though coagulation rates are high. This is because of two reasons; self-coagulation feeds the new generation of particles in the next bin because two particles combine to form one particle of a larger size; and as will become clear, the population in the core is continuously replenished by aerosol forming at the outer edges of the wake.

The lack of dilution in the first 50 m of the plume is explained by looking at Fig. 5.8b, which shows the intensity of various processes that contribute to the diffusion of a chemical species. On the left are the molecular and Brownian diffusion coefficient in blue, while the turbulent diffusion coefficient is shown in red. The value of the molecular diffusion coefficient ranges between 1 to 5 cm^2/s along the plume axis, while the Brownian diffusion coefficient for a particle of radius 0.79 nm is roughly equal to 0.5 cm^2/s for most of the domain. However, these contributions pale in comparison to the impact turbulence has on the diffusion of chemical species in the plume. As mentioned in Section 5.1, the turbulent mixing process only manages to reach the core of the plume after roughly 50 m and that's when you notice a strong rise in the turbulent diffusion coefficient along the plume axis, with magnitudes above 10 m^2/s. This is four to five orders of magnitude larger than the other diffusion mechanisms, and therefore solely considered in the advection-diffusion equation (see Section 4.3.1). As a result, no diffusion is present in the core of the plume until after 45 m.

Up until now, we have solely looked at one-dimensional locations in axial direction, either the plume's core or at a fixed distance from the core. Yet, two-dimensional views of the flow field are of interest as well as they help to identify locations of interests, and provide more information about the interaction between different regions inside the plume. Figure 5.9 highlights the areas where nucleation occurs, and provides the size of aerosol particles which are formed. Figure 5.10 shows the associated nucleation rates which give a notion of the amount of particles that are formed.

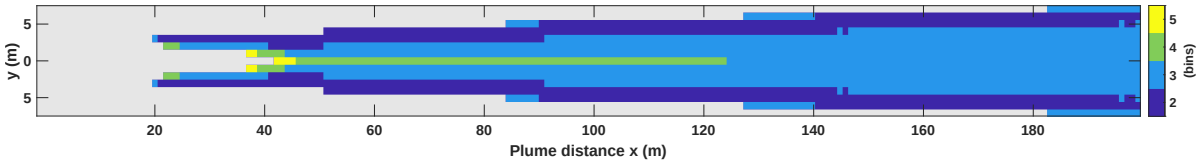

Figure 5.9: A 2D section cut of the axisymmetric wake showing the areas where nucleation occurs, and the size of the critical cluster expressed as the particle bin they are assigned to. Grey areas are locations where the nucleation rate lies below 1 particle/(cm^3 s).

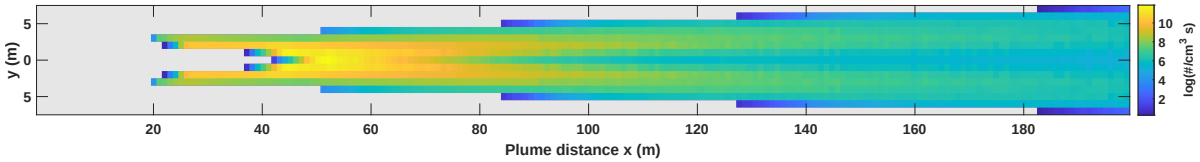

Figure 5.10: A 2D section cut of the axisymmetric wake showing the areas where nucleation occurs, and the associated rates. Grey areas are locations where the nucleation rate lies below 1 particle/(cm^3 s).

The section cut of the wake reveals that different particle sizes are formed depending on the location in the plume, and the range of sizes spans 4 bins. Interestingly, nucleation commences earliest in the shear line of the jet wake at 20 m past the engine exit, and nucleation in the core follows after about 40 to 45 m past the exit. Returning to Fig. 3.12, this is not surprising given that the conditions in the core are initially the least favorable for nucleation given how dry the environment is in the hot climate.

This is why larger critical embryos are required before a stable equilibrium is reached between the gas and the liquid droplets. At the edges of the plume, however, the relative humidity lies above ambient conditions because the temperature is low enough, and there are increased concentrations of water vapor available from the engine. This results in more favorable conditions, and allows for the formation of smaller particles, but at a lower rate because there is less sulfuric acid vapor available which is still largely trapped in the core (see Fig. B.3 in the appendix). This also explains why the PSD of the population in the core contains particles with radii smaller than 0.79 nm as seen in Fig. 5.5. In addition, the strong surge in nucleation at core shown by Fig. 5.6a and 5.7 is also clearly visible in Fig. 5.10 at 50 m plume distance. Through a combined effort of nucleation and subsequent condensation (see also Fig. 5.11), the abundance of sulfuric acid vapor in the core is depleted rapidly, and nucleation rates drop significantly due to decreasing supersaturation, eventually creating a “tear” in the nucleation field which is visible in Fig. 5.10. From there on, most of the nucleation happens at the outer regions of the wake. Nucleation is followed by condensation and coagulation, and their associated rates are plotted in Fig. 5.11 and Fig. 5.12, respectively. The rates are expressed in the amount of new aerosol particles per cubic centimeter per second that are added to a particular bin, in this case bin 6, or particles with a radius of 1.3 nm.

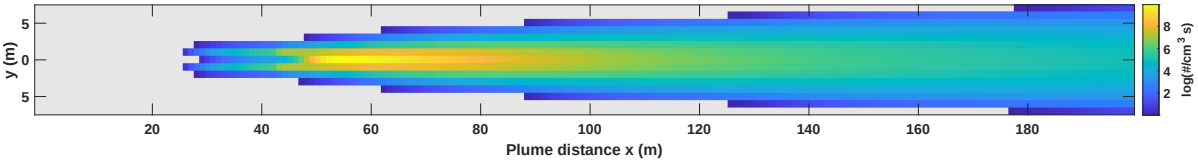

Figure 5.11: A 2D section cut of the axisymmetric wake showing the areas where condensation occurs, and the associated rates. Rates only count for particles with a radius of 1.3 nm. Grey areas are locations where the condensation rate lies below 1 particle/(cm^3 s).

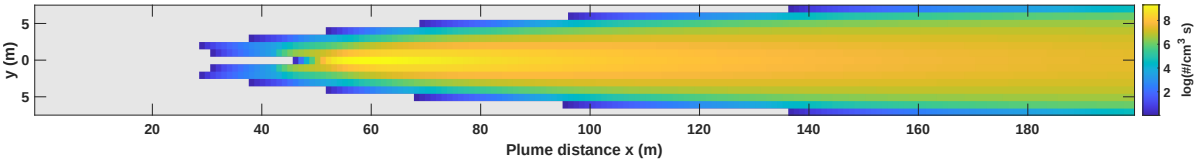

Figure 5.12: A 2D section cut of the axisymmetric wake showing the areas where coagulation occurs, and the associated rates. Rates only count for particles with a radius of 1.3 nm. Grey areas are locations where the coagulation rate lies below 1 particle/(cm^3 s).

The two-dimensional heat map of the condensation rates shows that freshly nucleated particles in the shear line are transported to the wake’s core early on as there is condensation happening in the core before nucleation is possible. While coagulation also starts early, it is slightly delayed because the number density of the aerosol population is still increasing. Both fields also show peak intensities in the wake’s core at 50 - 60 m. Self- coagulation among smaller particles eventually dies out for smaller-sized aerosol as the average particle radius grows larger throughout the domain. This is shown by Fig. 5.13, which depicts the volume-mean radius of the particles at that location in the wake, and the amount of particles that are added to bin 4 due to coagulation of smaller particles, shown in Fig. 5.14.

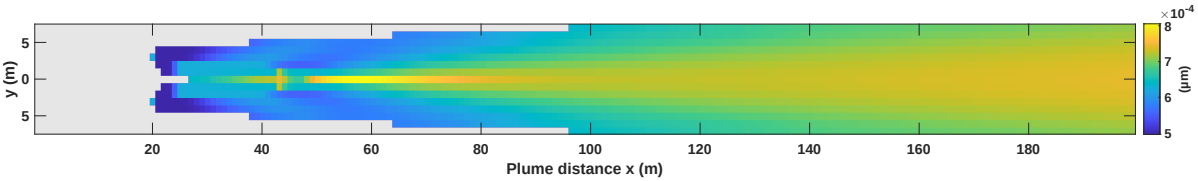

Figure 5.13: A 2D section cut of the axisymmetric wake showing the evolution of the volume-mean radius of the aerosol. Grey areas are locations where no aerosol resides.

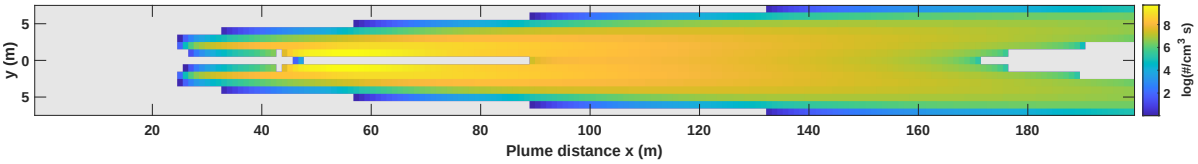

Figure 5.14: A 2D section cut of the axisymmetric wake showing the areas where coagulation occurs, and the associated rates. Rates only count for particles with a radius of 0.79 nm. Grey areas are locations where the coagulation rate lies below 1 particle/(cm^3 s).

There comes a point where the number densities of the populations in the lower bin sizes become too low to collide frequently, and to grow through coagulation. This happens rather soon in the core of the wake, but less rapidly at the edges of the plume because the growth rate in the core is significantly larger thanks to the high density of aerosol, and vapor supersaturation. Notice the void right at the peak of heavy particle formation which tells us there are little to no particles below 0.79 nm present at that location as bin 4 is not gaining any particles through coagulation. This is because the size of the critical cluster is already part of bin 4 from the moment it is formed. This void eventually gets filled by particles coming from the outer parts of the wake. At the end of the domain though, the population of particles in the lower bins are depleted for good. The border where gains through coagulation become insignificant lies very close to the areas where the volume-mean radius in Fig. 5.13 reaches values of 0.79 nm (this is difficult to see). This means that the major part of the aerosol population at that location already belongs to bin 4 or higher.

5.3. Effects of Temperature and Relative Humidity on Microphysics

For the verification study in Section 5.2, the choice was made to use a different distribution for the temperature and relative humidity based on more realistic mixing model from Kärcher (1998) instead of the RANS-resolved fields (see Section 3.3.1). To assess the impact that different distributions might have on the microphysical processes in the wake, the simulation was run again with the RANS fields. This section discusses the results of that analysis, starting again with plotting the evolution of the PSD at different distances along the plume axis. in Fig. 5.15.

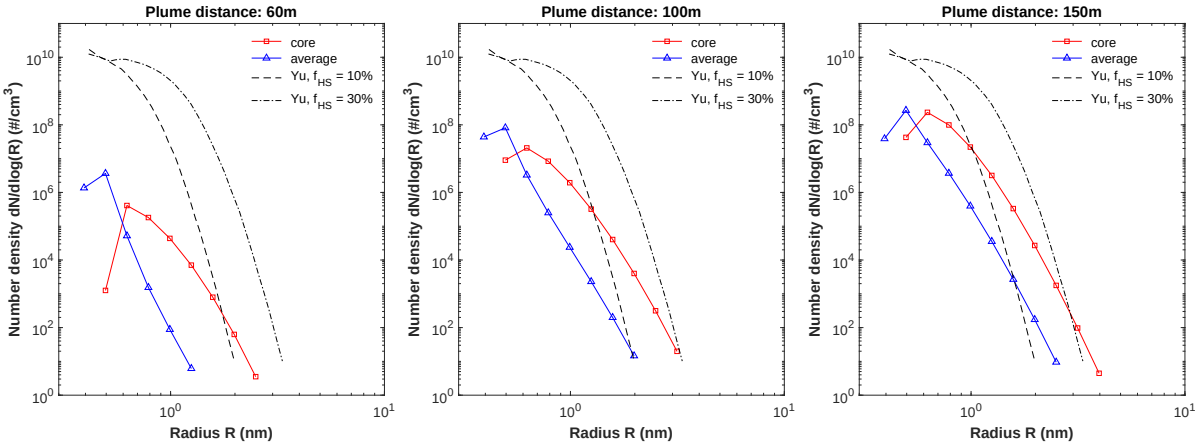

Figure 5.15: Evolution of the volatile particle size distribution as a function of plume distance (or age).

Comparing Fig. 5.15 to Fig. 5.5, we see that the predicted number densities at 150 m resemble each other relatively well, but there are two notable differences. The averaged PSD across the entire plume lies significantly higher, matching the core PSD, but shifted to smaller particles sizes. Secondly, the PSDs show a more linear growth trend, which is an indication of a more constant growth process. The PSD at a distance of 60 m, however, displays significant differences to the verification case. Instead of high particle counts in the core, there are more particles present away from the center and spread

out in radial direction. The amount of particles that has been formed at this instance is also less, which implies nucleation is delayed/quenched with respect to the conditions in the verification case.

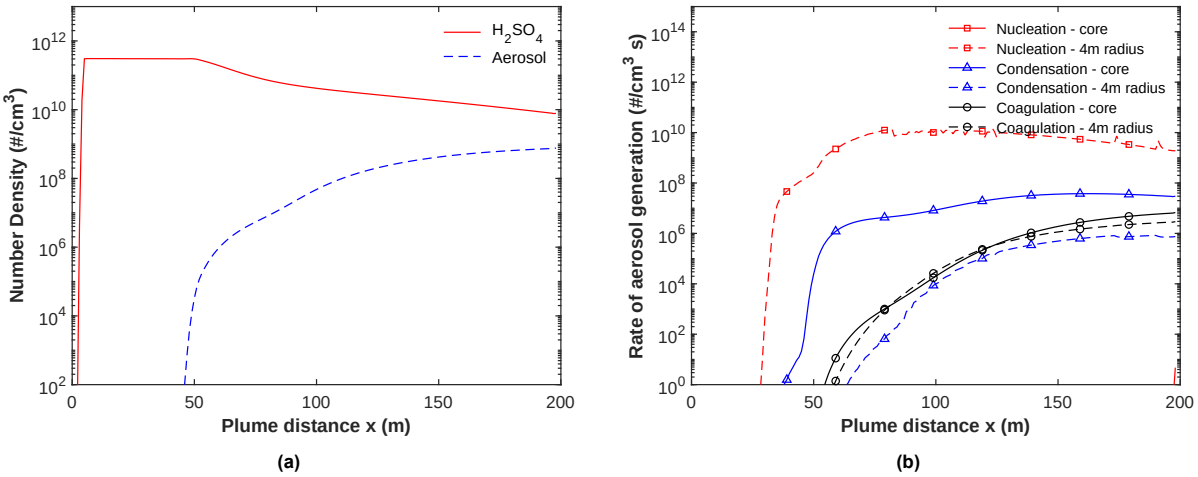

Figure 5.16: (a) Concentration of sulfuric acid vapor and aerosol in the plume's core versus plume distance. (b) Rates of binary homogeneous nucleation, homogeneous condensation, and Brownian self-coagulation versus plume distance at two radial locations. The condensation and coagulation rates are for particles with radii of 1.3 nm (bin 6), while the initial radii of the nucleated particles vary depending on the location.

Figure 5.16a shows that the sulfuric acid vapor concentrations in the core starts to decline at 50 m past the engine exit, but at a slower pace as the verification case in Fig. 5.8a. Aerosol is present in the core from that moment on as well. However, Fig. 5.16b reveals that there is no nucleation happening in the core until the very last moment (at 199 m, bottom right corner), and vapor depletion is purely happening through condensation on pre-existing particles. This means the aerosol appearing in the core is transported from somewhere else in the wake. The coagulation rates in the core and at a radial distance of 4 m look very similar, which could imply the population of smaller particles is well-distributed across the plume as they appear in similar quantities.

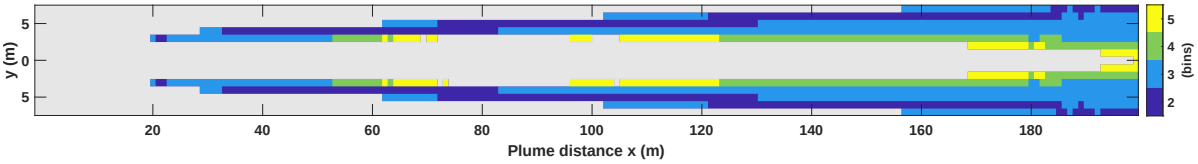

Figure 5.17: A 2D section cut of the axisymmetric wake showing the areas where nucleation occurs, and the size of the critical cluster expressed as the particle bin they are assigned to. Grey areas are locations where the nucleation rate lies below 1 particle/(cm^3 s).

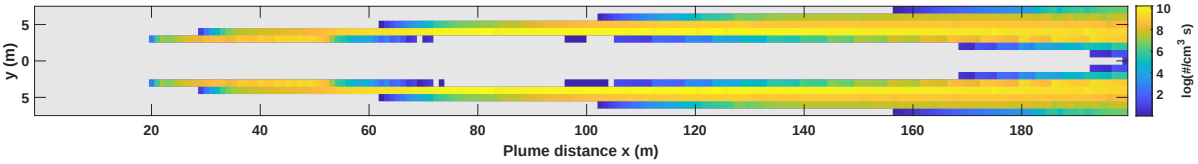

Figure 5.18: A 2D section cut of the axisymmetric wake showing the areas where nucleation occurs, and the associated rates. Grey areas are locations where the nucleation rate lies below 1 particle/(cm^3 s).

The section cuts of the nucleation field in Fig. 5.17 and Fig. 5.18 confirm that nucleation in the core of the plume is absent for most of the domain, because the temperature conditions remain unfavorable for a longer period of time. This is a significant difference with the verification case where the entire plume participates in nucleation from the start. Due to the absence of the strong surge in particle formation and growth in the center, a larger abundance of vapor reaches the edges of the plume resulting in bigger number densities and larger nucleation rates (see Fig. B.4 in the appendix). Most of the particles that

are formed initially have radii around 0.5 to 0.64 nm, but this increases to 0.79 - 0.99 nm as the edges get more saturated with vapor.

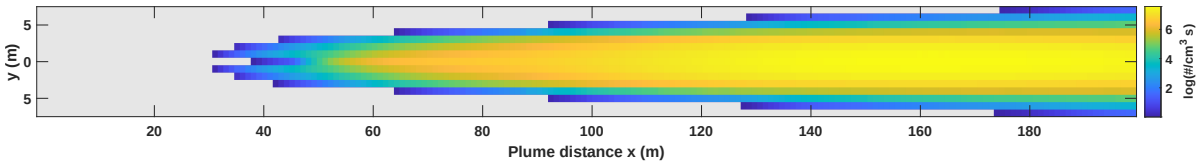

Figure 5.19: A 2D section cut of the axisymmetric wake showing the areas where condensation occurs, and the associated rates. Rates only count for particles with a radius of 1.3 nm. Grey areas are locations where the condensation rate lies below 1 particle/(cm^3 s).

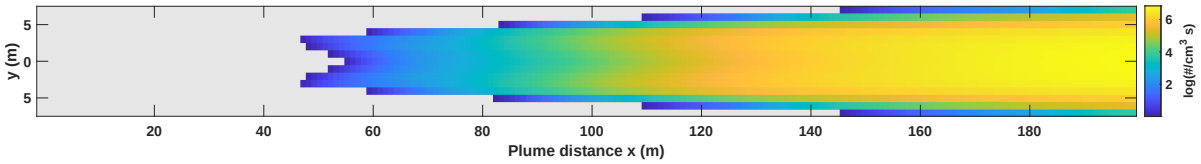

Figure 5.20: A 2D section cut of the axisymmetric wake showing the areas where coagulation occurs, and the associated rates. Rates only count for particles with a radius of 1.3 nm. Grey areas are locations where the coagulation rate lies below 1 particle/(cm^3 s).

Figure 5.19 and 5.20 finally confirm the process of particle transportation that was alluded to in the discussion of Fig. 5.8a. Both the condensation and coagulation rates showcase a gradual increase in intensity throughout the entire plume without any surges or discontinuities, although condensation starts to slow down by the end of the domain (see Fig. 5.16b). Yet, it was shown that aerosol is solely created at the edge of the plume. This means there is a steadily-increasing flux of aerosol material transported towards the core of the wake. This makes sense given the strong growth in the turbulent diffusion after 50 m (shown earlier in Fig. 5.2 and Fig. 5.8b). The contours in Fig. 5.20 even show the process of spreading by faint variations in the self-coagulation rates which are a good indicator for the number density of population. These contours are even more notable in the distribution of aerosol in Fig. B.6 in the appendix.

The transport of aerosol to the core eventually also results in strong growth as condensation and coagulation rates remain relatively high for the entire plume distance (see Fig. 5.16b). This is most likely the result of more abundance of sulfuric acid vapor as there has been no surge in nucleation at the start of the plume like in the verification case. The volume-mean radius distribution in Fig. 5.21 also resembles more of a one-dimensional streak-line, as the result of the merging of particles coming from the edge. The volume mean radius distribution of the verification case, on the other hand, shows more growth outwards from the core.

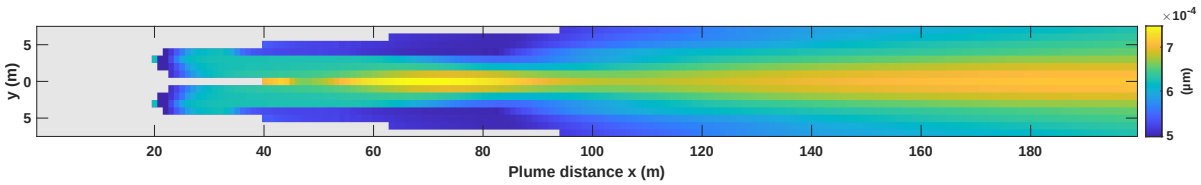

Figure 5.21: A 2D section cut of the axisymmetric wake showing the evolution of the volume-mean radius of the aerosol. Grey areas are locations where no aerosol resides.

5.4. Effects of Increased Concentrations on Microphysics

One of the effects of increasing the initial vapor concentration was illustrated previously in Fig. 5.4 on a small scale, where increasing the abundance of vapor at the start resulted in accelerated growth of the aerosol population. Yet, under extreme supersaturation levels, the classical modeling approach to

nucleation and condensation can predict unrealistic scenarios. The purpose of this section is to explore the limits of modeling particle microphysics as a thermodynamic equilibrium. To confidently answer any questions on the steerability of SAI, it is important that the physics are correct. Therefore, two study cases were considered in line with the investigation of Benduhn et al. (2016). Based on the assumption that fighter jets would carry out the logistical operation of transporting high amounts of sulfur up to the stratosphere, they concluded that a minimum injection concentration of 1e16 molecules/cm^3 would be required to be able to release their entire payload within cruise range, and minimize the amount of aircraft needed to carry out the mission. A second lower limit of 1e15 molecules/cm^3 could be possible, if an additional precursor gas is released besides H_2SO_4. Both concentrations are considerably bigger than the levels used in the verification study, and they lie outside the validity range of the parameterization for neutral particle formation from Määttänen et al. (2017), which is limited to 1e13 molecules/cm^3. Therefore, this study considered two versions of each case; one where the perceived particle concentrations are artificially lowered to limit the nucleation rates and particle properties to the validity range of the parameterization; and a second version where the predicted rates and particle properties are unregulated. In addition, ions are included in all cases with realistic concentrations to allow for the possibility of ion-induced nucleation. The validity range of the parameterization for IIN allows for concentrations up to 1e16 molecules/cm^3, and provides a good benchmark for neutral particle properties. However, although charged particle formation is included, the formed cluster does not behave differently than a neutral cluster due to ongoing development (see Section 3.2.2). Figure 5.22 shows the core and average particle size distributions of the two injection cases with limited concentrations of H_2SO_4 participating in nucleation. The case where the concentrations are unregulated is shown in Appendix C, but excluded from this discussion as the simulation showcased an inherent periodic instability in the aerosol mass, and unrealistic predictions of the critical cluster size.

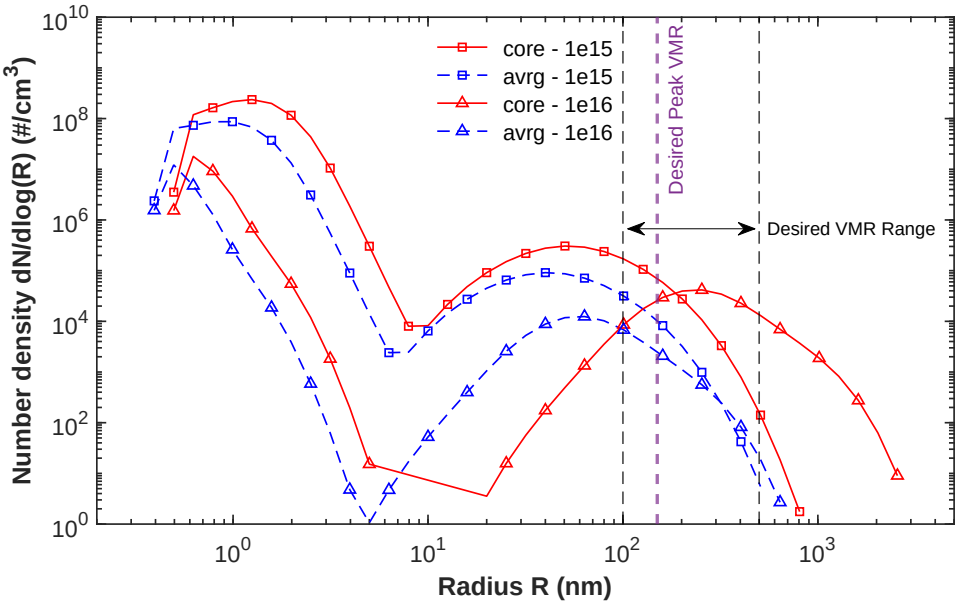

Figure 5.22: Approximate number densities versus radius of volatile aerosol particles in the early jet regime at 200 m of plume distance. Perceived H_2SO_4 concentrations in the nucleation routine are limited to the maximum values of the validity ranges. The desired range of volume-mean radii of the population at the end of the early growth period is shown by the vertical dashed lines, including the desired peak at 0.15 µm.

There is a clear indication that larger concentrations of condensable vapor increase the particle radius and accelerate particle growth on the short-term. Yet, the amount of the smaller-sized aerosol particles decreases as the initial vapor concentration goes up, which is the result of increasing condensation rates and decreasing nucleation rates. A small segment of large particles claims most of the vapor resource, and becomes increasingly more efficient at scavenging smaller aerosol through coagulation.

However, the results shown above are most likely unrealistic due to a number of reasons. To start, the dual-mode distribution in Fig. 5.22 is created almost artificially, and not the result of a physical difference in the growth process. The nanoscale left mode results from natural growth in the plume, while the submicroscopic mode on the right is created almost instantaneously early on in the wake. This is especially clear looking at the distribution of the volume-mean radius for both initial concentration levels in Fig. 5.23 and 5.24.

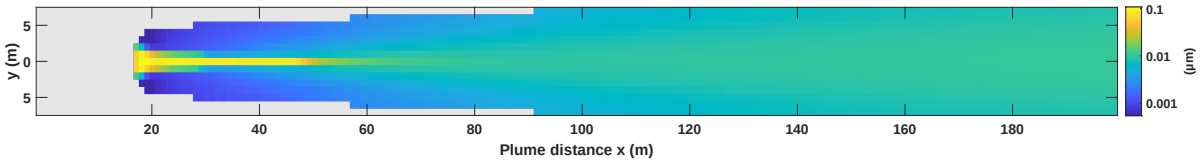

Figure 5.23: A 2D section cut of the axisymmetric wake showing the evolution of the volume-mean radius of the aerosol for an initial vapor number density of 1e15 molecules/cm^3. Grey areas are locations where no aerosol resides.

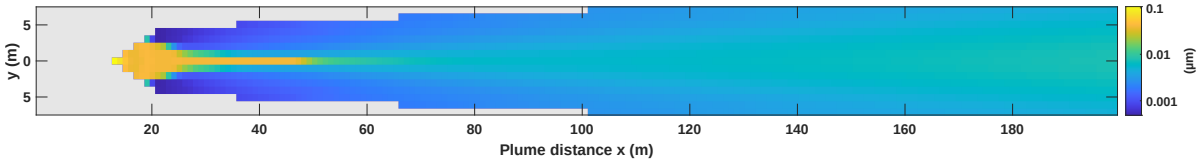

Figure 5.24: A 2D section cut of the axisymmetric wake showing the evolution of the volume-mean radius of the aerosol for an initial vapor number density of 1e16 molecules/cm^3. Grey areas are locations where no aerosol resides.

Both figures clearly show that the largest volume-mean radii are found early on in the wake. Right from the start, particles grow beyond radii of 0.1 µm almost instantaneously, and enter the desired VMR range to be useful for SAI applications. A second concern is the onset of nucleation, as visualized in Fig. 5.25 and 5.26, which moves upstream with increasing vapor concentrations. In the case of an initial concentration of 1e16 molecules/cm^3, nucleation occurs in the core at a point where the temperature is still above 400 K, outside the range of almost all of the thermodynamic parameterizations from Table 4.1. Remarkably, the nucleation event in the core is also limited to 1 grid point and does not take place at later instances downstream except in the outer regions in the wake.

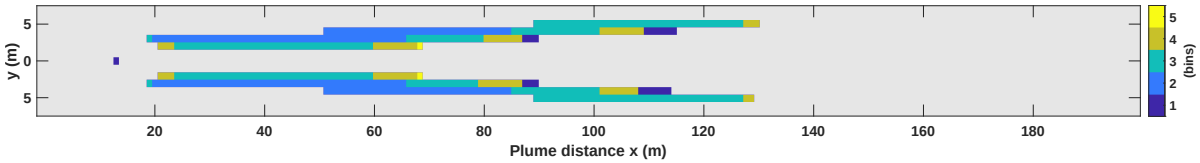

Figure 5.25: A 2D section cut of the axisymmetric wake showing the areas where neutral nucleation occurs, and the size of the critical cluster expressed as the particle bin they are assigned to. Grey areas are locations where the nucleation rate lies below 1 particle/(cm^3 s). Initial vapor number density of 1e16 molecules/cm^3.

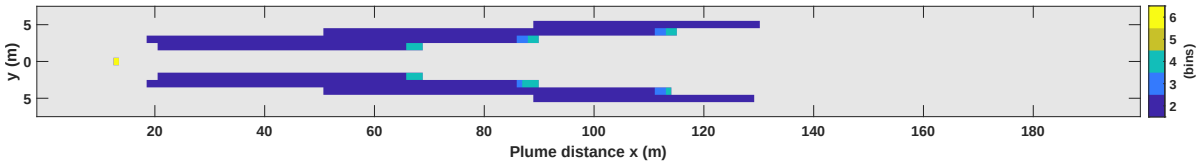

Figure 5.26: A 2D section cut of the axisymmetric wake showing the areas where ion-induced nucleation occurs, and the size of the charged critical cluster expressed as the particle bin they are assigned to. Grey areas are locations where the nucleation rate lies below 1 particle/(cm^3 s). Initial vapor number density of 1e16 molecules/cm^3.

A third issue with the validity of CNT is related to the size of the critical cluster. CNT predicts that most of the particles that are formed are neutral subnanoscopic particles with a high sulfur composition due to the extreme dry environment, nearing barrierless kinetic particle formation as a result of the

high vapor concentrations. Yet, as seen in Fig. 5.27a, the BKPF regime for both neutral and charged particle formation is never reached in the core, as the vapor concentration is depleted rapidly once nucleation commences (charged BKPF does occur in other regions of the wake, see Fig. C.2). The question is whether the single neutral nucleation event in the core is trustworthy, because the ion-induced nucleation prediction tells a different story. Figure 5.26 shows that charged critical clusters are generally smaller than neutral clusters, which makes sense based on the discussion in Section 2.4.2. The only exception is the size of the clusters in the core, where IIN predicts the formation of particles with bin size 6, which makes sense because it is more difficult to form stable smaller clusters in a hot climate (keep in mind that IIN is valid for concentrations up to 1e16 molecules/cm^3). Yet, the neutral clusters at the same location are significantly smaller which is contradictory to the fact that ions prevent cluster disintegration and allow for smaller, more stable clusters to be formed.

As a final observation, let us investigate why nucleation is absent in the plume core after that single burst at 13 m from the engine exit. Figure 5.27b reveals that significantly lower amounts of aerosol are formed compared to the verification case (9e6 particles/cm^3 vs. 9e9 particles/cm^3, see Fig. 5.8a). Still, large quantities of vapor are consumed as visible in Fig. 5.27a but not through nucleation. The dominant gas-to-particle conversion process in this case is condensation or the diffusion of vapor onto existing particles. Looking at the loss rates of H_2SO_4 vapor in Fig. 5.28, the initial condensation rate exceeds the nucleation rate tremendously with a rate above 1e18 molecules/(cm^3 s). Thus, a small amount of particles claims almost all the available vapor in less than 5 meters or a few grid cells, resulting in large volume-mean radii. This result is questionable because of three reasons: (1) the thermodynamic parameterizations for some of the variables that are used in the growth equation are not valid for the local temperature; (2) the growth equation assumes the impingement rate of H_2SO_4 is the limiting factor, and that the water concentration is sufficiently high to restore aerosol equilibrium instantaneously (see Section 2.5), but at this stage water is present in almost equal amounts as sulfuric acid which would decrease the efficiency of the growth process; (3) it was discovered that the growth routine allows for rapid mass diffusion across multiple bin sizes at a time which leads to unrealistic growth spurts among the aerosol population. The ion population in the core, on the other hand, shows a steady decline in numbers (even in the absence of nucleation) due to recombination and dilution of the plume, and follows the trend from Yu and Turco (1998) nicely.

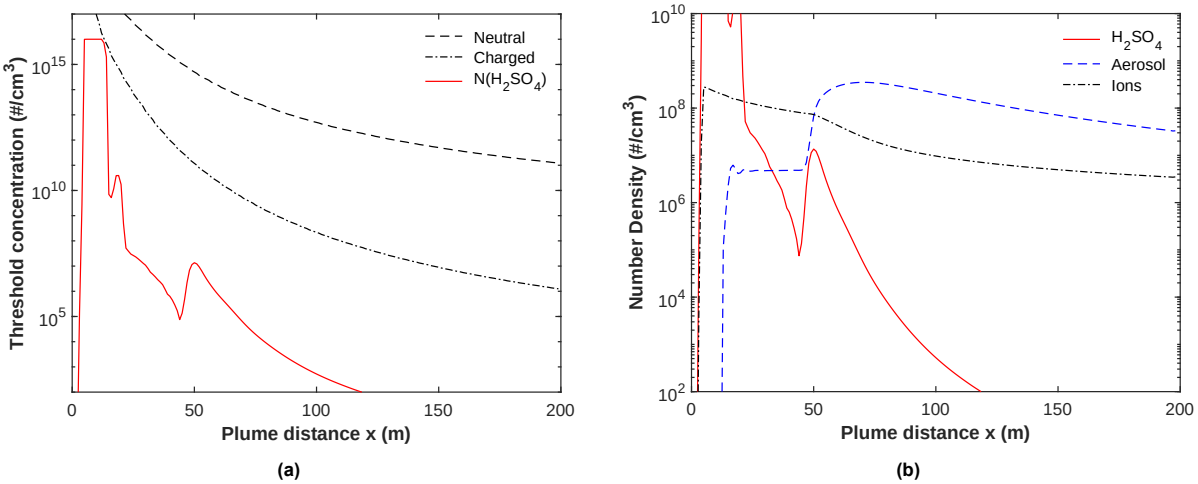

Figure 5.27: Initial vapor number density of 1e16 molecules/cm^3. (a) Concentration of sulfuric acid vapor in the plume core, and the thresholds for both neutral and charged barrierless kinetic particle formation, versus plume distance. (b) Concentration of sulfuric acid vapor, aerosol, and ions in the plume's core versus plume distance. Peaks that increase the aerosol and vapor numbers are the result of mass at the edge of the wake diffusing inward to the core.

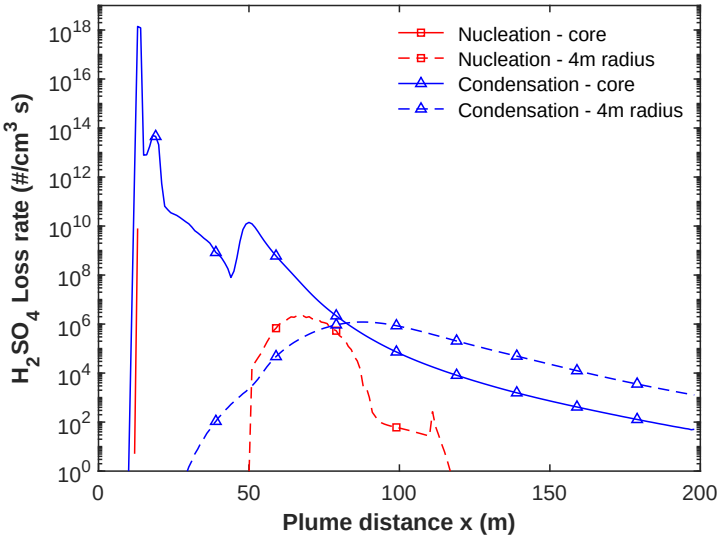

Figure 5.28: Loss rate of H_2SO_4 vapor molecules due to nucleation and condensation at two radial locations for an initial vapor number density of 1e16 molecules/cm^3.

6

Discussion

The aim of this study is to investigate the mechanisms within a jet engine wake that govern sulfate aerosol formation and growth, as well as the effect of elevated concentrations of gaseous H2SO4 on the model's accuracy in predicting the resulting particle size distribution. Through simulations, we were able to analyze the impact of temperature and relative humidity on the evolution of aerosols in the wake, as well as the effect of increasing H2SO4 concentrations on particle growth. In Section 6.1, we discuss the findings in more detail and provide an interpretation of the results, drawing on relevant literature to explain their relevance. The chapter concludes with Section 6.2 which presents the answers to the research questions that were posed at the start of this research.

6.1. Interpretation of the Results

Aircraft emissions have been shown to produce sulfate aerosol particles in their wake, and the number of these particles is heavily influenced by engine emissions, fuel sulfur content, and ambient conditions (Penner et al., 1999; Yu & Turco, 1998). This is accentuated by the large uncertainty bars in the particle size distribution from Kärcher (1998) in Fig. 5.3. The formation of these particles is complex and affected by various factors, including the initial sulfuric acid vapor concentration, and the plume mixing rate, in turn affecting the cooling rate and dispersion rate of several key chemical species such as H_2O, H_2SO_4, ions, and the aerosol itself. The presence of soot, and other nitrogen-based catalysts, is believed to have a negligible impact due to their low numbers. In addition, there are strong indications that "classical" binary nucleation theory, based on the assumption of thermodynamic equilibrium between the vapor and condensed states, is not suited to explain the process of high-density particle formation (Yu & Turco, 1998).

First, a verification study was conducted. Its goal was to ensure that the new nucleation routine and dilution mechanics were implemented correctly, by benchmarking it with the box model from Yu and Turco (1998). Before, the microphysical model was only capable of simulating homogeneous particle growth in a constant stratospheric environment (fixed temperature and relative humidity). This resulted in instantaneous particle formation, rapid growth, depletion of acid vapor within milliseconds, and a log normal particle size distribution with a VMR of rougly 0.1 µm spanning tree decades of particle radii after only 200m (which takes less than a second to develop). After the implementation of a realistic distribution of temperature and water vapor, typical of a jet engine wake, it quickly became apparent that the microphysics and the resulting PSD were very sensitive to the local conditions in the wake. This resulted in an entirely different outcome after 200 m as presented in Fig. 5.3. The PSD now only

spanned one decade of radii, with a VMR of rougly 0.75 nm. One of the significant factors leading to this decrease in particle size is the high initial temperatures of the exhaust, which hinder the formation of particles. Another factor is the dispersion of mass due to turbulent mixing between the wake and surrounding air which also contributes to this decline by preventing the condensation of vapor and coagulation of particles.

In general, the results agree remarkably well with the predictions from Yu and Turco (1998), given the difficulty to match plume ages, the high uncertainty factor on the initial conditions, and the fact that it is a one-dimensional box model with no partitioning in the cross-section of the plume, and different dilution mechanics. The biggest discrepancy lies in the particle counts of the smallest clusters, but this is suspected to be a consequence of differences in the onset of nucleation due to different dilution mechanics of the wake. Yu and Turco (1998) apply a constant diffusion coefficient of 300 m^2/s in the jet regime to estimate the expansion of the plume and the dispersion of all its chemical species. This about twenty times bigger than the maximum values in the RANS field (see Fig. 5.8b). While the dilution of temperature and water vapor is handled by Kärcher's box model (see Section 3.3.1), the dispersion of sulfuric acid vapor is still modeled through the advection-diffusion equation with the turbulent kinematic viscosity, and therefore it disperses at a significantly slower rate. This will advance/force the onset of nucleation as the supersaturation limit is reached earlier, but increase the required size of the critical cluster to achieve equilibrium. It will also significantly accelerate particle growth in the core because the vapor is still largely trapped here, leading to high condensation/coagulation rates (see Fig. 5.7). As a result, the sulfuric vapor mass is depleted at a considerably stronger pace (see Fig. 5.8a). By the time the plume has reached more favorable conditions for nucleation, the amount of vapor available for nucleation is significantly lower compared to Yu and Turco (1998), which is why they are able to produce larger amounts of smaller sized critical clusters at this point as the temperature has dropped further. This hypothesis is supported by Fig. 6.1 which depicts the sensitivity of the homogeneous nucleation rate to a variation in temperature (Dakhel, 2005).

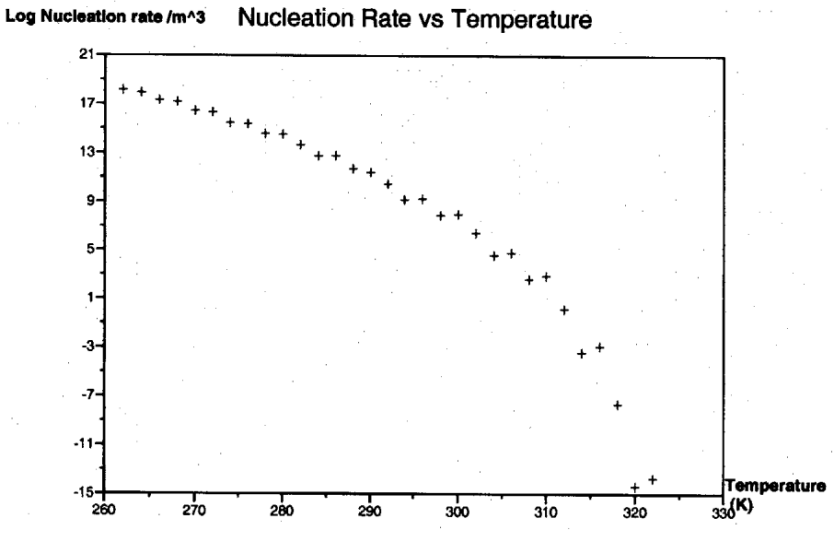

Figure 6.1: Nucleation rate as a function of temperature. The water mole fraction and the sulfuric acid mole fraction are at typical values for a 30m measurement. The nucleation rate is highly sensitive to temperature and can vary greatly in a temperature change of 10 degrees K (Dakhel, 2005).

The difference in the onset of nucleation between both models is roughly 40m, and the temperature drops from 300 K to 280 K over this distance (see Fig. 3.9a). A decrease by 20 K increases the nucleation rate for the same vapor concentration by 8 orders of magnitude. The takeaway here is that strong early diffusion of the condensable vapor might delay nucleation, and will create larger amounts of small-sized particles that are evenly distributed across the plume. Secondly, it prevents excessive

coagulation leading to slower growth. Strong concentrations in the core, however, result in bigger critical embryos, and lead to prompt coagulation/condensation, resulting in rapid growth to size, a less uniform population, and smaller amounts of smaller-sized particles scattered around the plume.

Another important factor, and one which was not shown as part of this investigation, is the effect of chemiions on the coagulation process early on in the plume (see Section 2.6.2). According to Yu and Turco (1998), charged clusters are highly effective at scavenging sulfuric acid vapor, often inhibiting neutral particle aggregation. However, the period of charge-assisted coagulation is very short, and Yu and Turco (1998) showed that the total number of ion mode particles that grow beyond the minimum, located between 1 to 2 nm in the size distribution of Fig. 5.3, is independent of the plume age after roughly one second. Thus, the number of charged particles that will attain radii larger than 1.5 - 2 nm stabilizes after one second regardless of the initial concentration. At this point, it is difficult to predict how this dual-mode behavior would respond over time under high initial vapor concentrations and areas of high supersaturation. It is possible that the ion mode particles will disrupt the growth process significantly, creating a small population of relatively large particles in contrast to a large population of small neutral particles which were inhibited to grow. Whatever the case, the effect of electrostatic enhancement could be retarded by injecting outside the area where ions reside, or by increasing the mixing rate early on in the wake.

By now, it is clear that an accurate mixing model of the wake is of big importance in setting the microphysics in the early growth period. The problem is that the jet wake and overall plume morphology is highly aircraft/engine specific. For this study, the choice was made to model the dilution of the wake in part by the box-equations from Kärcher (1995) and simulated entrainment rates of a B747 high-bypass jet engine, supplemented with information from the early RANS fields to include more detail in the radial direction. Although this is a makeshift solution awaiting the development of a more-inclusive RANS simulation, the approach did provide some new insights in the particle formation process as it was revealed that particulate formation does not start in the core of the wake, but in the shear line instead. In retrospect, this is not surprising because the highest relative humidities are seen in the outer edges of the plume. Particles formed in the outer regions of the plume tend to be smaller in size compared to the ones in the core (see Fig. 5.9). The elliptical closure of the nucleation zone is also a notable factor, which is predicted by another 2D mixing model from Starik (2007) for a B747 aircraft and the turbulent plume of the bypass engine, seen in Fig. 6.2a.

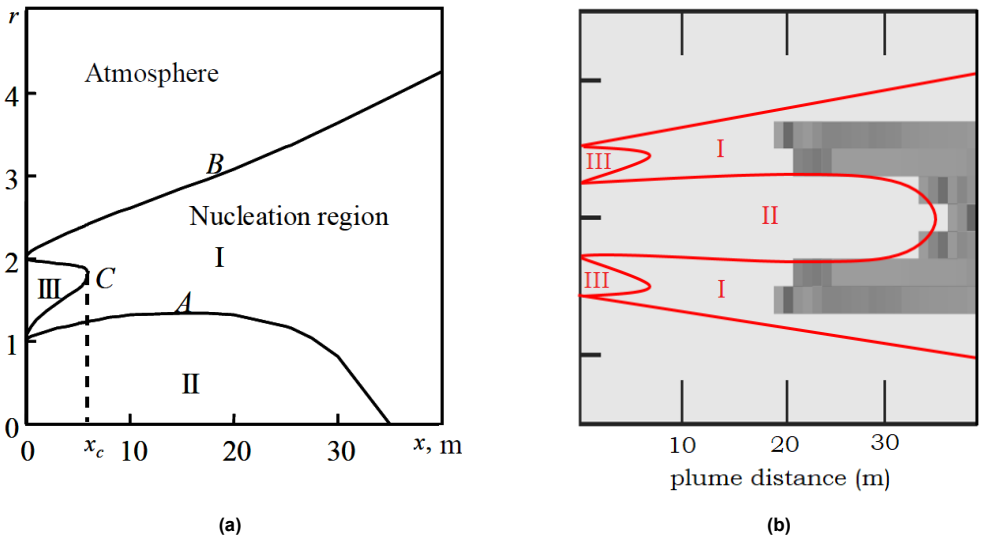

Figure 6.2: (a) Location of the nucleation region in the plume of B-747 aircraft at cruise ($\bar{r}$ is the normalized radius of the plume, A depicts the boundary of the engine core flow, B depicts the boundary of the plume) (Starik, 2007). (b) Overlay of Fig. 6.2a with a cutout of the nucleation field from Fig. 5.10.

The same boundaries are plotted over the nucleation field from Fig. 5.10 in Fig. 6.2b, which confirms that the onset of nucleation falls within the demarked nucleation region (I). Region (II) is the hot exhaust core flow preventing nucleation, which cools down sufficiently after about 35m. A similar region is found in the bypass (III), lasting for a shorter distance because the initial exit temperature is more moderate compared to the core. The delayed onset of nucleation in the shear line, and smaller spread of the nucleation region, might be explained by the fact that the radial distribution is modeled after the RANS field which was shown to decay rather slowly. The turbulence model might underestimate the rate of mixing, and therefore plume expansion (see Section 4.1.2).

To evaluate the variability in the microphysics under different dilution conditions, the box-model T and RH fields were replaced by the RANS-resolved T field and the associated RH field. This had a big impact on the microphysics because nucleation in the core was delayed considerably, and most of the nucleation happened in the shear line instead (Fig. 5.18). It also revealed that particles formed in the edge of the plume, diffuse inward towards the core where they collide and grow considerably through vapor condensation (Fig. 5.19 - 5.20). Yet surprisingly, the different evolution paths in particle growth did not result in widely different average volume-mean radii at the end of the domain, but there is a clear non-uniformity in the distribution of the volume-mean radius across the plume's cross-section. (compare Fig. 5.13 and Fig. 5.21). At this stage, it is difficult to further investigate the differences in particle growth as the result of how the plume develops over time, given the large number of unknowns in the mixing process. The plume morphology is highly case-specific, and depends on a number of factors including the type of engine as well as the interaction with the wingtip vortices in the near-field (Garnier et al., 1997; Kärcher, 1995).

A final observation as part of this sensitivity study is the relationship between the mass conservation error during advection and diffusion, and the total amount of mass in the system. The relative mass conservation error varied significantly depending on the conditions, and if most of the mass still resided in the vapor phase , or was converted to aerosol. If no nucleation occurred, the relative error could be significant (above 100%), but for vapor number densities above 1e10 molecules/cm^3, the resulting impact of twice the mass on the microphysics is relatively low. Yet, if heavy nucleation occurs, most of that mass is converted to aerosol, and the relative mass error in the vapor population drops to below 1%. The relative mass error in the aerosol population increases instead, but only to a value of 30%. This implies the error is also bound to the number of particles (or separate bodies of mass), and potentially the transition step from concentration to mass as the variable of interest when advecting the populations across the grid. Because the numerical schemes for diffusion-advection were not the focus of this research, the source of the error was not investigated further but this is considered as an area of improvement in future research.

6.2. Answers to the Research Questions

What follows is the synopsis of the results, and their interpretation, by answering the research questions that were posed at the start of this research in an effort to gain insight in the growth process of Accumulation-Mode H_2SO_4-H_2O aerosol in a jet engine wake after injection of condensable sulfuric acid vapor.

RQ.1 What are the mechanisms within the near-field of a jet engine wake that lead to the creation of aerosols and subsequent growth, when accounting for local variations in temperature and relative humidity?

The simulations show that the microphysics and resulting particle size distribution are very sensitive to the local conditions in the wake. The high initial temperatures of the exhaust hinder the formation of particles, while the dispersion of mass due to turbulent mixing between the wake and surrounding air

counters the effect of condensation of vapor and coagulation of particles. In all of the studied cases, particle formation starts in the shear line due to rapid cooling of the plume at the edges and expands to the core at a later stage. Clusters that are formed at the edge of the plume are typically smaller than nuclei in the core. A large part of the fresh aerosol particles in the outer regions is continuously transported inwards towards the core providing a continuous flux of small particles that feed the growth process of particles in the center. For large initial concentrations of sulfuric acid vapor in the core, and a low plume dilution rate, CNT predicts a strong surge in nucleation at a certain point in the core, followed by strong vapor condensation rates and rapid coagulation. In regions of strong condensation, coagulation is enhanced due to rapidly increasing particle volumes, and therefore the collision efficiency of the process goes up (Turco & Yu, 1999). As a result, the growth process in the core is considerably faster compared to other regions in the plume as vapor will continue to condense for a prolonged period of time. Over time, the larger particles in the core are also getting increasingly more efficient in scavenging smaller particles coming from the edges of the plume.

RQ.2 How can classical thermodynamic approaches to nucleation and condensation be improved to better model high-density aerosol formation from condensable vapor?

Exploratory simulations on aerosol formation with elevated concentrations of gaseous H_2SO_4 above 1e15 molecules/cm^3 revealed several modeling errors of classical thermodynamic approaches to nucleation and condensation. Increased vapor concentrations advance the onset of nucleation in the wake to a point where the parameterizations for several key thermodynamic parameters such as the gas species saturation pressures, aerosol surface tension, and density are no longer valid for the local temperature conditions. A second issue is the contradictory results between the neutral and ion-induced nucleation predictions of the critical cluster size (and composition). Under large vapor concentrations, predicted neutral cluster sizes were significantly smaller than their charged counterparts, despite the fact that ions prevent cluster disintegration and allow for smaller, more stable clusters to be formed. A third limitation is the nature of the condensation growth equation, and its underlying assumption that the aerosol is in equilibrium with the surrounding water vapor. The absence of a restriction on the available water content leads to unreasonably large growth rates, further exaggerated by inherent mass diffusion in the condensation routine. Overall, these weaknesses suggest that classical thermodynamic approaches may not accurately model high-density aerosol formation from condensable vapor, and alternative/improved approaches should be considered.

RQ.3 What are the key uncertainties in modeling aerosol mechanics in a jet engine wake and how do they impact our understanding of the microphysics?

One of the outcomes of the literature review is a long list of assumptions and limitations in modeling aerosol mechanics in a jet engine wake (see Section 4.4), which ultimately leads to a wide range of uncertainties in the simulation results. Due to time constraints, it was not feasible to conduct a thorough sensitivity study of various parameters to quantify these uncertainties. However, through this investigation, valuable insights were gained that allow for the prioritization of unpredictable factors based on their relative impact. Based on the observations that most of the particle formation happens within the first second of emission; nucleation commences in the plume's shear line; different particles sizes and compositions are obtained at different radial locations in the plume; condensation and coagulation are heavily tied to vapor dilution rates; and that there is strong temperature evolution in the near-jet regime, it is concluded that the mixing process of the core flow (with a possible bypass flow) and the ambient air is a strong driver of the uncertainty in all areas of the aerosol microphysics. A second large uncertainty is the exact nature of the particle formation process. While CNT suggests that increased concentrations

advance the onset of nucleation, creating low amounts of larger-sized critical clusters, there is reason to believe that particle formation under high gas concentrations is purely dependent on particle kinetics resulting in large amounts of smaller-sized clusters once the conditions allow for it. This schism in particle formation theory remains one of the larger uncertainties because it determines whether subsequent growth will be dominated by condensation or coagulation, and it remains largely invalidated due to a lack of experimental observations. A third and final key uncertainty are the efficiency factors of the condensation and coagulation processes, previously referred to as the accommodation and sticking coefficients. During this investigation, they were assumed to equal 1 which corresponds to optimum conditions for particle growth, but in reality they vary considerably depending on the size and nature of the particle as well as the surrounding conditions. In addition, the possibility of particle breakup after collision should not be ruled out. Especially nanoscale clusters may experience significant reductions in their growth rate if realistic collision/diffusion efficiencies were to be considered, retarding the effects of prompt coagulation and condensation. On a final note, the impact of turbulence and the effect of electrostatic enhancement on coagulation remains unknown, as they were not part of this investigation. It is plausible, however, that will form a substantial part of the uncertainty related to aerosol mechanics in future research.

7

Conclusion & Recommendations

This study focused on Stratospheric Aerosol Injection (SAI), a geoengineering method to mitigate the effects of increased greenhouse gas concentrations in the Earth's atmosphere, and to prevent further global warming. The motivation for this research stems from the imminent danger of climate change and its detrimental impact on society. SAI does not reverse climate change, it merely counteracts its symptoms by offsetting the radiative forcing of greenhouse gases, and it should be accompanied by aggressive programmes of Carbon Dioxide Removal to cool down the climate. Aside from scientific, ethical, legal and sociopolitical implications, a number of logistical and technological challenges remain to see this method correctly implemented. The choice of aerosol material, for example, is still uncertain. While this study only looked at liquid sulfate aerosol due to its natural analogues, solid aerosols such as calcite or diamond are also among the possibilities. A second issue is to identify the best delivery system to inject the aerosol in the stratosphere, and obtain the desired particle size distribution, and optical depth, to maximize the lifetime, and scattering ability of the aerosol population.

In the case of aqueous sulfate aerosol, operational studies suggest that the injection of condensable vapor from specialized high-altitude aircraft would be a reasonable option. They would transport sulfuric acid in liquid form to the desired altitude, which lies somewhere above 20 km, and evaporate its payload prior to injecting it as a condensable vapor into the engine exhaust stream. The sulfuric acid would then combine with the already available water vapor in the wake to create liquid aerosol droplets. Yet, remarkably little is known about the growth evolution of sulfate aerosol inside a jet engine wake, especially in light of SAI where high initial concentrations of condensable H_2SO_4 are injected. This is partly due to a lack of experimental validation, but also because the spatial and temporal scales of the problem, in combination with elevated temperatures, hamper accurate simulations. The lack of resolution in the flow field obscures a lot of the intricacies of the aerosol formation process in the early stages of the wake, and raises serious doubts on the steerability of SAI, which is the capacity to spatially and temporally control its effects both in nature and scale. Without reassurance that the steerability requirement can be satisfied, the potential risks to the global ecosystem, and public health would be too high.

This research is a continuation of the work from Golja et al. (2021), and follows up on the recommendation to identify any weaknesses in the modeling of high-density aerosol nucleation, condensation and coagulation in an aircraft wake. We investigated the microphysical processes related to aerosol growth in the near-field of a jet engine wake for the first milliseconds past emission up to half a second of plume age, or 199 m in axial direction. The flow domain was obtained by solving the Reynolds-averaged Navier Stokes (RANS) equations on an axisymmetric grid. The flow field is part of a decoupled plume

dispersion model that includes an aerosol chemistry module, and a Eulerian diffusion-advection module which calculates the displacement of vapor, aerosol, and ions. The skeleton for the chemistry and diffusion-advection modules was provided by Dr. C. Golja (*Linz Group, Harvard*), and further expanded upon to represent the conditions in a jet engine wake better. Accordingly, the entire nucleation routine was replaced by a new parameterization to increase the temperature range, and include the capacity to predict ion-induced nucleation; the thermodynamic parameterization for the equilibrium vapor pressure over a flat surface of liquid water was replaced; and the entire microphysical module was adapted to work with local (gridded) temperature and water vapor concentrations instead of a global uniform value. The evolution of peak temperature and mass concentrations in the wake's core was estimated with the approach from Kärcher (1995) using a first-order decay term with a turbulent entrainment rates. Overall, these adjustments increased the fidelity of the microphysics in the plume considerably.

Initial results for a standard emission case of a civil transport aircraft flying at cruise conditions in the lower stratosphere proved to be consistent with previous studies from Yu and Turco (1998) and Starik (2007), verifying that the new nucleation routine and dilution mechanics were implemented correctly. The observed discrepancy in the particle count of the smallest possible clusters is believed to be the result of different approaches to modeling plume dilution, and possibly the increased resolution in the cross-section of the plume compared to the one-dimensional box approach from Yu and Turco (1998). The onset of particle formation in the plume is complex, and is heavily dependent on the injection concentration of sulfuric acid vapor and the mixing rate of the plume. The study also found that classical binary nucleation theory on its own is not suited to explain the process of high-density particle formation in a jet engine wake.

At the start of this project, three research questions were established to define the scope and goals of the research: (1) What are the mechanisms within the near-field of a jet engine wake that lead to the creation of aerosols and subsequent growth, when accounting for local variations in temperature and relative humidity?; (2) How can classical thermodynamic approaches to nucleation and condensation be improved to better model high-density aerosol formation from condensable vapor?; and (3) What are the key uncertainties in modeling aerosol mechanics in a jet engine wake and how do they impact our understanding of the microphysics? The reader is advised to read Section 6.2, as the following paragraph focuses on the recommendations for future work based on the answers to these questions.

Concerning the mechanisms of particle growth, the simulations showed that microphysics and resulting particle size distribution are sensitive to local conditions in the wake. It remains difficult, however, to assess the long-term impact of differences in particle growth paths on the PSD due to the limited size and resolution of the domain. It is recommended to expand the current framework to a multi-gridded approach, as explained in Section 4.3.2, where multiple domains of varying length and resolution are used to simulate longer plume ages. This would allow for further refinement of the starting grid, and better reflect the contributions of the bypass region, and shear line, to aerosol growth.

With regards to the known modeling errors of classical thermodynamic approaches, the findings indicated that they may not model high-density aerosol formation accurately enough. Therefore, it is highly recommended to reformulate the one-dimensional growth equation for condensation to create a dependence on the impingement rate of water molecules. This includes tracking the amount of water vapor throughout the plume to account for sources and sinks. Secondly, the process of particle formation at the earliest possibility should be reevaluated using more scientifically sound approaches such as kinetic theory. Possible alternatives are the approach from Yu and Turco (1998), or the Atmospheric Cluster Dynamics Code (ACDC) from McGrath et al. (2012), which is based on a dynamic birth-death equation. Alternatively, one could follow the reasoning of Pierce et al. (2010), and assume that barrierless kinetic particle formation (BKPF) is the earliest possible mechanic to form aerosol, and don't allow (thermodynamic) nucleation to occur until the conditions are favorable.

Looking at the uncertainties related to aerosol mechanics in a jet engine wake, it is concluded that the mixing process of the core flow (with a possible bypass flow) and the ambient air is a strong driver of the uncertainty in all areas of the aerosol microphysics. A second large uncertainty is the exact nature of the particle formation process. To remove some of the variability, it is advised to improve the RANS model in two areas; (1) a new turbulent mixing model to better represent the mixing process and the plume dilution rate; and (2) a refined numerical representation of the bypass flow in the initial condition. This would likely require more investigation on the specific engine design that would be used to propel the aircraft. Including trace gases in the RANS simulation would also provide a good reference to verify the output of the diffusion-advection module without the effect of microphysical processes. Regarding the implementation of efficiency factors of condensation and coagulation, a good starting point are the low-complexity parameterizations from Yu and Turco (1998) (see Eq. 2.70) and Jacobson (2005) for the accommodation and sticking coefficients.

It is evident from the answers to the research questions that the lack of knowledge on the growth and dispersion of aerosol particles inside jet engine plumes poses a major challenge to the development of stratospheric aerosol injection as a geoengineering strategy for mitigating climate change.

The results showed that different aerosol particle sizes are formed depending on the location in the plume, leading to a non-uniform distribution of the volume-mean radius across the plume's cross-sectional area. There is also a strong indication that core particles experience preferential growth, which implies that the final particle distribution at the end of the plume's lifetime might not be as uni-modal as self-limited theory predicts (see Section 2.7.2). This begs the question whether the inter-process competition between nucleation and condensation should be considered more prominently in allocating the available vapor (priority scheme). While fast growth might be preferred to limit the undesirable participation of larger background particles, there is a real chance to overshoot the target size until the high-density gas-to-particle conversion process is better understood. Ultimately, this would result in a sub-ideal aerosol population with less capacity to cool, and shorter atmospheric lifetimes. Reducing the initial particle concentration would help, but this would require lower injection rates, and lead to additional flight activity, which then again affects payload and/or infrastructure.

More experimental investigation and integrated modeling approaches are needed to overcome these challenges and only when true steerability is obtained, one can consciously consider the risks and benefits of this approach. The number of previous studies on SAI by emission of condensable vapor from aircraft is very low. To the author's knowledge, only two PDM-based studies (Benduhn et al., 2016; Pierce et al., 2010) exist. Both investigations use one-dimensional expanding box models to represent the plume, omitting some key chemical processes that account for ion-assisted growth, and they rely on the principle of self-limited growth to justify the absence of detailed nucleation and condensation mechanics. In this respect, this study highlights the importance of considering the local conditions in the wake when analyzing the formation and growth of sulfate aerosol particles. It also showed that previous assumptions on self-limited growth may not be valid, and summarized the challenges that remain to truly understand the early growth evolution of sulfate aerosol in a jet engine wake.

References

Anderson, J. (2017). *Fundamentals of Aerodynamics* (6th international ed.). McGraw Hill Education.

Appleman, H. (1953). The Formation of Exhaust Condensation Trails by Jet Aircraft. *Bulletin of the American Meteorological Society*, *34 (1)*, 14–20. https://doi.org/10.1175/1520-0477-34.1.14

Arnold, F. (2006). Atmospheric Aerosol and Cloud Condensation Nuclei Formation: A Possible Influence of Cosmic Rays? *Space Science Reviews*, *125*, 169–186. https://doi.org/10.1007/s11214-006-9055-4

Arnold, F., Curtius, J., Sierau, B., Bürger, V., Busen, R., & Schumann, U. (1999). Detection of massive negative chemiions in the exhaust plume of a jet aircraft in flight. *Geophysical Research Letters*, *26*, 1577–1580. https://doi.org/10.1029/1999GL900304

Arnold, F., Wohlfrom, K. H., Klemm, M. W., Schneider, J., Gollinger, K., Schumann, U., & Busen, R. (1998). First gaseous ion composition measurements in the exhaust plume of a jet aircraft in flight: Implications for gaseous sulfuric acid, aerosols, and chemiions. *Geophysical Research Letters*, *25 (12)*, 2137–2140. https://doi.org/10.1029/98GL01579

Becker, R., & Döring, W. (1935). Kinetische behandlung der keimbildung in übersättigten dämpfen. *Annalen der Physik*, *416 (8)*, 719–752. https://doi.org/10.1002/andp.19354160806

Benduhn, F. (2008). *Implications of Aerosol Growth Dynamics and Aerosol-Cloud Interaction to the Sun-Cloud-Climate Hypothesis* [Doctoral dissertation, University of Hamburg]. https://ediss.sub.uni-hamburg.de/handle/ediss/2260

Benduhn, F., Schallock, J., & Lawrence, M. G. (2016). Early growth dynamical implications for the steerability of stratospheric solar radiation management via sulfur aerosol particles. *Geophysical Research Letters*, *43*, 9956–9963. https://doi.org/10.1002/2016GL070701

Brown, R. C., Miake-Lye, R. C., Anderson, M. R., & Kolb, C. E. (1996). Effect of aircraft exhaust sulfur emissions on near field plume aerosols. *Geophysical Research Letters*, *23*, 3607–3610. https://doi.org/10.1029/96GL03338

Budyko, M. I. (1977). *Climatic Changes* (Vol. 10). American Geophysical Union, Washington, D.C.

Calcote, H. F. (1948). Electrical properties of flames: Burner flames in transverse electric fields. *Symposium on Combustion and Flame, and Explosion Phenomena*, *3 (1)*, 245–253. https://doi.org/10.1016/S1062-2896(49)80033-X

Clegg, S. L., & Brimblecombe, P. (1995). Application of a Multicomponent Thermodynamic Model to Activities and Thermal Properties of 0-40 mol kg^{-1} Aqueous Sulfuric Acid from <200 to 328 K. *Journal of Chemical and Engineering Data*, *40 (1)*, 43–64. https://doi.org/10.1021/je00017a012

Crutzen, P. J. (2006). Albedo enhancement by stratospheric sulfur injections: A contribution to resolve a policy dilemma? *Climatic Change*, *77*, 211–220. https://doi.org/10.1007/s10584-006-9101-y

Dakhel, P. M. (2005). *Modeling of Particulate Matter Creation and Evolution in Aircraft Engines, Plumes and Particle Sampling Systems* [MSc. Thesis, Massachusetts Institute of Technology]. https://dspace.mit.edu/handle/1721.1/32452

Daley, B. (2016). *Air transport and the environment*. Taylor & Francis.

de Vries, I. E., Janssens, M., & Hulshoff, S. J. (2020). A specialised delivery system for stratospheric sulphate aerosols (part 2): Financial cost and equivalent CO_2 emission. *Climatic Change*, *162*, 87–103. https://doi.org/10.1007/s10584-020-02686-6

Dunne, E. M., Gordon, H., Kürten, A., Almeida, J., Duplissy, J., Williamson, C., Ortega, I. K., Pringle, K. J., Adamov, A., Baltensperger, U., Barmet, P., Benduhn, F., Bianchi, F., Breitenlechner,

M., Clarke, A., Curtius, J., Dommen, J., Donahue, N. M., Ehrhart, S., … Carslaw, K. S. (2016). Global atmospheric particle formation from CERN CLOUD measurements. *Science*, *354 (6316)*, 1119–1124. https://doi.org/10.1126/science.aaf2649

Duplissy, J., Merikanto, J., Franchin, A., Tsagkogeorgas, G., Kangasluoma, J., Wimmer, D., Vuollekoski, H., Schobesberger, S., Lehtipalo, K., Flagan, R. C., Brus, D., Donahue, N. M., Vehkamäki, H., Almeida, J., Amorim, A., Barmet, P., Bianchi, F., Breitenlechner, M., Dunne, E. M., … Kulmala, M. (2016). Effect of ions on sulfuric acid-water binary particle formation: 2. experimental data and comparison with qc-normalized classical nucleation theory. *Journal of Geophysical Research: Atmospheres*, *121 (4)*, 1752–1775. https://doi.org/10.1002/2015JD023539

Dürbeck, T., & Gerz, T. (1995). *Large-eddy simulation of aircraft exhaust plumes in the free atmosphere-effective diffusivities and cross-sections. Advances in Turbulence VI. Fluid Mechanics and its Applications, vol 36.* Springer, Dordrecht. https://doi.org/10.1007/978-94-009-0297-8_4

Einstein, A. (1905). Über die von der molekularkinetischen Theorie der Wärme geforderte Bewegung von in ruhenden Flüssigkeiten suspendierten Teilchen. *Annalen der Physik*, *322 (8)*, 549–560. https://doi.org/10.1002/andp.19053220806

EUMETSAT. (2004). *Contrails over Benelux, North Sea & Baltic Sea*. Retrieved June 2, 2022, from https://www.eumetsat.int/contrails-over-benelux-north-sea-baltic-sea

Fahey, D. W., Keim, E. R., Boering, K. A., Brock, C. A., Wilson, J. C., Jonsson, H. H., Anthony, S., Hanisco, T. F., Wennberg, P. O., Miake-Lye, R. C., Salawitch, R. J., Louisnard, N., Woodbridge, E. L., Gao, R. S., Donnelly, S. G., Wamsley, R. C., Negro, L. A. D., Solomon, S., Daube, B. C., … Chan, K. R. (1995). Emission Measurements of the Concorde Supersonic Aircraft in the Lower Stratosphere. *Science*, *270 (5233)*, 70–74. https://doi.org/10.1126/science.270.5233.70

Fialkov, A. B. (1997). Investigations on ions in flames. *Progress in Energy and Combustion Science*, *23 (5-6)*, 399–528. https://doi.org/10.1016/S0360-1285(97)00016-6

Fick, A. (1855). Ueber Diffusion. *Annalen der Physik*, *170 (1)*, 59–86. https://doi.org/10.1002/andp.18551700105

Fletcher, N. H. (1958). Size Effect in Heterogeneous Nucleation. *Journal of Chemical Physics*, *29 (3)*. https://doi.org/10.1063/1.1744540

Floerchinger, C., Dykema, J., Keith, D., & Keutsch, F. (2020). A need for in situ observations to inform nearfield plume transport and aerosol dynamics as well as chemistry of alternate geoengineering materials in the stratosphere [Letter to the National Academy of Science]. https://geoengineering.environment.harvard.edu/projects

Flood, H. (1934). Tröpfchenbildung in übersättigten Äthylalkohol-Wasserdampfgemischen. *Zeitschrift für Physikalische Chemie*, *A 170*, 280. https://doi.org/10.1515/zpch-1934-17026

Forstall Jr., W., & Shapiro, A. H. (1950). Momentum and Mass Transfer in Coaxial Gas Jets. *Journal of Applied Mechanics*, *17 (4)*, 399–408. https://doi.org/10.1115/1.4010167

Franke, J., Hirsch, C., Jensen, A. G., Krüs, H. W., Schatzmann, M., Westbury, P. S., Miles, S. D., Wisse, J. A., & Wright, N. G. (2004). Recommendations on the use of CFD in wind engineering.

Frenzel, A., & Arnold, F. (1994). Sulfuric acid cluster ion formation by jet engines: Implications for sulfuric acid formation and nucleation. *DLR-Mitt 94-06, DLR, D-51140 Köln*, 106–112.

Friedl, R. R., Anderson, B. E., Liou, K.-N., Singh, H. B., Field, M., Wuebbles, C. J. D., Seattle, S. L. B. B. C., Hallett, W. J., Rasch, N. J. P., Sassen, K., & Williams, L. R. (1997). *Atmospheric Effects of Subsonic Aircraft: Interim Assessment Report of the Advanced Subsonic Technology Program*. NASA, (No. NAS 1.61: 1400).

Friedlander, S. K., & Wang, C. S. (1966). The Self-Preserving Particle Size Distribution for Coagulation by Brownian Motion. *Journal of Colloid and Interface Science*, *22 (2)*, 126–132. https://doi.org/10.1016/0021-9797(66)90073-7

Friend, J. P., Barnes, R. A., & Vasta, R. M. (1980). Nucleation by free radicals from the photooxidation of sulfur dioxide in air. *Journal of Physical Chemistry*, *84 (19)*, 2423–2436. https://doi.org/10.1021/j100456a018

Fritz, T. M. (2018). *Micro-Physical Modeling of Aircraft Exhaust Plumes and Condensation Trails* [MSc. Thesis, Massachusetts Institute of Technology]. https://dspace.mit.edu/handle/1721.1/119298?show=full

Fritz, T. M., Eastham, S. D., Speth, R. L., & Barrett, S. R. (2020). The role of plume-scale processes in long-term impacts of aircraft emissions. *Atmospheric Chemistry and Physics*, *20 (9)*, 5697–5727. https://doi.org/10.5194/acp-20-5697-2020

Fuchs, N. A. (1964). *The Mechanics of Aerosols* (Rev. and enlarged ed.) [translated from Russian by R.E. Daisley and M. Fuchs; translation edited by C.N. Davies.]. Pergamon.

Fuchs, N. A., & Sutugin, A. G. (1971). *Topics in Current Aerosol Research: High-Dispersed Aerosols* (1st ed.) [edited by G. M. Hidy and J. R. Brock]. Pergamon.

Garnier, F., Baudoin, C., Woods, P., & Louisnard, N. (1997). Engine emission alteration in the near field of an aircraft. *Atmospheric Environment*, *31 (12)*, 1767–1781. https://doi.org/10.1016/S1352-2310(96)00329-9

Gerz, T., Dürbeck, T., & Konopka, P. (1998). Transport and effective diffusion of aircraft emissions. *Journal of Geophysical Research: Atmospheres*, *103 (D20)*, 25905–25913. https://doi.org/10.1029/98JD02282

Gmitro, J. I., & Vermeulen, T. (1964). Vapor-Liquid Equilibria for Aqueous Sulfuric Acid. *A.I.Ch.E. Journal*, *10 (5)*, 740–746. https://doi.org/10.1002/aic.690100531

Golja, C. M., Chew, L. W., Dykema, J. A., & Keith, D. W. (2021). Aerosol dynamics in the near field of the scopex stratospheric balloon experiment. *Journal of Geophysical Research: Atmospheres*, *126 (4)*. https://doi.org/10.1029/2020JD033438

Hamill, P. (1975). The time dependent growth of H_2O-H_2SO_4 aerosols by heteromolecular condensation. *Journal of Aerosol Science*, *6 (6)*, 475–482. https://doi.org/10.1016/0021-8502(75)90064-6

Hamill, P., Kiang, C. S., & Cadle, R. D. (1977). The Nucleation of H_2SO_4-H_2O Solution Aerosol Particles in the Stratosphere. *Journal of the Atmospheric Sciences*, *34 (1)*, 150–162. https://doi.org/10.1175/1520-0469(1977)034<0150:TNOHHS>2.0.CO;2

Hamill, P., Toon, O. B., & Kiang, C. S. (1977). Microphysical Processes Affecting Stratospheric Aerosol Particles. *Journal of the Atmospheric Sciences*, *34 (7)*, 1104–1119. https://doi.org/10.1175/1520-0469(1977)034<1104:MPASAP>2.0.CO;2

Hamill, P., Turco, R. P., Kiang, C. S., Toon, O. B., & Whitten, R. C. (1982). An analysis of various nucleation mechanisms for sulfate particles in the stratosphere. *Journal of Aerosol Science*, *13 (6)*, 561–585. https://doi.org/10.1016/0021-8502(82)90021-0

Hamill, P., & Yue, G. K. (1979). A simplified model for the production of sulfate aerosols. *Environmental and Climatic Impact of Coal Utilization*, 255–274.

Haverkamp, H., Wilhelm, S., Sorokin, A., & Arnold, F. (2004). Positive and negative ion measurements in jet aircraft engine exhaust: Concentrations, sizes and implications for aerosol formation. *Atmospheric Environment*, *38 (18)*, 2879–2884. https://doi.org/10.1016/j.atmosenv.2004.02.028

Heist, R. H., & Reiss, H. (1974). Hydrates in supersaturated binary sulfuric acid-water vapor. *The Journal of Chemical Physics*, *61 (2)*, 573–581. https://doi.org/10.1063/1.1681932

Hofmann, D. J., & Rosen, J. M. (1978). Balloon observations of a particle layer injected by a stratospheric aircraft at 23 km. *Geophysical Research Letters*, *5 (6)*, 511–514. https://doi.org/10.1029/GL005i006p00511

Hyman, J., Shashkov, M., & Steinberg, S. (1997). The Numerical Solution of Diffusion Problems in Strongly Heterogeneous Non-isotropic Materials. *Journal of Computational Physics*, *132 (1)*(1), 130–148. https://doi.org/10.1006/jcph.1996.5633

Irvine, P., Emanuel, K., He, J., Horowitz, L. W., Vecchi, G., & Keith, D. (2019). Halving warming with idealized solar geoengineering moderates key climate hazards. *Nature Climate Change*, *9*, 295–299. https://doi.org/10.1038/s41558-019-0398-8

Irvine, P. J., Kravitz, B., Lawrence, M. G., & Muri, H. (2016). An overview of the earth system science of solar geoengineering. *Wiley Interdisciplinary Reviews: Climate Change*, *7*, 815–833. https://doi.org/10.1002/wcc.423

Jacobson, M. Z. (2005). *Fundamentals of Atmospheric Modeling* (2nd ed.). Cambridge University Press.

Jacobson, M. Z. (2011). Numerical Solution to Drop Coalescence/Breakup with a Volume-Conserving, Positive-Definite, and Unconditionally Stable Scheme. *Journal of the Atmospheric Sciences*, *68 (2)*, 334–346. https://doi.org/10.1175/2010JAS3605.1

Jacobson, M. Z., & Turco, R. P. (1995). Simulating condensational growth, evaporation, and coagulation of aerosols using a combined moving and stationary size grid. *Aerosol Science and Technology*, *22 (1)*, 73–92. https://doi.org/10.1080/02786829408959729

Jaecker-Voirol, A., Mirabel, P., & Reiss, H. (1987). Hydrates in supersaturated binary sulfuric acid-water vapor: A reexamination. *The Journal of Chemical Physics*, *87 (8)*, 4849–4852. https://doi.org/10.1063/1.452847

Janssens, M., de Vries, I. E., & Hulshoff, S. J. (2020). A specialised delivery system for stratospheric sulphate aerosols: Design and operation. *Climatic Change*, *162*, 67–85. https://doi.org/10.1007/s10584-020-02740-3

Jones, W. P., & Launder, B. E. (1972). The prediction of laminarization with a two-equation model of turbulence. *International Journal of Heat and Mass Transfer*, *15 (2)*, 301–314. https://doi.org/10.1016/0017-9310(72)90076-2

Kärcher, B. (1995). A trajectory box model for aircraft exhaust plumes. *Journal of Geophysical Research: Atmospheres*, *100 (D9)*, 18835–18844. https://doi.org/10.1029/95JD01638

Kärcher, B. (1998). Physicochemistry of aircraft-generated liquid aerosols, soot, and ice particles 1. Model description. *Journal of Geophysical Research: Atmospheres*, *103 (d14)*, 17111–17128. https://doi.org/10.1029/98JD01044

Kärcher, B. (1999). Aviation-Produced Aerosols and Contrails. *Surveys in Geophysics*, *20*, 113–167. https://doi.org/10.1023/A:1006600107117

Kiang, C. S., Cadle, R. D., & Yue, G. K. (1975). H_2SO_4-HNO_3-H_2O ternary aerosol formation mechanism in the stratosphere. *Geophysical Research Letters*, *2 (2)*, 41–44. https://doi.org/10.1029/GL002i002p00041

Kiendler, A., Aberle, S., & Arnold, F. (2000). Negative chemiions formed in jet fuel combustion: New insights from jet engine and laboratory measurements using a quadrupole ion trap mass spectrometer apparatus. *Atmospheric Environment*, *34 (16)*, 2623–2632. https://doi.org/10.1016/S1352-2310(99)00475-6

Kirkby, J., Curtius, J., Almeida, J., Dunne, E., Duplissy, J., Ehrhart, S., Franchin, A., Gagné, S., Ickes, L., Kürten, A., Kupc, A., Metzger, A., Riccobono, F., Rondo, L., Schobesberger, S., Tsagkogeorgas, G., Wimmer, D., Amorim, A., Bianchi, F., … Kulmala, M. (2011). Role of sulphuric acid, ammonia and galactic cosmic rays in atmospheric aerosol nucleation. *Nature*, *476 (7361)*, 429–435. https://doi.org/10.1038/nature10343

Kraabøl, A. G., Konopka, P., Stordal, F., & Schlager, H. (2000). Modelling chemistry in aircraft plumes 1: Comparison with observations and evaluation of a layered approach. *Atmospheric Environment*, *34 (23)*, 3939–3950. https://doi.org/10.1016/S1352-2310(00)00156-4

Kulmala, M., & Laaksonen, A. (1990). Binary nucleation of water–sulfuric acid system: Comparison of classical theories with different H2SO4 saturation vapor pressures. *Journal of Chemical Physics*, *93 (996)*. https://doi.org/10.1063/1.459519

Laakso, L., Mäkelä, J. M., Pirjola, L., & Kulmala, M. (2002). Model studies on ion-induced nucleation in the atmosphere. *Journal of Geophysical Research: Atmospheres*, *107 (20)*, AAC 5-1 - AAC 5–19. https://doi.org/10.1029/2002JD002140

Laaksonen, A., & Napari, I. (2001). Breakdown of the Capillarity Approximation in Binary Nucleation: A Density Functional Study. *Journal of Physical Chemistry B*, *105 (47)*. https://doi.org/10.1021/jp0116454

Lai, F. S., Friedlander, S. K., Pich, J., & Hidy, G. M. (1972). The Self-Preserving Particle Size Distribution for Brownian Coagulation in the Free-Molecule Regime. *Journal of Colloid and Interface Science*, *39 (2)*, 395–405. https://doi.org/10.1016/0021-9797(72)90034-3

Lindsey, R., & Dahlman, L. (2022). *Climate Change: Global Temperature*. NOAA National Centers for Environmental Information. https://www.climate.gov/news-features/understanding-climate/climate-change-global-temperature

Lovejoy, E. R., Curtius, J., & Froyd, K. D. (2004). Atmospheric ion-induced nucleation of sulfuric acid and water. *Journal of Geophysical Research D: Atmospheres*, *109 (8)*. https://doi.org/10.1029/2003JD004460

Määttänen, A., Merikanto, J., Henschel, H., Duplissy, J., Makkonen, R., Ortega, I. K., & Vehkamäki, H. (2017). New parameterizations for neutral and ion-induced sulfuric acid-water particle formation in nucleation and kinetic regimes. *Journal of Geophysical Research: Atmospheres*, *123*, 1269–1296. https://doi.org/10.1002/2017JD027429

Määttänen, A., Vehkamäki, H., Lauri, A., Napari, I., & Kulmala, M. (2007). Two-component heterogeneous nucleation kinetics and an application to Mars. *Journal of Chemical Physics*, *127 (13)*. https://doi.org/10.1063/1.2770737

McGrath, M. J., Olenius, T., Ortega, I., Loukonen, V., Paasonen, P., Kurtén, T., Kulmala, M., & Vehkamäki, H. (2012). Atmospheric Cluster Dynamics Code: a flexible method for solution of the birth-death equations. *Atmospheric Chemistry and Physics*, *12 (5)*, 2345–2355. https://doi.org/10.5194/acp-12-2345-2012

Merikanto, J., Duplissy, J., Määttänen, A., Henschel, H., Donahue, N. M., Brus, D., Schobesberger, S., Kulmala, M., & Vehkamäki, H. (2016). Effect of ions on sulfuric acid-water binary particle formation: 1. Theory for kinetic- and nucleation-type particle formation and atmospheric implications. *Journal of Geophysical Research*, *121 (4)*, 1736–1751. https://doi.org/10.1002/2015JD023538

Merikanto, J., Zapadinsky, E., Lauri, A., & Vehkamäki, H. (2007). Origin of the failure of classical nucleation theory: Incorrect description of the smallest clusters. *Physical Review Letters*, *98 (14)*. https://doi.org/10.1103/PhysRevLett.98.145702

Miller, T. M., Ballenthin, J. O., Hunton, D. E., Viggiano, A. A., Wey, C. C., & Anderson, B. E. (2003). Nitric acid emission from the f100 jet engine. *Journal of Geophysical Research: Atmospheres*, *108 (D1)*, ACH 10-1 - ACH 10–9. https://doi.org/10.1029/2001JD001522

Mirabel, P., & Reiss, H. (1987). Resolution of the "Renninger-Wilemski problem" concerning the identification of heteromolecular nuclei. *Langmuir*, *3 (2)*, 228–234. https://doi.org/10.1021/la00074a015

Modgil, M. S., Kumar, S., Tripathi, S. N., & Lovejoy, E. R. (2005). A parameterization of ion-induced nucleation of sulphuric acid and water for atmospheric conditions. *Journal of Geophysical Research: Atmospheres*, *110 (D 19)*. https://doi.org/10.1029/2004JD005475

Murphy, D. M., & Koop, T. (2005). Review of the vapour pressures of ice and supercooled water for atmospheric applications. *Quarterly Journal of the Royal Meteorological Society*, *131 (608)*, 1539–1565. https://doi.org/10.1256/qj.04.94

Noppel, M., Vehkamäki, H., & Kulmala, M. (2002). An improved model for hydrate formation in sulfuric acid-water nucleation. *Journal of Chemical Physics*, *116 (1)*, 218–228. https://doi.org/10.1063/1.1423333

Paoli, R., & Shariff, K. (2016). Contrail modeling and simulation. *Annual Review of Fluid Mechanics*, *48*, 393–427. https://doi.org/10.1146/annurev-fluid-010814-013619

Paoli, R., Vancassel, X., Garnier, F., & Mirabel, P. (2008). Large-eddy simulation of a turbulent jet and a vortex sheet interaction: Particle formation and evolution in the near field of an aircraft wake. *Meteorologische Zeitschrift*, *17 (2)*, 131–144. https://doi.org/10.1127/0941-2948/2008/0278

Penner, J. E., Lister, D., Griggs, D. J., Dokken, D. J., & McFarland, M. (1999). *Aviation and the global atmosphere: a special report of the Intergovernmental Panel on Climate Change (IPCC)*. Cambridge University Press.

Petry, H., Hendricks, J., Möllhoff, M., Lippert, E., Meier, A., Ebel, A., & Sausen, R. (1998). Chemical conversion of subsonic aircraft emissions in the dispersing plume: Calculation of effective emission indices. *Journal of Geophysical Research: Atmospheres*, *103 (D5)*, 5759–5772. https://doi.org/10.1029/97JD03749

Picht, J., Friedlander, S. K., & Lai, F. S. (1970). The self-preserving particle size distribution for coagulation by brownian motion - III. Smoluchowski Coagulation and simultaneous Maxwellian Condensation*. *Journal of Aerosol Science*, *1 (2)*, 115–126. https://doi.org/10.1016/0021-8502(70)90015-7

Pierce, J. R., Weisenstein, D. K., Heckendorn, P., Peter, T., & Keith, D. W. (2010). Efficient formation of stratospheric aerosol for climate engineering by emission of condensible vapor from aircraft. *Geophysical Research Letters*, *37*. https://doi.org/10.1029/2010GL043975

Poling, B. E., Prausnitz, J. M., & O'Connell, J. P. (2001). *The Properties of Gases and Liquids* (5th ed.). McGraw-Hill.

Preining, O., Wagner, P. E., Pohl, F. G., & Szymanski, W. (1981). *Heterogeneous nucleation and droplet growth, report*. Institute of Experimental Physics, University of Vienna.

Priezjev, N. V. (2020). Diffusion and Kinetics. Lecture: Solidification and Growth Kinetics. *Wright State University*. Retrieved July 22, 2022, from http://www.wright.edu/~nikolai.priezjev/papers/Lecture_7_Ch_4_solidification.pdf

Pueschel, R. F., Snetsinger, K. G., Goodman, J. K., Toon, O. B., Ferry, G. V., Oberbeck, V. R., Livingston, J. ., Verma, S., Fong, W., Starr, W., & Chan, K. (1989). Condensed nitrate, sulfate, and chloride in Antarctic stratospheric aerosols. *Journal of Geophysical Research: Atmospheres*, *94 (D9)*, 11271–11284. https://doi.org/10.1029/JD094iD09p11271

Quadros, F. D. A., Snellen, M., Sun, J., & Dedoussi, I. C. (2022). Global Civil Aviation Emissions Estimates for 2017–2020 Using ADS-B Data. *Journal of Aircraft*, *(article in advance)*. https://doi.org/10.2514/1.c036763

Rasch, P. J., Tilmes, S., Turco, R. P., Robock, A., Oman, L., Chen, C. C., Stenchikov, G. L., & Garcia, R. R. (2008). An overview of geoengineering of climate using stratospheric sulphate aerosols. *Philosophical Transactions of the Royal Society A: Mathematical, Physical and Engineering Sciences*, *366*, 4007–4037. https://doi.org/10.1098/rsta.2008.0131

Reiss, H. (1950). The Kinetics of Phase Transitions in Binary Systems. *Journal of Chemical Physics*, *18 (6)*. https://doi.org/10.1063/1.1747784

Reynolds, O. (1895). IV. On the Dynamical Theory of Incompressible Viscous Fluids and the Determination of the Criterion. *Philosophical Transactions of the Royal Society of London. (A.)*, *186*, 123–164. https://doi.org/10.1098/rsta.1895.0004

Roberts, P. J., & Webster, D. R. (2002). Turbulent diffusion. *Environmental Fluid Mechanics - Theories and Application*, 7–47.

Rumsey, C. (2017). *Implementing Turbulence Models into the Compressible RANS Equations*. Langley Research Center. https://turbmodels.larc.nasa.gov/implementrans.html

Sander, S. P., Friedl, R. R., Ravishankara, A. R., Kolb, C. E., Nasa, M. J. K., Washington, H., Molina, D. C. M. J., Moortgat, G. K., Keller-Rudek, H., Finlayson-Pitts, B. J., Wine, P. H., Huie, R. E., &

Orkin, V. L. (2006). *Chemical kinetics and photochemical data for use in atmospheric studies: Evaluation number 15*. NASA Panel for Data Evaluation, JPL Publication 06-2. http://jpldataeval.jpl.nasa.gov/

Savel'ev, A. M., & Starik, A. M. (2006). Interaction of Ions and Electrons with Nanoparticles in Hydrocarbon Combustion Plasmas. *Technical Physics*, *51 (4)*, 444–452. https://doi.org/10.1134/S1063784206040086

Schumann, U., Arnold, F., Busen, R., Curtius, J., Kärcher, B., Kiendler, A., Petzold, A., Schlager, H., Schröder, F., & Wohlfrom, K. H. (2002). Influence of fuel sulfur on the composition of aircraft exhaust plumes: The experiments sulfur 1-7. *Journal of Geophysical Research: Atmospheres*, *107 (15)*, AAC 2-1 - AAC 2–27. https://doi.org/10.1029/2001JD000813

Schumann, U., Schlager, H., Arnold, F., Baumann, R., Haschberger, P., & Klemm, O. (1998). Dilution of aircraft exhaust plumes at cruise altitudes. *Atmospheric Environment*, *32 (18)*, 3097–3103. https://doi.org/10.1016/S1352-2310(97)00455-X

Schumann, U., Ström, J., Busen, R., Baumann, R., Gierens, K., Krautstrunk, M., Schröder, F. P., & Stingl, J. (1996). In situ observations of particles in jet aircraft exhausts and contrails for different sulfur-containing fuels. *Journal of Geophysical Research: Atmospheres*, *101 (D3)*, 6853–6869. https://doi.org/10.1029/95JD03405

Seinfeld, J. H., & Pandis, S. N. (2016). *Atmospheric Chemistry and Physics : From Air Pollution to Climate Change* (3th ed.). John Wiley & Sons.

Shepherd, J. G., Caldeira, K., Cox, P., Haigh, J., Keith, D., Launder, B. E., Mace, G., MacKerron, G., Pyle, J., Raynor, S., Redgwell, C., & Watson, A. (2009). *Geoengineering the Climate: Science, governance and uncertainty* (Vol. 10/09) [Royal Society policy document]. The Royal Society Publishing, London. https://royalsociety.org/~/media/royal_society_content/policy/publications/2009/8693.pdf

Smits, A. (1999). *A Physical Introduction to Fluid Mechanics* (1st ed.). Wiley & Sons.

Starik, A. M. (2007). Gaseous and particulate emissions with jet engine exhaust and atmospheric pollution. *NATO - STO*, *RTO-EN-AVT-150*. https://www.sto.nato.int/publications/Pages/default.aspx

Starik, A., Popovicheva, O. B., Savel'ev, A. M., Titova, N. S., & Rein, O. E. (2006). *On the effects of processes inside the engine and in the exhaust plume on the CCN activation of combustion particles. Chemical Engineering Transaction* (Ed. by E. Ranzi). Proceedings of Advanced Atmospheric Aerosol Symposium, 10, 541-546. https://www.researchgate.net/publication/247778091_On_mechanisms_of_engine_soot_particle_activation_to_be_a_water_condensation_nuclei

Stauffer, D. (1976). Kinetic theory of two-component ("hetero-molecular") nucleation and condensation. *Journal of Aerosol Science*, *7 (4)*, 319–333. https://doi.org/10.1016/0021-8502(76)90086-0

Steele, H. M., & Hamill, P. (1981). Effects of temperature and humidity on the growth and optical properties of sulphuric acid—water droplets in the stratosphere. *Journal of Aerosol Science*, *12 (6)*, 517–528. https://doi.org/10.1016/0021-8502(81)90054-9

Stocker, T. (2011). *Introduction to Climate Modelling*. Springer Science & Business Media.

Sutherland, W. (1905). LXXV. A dynamical theory of diffusion for non-electrolytes and the molecular mass of albumin. *Philosophical Magazine Series 6 (1901-1925)*, *9 (54)*, 781–785. https://doi.org/10.1080/14786440509463331

Suzuki, K., & Mohnen, V. A. (1981). Binary homogeneous nucleation theory by cluster-cluster interaction with application to the H_2SO_4-H_2O system. *Journal of Aerosol Science*, *12 (1)*, 61–73. https://doi.org/10.1016/0021-8502(81)90012-4

Tabazadeh, A., Toon, O. B., Clegg, S. L., & Hamill, P. (1997). A new parameterization of H_2SO_4/H_2O aerosol composition: Atmospheric implications. *Geophysical Research Letters*, *24 (15)*. https://doi.org/10.1029/97GL01879

Tait, K. N., Khan, M. A. H., Bullock, S., Lowenberg, M. H., & Shallcross, D. E. (2022). Aircraft emissions, their plume-scale effects, and the spatio-temporal sensitivity of the atmospheric response: A review. *Aerospace*, *9 (7)*, 355. https://doi.org/10.3390/aerospace9070355

Tluk, A. (2023). Modelling of Sulfuric Acid Aerosols in an Engine Plume. [Unpublished manuscript]. *Faculty of Aerospace Engineering, Delft University of Technology*.

Tominaga, Y., & Stathopoulos, T. (2007). Turbulent Schmidt numbers for CFD analysis with various types of flowfield. *Atmospheric Environment*, *41 (37)*, 8091–8099. https://doi.org/10.1016/j.atmosenv.2007.06.054

Trachenko, K., & Brazhkin, V. V. (2020). Minimal quantum viscosity from fundamental physical constants. *Science Advances*, *6 (17)*. https://doi.org/10.1126/sciadv.aba3747

Turco, R. P., Hamill, P., Toon, O. B., Whitten, R. C., & Kiang, C. S. (1979). The NASA-Ames Research Center Stratospheric Aerosol Model. 1. Physical Processes and Computational Analogs. *NASA Technical Publication 1362*. https://ntrs.nasa.gov/citations/19790013550

Turco, R. P., & Yu, F. (1997). Aerosol invariance in expanding coagulating plumes. *Geophysical Research Letters*, *24 (10)*, 1223–1226. https://doi.org/10.1029/97GL01092

Turco, R. P., & Yu, F. (1998). Aerosol size distribution in a coagulating plume: Analytical behavior and modeling applications. *Geophysical Research Letters*, *25 (6)*, 927–930. https://doi.org/10.1029/98GL00324

Turco, R. P., & Yu, F. (1999). Particle size distributions in an expanding plume undergoing simultaneous coagulation and condensation. *Journal of Geophysical Research: Atmospheres*, *104 (D16)*, 19227–19241. https://doi.org/10.1029/1999JD900321

UNFCCC United Nations / Framework Convention on Climate Change. (2015). *Adoption of the Paris Agreement*. 21st Conference of the Parties, Paris: United Nations. https://unfccc.int/sites/default/files/english_paris_agreement.pdf

Unterstrasser, S., Paoli, R., Sölch, I., Kühnlein, C., & Gerz, T. (2014). Dimension of aircraft exhaust plumes at cruise conditions: Effect of wake vortices. *Atmospheric Chemistry and Physics*, *14 (5)*, 2713–2733. https://doi.org/10.5194/acp-14-2713-2014

van Pelt, T., Sinnige, T., & Raijmakers, E. (2020). *AE4115: Experimental Simulations* [Reader based on lectures by G. Eitelberg]. Delft University of Technology.

Vattioni, S., Weisenstein, D., Keith, D., Feinberg, A., Peter, T., & Stenke, A. (2019). Exploring accumulation-mode H_2SO_4 versus SO_2 stratospheric sulfate geoengineering in a sectional aerosol-chemistry-climate model. *Atmospheric Chemistry and Physics*, *19*, 4877–4897. https://doi.org/10.5194/acp-19-4877-2019

Vehkamäki, H., Kulmala, M., Napari, I., Lehtinen, K. E., Timmreck, C., Noppel, M., & Laaksonen, A. (2002). An improved parameterization for sulfuric acid-water nucleation rates for tropospheric and stratospheric conditions. *Journal of Geophysical Research Atmospheres*, *107 (D22)*, AAC 3-1 - AAC 3–10. https://doi.org/10.1029/2002JD002184

Viggiano, A. A., Perry, R. A., Albritton, D. L., Ferguson, E. E., & Fehsenfeld, F. C. (1980). Investigations on ions in flames. *Journal of Geophysical Research: Oceans*, *85 (C8)*, 4551–4555. https://doi.org/10.1029/JC085iC08p04551

Volmer, M., & Weber, A. Z. (1926). Nucleus formation in supersaturated systems. *Zeitschrift für Physikalische Chemie*, *119*, 277–301. https://doi.org/10.1515/zpch-1926-11927

von Helmholtz, R. (1886). Untersuchungen über Dämpfe und Nebel, besonders über solche von Lösungen. *Annalen der Physik*, *263 (4)*, 508–543. https://doi.org/10.1002/andp.18862630403

Wang, C. S., & Friedlander, S. K. (1967). The Self-Preserving Particle Size Distribution for Coagulation by Brownian Motion II. Small Particle Slip Correction and Simultaneous Shear Flow. *Journal of Colloid and Interface Science*, *24 (2)*, 170–179. https://doi.org/10.1016/0021-9797(67)90215-9

Weisenstein, D. K., Keith, D. W., & Dykema, J. A. (2015). Solar geoengineering using solid aerosol in the stratosphere. *Atmospheric Chemistry and Physics*, *15*, 11835–11859. https://doi.org/10.5194/acp-15-11835-2015

Weisenstein, D. K., Yue, G. K., Ko, M. K. W., Sze, N., Rodriguez, J. M., & Scott, C. J. (1997). A two-dimensional model of sulfur species and aerosols. *Journal of Geophysical Research: Atmospheres*, *102 (D11)*, 13019–13035. https://doi.org/10.1029/97JD00901

Wexler, A. (1971). Vapor Pressure Formulation for Water in Range 0 to 100 °C. A Revision. *Journal of Research National Bureau of Standards - A. Physics and Chemistry*, *80A (5-6)*, 775–785. https://doi.org/10.6028/jres.080A.071

Wilhelm, S., Eichkorn, S., Wiedner, D., Pirjola, L., & Arnold, F. (2004). Ion-induced aerosol formation: New insights from laboratory measurements of mixed cluster ions $HSO_4^- (H_2SO_4)_a (H_2O)_w$ and $H^+ (H_2SO_4)_n (H_2O)_m$. *Atmospheric Environment*, *38 (12)*, 1735–1744. https://doi.org/10.1016/j.atmosenv.2003.12.025

Yu, F. (2002). Altitude variations of cosmic ray induced production of aerosols: Implications for global cloudiness and climate. *Journal of Geophysical Research: Space Physics*, *107 (A7)*. https://doi.org/10.1029/2001JA000248

Yu, F. (2003). Nucleation rate of particles in the lower atmosphere: Estimated time needed to reach pseudo-steady state and sensitivity to H_2SO_4 gas concentration. *Geophysical Research Letters*, *30 (10)*. https://doi.org/10.1029/2003gl017084

Yu, F. (2005). Modified kelvin-thomson equation considering ion-dipole interaction: Comparison with observed ion-clustering enthalpies and entropies. *Journal of Chemical Physics*, *122 (8)*. https://doi.org/10.1063/1.1845395

Yu, F. (2006a). Effect of ammonia on new particle formation: A kinetic H_2SO_4-H_2O-NH_3 nucleation model constrained by laboratory measurements. *Journal of Geophysical Research: Atmospheres*, *111 (1)*. https://doi.org/10.1029/2005JD005968

Yu, F. (2006b). From molecular clusters to nanoparticles: Second-generation ion-mediated nucleation model. *Atmospheric Chemistry and Physics*, *6 (12)*, 5193–5211. https://doi.org/10.5194/acp-6-5193-2006

Yu, F., & Turco, R. P. (1997). The role of ions in the formation and evolution of particles in aircraft plumes. *Geophysical Research Letters*, *24*, 1927–1930. https://doi.org/10.1029/97GL01822

Yu, F., & Turco, R. P. (1998). The formation and evolution of aerosols in stratospheric aircraft plumes: Numerical simulations and comparisons with observations. *Journal of Geophysical Research Atmospheres*, *103 (D20)*, 25915–25934. https://doi.org/10.1029/98JD02453

Yu, F., & Turco, R. P. (2001). From molecular clusters to nanoparticles: Role of ambient ionization in tropospheric aerosol formation. *Journal of Geophysical Research Atmospheres*, *106 (D5)*, 4797–4814. https://doi.org/10.1029/2000JD900539

Yue, G. K., & Deepak, A. (1979). Modeling of coagulation-sedimentation effects on transmission of visible/IR laser beams in aerosol media. *Applied Optics*, *18 (23)*, 3918–3925. https://doi.org/10.1364/AO.18.003918

Yue, G. K., & Deepak, A. (1982). Temperature dependence of the formation of sulfate aerosols in the stratosphere. *Journal of Geophysical Research: Oceans*, *87 (C4)*, 3128–3134. https://doi.org/10.1029/jc087ic04p03128

Zannetti, P. (2013). *Air pollution modeling: theories, computational methods and available software*. Springer Science & Business Media.

Zeldovich, J. B. (1943). On the theory of new phase formation, cavitation. *Acta Physicochimica USSR*, *18*, 1–22. https://doi.org/10.1515/9781400862979.120

Zhao, J., & Turco, R. P. (1995). Nucleation simulations in the wake of a jet aircraft in stratospheric flight. *Journal of Aerosol Science*, *26 (5)*, 719–795. https://doi.org/10.1016/0021-8502(95)00010-A

A

Evolution of Water Vapor Concentrations in the Wake

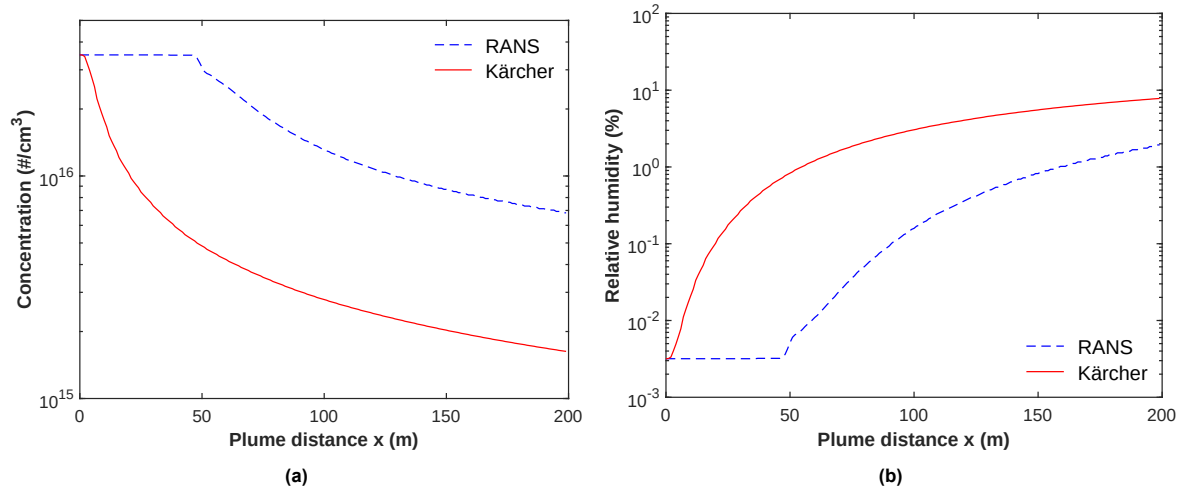

Figure A.1: (a) Evolution of the peak water vapor concentration versus plume distance for both the RANS simulation and box-model equation from Kärcher (1995). (b) Evolution of the relative humidity versus plume distance for both the RANS simulation and box-model equation from Kärcher (1995).

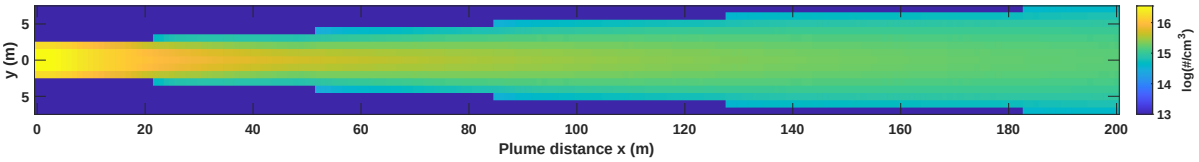

Figure A.2: Water vapor concentration distribution for an axisymmetric plume based on the peak concentration evolution from Kärcher (1995), and radial profile from RANS, section cut at $z = 0$ m. Values are log-scaled for illustrative purposes.

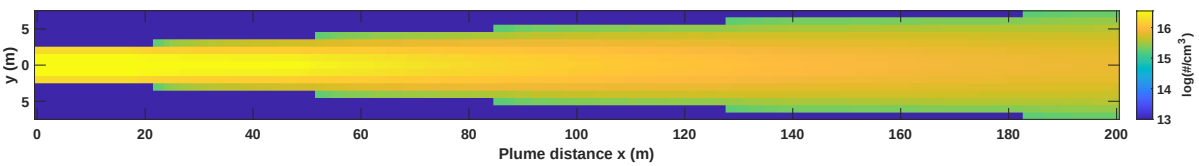

Figure A.3: Water vapor concentration distribution for an axisymmetric plume based on the RANS-resolved temperature distribution and $Le_t = 1$, section cut at $z = 0$ m. Values are log-scaled for illustrative purposes.

B

Supplemental Material on the Effects of Variations in Temperature and Relative Humidity

B.1. Mass difference between the Scaled and Critical Cluster

Kärcher

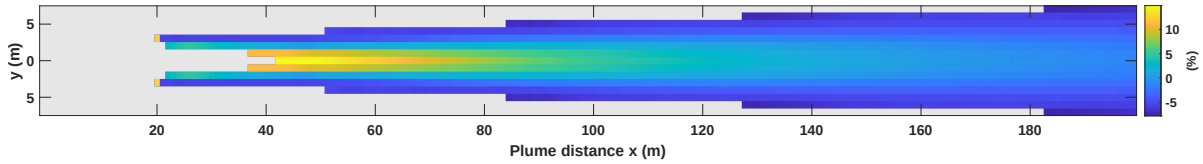

Figure B.1: A 2D section cut of the axisymmetric wake showing the percentage of mass which is added to, or subtracted from, the critical cluster to match the bin weight composition. Grey areas are locations where the nucleation rate lies below 1 particle/(cm^3 s).

RANS

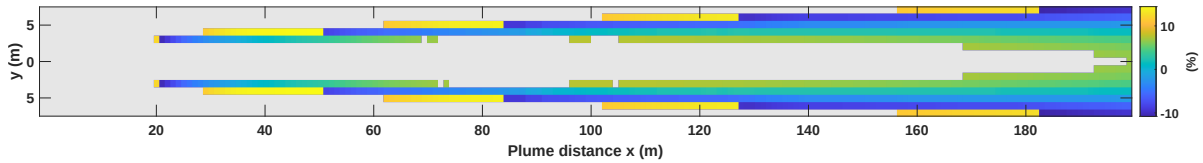

Figure B.2: A 2D section cut of the axisymmetric wake showing the percentage of mass which is added to, or subtracted from, the critical cluster to match the bin weight composition. Grey areas are locations where the nucleation rate lies below 1 particle/(cm^3 s).

B.2. Number Densities of Sulfuric Acid Vapor in the Wake

Kärcher

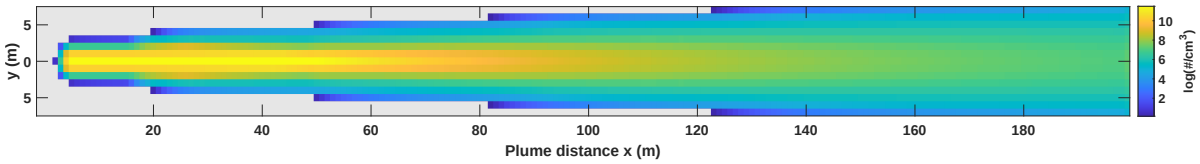

Figure B.3: A 2D section cut of the axisymmetric wake showing the number density distribution of sulfuric acid vapor. Grey areas are locations where no vapor resides.

RANS

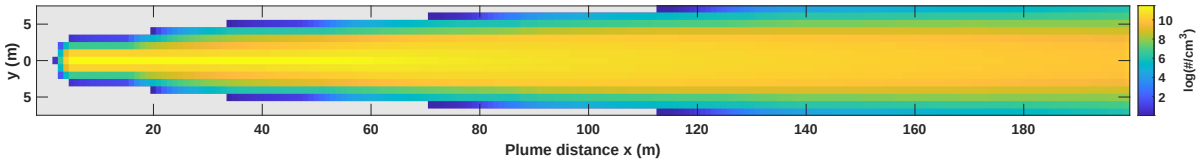

Figure B.4: A 2D section cut of the axisymmetric wake showing the number density distribution of sulfuric acid vapor. Grey areas are locations where no vapor resides.

B.3. Number Densities of Aerosol in the Wake

Kärcher

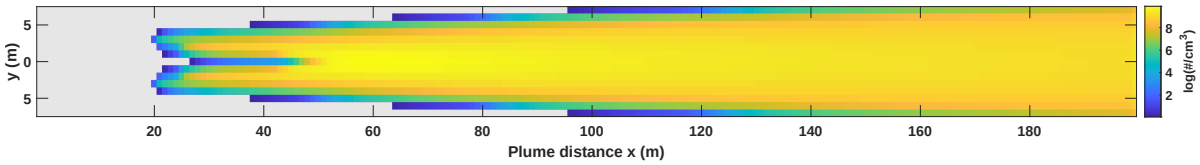

Figure B.5: A 2D section cut of the axisymmetric wake showing the number density distribution of aerosol. Grey areas are locations where no aerosol resides.

RANS

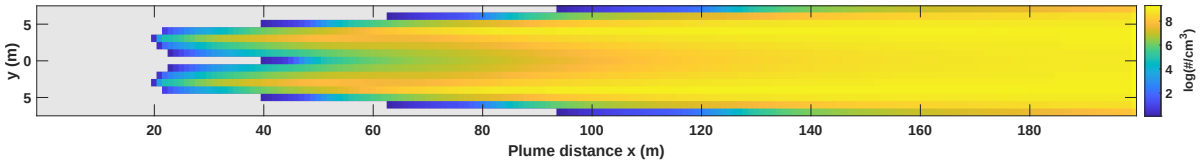

Figure B.6: A 2D section cut of the axisymmetric wake showing the number density distribution of aerosol. Grey areas are locations where no aerosol resides.

C

Supplemental Material on the Effects of Increased Concentrations

C.1. Particle Size Distribution with Unregulated Microphysics

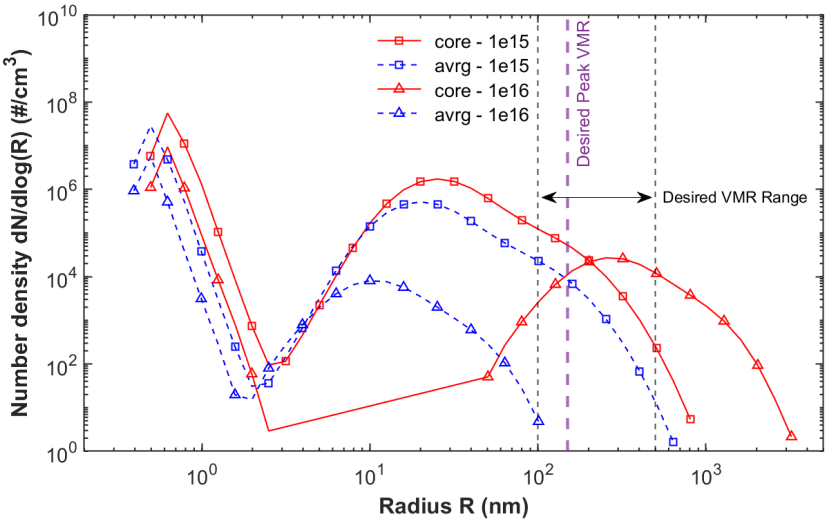

Figure C.1: Approximate number densities versus radius of volatile aerosol particles in the early jet regime at 200 m of plume distance. Perceived H_2SO_4 concentrations are not limited in the nucleation routine and lie outside the validity ranges. The desired range of volume-mean radii of the population at the end of the early growth period is shown by the vertical dashed lines, including the desired peak at 0.15 µm.

C.2. Locations of charged barrierless kinetic particle formation

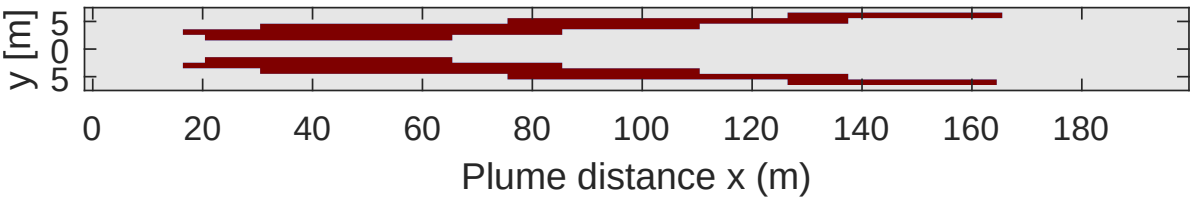

Figure C.2: A 2D section cut of the axisymmetric wake showing the areas where charged kinetic particle formation occurs. Grey areas are locations where no barrierless kinetic particle formation is possible due to insufficient vapor concentration.